RICE UNIVERSITY

Advanced transition metal phosphide materials from single-source molecular precursors

by

Adam Caleb Colson

A THESIS SUBMITTED
IN PARTIAL FULFILLMENT OF THE
REQUIREMENTS FOR THE DEGREE

Doctor of Philosophy

APPROVED, THESIS COMMITTEE

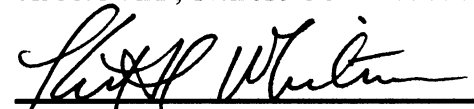

Kenton H. Whitmire, Chair
Professor of Chemistry
Associate Dean for Academic Affairs
Wiess School of Natural Sciences

Lon J. Wilson
Professor of Chemistry

Emilia Morosan
Assistant Professor of Physics and
Astronomy and Chemistry

HOUSTON, TEXAS
December 2011

Abstract

Advanced transition metal phosphide materials from single-source molecular precursors

by

Adam Caleb Colson

In this thesis, the feasibility of employing organometallic single-source precursors in the preparation of advanced transition metal pnictide materials such as colloidal nanoparticles and films has been investigated. In particular, the ternary FeMnP phase was targeted as a model for preparing advanced heterobimetallic phosphide materials, and the iron-rich Fe_3P phase was targeted due to its favorable ferromagnetic properties as well as the fact that the preparation of advanced Fe_3P materials has been elusive by commonly used methods.

Progress towards the synthesis of advanced $Fe_{2-x}Mn_xP$ nanomaterials and films was facilitated by the synthesis of the novel heterobimetallic complexes $FeMn(CO)_8(\mu\text{-}PR^1R^2)$ (R^1 = H, R^2 = H or R^1 = H, R^2= Ph), which contain the relatively rare μ-PH2 and μ-PPhH functionalities. Iron rich $Fe_{2-x}Mn_xP$ nanoparticles were obtained by thermal decomposition of $FeMn(CO)_8(\mu\text{-}PH_2)$ using solution-based synthetic methods, and empirical evidence suggested that oleic acid was responsible for manganese depletion. Films containing Fe, Mn, and P with the desired stoichiometric ratio of 1:1:1 were prepared using $FeMn(CO)_8(\mu\text{-}PH_2)$ in a simple low-pressure metal-organic chemical vapor deposition (MOCVD) apparatus. Although the elemental composition of the precursor was conserved in the

deposited film material, spectroscopic evidence indicated that the films were not composed of pure-phase FeMnP, but were actually mixtures of crystalline FeMnP and amorphous FeP and Mn_xO_y.

A new method for the preparation of phase-pure ferromagnetic Fe_3P films on quartz substrates has also been developed. This approach involved the thermal decomposition of the single-source precursors $H_2Fe_3(CO)_9PR$ (R = ^{t}Bu or Ph) at 400 °C. The films were deposited using a simple home-built MOCVD apparatus and were characterized using a variety of analytical methods. The films exhibited excellent phase purity, as evidenced by X-ray diffraction, X-ray photoelectron spectroscopy, and field-dependent magnetization measurements, the results of which were all in good agreement with measurements obtained from bulk Fe_3P. As-deposited Fe_3P films were found to be amorphous, and little or no magnetic hysteresis was observed in plots of magnetization versus applied field. Annealing the Fe_3P films at 550 °C resulted in improved crystallinity as well as the observation of magnetic hysteresis.

Acknowledgments

During my time at Rice, I have benefited from a tremendous amount of support, guidance, and fellowship from friends, colleagues, and mentors, and I would be remiss if I did not acknowledge the individuals who have made this work possible. First, I would like to express my gratitude to Professor Kenton H. Whitmire for accepting the challenge of mentoring an uncultured and stubborn aspiring scientist from rural Idaho. In addition to teaching me a great deal about inorganic chemistry, he has also taught me about temperance, patience, and industriousness, and I am truly a better person for having spent time in his research group. I would also like to thank Professor Lon J. Wilson for being a member of my thesis committee and for chairing my qualifying exam committee, in addition to being an excellent source of professional and personal advice. My thanks are also extended to Professor Emilia Morosan for agreeing to be a member of my thesis committee and especially for being an ideal collaborator.

I am grateful to the past and present members of the Whitmire research group for providing a welcoming and warm environment. Thanks to Dr. Cristina Hofmann, Dr. Anna Kelly, and Dr. Trinanjana Mandal for pointing me in the right direction, and thanks to Sean Walsh for having the metaphorical (and literal) fire extinguisher ready all these years. I am also indebted to the many friends I have made in the chemistry department who have lifted my spirits when I've been discouraged and who have been a sounding board to my occasional frustrations.

I would also like to acknowledge Chih-Wei Chen from the Morosan research group for his diligence and professionalism in obtaining magnetic measurements, and I wish him success in his own research efforts. Additionally, I would like to thank Dr. Caroline McNeil for her help in teaching and her assistance with GC-MS data collection.

I am indebted to the research scientists from the Chemistry Department and the Shared Equipment Authority, especially Richard Crouse, Dr. Bo Chen, Dr. Wenh Guo, Dr. Christopher Pennington, and Dr. Lawrence B. Alemany. Without their tireless efforts, none of this work would have been possible. I would also like to acknowledge the support and guidance of the Rice University faculty and staff who have selflessly given logistical, professional, and personal advice.

I will be forever grateful for the support and encouragement of my family members. I thank my mom and dad for the daily sacrifice of their time and resources that they have made on my behalf for over three decades. They are my heroes and they have always kept me grounded in reality. I also thank my grandparents, in-laws, and extended family for teaching me about the important things in life. My wife Jenna will never know how much she means to me, and I do not have the words to express my gratitude for the sacrifices she has made over the years. My son Caleb is the inspiration for everything I do, and he is my daily source of pride and joy.

Finally, I humbly acknowledge the Divine Presence that has given me strength and guided my path throughout my life.

Table of Contents

List of Figures

List of Tables

Chapter 1. General Introduction

1.1 Survey of the Bulk Metal Pnictides

Materials composed of transition metals and group 15 elements, commonly known as metal pnictides, have been the object of scientific inquiry for at least fifty years, due in large part to the diversity of physical, structural, and chemical properties observed among the many possible phases. This diversity can be explained by the fact that transition metals can readily adopt a variety of oxidation states and can therefore form a number of stoichiometric phases with Group 15 elements. The simplest metal pnictides have the general form M_AE_B, where M is a transition metal and E is a Group 15 element. The rich solid-state chemistry of the binary first row transition metal phosphides and arsenide is summarized in Table 1.1. Although Table 1.1 contains data for only the first ten metals of the transition series, more than fifty binary metal pnictide phases with unique stoichiometric compositions are represented. It is worth noting that most of the metals listed in Table 1.1 form both metal-rich and pnictide-rich phases.

Table 1.1 Binary phosphides and arsenides of the first row transition metals.

Sc	Ti	V	Cr	Mn	Fe	Co	Ni	Cu	Zn
Sc_3P	Ti_3P	V_3P	Cr_3P	Mn_3P	Fe_3P	Co_2P	Ni_3P	Cu_3P	Zn_3P_2
ScP	Ti_2P	V_2P	Cr_2P	Mn_2P	Fe_2P	CoP	Ni_2P	CuP_2	ZnP_2
ScAs	Ti_5P_3	VP	CrP	MnP	FeP	CoP_2	NiP_2	Cu_3As	ZnP_4
	TiP	VP_2	CrP_2	MnP_4	FeP_2	Co_2As	NiAs	Cu_2As	Zn_3As_2
	TiP_2	VP_4	CrP_4	Mn_3As	FeP_4	CoAs	$NiAs_2$		$ZnAs_2$
		V_3As	Cr_2As	Mn_2As	Fe_2As				
		VAs	CrAs	MnAs	FeAs				
		VAs_2	$CrAs_2$		$FeAs_2$				
[1-3]	[4]	[5-11]	[12-18]	[12, 14, 19-23]	[12, 14, 24-29]	[9, 14, 27, 30, 31]	[12, 19, 29, 32, 33]	[34-37]	[38-42]

The solid-state chemistry of the metal pnictides becomes more complex as the ternary metal pnictide phases of the general form $M_AM'_BE_X$ are considered. Table 1.2 contains several representative ternary metal pnictide phases. In most cases, the ternary metal pnictides exist as solid solutions of two binary phases of the form M_AE_B. For example, the ternary phase FeMnP can be considered a solid solution of the binary phases Fe_2P and Mn_2P. The degree of stoichiometric complexity increases further in the case of the quaternary metal pnictide phases of the form $M_AM'_BE_XE'_Y$. An example of a quaternary metal pnictide phase is $FeMnP_{0.5}As_{0.5}$, a material known to exhibit magnetocaloric behavior.[43] As might be expected, quaternary metal pnictide phases are less abundant than binary or ternary phases.

Table 1.2 Ternary phosphides and arsenides of the first row transition metals. [22]

CrMnP	MnNiP	CrMnAs	MnNiAs
CrFeP	FeMnP	CrFeAs	FeMnAs
CrCoP	FeCoP	CrCoAs	FeCoAs
CrNiP	FeNiP	CrNiAs	FeNiAs
MnCoP	CoNiP	MnCoAs	CoNiAs

The variability in the compositions of metal pnictide phases also gives rise to considerable differences in physical properties. This principle is best illustrated by considering the properties of several phases containing the same elements, but differing in the stoichiometric contribution from those elements. Table 1.3 contains structural and magnetic data for a number of iron- and manganese-rich pnictide phases. In the case of the iron phosphide series, the Fe_3P, Fe_2P, and FeP phases are known and well-characterized in the bulk. Although all three phases consist solely of iron and phosphorus, the structural and magnetic properties differ significantly according to the overall stoichiometry of the phase. Fe_3P crystallizes in the tetragonal crystal structure and exhibits ferromagnetic behavior with a relatively high Curie temperature of 716 K. Fe_2P has a hexagonal crystal structure and is also ferromagnetic, but with an ordering temperature of 217 K. The FeP phase is orthorhombic and displays antiferromagnetic properties below 115 K. The series of manganese phosphides exhibits similar composition-dependent variability in structure and physical properties.

Table 1.3 Structural and magnetic properties of selected iron and manganese pnictide phases.

Phase	Prototype Structure	Magnetic Properties	Ref.
Fe_3P	Fe_3P (tetragonal)	Ferromagnetic, T_C = 716 K	[12]
Fe_2P	Fe_2P (hexagonal)	Ferromagnetic, T_C = 217 K	[24]
FeP	FeP (orthorhombic)	Antiferromagnetic, T_N = 115 K	[44]
Mn_3P	Fe_3P (tetragonal)	Antiferromagnetic, T_N = 115 K	[45]
Mn_2P	Fe_2P (hexagonal)	Antiferromagnetic, T_N = 103 K	[46]
MnP	MnP (orthorhombic)	Ferromagnetic, T_C = 291 K	[45]
FeMnP	Co_2P (orthorhombic)	Antiferromagnetic, T_N = 340 K	[47]
FeMnAs	Cu_2Sb (tetragonal)	Antiferromagnetic, T_N = 463 K	[48]
$FeMnP_{0.5}As_{0.5}$	Fe_2P (hexagonal)	Ferromagnetic, T_C = 270 K	[49]

Although the metal pnictides have been the object of scholarly research for decades, interest in these materials extends beyond the purely academic. Several metal pnictide phases possess properties that may be commercially and technologically valuable. Giant magnetostriction, a phenomenon that may lead to the development of magnetically activated sensors and transducers, has been observed in the binary MnAs phase.[50] A significant magnetocaloric effect has been observed in the quaternary phase $FeMnP_{0.5}As_{0.5}$.[43] The magnetocaloric effect is brought about by a first-order structural and magnetic phase transition, leading to a magnetic field-induced entropy change, and it has been suggested that efficient magnetic refrigeration may be achieved using magnetocaloric materials.[51] Due to its relatively high ferromagnetic transition temperature and semiconducting properties, Fe_3P has been identified as a possible component in the fabrication of semiconductor spintronic devices.[52]

Several of the metal pnictide phases are also capable of catalyzing reactions of significant industrial importance, especially in the field of petroleum refining. Ni_2P, WP, MoP, and CoP have been investigated as catalysts for the hydrodenitrogenation (HDN) and hydrodesulfurization (HDS) of hydrocarbons. In the preceding series, Ni_2P was found to have the highest catalytic activity for both the HDS and HDN reactions.[53] The bimetallic phosphide phases $Fe_xNi_{2-x}P_y$ and $Co_xNi_{2-x}P_y$ have also exhibited excellent HDS catalytic activity.[54] The development of effective HDN and HDS catalysts is becoming increasingly important as lower quality petroleum sources containing high levels of sulfur and nitrogen are utilized to meet increasing global energy demands.

In considering how the metal pnictide phases may be employed in practical applications, two important observations from the preceding discussion are worth reiterating. First, transition metals and pnictides can combine to form multiple stable phases that differ from one another only by the stoichiometric contributions from the constituent elements. Second, the various stoichiometric phases exhibit physical properties that are unique to the specific phase. If the desirable physical properties of a certain metal pnictide material are to be exploited, then the material must be prepared under synthetic conditions that favor the formation of a single pure phase, and the formation of competing phases must be discouraged. In the case of the bulk binary and ternary metal pnictide materials, phase purity has been achieved in a relatively straightforward manner by combining the pure elements in the desired stoichiometric ratios and heating to temperatures above 1000 K.[12, 48, 55] The more complex quaternary phases have been prepared by combining appropriate quantities of the ternary phases under similar thermal conditions.[56] However, the high temperatures used to prepare bulk transition metal pnictides do not generally lend themselves to the preparation of well-defined advanced materials such as colloidal nanoparticles or films, and alternative methodologies for preparing such materials have been investigated by various research groups (*vide infra*). At present, achieving synthetic control over phase identity and purity in metal pnictide nanoparticles and films presents a fundamental challenge, and will be a recurring theme throughout this thesis.

1.2 Advanced Metal Pnictide Materials

Metal pnictide chemistry has experienced something of a renaissance in recent years as research groups have worked to prepare advanced metal pnictide materials such as nanoparticles and films. In the following sections, notable accomplishments in the field of advanced metal pnictide materials synthesis will be summarized.

1.2.1 Metal Pnictide Nanoparticles

Several research groups are actively researching the synthesis of metal pnictide nanomaterials using solution-based methods, and a number of important advances have been reported. Most of the methods involve the thermal decomposition of multiple molecular precursors containing the desired metals and pnictides along with a stabilizing agent used to passivate the particle surface and prevent agglomeration. A listing of several metal pnictide nanoparticle phases is presented in Table 1.4, along with descriptions of the metal and pnictide sources used in the syntheses, the identity of the stabilizing agent, and the morphology of the resulting particles.

Several general observations concerning Table 1.4 are worth considering. First, it is apparent that the majority of metal pnictide nanoparticle syntheses are carried out using separate sources of metal and pnictogen. The metal sources are often, but not always, low-valent organometallic species with thermally labile ligands. The pnictide sources are almost exclusively trialkyl- or *tris*(trialkyl)silyl-phosphine species. The most commonly employed pnictide source is tri-*n*-octylphosphine, a high-boiling compound that often serves a triple role as solvent, stabilizing agent, and phosphorus source. In several cases, single-source molecular

precursors containing metal and phosphorus atoms in a predetermined ratio have been employed.

Table 1.4 Examples of metal pnictide nanoparticle syntheses.

Phase	Metal Source	Pnictide Source	Stabilizing Agent	Particle Morphology	Ref.
Fe_2P	Fe nanoparticles	TOP	OAm	Rods, Spheres	[57]
	$H_2Fe_3(CO)_9P^tBu$	$H_2Fe_3(CO)_9P^tBu$	OA/ TOA	Rods, bundles, spherulites	[58]
	$Fe(CO)_5$	TOP	OAm	Rods	[59]
FeP	$(\eta^4\text{-}C_6H_8)Fe(CO)_3$	TOP	TOPO	Rods	[60]
	Fe nanoparticles	TOP	OAm	Rods, Spheres	[57]
	$Fe(CO)_5$	TOP	TOPO	Rods	[61, 62]
	$Fe(acac)_3$	$P(SiMe_3)_3$	TOPO	Spheres	[63]
MnP	$Mn_2(CO)_{10}$	TOP	TOPO	Rods	[61, 64]
	$Mn_2(CO)_{10}$	$P(SiMe_3)_3$	TOPO	Spheres	[65]
Co_2P	$Co(acac)_2$	TOP	HAD	Rods	[61]
	$CpCo(CO)_2$	TOP	OAm	Rods	[61]
	Cp_2Co	TOP	OAm	Rods	[61]
	$[Co(Se_2P^tBu_2)_2]$	TOP	HAD	Spheres	[66]
	ε-Co nanoparticles	TOP	TOP	Spheres	[67]
CoP	$[Co(Se_2P^tBu_2)_2]$	TOP	OAm	Spheres	[66]
Ni_2P	$Ni(acac)_2$	TOP	TOPO	Rods	[61]
	$Ni(COD)_2$	TOP	TOPO	Spheres	[68]
MnAs	$Mn_2(CO)_{10}$	Ph_3AsO	TOPO	Spheres	[69]
$Fe_{2-x}Ni_xP$	$Fe(CO)_5$, $Ni(acac)_2$	TOP	TOP	Rods	[70]
$Co_{2-x}Fe_xP$	Fe(III)oleate, Co(II)oleate	TOP	OAm	Rods	[71]

TOP = tri-*n*-octylphosphine, OAm = oleylamine, OA = oleic acid, TOPO = tri-*n*-octylphosphine oxide, HAD = hexadecylamine

Inspection of Table 1.4 also reveals that the metal pnictide phases that have been prepared and fully characterized at the nanoscale represent only a handful of the phases that are known in the bulk. This is somewhat surprising given the diversity of interesting properties observed in the bulk phases. The relative scarcity of reports on this topic can be attributed to several factors. First, there are relatively few groups pursuing this line of research, both in terms of methodology

development and intensive physical property investigation. Furthermore, the metal pnictides represent a complex class of materials for which phase control has proven difficult to achieve at the nanoscale. One of the fundamental requirements that must be met in the synthesis of metal pnictide nanomaterials is achieving uniform decomposition of all precursors in such a way that particles with the desired stoichiometric composition are produced. This requirement can be difficult to meet because of differences in the thermal stability and decomposition rates of the individual precursors and becomes ever more complicated when multiple precursors are employed. If one of the precursors is used in excess, as is the case in many of the preparatory methods shown in Table 1.4, precise and predetermined phase control may be difficult to achieve. As an example, Qian and coworkers reported the synthesis of phase-pure FeP nanorods through the injection of $Fe(CO)_5$ dissolved in tri-*n*- octylphosphine (TOP) into a hot solution of TOP and tri-*n*-octylphosphine oxide (TOPO).[62] Given the stoichiometric excess of phosphine sources used, one might have expected that the formation of the phosphorus-rich FeP_2 and FeP_4 phases would occur as well, and it remains uncertain as to why only the FeP phase was formed.

A number of phases and phase types are conspicuously absent or underrepresented in Figure 1.4. While nanoparticles of Fe_2P and FeP have been prepared using solution-based methods, the preparation of well-defined advanced Fe_3P materials has been an elusive goal, despite the fact that Fe_3P is arguably one of the most technologically relevant binary pnictide phases. Similarly, the only manganese phosphide phase to be synthesized at the nanoscale has been MnP,

despite the fact that at least three other manganese phosphide phases have been described in the bulk. Additionally, accounts of ternary phase metal pnictide nanomaterials are quite rare and few examples have appeared in the literature, despite the fact that bulk ternary phases are relatively common and can be prepared using simple solid-state synthetic methods. One of the primary objectives described in this thesis is the development and analysis of methods whereby synthetically challenging metal pnictide advanced materials can be accessed.

1.2.2 Metal Pnictide Films

Several of the metal pnictide phases have been prepared in the form of films, and a summary of the phases and synthetic conditions is presented in Table 1.5. With few exceptions, most of the films shown in Table 1.5 have been prepared by chemical vapor deposition, a process in which volatile sources of metal and pnictide are thermally decomposed at elevated temperatures, depositing a thin film onto a substrate material. In most of the film syntheses, separate sources of metals and pnictides have been employed, with the latter often being used in excess. The presence of excess pnictide precursor during film preparation often results in the formation of phases that have metal to pnictide ratios of nearly 1:1, or phases that are pnictide-rich. Metal phosphide films of most of the early transition metals have been reported, but synthetic methods for the preparation of mid to late transition metal pnictide films are less well-developed.

Table 1.5 Examples of metal pnictide film syntheses.

Phase	Metal Source	Pnictide Source	Method	Comments	Ref
TiP	$TiCl_4[PCy_2H]$	$TiCl_4[PCy_2H]$	LP-CVD		[72]
	$Ti[N(CH_3)_2]_4$	$CyPH_2$	AP-CVD		[72]
TiAs	$TiCl_4$	$^tBuAsH_2$	AP-CVD		[73]
ZrP	$Zr[N(CH_3)_2]_4$	$CyPH_2$	AP-CVD	P-rich films	[74]
HfP	$Hf[N(CH_3)_2]_4$	$CyPH_2$	AP-CVD	P-rich films	[74]
VP	VCl_4	$CyPH_2$	AP-CVD	P-rich films	[75]
NbP	$NbCl_5$	$CyPH_2$	AP-CVD	P-rich films	[75]
	$[(CyPH_2)_2Cl_2Nb]_2(\mu\text{-}Cl)_4$	$[(CyPH_2)_2Cl_2Nb]_2(\mu\text{-}Cl)_4$	LP-CVD	P-rich films	[76]
TaP	$TaCl_5$	$CyPH_2$	AP-CVD	P-rich films	[75]
CrP	$Cr(CO)_5PH_3$	$Cr(CO)_5PH_3$	LP-CVD		[77]
	$Cr(CO)_6$	$CyPH_2$	AP-CVD		[78]
MoP	$MoCl_5$	$CyPH_2$	AP-CVD	P-rich films	[79]
WP	WCl_5	PCl_3 (with H_2)	AP-CVD	Poorly Characterized	[80]
MnP	Mn	P	MBE		[81]
MnAs	$(MeCp)Mn(CO)_3$	AsH_3	LP-CVD		[82]
$FeAs_2$	$Fe(CO)_5$	AsH_3	AP-CVD		[83]
Ru_xP_y	$H_2Ru[P(CH_3)_3]_4$	$H_2Ru[P(CH_3)_3]_4$	LP-CVD	Amorphous alloy	[84]
CoP	$[Co\{(SeP^iPr_2)_2N\}_2]$	$[Co\{(SeP^iPr_2)_2N\}_2]$	AA-CVD	P-rich films	[85]
CoP_2	$[Co\{(SeP^iPr_2)_2N\}_2]$	$[Co\{(SeP^iPr_2)_2N\}_2]$	AA-CVD	P-rich films	[85]
CoAs	1,3-bis(*tert*-butyl)-2-(tetracarbonylcobalt)-1,3,2-diazarsolidine	1,3-bis(*tert*-butyl)-2-(tetracarbonylcobalt)-1,3,2-diazarsolidine	LP-CVD	Co_2As and $CoAs_2$ also present	[86]
Ni_2P	$Ni[^iPr_2P(S)NP(Se)^iPr_2]_2$	$Ni[^iPr_2P(S)NP(Se)^iPr_2]_2$	LP-CVD		[87]
Cu_3P	Cu (surface)	$^tBuPCl_2$	LP-CVD	Formed by surface reaction between bulk Cu and $^tBuPCl_2$	[88]

Cy = cyclohexyl, MeCp = methylcyclopentadienyl, CVD = chemical vapor deposition, LP = low-pressure, AP = atmospheric pressure, MBE = molecular beam epitaxy, AA = aerosol assisted

Films of the metal-rich binary pnictide phases and bimetallic ternary phases have not yet been extensively studied, most likely due to the inherent difficulty in preparing such films. In order to achieve phase-purity during film preparation, considerable engineering is required to achieve suitable precursor mixing and control over the stoichiometry of the precursor materials, and this can be difficult

when employing multiple precursors with different volatilities and decomposition temperatures.

Several of the syntheses described in Table 1.5 have employed single-source molecular precursors that, by definition, are designed to contain all of the elements necessary to form a desired phase upon decomposition of the precursor molecule. It is worth noting that the final composition of the films prepared by single-source precursors did not necessarily reflect the overall stoichiometry of the precursor molecules. For example, while CoAs films prepared from 1,3-bis(*tert*-butyl)-2-(tetracarbonylcobalt)-1,3,2-diazarsolidine retained the 1:1 Co:As stoichiometry of the precursor, metal-rich RuP films (P = 15-20%) were formed upon decomposition of $H_2Ru(PMe_3)_4$.[84, 86] In the former case, the presence of a covalent Co–As bond may have prevented the fragmentation of the precursor and subsequent formation of a metal-rich phase. In the latter case, the formation of metal-rich films can almost certainly be attributed to the loss of trimethylphosphine due to the increased lability of the R–P dative bond, and it should be noted that the authors had originally intended to exploit this lability in order to prepare metallic ruthenium films rather than Ru_xP_y films. These results suggest that both stoichiometry and bonding should be carefully evaluated when selecting a single-source precursor as a candidate to target a specific metal pnictide phase. Although the selection and preparation of suitable single-source precursors can be challenging, their use in thin film preparation has several advantages over the use of multiple precursors. Because single-source molecular precursors contain all of the elements required to form a targeted phase with pre-determined stoichiometry, the problems associated with

mixing and delivering stoichiometric amounts of separate precursors are circumvented. Furthermore, the delivery and decomposition of single-source precursors is expected to occur in a more uniform manner under narrowly defined thermal conditions, unlike separate precursors that can have significantly different volatilities and decomposition temperatures.

1.3 Summary and Thesis Overview

In this chapter, the rich chemistry of the transition metal pnictides has been introduced. The metal pnictides possess a number of interesting properties that are dependent on the stoichiometric composition of the many possible phases. At present, there is considerable interest in the preparation of advanced metal pnictide materials such as nanoparticles and films, but the scope of commonly used synthetic methods has thus far proven to be limited.

For several years, the Whitmire research group has been interested in addressing fundamental problems in advanced metal pnictide materials synthesis. We have been most interested in employing organometallic clusters and complexes as single-source molecular precursors to advanced metal pnictide materials that have proven difficult to synthesize by existing strategies. As mentioned previously, the stoichiometry of single-source precursors can be designed to reflect the stoichiometry of a desired metal pnictide phase, and the decomposition of these precursors should provide a means of preparing advanced metal pnictide materials with predetermined stoichiometries.

In the following chapters, progress in the field of single-source precursor-enabled synthesis of advanced metal pnictide materials will be discussed.

Specifically, we have targeted the ternary phase $Fe_{2-x}Mn_xP$ and the metal-rich binary phase Fe_3P. The $Fe_{2-x}Mn_xP$ phase was selected as a test bed for studying the synthesis of ternary phase advanced metal pnictide materials using single-source precursor strategies. The Fe_3P phase was targeted due to its favorable ferromagnetic properties as well as the fact that the preparation of advanced Fe_3P materials has been elusive by commonly used methods. Chapter 2 of this thesis focuses on the synthesis and fundamental organometallic chemistry of molecular precursors containing iron, manganese, and phosphorus. Chapter 3 describes efforts to prepare $Fe_{2-x}Mn_xP$ nanoparticles using the precursors described in Chapter 2. The preparation and physical characterization of phase-pure Fe_3P films prepared from a single-source molecular precursor is described in Chapter 4. The synthetic methods used to prepare Fe_3P films have been extended in an effort to prepare FeMnP films, and the results of this investigation are documented in Chapter 5 of this thesis.

Chapter 2. Synthesis and Characterization of Single-source Molecular Precursors to Advanced $Fe_{2-x}Mn_xP$ Materials

*(Note: This chapter contains a significant amount of material previously published in Organometallics, **2010**, 29, 4611-4618.)*

2.1 Introduction

One of the objectives described in this thesis is the synthesis of advanced FeMnP materials such as nanoparticles and films using single-source molecular precursors. The first step in this undertaking was the identification of a suitable precursor candidate. We surmised that an ideal precursor molecule would contain iron, manganese, and phosphorus in a 1:1:1 ratio and would possess relatively labile ancillary ligands that would readily dissociate at elevated temperatures. A search of the relevant literature revealed that Yasafuku and Yamazaki had previously reported the synthesis of the organometallic complex $FeMn(CO)_8(\mu\text{-}PPh_2)$, which seemed to be a suitable precursor for our experiments.[89] However, this complex proved ineffective as a precursor to $Fe_{2-x}Mn_xP$ materials (See Chapters 3 and 5).

The syntheses of previously unknown $\mu\text{-}PH_2$ and $\mu\text{-}PRH$ analogues of $FeMn(CO)_8(\mu\text{-}PPh_2)$ were carried out to determine if these might prove more effective precursors by virtue of having lower barriers to decomposition due to the replacement of the relatively robust phosphorus-carbon bonds by more labile P-H bonds.

Extensive research has been conducted on transition metal complexes exhibiting one or more bridging phosphido functionalities, and the bridging phosphide has been observed to prevent fragmentation of the complex during reactions with organic substrates.[90-93] The vast majority of these studies have focused on complexes containing the μ-PR_2 (R = aryl, alkyl) group. According to the Cambridge Crystallographic Data Centre (CCDC), more than 2200 compounds containing the μ-PR_2 (R = aryl, alkyl) functionality have been characterized crystallographically, and a substantial number of these complexes are heterometallic.[94, 95] Significantly fewer examples of complexes containing the μ-PRH (R = aryl, alkyl) group have been structurally characterized. Of the 104 complexes containing the μ-PRH functionality, only 11 complexes are heterometallic. Structurally-characterized complexes containing the μ-PH_2 functionality are even more rare. Fewer than 25 crystal structures containing a μ-PH_2 group have been deposited with the CCDC, and only 5 complexes are heterometallic.[94, 95] Together, heterometallic μ-PRH and μ-PH_2 complexes represent less than 1% of all μ-PR_2 (R = aryl, alkyl, H) complexes listed with the CCDC.

In addition to serving as precursors to advanced materials, complexes containing the μ-PRH and μ-PH_2 functionalities are of interest because the presence of a P-H bond can be a useful synthetic scaffold for additional derivatization and tuning of the complex (*vide infra*). Additionally, the inherent electronic differences between homometallic and heterometallic species may affect catalytic cycles or reactive pathways.[96-103]

In this chapter, the synthesis and structural characterizations of two new heterobimetallic carbonyl complexes containing the μ-PRH and μ-PH_2 functionalities are described. The synthetic strategy for preparing $FeMn(CO)_8(\mu\text{-}PH_2)$ (**1a**) and $FeMn(CO)_8(\mu\text{-}PPhH)$ (**1b**) is shown in Figure 2.1. Derivatization of **1b** was achieved to give $FeMn(CO)_8[\mu\text{-}PPh(Mn(CO)_5)]$ (**3a**) and $FeMn(CO)_8[\mu\text{-}PPh(AuPPh_3)]$ (**3b**). Deprotonation of **1a** at room temperature, on the other hand, led to rapid coupling of the deprotonated product **[2a]**$^-$ and neutral **1a** to form $M^+[FeMn(CO)_8(\mu_3\text{-}PH)Mn(CO)_4(\mu\text{-}PH_2)Fe(CO)_4]^-$ (M^+**[4]**$^-$) ($M^+ = Li^+, Na^+, K^+$).

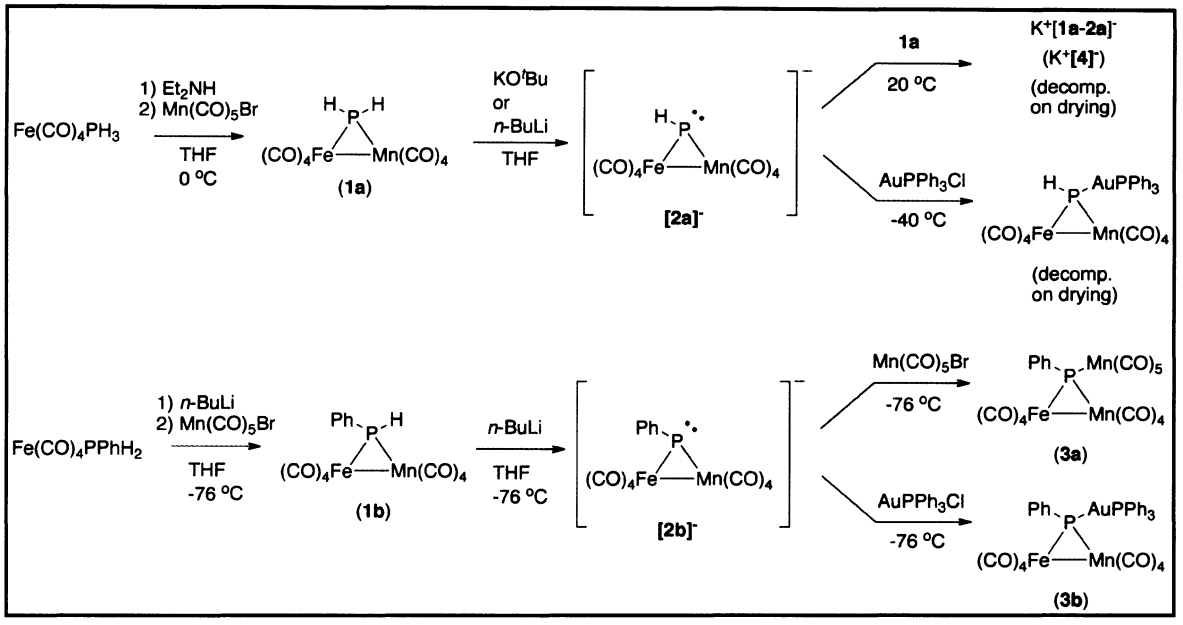

Figure 2.1 Synthesis and reactivity of $FeMn(CO)_8(\mu\text{-}PH_2)$ (1a) and $FeMn(CO)_8(\mu\text{-}PPhH)$ (1b).

2.2 Experimental

General Considerations: All manipulations were carried out under an argon atmosphere using standard Schlenk techniques in order to exclude moisture and oxygen. Argon was pre-purified by passing through columns of BTS catalyst and molecular sieves. All

solvents were dried and distilled prior to use according to standard procedures.[104] $P(SiMe_3)_3$, $Mn(CO)_5Br$, and $Fe(CO)_4PPhH_2$ were prepared according to previously published procedures.[105-107] $Fe(CO)_4PH_3$ was prepared using a modified literature procedure.[108] $AuPPh_3Cl$ and $Fe(CO)_5$ were purchased from Strem and used without further purification. Potassium *tert*-butoxide was purchased from Sigma-Aldrich and was sublimed prior to use. General infrared (FTIR) spectra were obtained using a Thermo-Nicolet 670 FT-IR with 0.1 mm CaF_2 cell. *In situ* FTIR data were collected on a Mettler Toledo 45m ReactIR system using an immersion probe with a Si sampling tip coupled to a silver halide fiber. ^1H and ^{31}P NMR data were recorded on Bruker spectrometers operating at 400 MHz (162 MHz for ^{31}P) or 500 MHz (202 MHz for ^{31}P). Mass spectrometry measurements were carried out at the Mass Spectrometry Lab at the University of Illinois at Chicago.

Modified Synthesis of $Fe(CO)_4PH_3$: $P(SiMe_3)_3$ (2.50 mL, 8.61 mmol) and $Fe(CO)_5$ (1.30 mL, 9.89 mmol) were added to a standard Schlenk flask and dissolved in 100 mL THF. The flask was then irradiated with a 450 W mercury-vapor UV lamp for 4 hours. After irradiation, THF and unreacted $Fe(CO)_5$ were removed under reduced pressure and the remaining residues were redissolved in diethyl ether and cooled to 0 °C. Methanol (2.10 mL, 51.9 mmol) was added dropwise, and the reaction mixture was stirred at 0 °C for 20 minutes in the dark. Diethyl ether and unreacted methanol were removed in *vacuo* at 0 °C, leaving behind a brown solid residue. The Schlenk flask was then fitted with a jacketed condenser and a stopcock and the assembly was placed in a horizontal position and connected to a vaccum line (10^{-7} Torr). The jacketed condenser was filled with liquid nitrogen, and pure $Fe(CO)_4PH_3$ was sublimed from the Schlenk flask into the cooled

condenser. The sublimation apparatus was refilled with argon and the pale yellow $Fe(CO)_4PH_3$ was transferred to a tared Schlenk flask under a vigorous flow of argon (1.11 g, 64 % yield based on phosphorus). Spectral analysis of the solid was consistent with data reported elsewhere.[108]

$FeMn(CO)_8(\mu\text{-}PH_2)$ (1a): Freshly prepared $Fe(CO)_4PH_3$ (498 mg, 2.47 mmol) was added to a Schlenk flask and dissolved in 50 mL THF. The solution was cooled to 0 °C and one equivalent (255 μL, 2.47 mmol) of diethylamine was added. The solution was stirred at 0 °C for five minutes, followed by the addition of 679 mg (2.47 mmol) $Mn(CO)_5Br$. The reaction was covered with a dark cloth and stirred at 0 °C for four hours. The solvent was removed under reduced pressure and the residue was chromatographed on silica using hexane as the eluent. The hexane was removed under reduced pressure, leaving red-orange crystals that could be further purified by sublimation (467 mg, 51% yield). Single crystals for X-ray diffraction studies were obtained by slow sublimation in a Schlenk tube at 30 °C and 10^{-7} Torr. IR (hexanes, cm^{-1}) ν_{CO} 2096 (w), 2042 (s), 2026 (w), 2017 (vs), 2007 (m), 1992 (w), 1971 (w), 1963 (m), 1942 (vw). ^1H NMR (400 MHz, C_6D_6), δ = 3.00 (d, $^1J_{HP}$ = 364 Hz, 2H); ^{31}P NMR (162 MHz, C_6D_6, H_3PO_4 standard), δ = 2.91 (t, $^1J_{PH}$ = 365 Hz). MS(EI): *m/z* 367.8 (M^+), 339.8 (M^+- CO), 311.8 (M^+- 2CO), 283.8 (M^+-3CO), 255.8 (M^+ - 4CO), 227.8 (M^+ - 5CO), 199.8 (M^+ - 6CO), 171.8 (M^+ - 7CO), 143.8 (M^+ - 8CO). Anal. Calc. for $FeMnC_8O_8PH_2$: C, 26.12; H, 0.55. Found: C, 25.79; H, 0.74.

$FeMn(CO)_8(\mu\text{-}PPhH)$ (1b): $Fe(CO)_4PPhH_2$ (285 mg, 1.02 mmol) was added to a Schlenk flask and dissolved in 30 mL THF. The solution was cooled to -76 °C and one equivalent (1.02 mmol) *n*-butyllithium was added dropwise, followed by the addition of $Mn(CO)_5Br$ (282 mg, 1.02 mmol). The solution was then transferred to a 0 °C bath and

stirred for four hours. The solvent was removed in *vacuo* and the oily residue was extracted with hexanes. The hexanes extract was concentrated and chromatographed on a silica column using hexanes as eluent. **1b** eluted jointly with $Mn_2(CO)_{10}$ which formed as a byproduct of the reaction. The collected fractions were concentrated and cooled to -40 °C for several days, whereupon red crystals of **1b** and yellow crystals of $Mn_2(CO)_{10}$ formed and were separated manually using a hand lens and were further purified by sublimation (93 mg, 21% yield). Single crystals suitable for X-ray diffraction studies were prepared by slow sublimation in a Schlenk tube at 30 °C and 10^{-7} Torr. IR (hexanes, cm^{-1}) ν_{CO} 2092 (w), 2075 (vw), 2039 (s), 2024 (m), 2015 (vs), 2002 (m), 1988 (w), 1967 (m), 1957 (m). ^1H NMR (400 MHz, C_6D_6), δ = 7.37 (m, 2H); 6.89 (m, 2H); 5.28 (d, $^1J_{HP}$ = 357 Hz, 1H); ^{31}P NMR (162 MHz, C_6D_6, H_3PO_4 standard), δ = 100 (d, $^1J_{PH}$ = 357 Hz). MS(EI): *m/z* 443.8 (M^+), 415.9 (M^+ - CO), 387.8 (M^+ - 2CO), 359.8 (M^+ - 3CO), 331.8 (M^+ - 4CO), 303.9 (M^+ - 5CO), 275.9 (M^+ - 6CO), 247.9 (M^+ - 7CO), 219.9 (M^+ - 8CO). Anal. Calc. for $FeMnC_{14}O_8PH_6$: C, 37.88; H, 1.36. Found: C, 37.32; H, 1.32.

$FeMn(CO)_8[\mu$-PPh$(Mn(CO)_5)]$ (3a): A solution of **1b** (132 mg, 0.297 mmol) in 30 mL THF was cooled to -78 °C and treated with one equivalent (0.297 mmol) *n*-butyllithium, whereupon the color of the solution changed from bright red-orange to dark red. $Mn(CO)_5Br$ (82.0 mg, 0.297 mmol) was then added and the solution was removed from the cold bath and allowed to warm to room temperature. As the solution warmed, the color gradually became a lighter shade of red. The solution was stirred at room temperature for two hours, after which the solvent was removed under reduced pressure, leaving behind a viscous, oily residue. The residue was extracted with a 3:1 hexanes/toluene solution and filtered through diatomaceous earth. The filtrate was

chromatographed on silica using 3:1 hexanes/toluene as eluent. The collected fractions that were not contaminated with $Mn_2(CO)_{10}$ were dried in *vacuo*, redissolved in minimal pentane, and cooled to -40 °C for several days, whereupon red crystals of **3a** formed (32.2 mg, 17% yield). **3a** exhibits considerable thermal instability in solution and in the solid state, resulting in larger-than-expected deviations in the observed C and H elemental analyses. IR (hexanes, cm^{-1}) ν_{CO} 2117 (w), 2078 (m), 2061 (vw), 2036 (vs), 2015 (m), 1998 (m), 1992 (m), 1979 (w), 1955 (w), 1942 (w). ^1H NMR (400 MHz, C_6D_6), δ = 7.70 (m, 1H); 7.45 (m, 1H); 6.83 (m, 3H); ^{31}P NMR (162 MHz, C_6D_6, H_3PO_4 standard), δ = 144 (s, br). MS(EI): *m/z* 637.8 (M^+), 609.8 (M^+ - CO), 553.8 (M^+ - 3CO), 525.8 (M^+ - 4CO), 497.8 (M^+ -5CO), 469.8 (M^+ - 6CO), 441.8 (M^+ - 7CO), 413.8 (M^+ - 8CO), 385.8 (M^+ - 9CO), 357.8 (M^+ - 10CO), 329.8 (M^+ - 11CO), 301.8 (M^+ - 12CO), 273.8 (M^+ - 13CO), 218.9 (M^+ - 13CO, -Mn). Anal. Calc. for $FeMn_2C_{19}O_{13}PH_5$: C, 35.77; H, 0.79. Found: C, 35.07; H, 0.92.

$FeMn(CO)_8[\mu$-PPh(AuPPh$_3$)] (3b): A solution of **1b** (118 mg, 0.266 mmol) in 30 mL THF was cooled to -78 °C and treated with *n*-butyllithium (0.266 mmol), causing the bright red-orange solution to darken. $AuPPh_3Cl$ (132 mg, 0.266 mmol) was then added and the reaction mixture was removed from the cold bath and allowed to warm to room temperature. As the reaction mixture warmed, the dark coloration dissipated and the solution took on a bright orange/yellow color. The reaction mixture was stirred at room temperature for two hours, after which the solvent was removed in *vacuo*. The resulting residue was extracted with hexanes, passed through a short pad of silica gel, and dried under reduced pressure. The slightly oily residue was then dissolved in minimal CH_2Cl_2, layered with two volumes of hexanes, and placed in a -40 °C freezer. Red-orange crystals

of **3b** formed after several days (176 mg, 73 % yield). **3b** displays slight thermal instability in solution and in the solid state, resulting in larger-than-expected deviations in the observed C and H elemental analyses. The agreement between observed and calculated values for the elemental analyses improved when the shipping and holding times of the samples were reduced. IR (hexanes, cm^{-1}) ν_{CO} 2076 (m), 2047 (w), 2022 (vs), 2008 (s), 1995 (s), 1980 (s), 1969 (m), 1947 (m), 1935 (m). ^1H NMR (400 MHz, C_6D_6), δ = 7.97 (m, 2H); 7.23 (m, 6H), 6.99-6.86 (m, 12H); ^{31}P NMR (162 MHz, C_6D_6, H_3PO_4 standard), δ = 151 (d, $^2J_{PP}$ = 281 Hz); 43 (d, $^2J_{PP}$ = 281 Hz). Anal. Calc. for $FeMnC_{32}O_8P_2H_{20}Au$: C, 42.60; H, 2.23. Found: C, 41.93; H, 2.25. MS(EI) data for **3b** showed no evidence of the M^+ ion or any readily identifiable fragments, leading us to conclude that the complex decomposed completely upon heating.

Deprotonation of 1a using the Mettler Toledo 45m ReactIR System: A solution of **1a** (85.0 mg, 0.230 mmol) in 50 mL THF was titrated with successive 23.0 μmol portions of potassium *tert*-butoxide until the presence of **1a** could no longer be detected by *in situ* IR spectroscopy, which occurred after 0.115 mmol KO^{t}Bu had been added. After the addition of 0.115 mmol KO^{t}Bu, ^1H and ^{31}P NMR showed only peaks corresponding to **[4]**$^-$ and *tert*-butanol. Attempts to isolate K^+**[4]**$^-$ for elemental and structural analysis resulted in decomposition, as evidenced by the formation of an insoluble brown solid upon concentration. IR (THF, cm^{-1}) ν_{CO} 2080 (w), 2054 (m), 2043 (w), 2026 (m, sh), 2018 (vs), 1997 (s), 1942 (s), 1920 (s), 1868 (w). ^1H NMR (500 MHz, THF-d_8), δ = 3.32 (d, $^1J_{HP}$ = 243 Hz, $^3J_{HP}$ = 19.6 Hz, 1H); 3.14 (ddd, $^1J_{HP}$ = 295 Hz, $^3J_{HP}$ = 12.4 Hz, $^2J_{HH}$ = 6.25 Hz, 1H); 3.04 (ddd, $^1J_{HP}$ = 292 Hz, $^3J_{HP}$ = 13.8 Hz, $^2J_{HH}$ = 6.25 Hz, 1H); ^{31}P NMR (202

MHz, THF-d_8, H_3PO_4 standard), δ = 98.0 (s, br); -74.0 (s, br). HRMS (ESI-TOF; negative ion mode): Calculated for $[C_{16}O_{16}H_3P_2Mn_2Fe_2]^-$: m/z 734.6356. Found 734.6336 (M^-).

Crystal Structure Determinations of 1a, 1b, 3a, and 3b: Diffraction data were collected on a Bruker SMART 1000 CCD diffractometer equipped with a Mo-target X-ray tube in a hemisphere with exposure times of 10-50 seconds. The collected frames were integrated with the Bruker SAINTPLUS software package and corrected for absorption effects using empirical methods (SADABS).[109, 110] Structures were solved using direct methods and refined by full-matrix least-squares on F^2 using the SHELXTL software package.[111, 112] Optimum refinements were achieved by treating the iron and manganese sites as a statistical mixture of the two metal atoms. The hydrogen atoms bound to phosphorus in **1a** and **1b** were refined isotropically, and all other protons were assigned idealized locations. Anisotropic displacement parameters were assigned to all non-hydrogen atoms. All thermal ellipsoid plots were generated using the Diamond software package.[113] A summary of X-ray data collection and refinement parameters for complexes **1a**, **1b**, **3a**, and **3b** is provided in Table 2.1. Additional tables of crystallographic data can be found in the Appendices.

Table 2.1 X-ray collection and refinement parameters for complexes 1a, 1b, 3a, and 3b.

	1a	1b	3a	3b
Formula	$C_8H_2FeMnO_8P$	$C_{14}H_6FeMnO_8P$	$C_{19}H_5FeMn_2O_{13}P$	$C_{32}H_{20}AuFeMnO_8P_2$
Formula weight	367.86	443.95	637.93	902.18
crystal system	triclinic	monoclinic	triclinic	orthorhombic
space group	P-1	P 21/c	P-1	Pbcn
a (Å)	7.8647(8)	10.242(4)	12.325(2)	18.4784(14)
b (Å)	9.2226(10)	14.193(6)	14.204(3)	12.6296(9)
c (Å)	9.3681(10)	11.935(5)	14.926(3)	28.196(2)
α (deg)	90.966(2)	90.00	107.600(3)	90.00
β (deg)	91.141(2)	97.927(8)	106.384(3)	90.00
γ (deg)	110.032(2)	90.00	95.561(4)	90.00
V (Å^3)	638.06(12)	1718.4(13)	2341.8(8)	6580.3(8)
Z	2	4	4	8
D_{calc} (g·cm^{-3})	1.915	1.716	1.809	1.821
λ (Mo Kα), (Å)	0.71073	0.71073	0.71073	0.71073
T (K)	223(2)	293(2)	213(2)	213(2)
θ_{max} (deg)	28.33	28.370	28.420	28.29
abs. coeff (mm^{-1})	2.280	1.710	1.808	5.407
rflns(coll)	5030	20831	23216	76896
rflns (unique)	2066	4226	9627	8102
Params	181	230	649	407
F(000)	360	880	1256	3488
R_1 [I > 2σ(I)]	0.0276	0.0775	0.0310	0.0249
wR_2 [I > 2σ(I)]	0.0591	0.1328	0.0532	0.0551
GOF (on F^2)	0.795	1.122	0.453	1.111

2.3 Results and Discussion

Complexes **1a** and **1b** were both prepared by employing the strategy described by Yasufuku and Yamazaki to prepare the structurally analogous $FeMn(CO)_8(\mu\text{-}PPh_2)$ complex.[89] The preparations of **1a** and **1b** were achieved through the intermediacy of the highly air, light, and moisture sensitive complexes $Fe(CO)_4PH_3$ and $Fe(CO)_4PPhH_2$. $Fe(CO)_4PH_3$ was also observed to be thermally sensitive, and began to degrade at room temperature. Manipulation of $Fe(CO)_4PH_3$ in the glovebox was therefore found to be impractical, and all manipulations of $Fe(CO)_4PH_3$ were carried out using standard Schlenk techniques. Freshly prepared samples of $Fe(CO)_4PH_3$ were treated with diethylamine and $Mn(CO)_5Br$ in THF to yield **1a** via a bridge-assisted displacement reaction, the metal centers being brought sufficiently close together for a metal-metal bond to form. The formation of the metal-metal bond is also accompanied by the loss of one CO ligand. Similarly, **1b** was prepared from $Fe(CO)_4PPhH_2$ and $Mn(CO)_5Br$, with *n*-butyllithium being used as the base. The preparation of **1b** appears to be more prone to redox side-reactions than **1a**, as $Mn_2(CO)_{10}$ was isolated jointly with the desired product. Although $Fe(CO)_4PH_3$ and $Fe(CO)_4PPhH_2$ are both extremely sensitive to air and moisture, complexes **1a** and **1b** can be handled in the air for short periods of time with no discernible decomposition. Complexes **1a** and **1b** obey the EAN rule, and all metal centers can be assigned 18 electrons.

The ^1H NMR spectra of **1a** and **1b** in C_6D_6 show doublets centered at 3.00 ppm and 5.28 ppm, respectively. The large coupling constants, 364 Hz for **1a** and

357 Hz for **1b**, are consistent with direct phosphorus-hydrogen coupling over a single bond.[114] The ^{31}P NMR spectrum of **1a** contains a single phosphorus resonance centered at 2.91 ppm and appears as a triplet in the proton-coupled experiment. The proton-coupled ^{31}P NMR spectrum of **1b** shows a doublet at 100 ppm, the downfield shift being attributed to deshielding of the phosphorus nucleus by the replacement of a hydrogen atom by a more electronegative carbon atom.[107, 108, 114] The structures of **1a** and **1b** were confirmed by single crystal X-ray diffraction studies (*vide infra*).

The possibility of derivatizing **1b** by reaction at the phosphorus atom was investigated. Complexes **3a** and **3b** were prepared by addition of $Mn(CO)_5Br$ and $AuPPh_3Cl$, respectively, to a solution of **[2b]**$^-$, which was prepared by treating **1b** with one equivalent of *n*-butyllithium at -76 °C. The reaction of **[2b]**$^-$ with $AuPPh_3Cl$ appeared to proceed rapidly and cleanly when monitored by IR spectroscopy, and **3b** was isolated with a relatively good yield of 73%. By contrast, **3a** was isolated with a significantly lower yield of 17%. This difference in isolated yields may be accounted for in several ways. First, the pseudo-tetrahedral phosphorus atom of **2b** is already sterically crowded due to the presence of the phenyl ring and the carbonyl ligands of the attached metal centers (see Figure 2.11), and the reaction with the sterically encumbered $Mn(CO)_5Br$ fragment would be expected to be less favorable than the reaction with $AuPPh_3Cl$, which is more accessible. Additionally, the reaction of **2b** with $Mn(CO)_5Br$ is prone to redox side reactions, as evidenced by the formation of $Mn_2(CO)_{10}$. Finally, **3b** was observed to exhibit thermal instability and decomposed slowly in solution and in the solid state. Davies and coworkers have

reported similar instability during the preparation of $Cp_2Mo_2(CO)_4(\mu\text{-}H)[\mu\text{-}PH(Mn(CO)_5)]$.[115]

The ^{31}P NMR spectrum of **3a** displays a singlet at 144 ppm that exhibits considerable broadening due to coupling to two quadrupolar Mn nuclei (I = 5/2). The ^{31}P NMR spectrum of **3b** contains a doublet centered at 43.0 ppm (PPh_3) and another doublet centered at 151 ppm (μ-$PPh(AuPPh_3)$), the large $^2J_{PP}$ value of ~ 280 Hz indicating a nearly linear P-Au-P bond angle, as confirmed by the X-ray structure (*vide infra*). The downfield shifting of the phosphorus resonances of **3a** and **3b** reflects the deshielding of the phosphorus nuclei by addition of metals with larger Pauling electronegativities. The molecular structures of **3a** and **3b** (Figures 2.13 and 2.14) derived from X-ray diffraction experiments are consistent with the spectroscopic data.

Similar attempts at metallation using **1a** were made using a variety of reaction conditions. Deprotonation of **1a** using potassium *tert*-butoxide or sodium hydride at room temperature or 0 °C gave rise to a product M^+**[4]**$^-$ ($M^+ = K^+$ or Na^+) that decomposed upon removal of solvent. The infrared spectrum of this product (Figure 2.2) in solution appeared more complex than the shift towards lower wavenumbers that one would expect from simple deprotonation of **1a**. Furthermore, the complete consumption of **1a** was observed even when substoichiometric amounts of base were used.

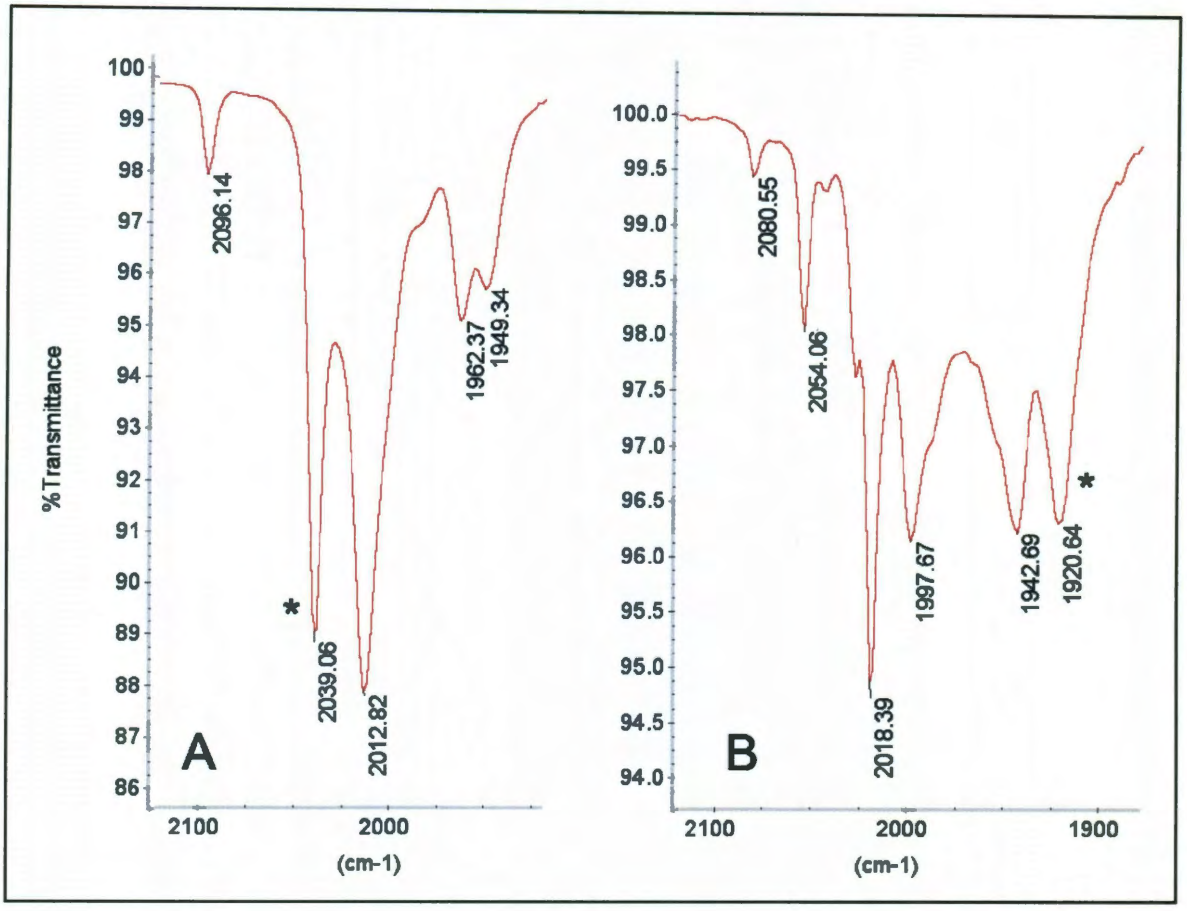

Figure 2.2 FTIR spectra of 1a before (A) and after (B) deprotonation to form [4]$^-$ in THF. The peaks marked with (*) were used as reference peaks for *in situ* IR studies.

In order to study this result in more detail, a careful titration of **1a** with potassium *tert*-butoxide was performed and the reaction was monitored using *in situ* infrared spectroscopy. The strong IR peak at 2039 cm^{-1} of **1a** and the peak at 1920 cm^{-1} of the unknown product **[4]**$^-$ were selected as representative peaks to monitor the concentrations of each species in solution. Figure 2.3 contains a plot depicting the change in the absorbance values of the representative peaks as a function of the amount of base added. According to this plot, the representative peak for **1a** at 2039 cm^{-1} had a maximum absorbance when no base had been added, and the absorbance decreased linearly with incremental base addition, reaching a

minimum when 0.50 molar equivalents of base had been added. Conversely, the representative peak for **[4]**$^-$ at 1920 cm^{-1} displayed minimum absorbance before base addition and increased linearly with base addition, attaining a maximum absorbance at 0.50 equivalents of base. In both cases, the absorbance reached one-half of the maximum absorbance after 0.25 molar equivalents of base had been added. Based on these data and the reaction stoichiometry, we began to suspect that deprotonated **1a** underwent a coupling reaction with its neutral parent compound.

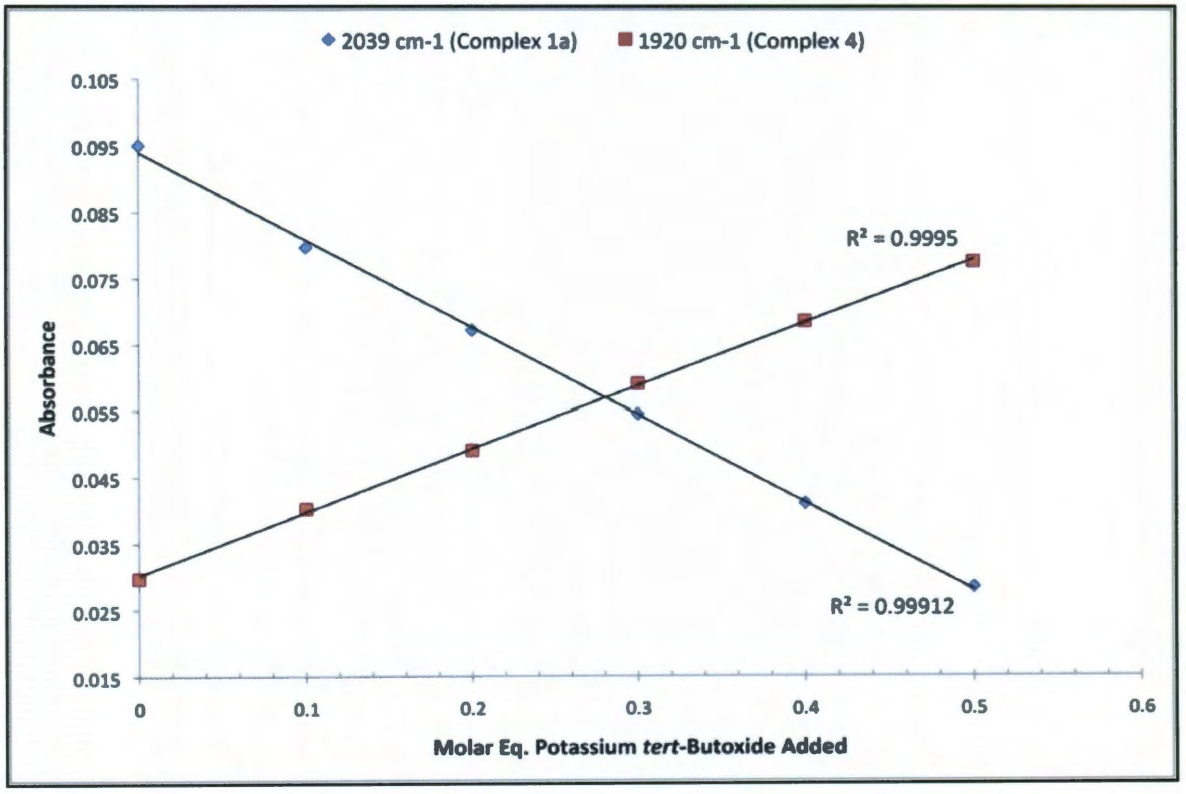

Figure 2.3 Absorbance of representative peaks of 1a and [4]$^-$ as a function of amount of base added.

^{31}P and ^{1}H NMR data support the hypothesis of a base-induced coupling reaction. The proton coupled ^{31}P NMR spectrum obtained after treating **1a** with 0.50

equivalents of potassium *tert*-butoxide in THF-d_8 showed complete consumption of **1a** and two new phosphorus resonances at -74.0 and 97.6 ppm. Unfortunately, coupling constants and multiplicities could not be determined from these peaks due to their considerable width, each peak having a full width of ~600 Hz at one-half of the maximum intensity due to coupling to quadrupolar manganese nuclei. The ^{1}H NMR spectrum, however, provides much more insight into the structure of **[4]**$^-$. This spectrum, shown in Figure 2.4, is characterized by a first-order [ABMX] spin system and a first-order [AMX] spin system. The [ABMX] system is manifested as a pair of doublets of doublets of doublets (ddd) centered at 3.14 and 3.04 ppm arising from two geminal diastereotopic protons H_A and H_B ($^2J_{HH}$ = 6.25 Hz). The geminal protons H_A and H_B appear to reside on a single common phosphorus atom, as evidenced by large $^1J_{HP}$ coupling constants of 295 Hz and 292 Hz for H_A and H_B, respectively. The coupling of H_A and H_B to a second phosphorus nucleus completes the observed ddd pattern, the coupling constants being consistent with coupling over three bonds ($^3J_{H_AP}$ = 12.4 Hz, $^3J_{H_BP}$ = 13.8 Hz). The [AMX] spin system observed in Figure 2.4 appears as a doublet of doublets and arises as a result of a single proton H_C coupling to two phosphorus atoms with coupling constants $^1J_{HP}$ = 243 Hz and $^3J_{HP}$ = 19.6 Hz, indicating that H_C is directly bound to one phosphorus atom but is additionally arranged so that it can couple to a second phosphorus atom over three bonds.

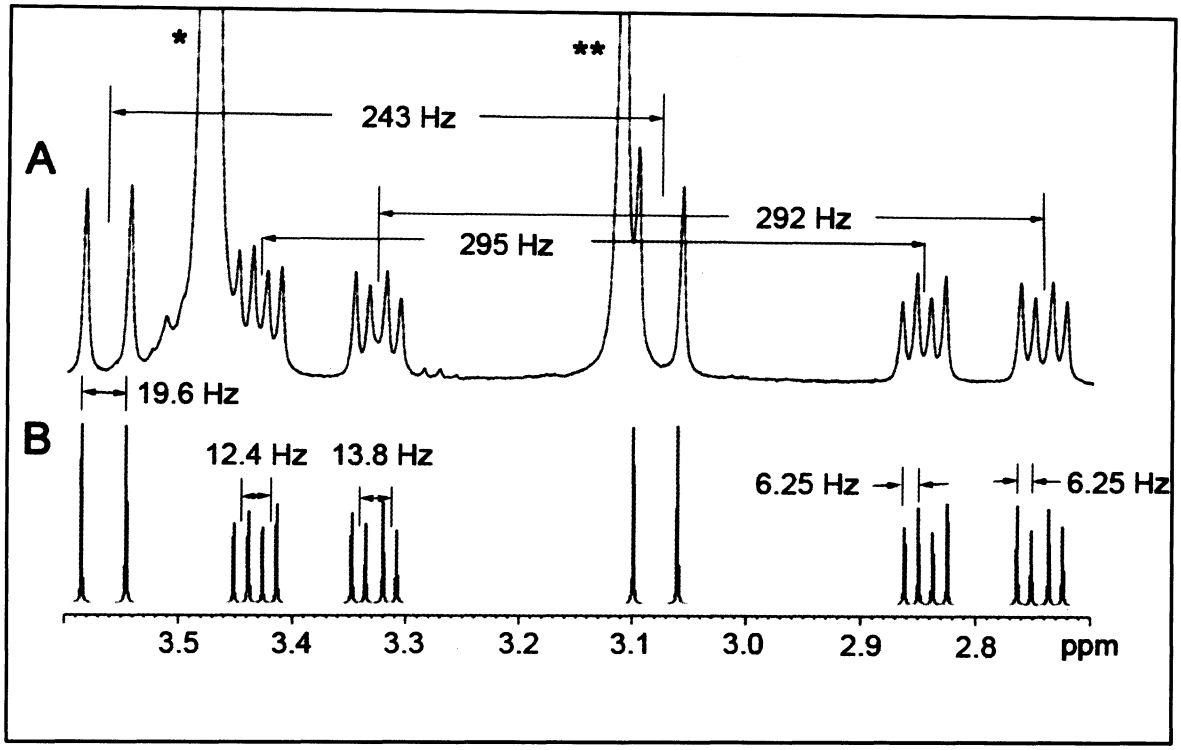

Figure 2.4 Experimental (A) and simulated (B) ^{1}H NMR (500 MHz) spectrum of [4]$^-$ in THF-d_8. The peaks indicated by (*) and (**) arise from residual THF and *tert*-butanol, respectively.

Based on the NMR and *in situ* IR data, we have assigned M^+**[4]**$^-$ ($M^+ = Li^+$, Na^+, K^+) the structure shown in Figure 2.5. Negative-ion electrospray mass spectrometry of M^+**[4]**$^-$ displays a base peak with m/z = 734.63, which is twice the mass of **1a** less a proton, supporting the hypothesis that **1a** undergoes base-induced coupling without loss of any CO ligands. Thus, it is likely that the condensation reaction results in the breaking of a Fe-Mn bond in order to satisfy the EAN rule at all metal sites. The absence of peaks in the region 1900 to 1700 cm^{-1} in the IR spectrum also indicates that isomers containing bridging carbonyls are not present in **[4]**$^-$. We have rationalized the connectivity of **[4]**$^-$ based on the EAN rule, the terminal $Fe(CO)_4$ fragment being satisfied by a 2-electron dative bond from phosphorus, and

manganese assuming the common $LMn(CO)_4X$ motif, where L = $[FeMn(CO)_8(\mu\text{-}PH)]^-$ and X = $[Fe(CO)_4PH_2]^-$. Lindner and Funk proposed a similar, albeit charge-neutral, bonding arrangement upon treating $FeMn(CO)_8(\mu\text{-}PPh_2)$ with trimethylphosphine.[116] The alternative possibility in which addition occurs at the iron atom of **1a** to produce a terminal $Mn(CO)_4$ group is less likely as the EAN rule would not be satisfied for at least one of the metal centers. Five-coordinate $Mn(CO)_4L$ species are rare, and in order for the metal center to achieve an eighteen electron count, it would need to be the location of a negative charge. This does not fit the chemistry of the system as the negative charge should reside on the phosphorus atom of the $[FeMn(CO)_8(\mu\text{-}PH)]^-$ fragment to produce an anionic 2-electron donor that adds to the metal center of an adjacent molecule of **1a**. Additionally, one would expect a $Mn(CO)_4L^-$ complex to readily undergo protonation to produce an octahedral $HMn(CO)_4L$ species. No reaction, however, is observed when **[4]**$^-$ is treated with acid. Attempts to crystallize M^+**[4]**$^-$ ($M^+ = Li^+, Na^+, K^+$) were unsuccessful as the complex decomposed upon removal of solvent and upon concentration. Although **[4]**$^-$ decomposes upon concentration, it is worth noting that the complex does not appear to be particularly sensitive to air or moisture. In fact, a THF solution containing **[4]**$^-$ was diluted with water prior to analysis by electrospray mass spectrometry.

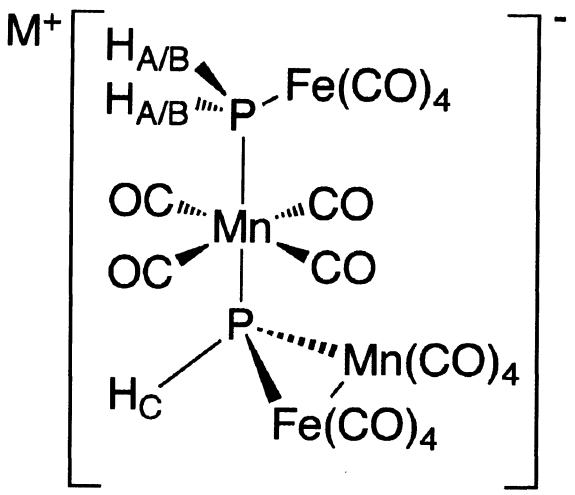

Figure 2.5 . Proposed structure of complex $M^+[4]^-$ ($M^+ = Li^+, Na^+, K^+$).

In an effort to achieve deprotonation while avoiding the aforementioned coupling, a solution of **1a** in THF was cooled to -40 °C and treated with *n*-butyllithium, and the reaction was monitored by *in situ* IR spectroscopy. Under these conditions, complete consumption of **1a** was not observed until 1.0 molar equivalent of *n*-butyllithium had been added, suggesting that the previously observed coupling was inhibited at lower temperatures, favoring complete deprotonation to form the ion **[2a]**$^-$. The IR spectrum of the product displayed similar peak patterns and intensities to **1a**, but was shifted to lower wavenumbers by approximately 40-50 units, as one would predict from the formation of an anion by simple deprotonation (Figure 2.6). A similar shifting is observed during the deprotonation of **1b** to form **[2b]**$^-$ (Figure 2.7).

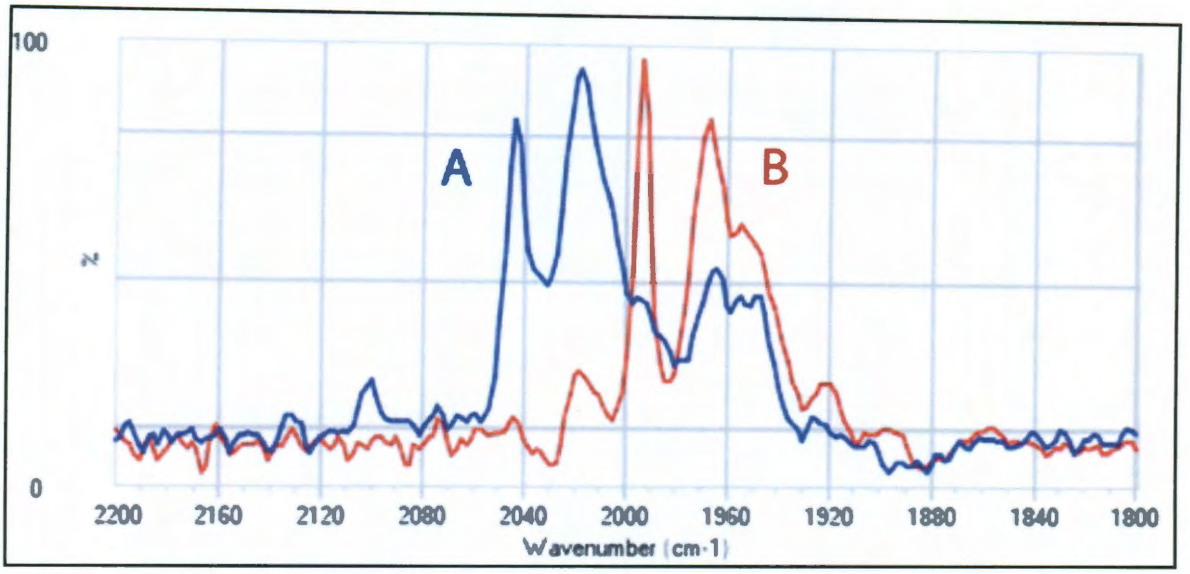

Figure 2.6 *In situ* FTIR spectrum of 1a before (A) and after (B) addition of *n*-butyllithium to form [2a]⁻ in THF. Note that the *in situ* FTIR data are presented in absorbance mode.

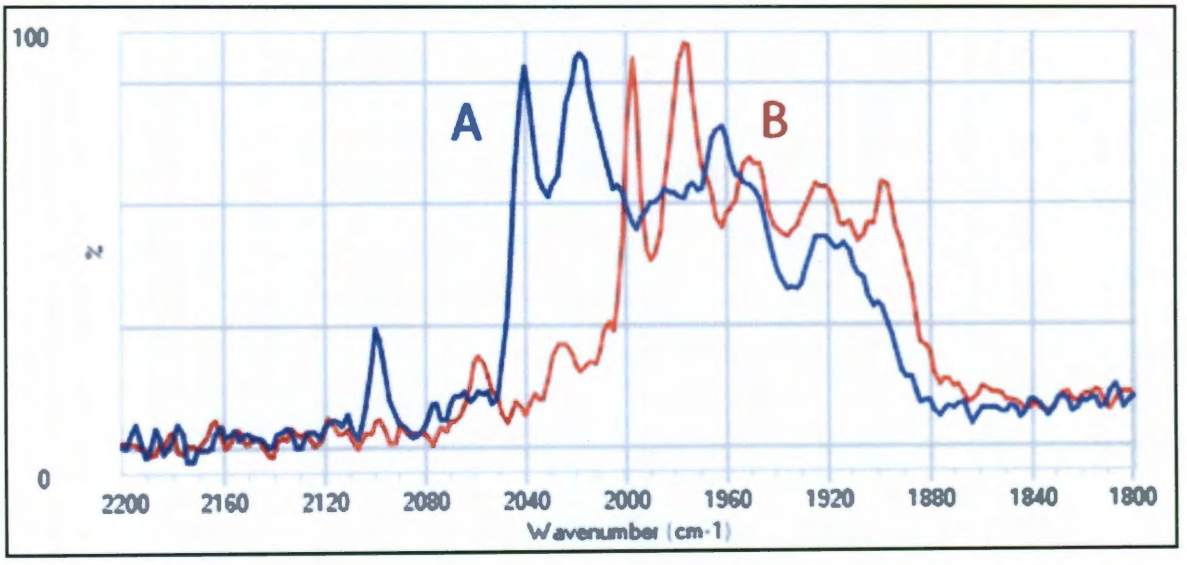

Figure 2.7 *In situ* FTIR spectrum of 1b before (A) and after (B) addition of *n*-butyllithium to form [2b]⁻ in THF.

Continued monitoring of the characteristic peaks of **[2a]**⁻ at -40 °C revealed that the intensities of the peaks diminished linearly over time, becoming unobservable after 30 minutes (Figure 2.8). The disappearance of the IR peaks of **[2a]**⁻ was accompanied by the appearance of a broad distribution of peaks in the

range 1980-1830 cm^{-1}, suggesting that a new species had formed (Figure 2.9). Although the latter material was not isolated, it was observed that brief exposure to the atmosphere lead to rapid conversion to **[4]**$^{-}$, suggesting the possibility that **[2a]**$^{-}$ may first condense to form a dianionic dimer that is readily protonated upon contact with ambient moisture.

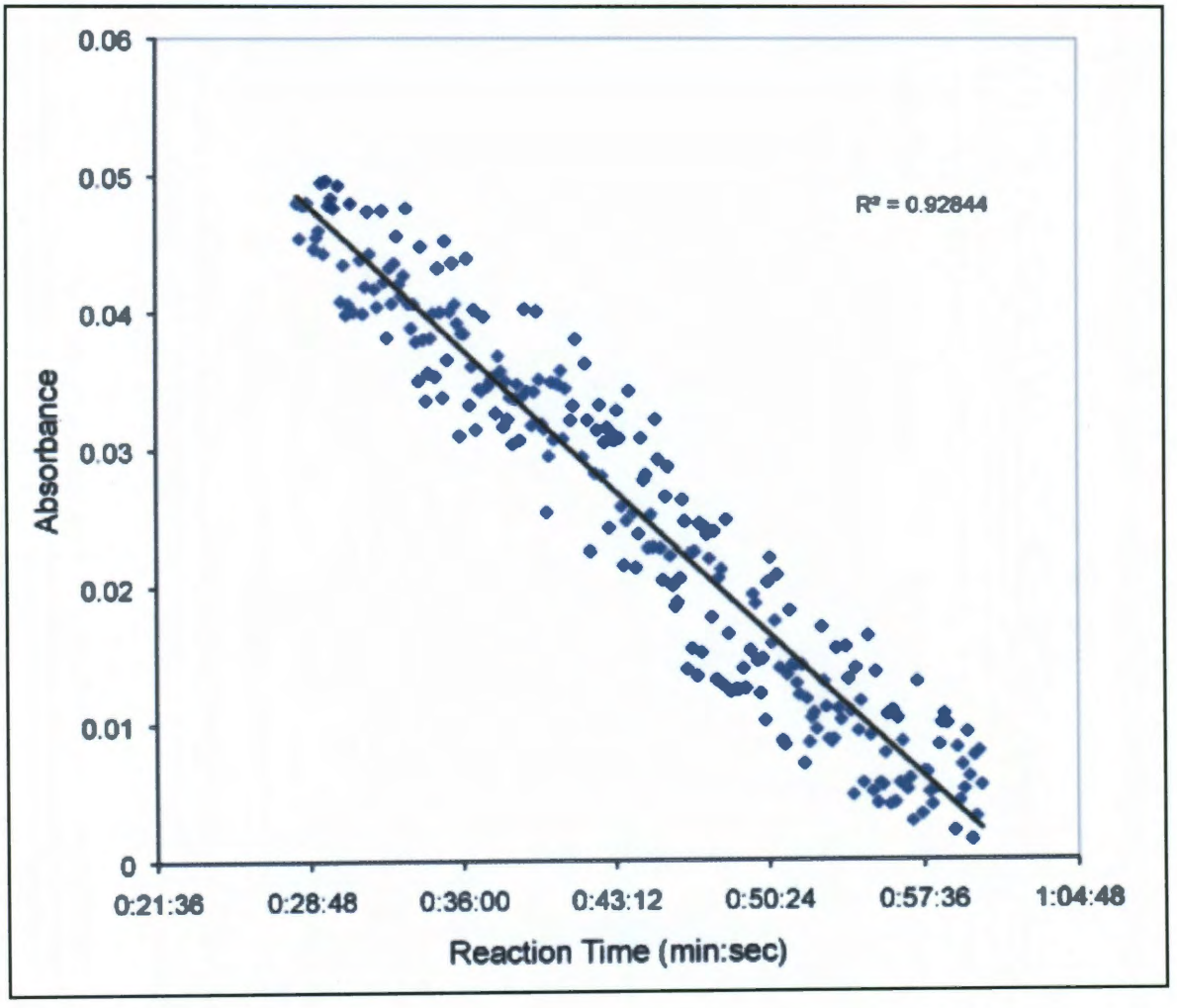

Figure 2.8 Change in IR absorbance of representative peak of [2a]$^{-}$ (1993 cm^{-1}) over time.

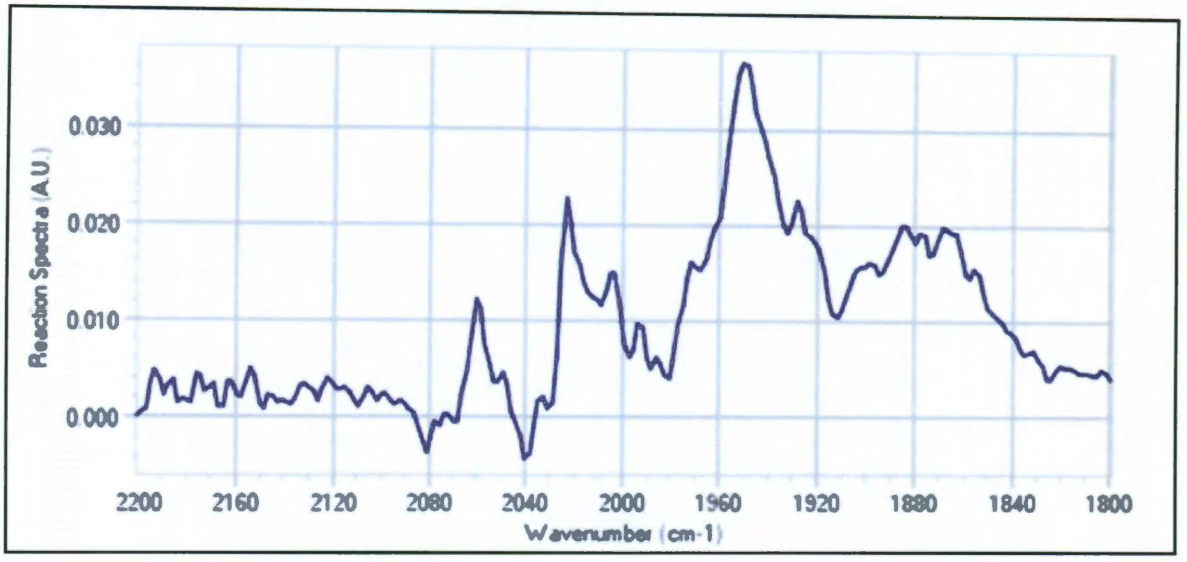

Figure 2.9 *In situ* FTIR spectrum obtained after stirring [2a]⁻ at -40 °C for 30 minutes in THF. Exposure of this product to atmosphere immediately gave rise to [4]⁻.

In an attempt to trap **[2a]⁻**, $AuPPh_3Cl$ was added to a solution of **1a** immediately after deprotonation with *n*-butyllithium at -40 °C. IR spectroscopy indicated rapid consumption (< 10 s) of **[2a]⁻**. The product formed from this reaction was observed to decompose gradually in solution, and rapidly decomposed as the solvent was removed. Although the product of this reaction could not be isolated for complete analysis, the infrared spectrum in THF is markedly similar to that of $FeMn(CO)_8[\mu\text{-}PPh(AuPPh_3)]$ **(3b)**, indicating that the desired product $FeMn(CO)_8[\mu\text{-}PH(AuPPh_3)]$ was likely formed (Figure 2.10). The instability of **[4]⁻** and $FeMn(CO)_8[\mu\text{-}PH(AuPPh_3)]$ towards concentration and solvent removal may be a result of the high reactivity of the P-H bond of the triply-bridging phosphide.

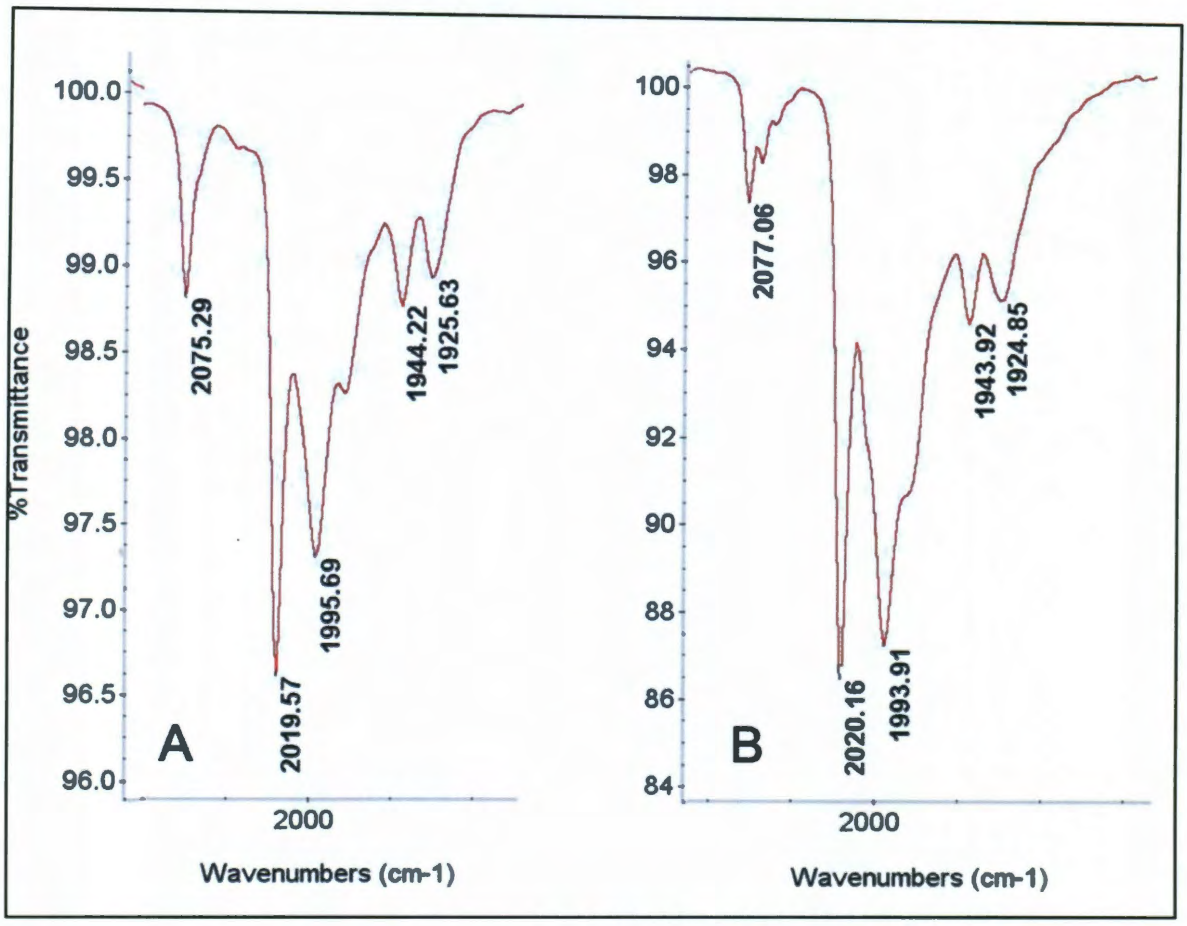

Figure 2.10 FTIR spectra of A) $FeMn(CO)_8[\mu\text{-}PPh(AuPPh_3)]$ (3b) and B) product of reaction of $[2a]^-$ with $AuPPh_3Cl$ in THF.

X-ray quality single crystals of **1a** and **1b** were grown by slow sublimation at 30 °C and approximately 10^{-7} Torr, and their molecular structures were determined (Figure 2.11). Selected bond angles and distances for **1a**, **1b**, and the analogous diphenyl complex $FeMn(CO)_8(\mu\text{-}PPh_2)$ are given in Table 2.2. In all three cases, the bridging phosphorus atom adopts a distorted tetrahedral geometry with acute M-P-M bond angles of 78.887(30)° for **1a**, 78.599(69)° for **1b**, and 77.8(2)° for $FeMn(CO)_8(\mu\text{-}PPh_2)$. The M-M bond lengths of **1a** (2.8374(8) Å) and **1b** (2.8361(16) Å) are very similar, differing from the M-M bond length of $FeMn(CO)_8(\mu\text{-}PPh_2)$ by

only 0.02 Å. Structural comparisons between **1a** and **1b** and isoelectronic homometallic dinuclear complexes containing iron and manganese can also be made. The Fe-Fe bond length in $Cp_2Fe_2(CO)_2(\mu\text{-}H)(\mu\text{-}PHMes)$ is 2.6969(6) Å, considerably shorter than the M-M bonds of **1a** and **1b**.[117] Conversely, the Mn-Mn distance (2.937(5) Å) in $Mn_2(CO)_8(\mu\text{-}PPh_2)(\mu\text{-}H)$ is longer than the M-M distance observed in **1a** and **1b**.[118] Interestingly, the M-M distance in **1a** and **1b** very nearly matches the arithmetic mean of the M-M distances in $Cp_2Fe_2(CO)_2(\mu\text{-}H)(\mu\text{-}PHMes)$ and $Mn_2(CO)_8(\mu\text{-}PPh_2)(\mu\text{-}H)$. The major differences between **1a** and **1b** are the torsion angles between complementary carbonyl ligands on opposite metal centers, shown in Figure 2.12. The twisting observed in **1b** likely results from the minimization of steric interactions between the phenyl ring and equatorial CO ligands. The twisting observed in **1b** is absent in $FeMn(CO)_8(\mu\text{-}PPh_2)$, presumably because the steric interactions between phenyl rings and equatorial CO ligands are equally distributed on both faces of the molecule.

The molecular structures of **3a** and **3b** are presented in Figures 2.13 and 2.14. The steric congestion around the triply-bridging phosphorus atom and the six-coordinate manganese atom in **3a** are readily apparent, and may contribute to the low yields obtained for **3a,** as mentioned earlier. The M-M bond of **3a** remains intact after deprotonation and metallation of **1b**, and is only slightly shorter than the M-M bond lengths in **1a** and **1b**.

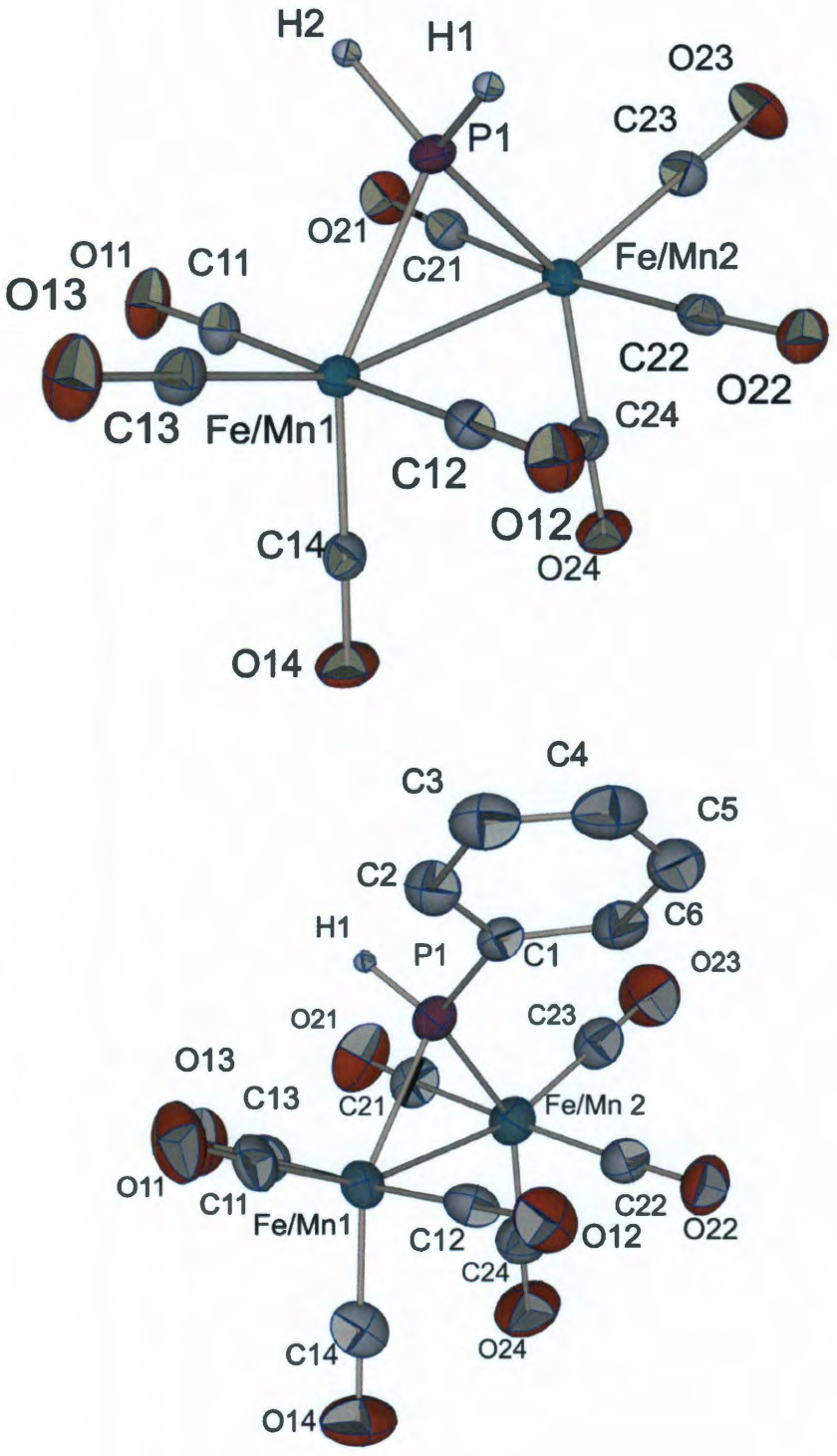

Figure 2.11 Molecular structure of 1a (top) and 1b (bottom). The thermal ellipsoids are shown at the 30% probability level with the exception of the hydrogen atoms, which were refined isotropically. Optimal refinement was achieved by treating the occupancies of the metal centers as a statistical mixture.

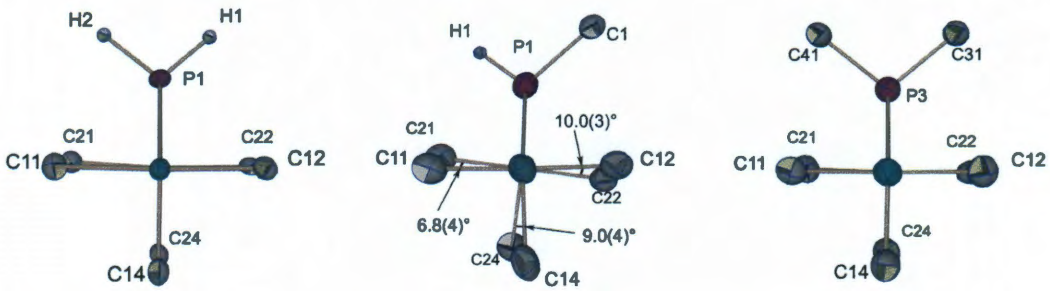

Figure 2.12 Projections of 1a (left), 1b (center), and $FeMn(CO)_8(\mu\text{-}PPh_2)$[119] (right) down the metal-metal bond showing the differences in torsion angles between complimentary carbonyl ligands. Oxygen atoms have been omitted for clarity. Only the ipso carbons of the phenyl rings have been shown.

Table 2.2 Selected bond lengths and angles for complexes 1a, 1b and $FeMn(CO)_8(\mu\text{-}PPh_2)$ (1c).

	(1a)	(1b)	(1c)[119]
		Length (Å)	
Fe/Mn1-Fe/Mn2	2.8374(8)	2.8361(16)	2.8182(8)
Fe/Mn1-P1	2.2328(9)	2.2521(21)	2.2498(1)
Fe/Mn2-P1	2.2334(10)	2.2255(22)	2.2457(11)
P1-H	1.23(4), 1.35(3)	1.15(5)	
P1-C		1.8199(61)	1.8250(34), 1.8297(34)
		Angles (°)	
Fe/Mn1-P1-Fe/Mn2	78.887(30)	78.599(69)	77.641(64)
R_1-P1-R_2 (R = H or C)	101(2)	102(2)	100(2)

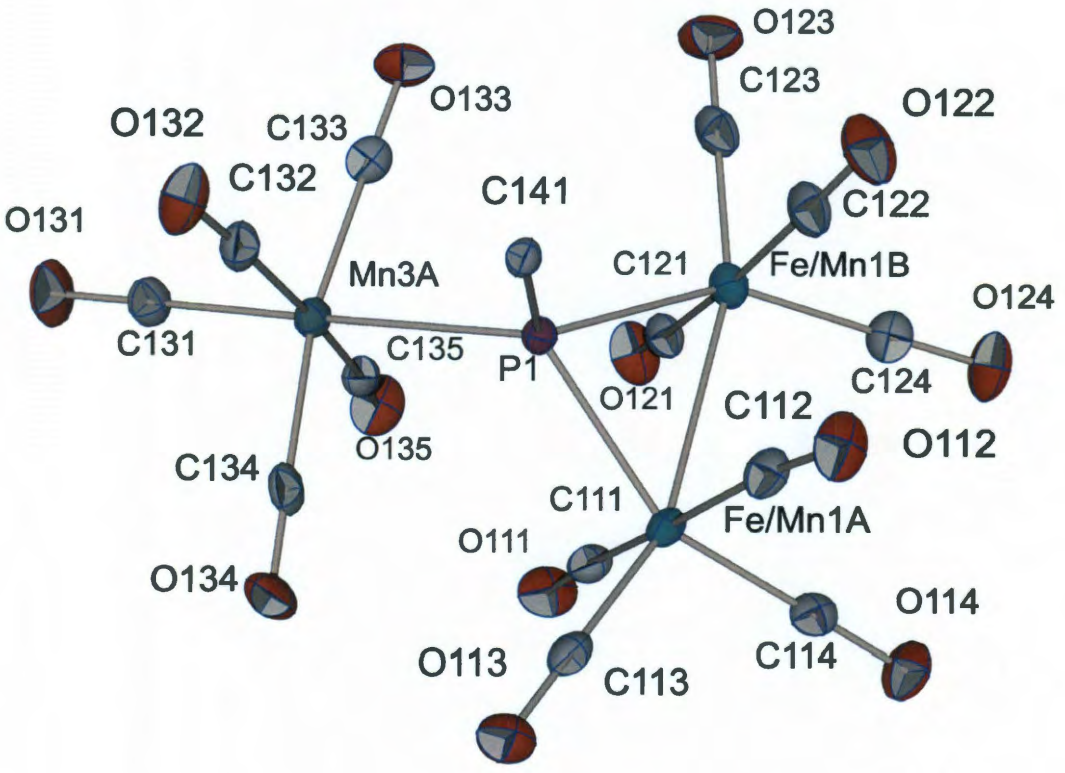

Figure 2.13 Molecular structure of 3a with thermal ellipsoids at the 30% probability level. For clarity, only the ispo carbon (C141) of the phenyl ring is shown. Selected bond distances (Å) and angles (°): Fe/Mn1A-Fe/Mn1B 2.7954(9), Fe/Mn1A-P1 2.3067(10), Fe/Mn1B-P1 2.2891(11), P1-Mn3A 2.4774(11); Fe/Mn1A-P1-Fe/Mn1B 74.9(6).

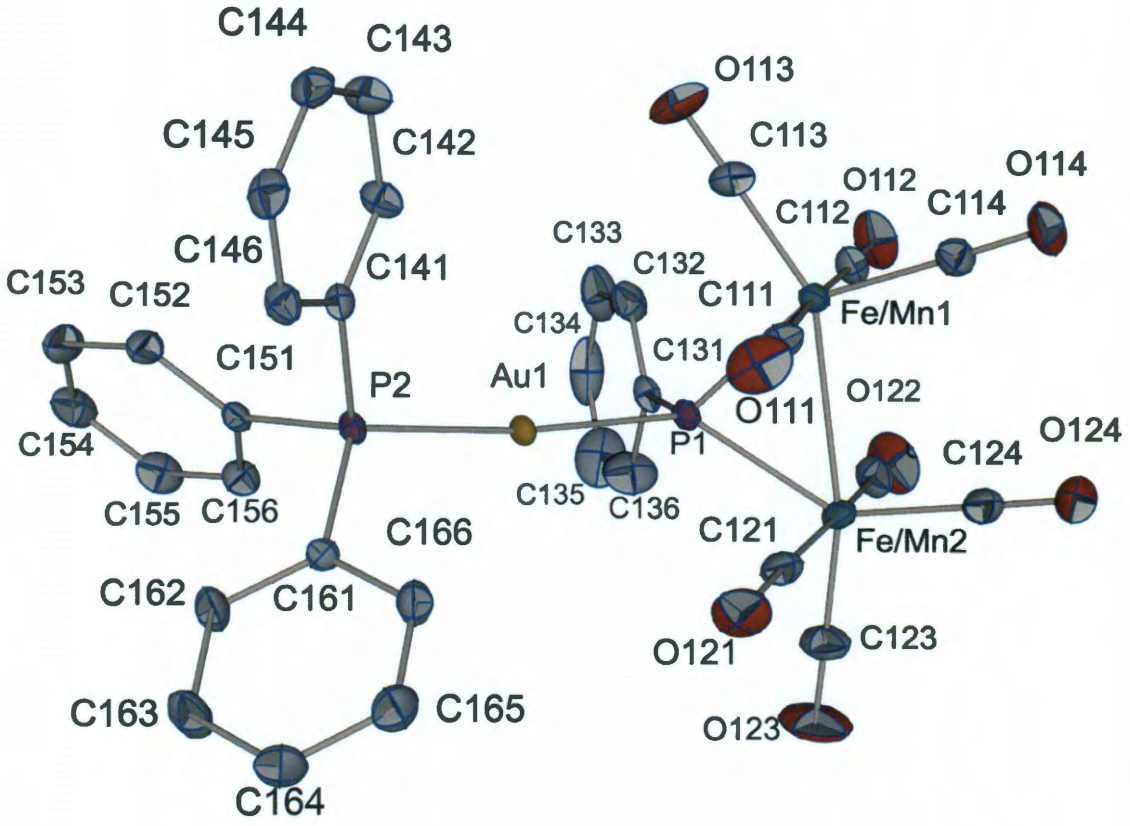

Figure 2.14 Molecular structure of 3b with ellipsoids shown at 30% probability. Selected bond distances (Å) and angles (°): Fe/Mn1-Fe/Mn2 2.7894(7), Fe/Mn1-P1 2.2969(9), Fe/Mn2-P1 2.2785(9), Au1-P1 2.3126(8), Au1-P2 2.3009(8); Fe/Mn1-P1-Fe/Mn2 75.1(6), P1-Au1-P2 173.7(3)

The triply-bridging phosphorus atom of **3b** is less sterically crowded than the phosphorus atom of **3a** due to the longer P-Au-P distance separating the bulky triphenylphosphine group from the rest of the molecule. Similar to **3a**, the M-M bond of **3b** also remains intact upon metallation and is also slightly shorter than the M-M bonds observed in **1a** and **1b**. The P-Au-P bond angle (173.7(3)°) is slightly less than the ideal angle of 180°. A similar deviation from the ideal 180° P-Au-P bond angle was observed in the isoelectronic homometallic complex $Mn_2(CO)_8[\mu\text{-}P(Cy)(AuPCy_3)](\mu\text{-}H)$, which was reported to have a P-Au-P angle of 171.12(5)°.[120]

2.4 Conclusions

Complexes **1a** and **1b** represent rare examples of dinuclear heterometallic complexes containing a μ-PH_2 or μ-PRH functionality. Although structurally similar, these two complexes differ greatly in their reactivities. **1b** can be deprotonated and metallated to yield the isolable complexes **3a** and **3b**, which contain a triply bridging phosphorus atom. By contrast, deprotonation of **1a** at room temperature leads to rapid and complete coupling with the parent complex to form complex M^+**[4]**$^-$ (M^+ = Li^+, Na^+, K^+), which decomposes upon concentration. At lower temperatures, coupling of **1a** and **[2a]**$^-$ is arrested and metallation of **[2a]**$^-$ can be achieved via addition of $AuPPh_3Cl$. However, the product of this metallation decomposes slowly in solution and rapidly decomposes as the solvent is removed.

Complexes **1a** and **1b** were specifically designed to serve as molecular precursors to advanced $Fe_{2-x}Mn_xP$ materials. **1a** can be prepared in reasonable yields and can be sublimed without decomposition at reduced pressures, and is therefore an attractive candidate for use in the preparation of materials such as nanoparticles and films. The following chapter will describe efforts to prepare $Fe_{2-x}Mn_xP$ nanoparticles from the single-source precursors described in this chapter.

Chapter 3. Synthesis of $Fe_{2-x}Mn_xP$ Nanoparticles from Single-Source Molecular Precursors

*(Note: This chapter contains a significant amount of material previously published in Chemistry of Materials, **2011**, 23, 3731-3739.)*

3.1 Introduction

As discussed in Chapter 1, nanoscale metal pnictide research has largely focused on the preparation of binary materials of the form M_AE_B, where M is a transition metal and E is a group 15 element. By comparison, relatively few reports of ternary phase metal pnictides of the form $M_AM'_BE_X$ have been reported in the literature (Chapter 1, Table 1.4). Brock and coworkers recently described the stepwise and one-pot syntheses of heterostructured MnP@InP nanoparticles using $Mn_2(CO)_{10}$, $P(SiMe_3)_3$, and $InCl_3$ as the sources of manganese, phosphorus, and indium, respectively.[121] Hyeon and coworkers reported the preparation of iron-rich, ternary phosphide nanoparticles with composition $Fe_{2-x}Ni_xP$ ($0.2 \leq x \leq 0.5$) using $Fe(CO)_5$ and $Ni(acac)_2$ as the metal sources and trioctylphosphine (TOP) as the phosphorus source.[70] The synthesis of cobalt-rich $Co_{2-x}Fe_xP$ ($0.3 \leq x \leq 0.5$) nanoparticles using iron(III) oleate and Co(II) oleate as metal sources and trioctylphosphine as the source of phosphorus has also been reported.[71]

In this work, we describe our efforts to prepare heterobimetallic $Fe_{2-x}Mn_xP$ nanoparticles using single-source molecular precursors. The ternary phase

$Fe_{2-x}Mn_xP$ was selected in part for its relationship to the quaternary phase $FeMnP_{1-x}As_x$, which has been extensively studied in the bulk due to its substantial magnetocaloric effect.[49, 51, 122] The $Fe_{2-x}Mn_xP$ phase serves as a step towards preparing ternary and higher order metal pnictide nanomaterials from single-source precursors. The $Fe_{2-x}Mn_xP$ system also demonstrates interesting structural properties that are dependent on the stoichiometry of the phase. In the range $0.31 \leq x \leq 0.62$, $Fe_{2-x}Mn_xP$ has an orthorhombic structure, but adopts a hexagonal structure outside this compositional range.[55] The orthorhombic phase has been found to undergo a phase transformation to the hexagonal structure at high temperatures due to disordering of the metal sites.[123] Because the formation of metastable phases is common when relatively soft synthetic methods are employed, the question arises as to whether $Fe_{2-x}Mn_xP$ nanomaterials prepared *via* solution-based methods would crystallize with the orthorhombic structure or a metastable hexagonal structure.[124-127]

In this chapter, efforts to prepare $Fe_{2-x}Mn_xP$ nanoparticles from the thermal decomposition of single-source molecular precursors $FeMn(CO)_8(\mu\text{-}PR_2)$(R = Ph or R = H) are described. The final compositions of the nanoparticles are largely determined by the identity of the precursors, with the $FeMn(CO)_8(\mu\text{-}PH_2)$ precursor yielding the most favorable results. Curiously, it was observed that the elemental composition of nanoparticles prepared in solution did not match the composition of the bulk solid prepared from solventless decomposition of $FeMn(CO)_8(\mu\text{-}PH_2)$, suggesting a non-innocent interaction between stabilizing agents and the growing nanoparticles. Furthermore, appreciable nanoparticle growth was invariably

accompanied by an elemental composition that deviated from the expected FeMnP stoichiometry.

3.2 Experimental

General Considerations. Except where indicated, all reactions were carried out under an inert argon atmosphere using standard Schlenk techniques. Dioctyl ether (99%, Sigma-Aldrich), 1-octadecene (technical 90%, Sigma-Aldrich), oleic acid (technical 90%, Sigma-Aldrich), oleylamine (technical 70%, Sigma-Aldrich), trioctylamine (98%, Sigma-Aldrich), and trioctylphosphine oxide (99%, Strem) were all heated to 100 °C under vacuum for several hours to remove dissolved oxygen and water. Tetrakis(decyl)ammonium bromide (98%, Sigma-Aldrich), hexadecylamine (technical 90%, Sigma-Aldrich), quinoline (98%, Sigma-Aldrich), iron pentacarbonyl (Sigma-Aldrich), manganese carbonyl (98% Sigma-Aldrich) and stearonitrile (92%, TCI) were used as received. Hexadecylisocyanide, tetrakis(decyl)ammonium tetraphenylborate, and tris(trimethylsilyl)phosphine were prepared according to literature procedures.[128-130] $FeMn(CO)_8(\mu\text{-}PPh_2)$, $FeMn(CO)_8(\mu\text{-}PPhH)$, and $FeMn(CO)_8(\mu\text{-}PH_2)$ were synthesized using methods reported previously.[89, 131]

Thermal Decomposition of $FeMn(CO)_8(\mu\text{-}PPh_2)$.

Method A. $FeMn(CO)_8(\mu\text{-}PPh_2)$ (155 mg, 0.298 mmol) was added to a three-neck flask equipped with a reflux condenser and a 90° stopcock under an argon atmosphere. Trioctylamine (3.0 mL) and oleic acid (1.0 mL) were then introduced,

and the solution was heated using a heating mantle and stirred magnetically. Heating was continued until the solution reached 350 °C, whereupon the solution turned dark black. After heating for an additional 20 minutes, the flask was removed from the heating mantle and cooled to room temperature. Nanoparticles were precipitated using absolute ethanol and were isolated *via* centrifugation.

Method B. $FeMn(CO)_8(\mu\text{-}PPh_2)$ (155 mg, 0.298 mmol) was dissolved in dioctyl ether (4.0 mL) and injected into a solution containing dioctyl ether (4.0 mL), oleic acid (94.0 μL, 0.298 mmol), and hexadecylamine (360 mg, 1.49 mmol) at 300 °C. After several minutes, the solution became dark black. After heating for an additional 2 hours, the reaction mixture was removed from heat and allowed to cool to room temperature. Nanoparticles were precipitated using absolute ethanol and were isolated by centrifugation.

Preparation of $Fe_{2-x}Mn_xP$ ($0.15 \leq x \leq 0.7$) Nanoparticles from Decomposition of $FeMn(CO)_8(\mu\text{-}PH_2)$. $FeMn(CO)_8(\mu\text{-}PH_2)$ (110 mg, 0.299 mmol) was dissolved in dioctyl ether (3.0 mL) and injected into a magnetically stirred solution containing dioctyl ether (4.0 mL), oleic acid (95.0 μL. 0.299 mmol), and hexadecylamine (361 mg, 1.50 mmol) that had been preheated to 220 °C. The solution became dark black upon injection, and the reaction was stirred for an additional 2 hours at 220 °C, after which the solution was allowed to cool to room temperature. Nanoparticles were precipitated from the solution by addition of absolute ethanol and were isolated by centrifugation. The isolated particles were then dispersed in hexane and ethanol was added to induce precipitation, and the particles were isolated by centrifugation.

The related $FeMn(CO)_8(\mu\text{-}PPhH)$ precursor was also decomposed under similar conditions, but failed to yield well-defined nanoparticles. This observation, along with the relatively low yields associated with the preparation of the precursor, prompted us to abandon further experiments using $FeMn(CO)_8(\mu\text{-}PPhH)$.

Solventless Decomposition of $FeMn(CO)_8(\mu\text{-}PH_2)$. $FeMn(CO)_8(\mu\text{-}PH_2)$ (100 mg, 0.272 mmol) was placed in a Schlenk tube under a flow of argon. The tube was then placed in a sand bath that had been preheated to 300 °C in order to promote rapid decomposition of the precursor with minimal sublimation. The resulting black solid was then washed with dried, distilled hexanes under argon. In some cases, the black solid was subjected to annealing at 500 °C for several hours, but the PXRD patterns of the solid before and after annealing were identical. Solventless decomposition of $FeMn(CO)_8(\mu\text{-}PPh_2)$ at 400 °C also produced a dark black solid, but the material was found to be amorphous, even after annealing at 550 °C for several hours.

Co-decomposition of Multiple Precursors

Method A. $Fe(CO)_5$ (50.0 μL, 0.380 mmol), $Mn_2(CO)_{10}$ (74.1 mg, 0.190 mmol), and $P(SiMe_3)_3$ (110 μL, 0.380 mmol) were combined in 1-octadecene (4.0 mL) and gently heated until $Mn_2(CO)_{10}$ was completely dissolved. The solution was then injected into preheated trioctylphosphine oxide (350 °C). The solution immediately became dark brown/black upon injection, and the reaction mixture was heated at 350 °C for an additional two hours. The solution was allowed to cool to 70 °C, whereupon absolute ethanol was added to induce nanoparticle precipitation. The particles were isolated by centrifugation, redispersed in hexane, precipitated with ethanol, and isolated once again by centrifugation.

Method B. $Fe(CO)_5$ (50.0 μL, 0.380 mmol), $Mn_2(CO)_{10}$ (74.1 mg, 0.190 mmol), and $P(SiMe_3)_3$ (110 μL, 0.380 mmol) were dissolved in warm dioctyl ether (4.0 mL) and injected into a solution containing dioctyl ether (5.0 mL), oleic acid (120 μL, 0.380 mmol), and hexadecylamine (459 mg, 1.90 mmol) that had been preheated to 220 °C. The solution became dark brown after several minutes, and was heated at 220 °C for an additional two hours. The solution was cooled to room temperature, and absolute ethanol was added until an oily residue precipitated from the solution. The supernatant was decanted, and the oily residue was taken up in hexanes. Attempts to induce precipitation again by addition of ethanol were ineffective.

Decomposition of $FeMn(CO)_8(\mu\text{-}PH_2)$ in neat dioctyl ether or 1-octadecene. $FeMn(CO)_8(\mu\text{-}PH_2)$ (55.0 mg, 0.150 mmol) was dissolved in dioctyl ether or 1-octadecene (2.0 mL) and injected into dioctyl ether or 1-octadecene (3.0 mL) at 220 °C. The solution became dark brown upon injection, and the reaction was stirred for an additional 2 hours at 220 °C, after which the solution was allowed to cool to room temperature. Nanoparticles were precipitated from the solution by addition of absolute ethanol and were isolated by centrifugation. The isolated particles were then dispersed in hexane and ethanol was added to induce precipitation, and the particles were isolated by centrifugation.

Decomposition of $FeMn(CO)_8(\mu\text{-}PH_2)$ in the presence of hexadecylamine. $FeMn(CO)_8(\mu\text{-}PH_2)$ (55.0 mg, 0.150 mmol) was dissolved in dioctyl ether (2.0 mL) and injected into a solution containing dioctyl ether (3.0 mL) and hexadecylamine (0.750 mmol, 2.25 mmol, or 4.50 mmol) that had been preheated to 220 °C. The solution became dark brown upon injection, and the reaction was stirred for an

additional 2 hours at 220 °C, after which the solution was allowed to cool to room temperature. The particles were washed and isolated as described above.

Decomposition of $FeMn(CO)_8(\mu\text{-}PH_2)$ in the presence of oleic acid. $FeMn(CO)_8(\mu\text{-}PH_2)$ (55.0 mg, 0.150 mmol) was dissolved in dioctyl ether (2.0 mL) and injected into a solution containing dioctyl ether (3.0 mL) and oleic acid (0.150 mmol or 1.50 mmol) that had been preheated to 220 °C. The solution became dark black upon injection, and the reaction was stirred for an additional 2 hours at 220 °C, after which the solution was allowed to cool to room temperature. The reaction was worked-up as described above.

Decomposition of $FeMn(CO)_8(\mu\text{-}PH_2)$ in the presence of hexadecylisocyanide. $FeMn(CO)_8(\mu\text{-}PH_2)$ (55.0 mg, 0.150 mmol) was dissolved in dioctyl ether (2.0 mL) and injected into a solution containing dioctyl ether (3.0 mL) and hexadecylisocyanide (37.7 mg, 0.150 mmol) that had been preheated to 220 °C. The solution became dark brown upon injection, and the reaction was stirred for an additional 2 hours at 220 °C, after which the solution was allowed to cool to room temperature. Nanoparticles were isolated as described earlier.

Decomposition of $FeMn(CO)_8(\mu\text{-}PH_2)$ in the presence of trioctylphosphine oxide. $FeMn(CO)_8(\mu\text{-}PH_2)$ (61.0 mg, 0.166 mmol) was dissolved in 1-octadecene (2.5 mL) and injected into a solution containing hot (220 °C) trioctylphosphine oxide (3.0 g) and oleylamine (0.166 mmol). The solution became dark brown upon injection, and the reaction was stirred for an additional hour at 220 °C, after which the solution was allowed to cool to 70 °C, whereupon ethanol was added to induce

nanoparticle precipitation. The nanoparticles were isolated by centrifugation, and washed several times with ethanol before being re-isolated by centrifugation.

Decomposition of $FeMn(CO)_8(\mu\text{-}PH_2)$ in the presence of quinoline. $FeMn(CO)_8(\mu\text{-}PH_2)$ (55.0 mg, 0.150 mmol) was dissolved in dioctyl ether (2.0 mL) and injected into a solution containing dioctyl ether (3.0 mL) and quinoline (0.750 mmol) that had been preheated to 220 °C. The solution became dark black upon injection, and the reaction was stirred for an additional 15 minutes at 220 °C, after which the solution appeared to lose homogeneity and a black precipitate was observed. The reaction mixture was allowed to cool to room temperature, and nanoparticles were completely precipitated from the solution by addition of absolute ethanol and were isolated by centrifugation. The isolated particles were dispersed in hexanes and precipitated again with ethanol, after which the particles were isolated by centrifugation.

Decomposition of $FeMn(CO)_8(\mu\text{-}PH_2)$ in the presence of stearonitrile. $FeMn(CO)_8(\mu\text{-}PH_2)$ (65.0 mg, 0.176 mmol) was dissolved in dioctyl ether (2.0 mL) and injected into a solution containing dioctyl ether (3.0 mL) and stearonitrile (701 mg, 2.64 mmol) that had been preheated to 220 °C. The solution became dark brown upon injection, and the reaction was stirred for an additional hour at 220 °C, after which the solution was allowed to cool to room temperature. The reaction was worked-up as described above.

Decomposition of $FeMn(CO)_8(\mu\text{-}PH_2)$ in the presence of tetrakis(decyl)ammonium bromide. $FeMn(CO)_8(\mu\text{-}PH_2)$ (55.0 mg, 0.150 mmol) was dissolved in 1-octadecene (2.0 mL) and injected into a magnetically stirred

solution containing 1-octadecene (3.0 mL), tetrakis(decyl)ammonium bromide (422 mg, 0.600 mmol), and oleylamine (2.25 mmol) that had been preheated to 220 °C. The solution became dark brown upon injection, and the reaction was stirred for an additional 2 hours at 220 °C, after which the solution was allowed to cool to room temperature. Nanoparticles were precipitated from the solution and isolated as described previously.

Decomposition of $FeMn(CO)_8(\mu\text{-}PH_2)$ in the presence of tetrakis(decyl)ammonium tetraphenylborate. $FeMn(CO)_8(\mu\text{-}PH_2)$ (55.0 mg, 0.150 mmol) was dissolved in 1-octadecene (2.0 mL) and injected into a magnetically stirred solution containing 1-octadecene (3.0 mL), tetrakis(decyl)ammonium tetraphenylborate (539 mg, 0.600 mmol), and oleylamine (2.25 mmol) that had been preheated to 220 °C. The solution became dark brown upon injection, and the reaction was stirred for an additional hour at 220 °C, after which the solution was allowed to cool to room temperature. Nanoparticles were precipitated from the solution and isolated as described previously.

Characterizations. Transmission electron microscopy (TEM) experiments were performed by drop-casting a dilute suspension of nanoparticles in hexane on a carbon-coated copper grid. TEM images were obtained with JEOL 1230 and JEOL 2010 microscopes operated at 100 kV.

Powder X-ray diffraction (PXRD) data were obtained with a Rigaku D/Max-2100PC powder diffractometer using unfiltered Cu Kα radiation (λ = 1.5406 Å) at 40 kV and 40 mA and a step size of 0.02°. The contribution from *Kα2* radiation was

removed using the Rachinger algorithm. Goniometer alignment was performed regularly with the use of a SiO_2 reference standard. Post-acquisition PXRD data processing was carried out using MDI's Jade 9.0. Powder diffraction files (PDF) from the International Centre for Diffraction Data (ICDD) were used as references for phase identification.

Quantitative elemental analyses of iron, manganese, and phosphorus were carried out by inductively coupled plasma optical emission spectroscopy (ICP-OES) using a Perkin-Elmer instrument with internal yttrium standard. The spectral emission lines at 238.204 nm, 257.610 nm, and 213.617 nm were employed for analysis of iron, manganese, and phosphorus, respectively. Iron and manganese were analyzed by radial plasma viewing, while phosphorus was analyzed by axial plasma viewing. Samples were prepared by digestion in concentrated nitric acid and diluted to a suitable concentration for analysis. Selected samples were also sent to an independent commercial laboratory for analysis.

X-Ray photoelectron spectroscopy (XPS) was carried out using a Physical Electronics PHI Quantera SXM instrument using a monochromatic Al K_α source (1486.6 eV) operated at 40.7 W with a beam size of 200 μm and a take off angle of 45°. Powdered samples were pressed into indium foil prior to analysis.

3.3 Results and Discussion

Attempts to prepare $Fe_{2-x}Mn_xP$ nanoparticles using solution-based methods began with the selection of a single-source precursor candidate. We surmised that

an ideal precursor molecule would contain iron, manganese, and phosphorus in a 1:1:1 ratio and would possess relatively labile ligands that would readily disassociate at elevated temperatures. A search of the relevant literature revealed that Yasafuku and Yamazaki had previously reported the synthesis of the organometallic complex $FeMn(CO)_8(\mu\text{-}PPh_2)$, which seemed to be a suitable precursor for our experiments.[89] Early in our studies, we chose to avoid the use of phosphorus-containing solvents and stabilizers such as trioctylphosphine (TOP) and trioctylphosphine oxide (TOPO) to ensure that any phosphorus found in the resulting nanoparticles could be traced back to the single-source precursor and so that we could conduct precise elemental analyses of the particles without detecting adventitious or surface-bound phosphorus.

Initial thermal decompositions of $FeMn(CO)_8(\mu\text{-}PPh_2)$ were carried out by combining the precursor with trioctylamine and oleic acid and heating the mixture slowly from room temperature. At approximately 200 °C, the solution darkened from a bright orange-red color to deep red, then began to lighten to a pale yellow color at 225 °C. At 270 °C, the solution turned clear and almost completely colorless. Heating continued until the solution reached 350 °C, whereupon the solution turned black. TEM analysis of the resulting nanoparticles showed the formation of semi-spherical particles with a size of 15-20 nm (Figure 3.1). However, PXRD and ICP-OES analyses indicated that the particles were composed solely of wüstite (FeO).

The appearance of a clear, colorless solution, along with the failure to recover any manganese or phosphorus-containing materials, suggested that manganese may have been solubilized by the large excess of coordinating stabilizers present in the

solution. The exact source of oxygen in the FeO phase is unknown, but we suspect that the oxygen originates from the thermal decomposition of metal oleate species as opposed to air oxidation, as the decomposition was carried out under an inert atmosphere using rigorously degassed solvents. It should be noted that decomposition of metal oleate species is an established method to produce metal oxide phases under appropriate conditions.[132, 133]

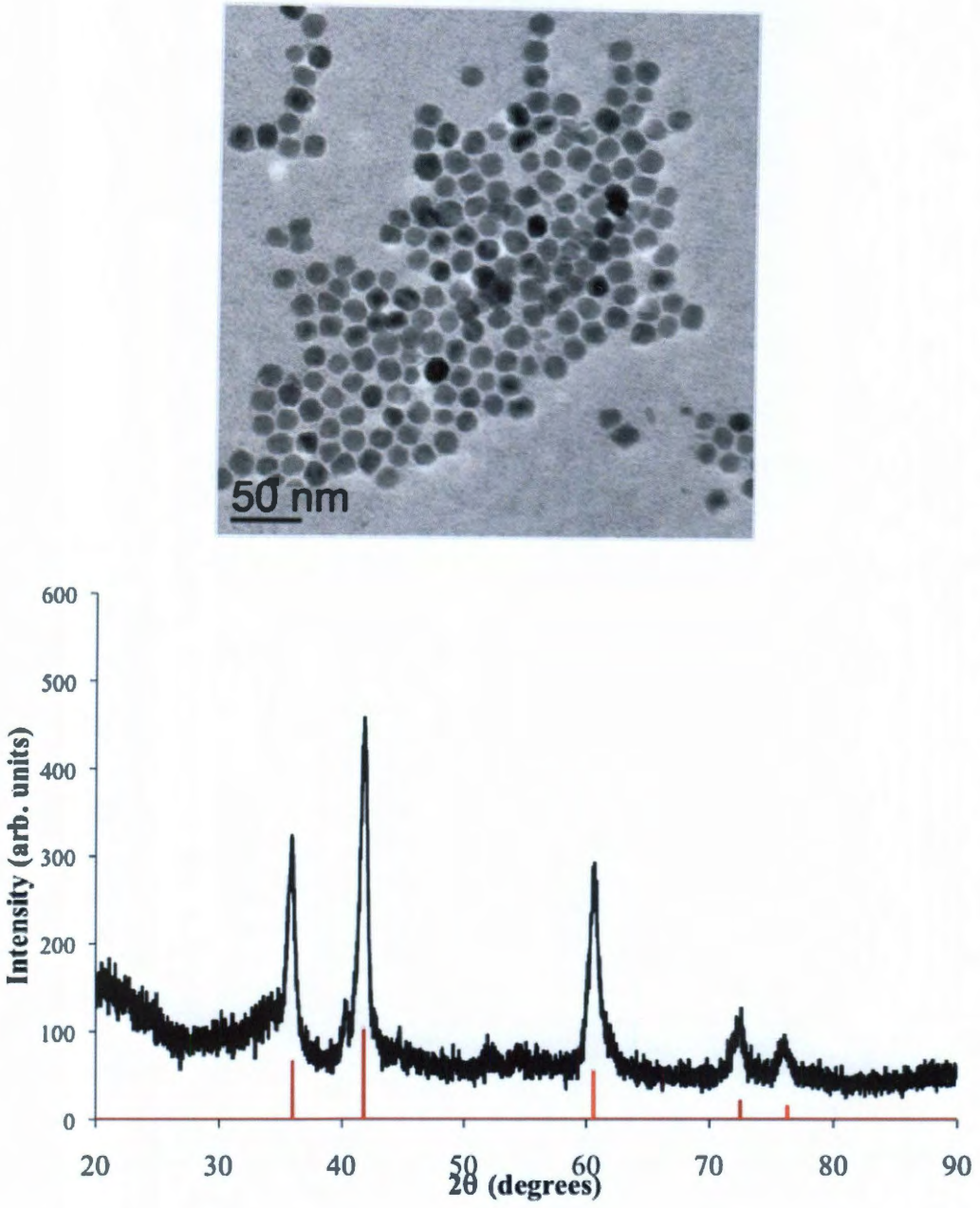

Figure 3.1 TEM micrograph (top) and PXRD pattern (bottom) of FeO nanoparticles formed by the thermal decomposition of $FeMn(CO)_8(\mu\text{-}PPh_2)$ in oleic acid and trioctylamine. The line diagram below the experimental PXRD data represents the reference diffraction pattern of FeO (ICDD PDF # 000-0464).

Additional experiments were carried out in which the amount of oleic acid was greatly reduced (1 molar equivalent relative to the $FeMn(CO)_8(\mu\text{-}PPh_2)$

precursor) and the precursor was injected into a solution of dioctyl ether, hexadecylamine, and oleic acid at reflux. Again, FeO nanoparticles with nearly identical morphologies as those shown in Figure 2 were isolated (Figure 3.2).

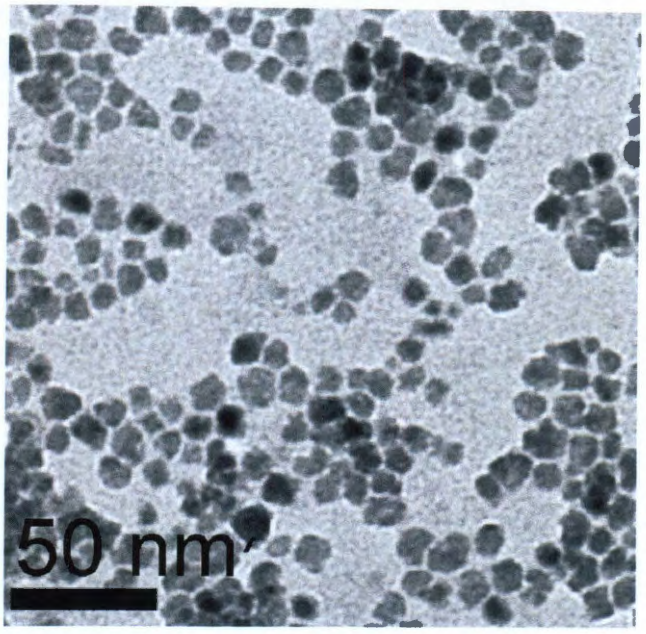

Figure 3.2 TEM micrograph of FeO nanoparticles formed from decomposition of $FeMn(CO)_8(\mu\text{-}PPh_2)$ in dioctyl ether in the presence of oleic acid and hexadecylamine ($FeMn(CO)_8(\mu\text{-}PPh_2)$: oleic acid: hexadecylamine molar ratio = 1:1:5).

After considering the unexpected results of the thermal decomposition of $FeMn(CO)_8(\mu\text{-}PPh_2)$, we proposed that the relatively high temperature (> 350 °C) required for decomposition could possibly cause cluster disintegration before conversion to the nanoparticles. The analogous precursor, $FeMn(CO)_8(\mu\text{-}PH_2)$, was targeted as the relatively robust phosphorus-carbon bonds would be replaced by more labile P-H bonds to yield a precursor with a lower decomposition threshold.

Thermal decomposition of $FeMn(CO)_8(\mu\text{-}PH_2)$ was carried out by dissolving the precursor in dioctyl ether and injecting into a hot solution (220 °C) containing

dioctyl ether, oleic acid, and hexadecylamine. $FeMn(CO)_8(\mu\text{-}PH_2)$, oleic acid, and hexadecylamine were used with a molar ratio of 1:1:5, respectively. The resulting nanoparticles were isolated and analyzed by TEM, PXRD, and ICP-OES. Transmission electron micrographs of the particles showed the formation of roughly-textured, needle-like particles with an average length and width of about 125 nm and 10 nm, respectively. ICP-OES analysis of the particles suggested an elemental composition of $Fe_{1.3}Mn_{0.7}P$, and the PXRD pattern is consistent with a hexagonal crystal structure (Figure 3.3). Ideally, the aggregate elemental composition and the diffraction data would be correlated using a Vegard's law plot of cell volume *vs.* composition. Unfortunately, the cell volume could not be conclusively refined from the XRPD data due to significant peak broadening. Curiously, repeated experiments carried out under identical conditions resulted in similar anisotropic morphologies, but the elemental composition of the particles ranged from $Fe_{1.85}Mn_{0.15}P$ to $Fe_{1.3}Mn_{0.7}P$. Manganese-rich phases were never observed. Although experimental evidence suggests that manganese sequestration can be attributed to additives in solution (*vide infra*), the exact mechanistic details are not fully understood. It is clear that the process through which manganese depletion occurs is complex and appears to be highly sensitive to relatively small changes in experimental parameters. Minor fluctuations in temperature and homogeneity brought about by "hot-spots" from the heating apparatus or stirring speed are common, and may result in the variation in composition observed over many trials.

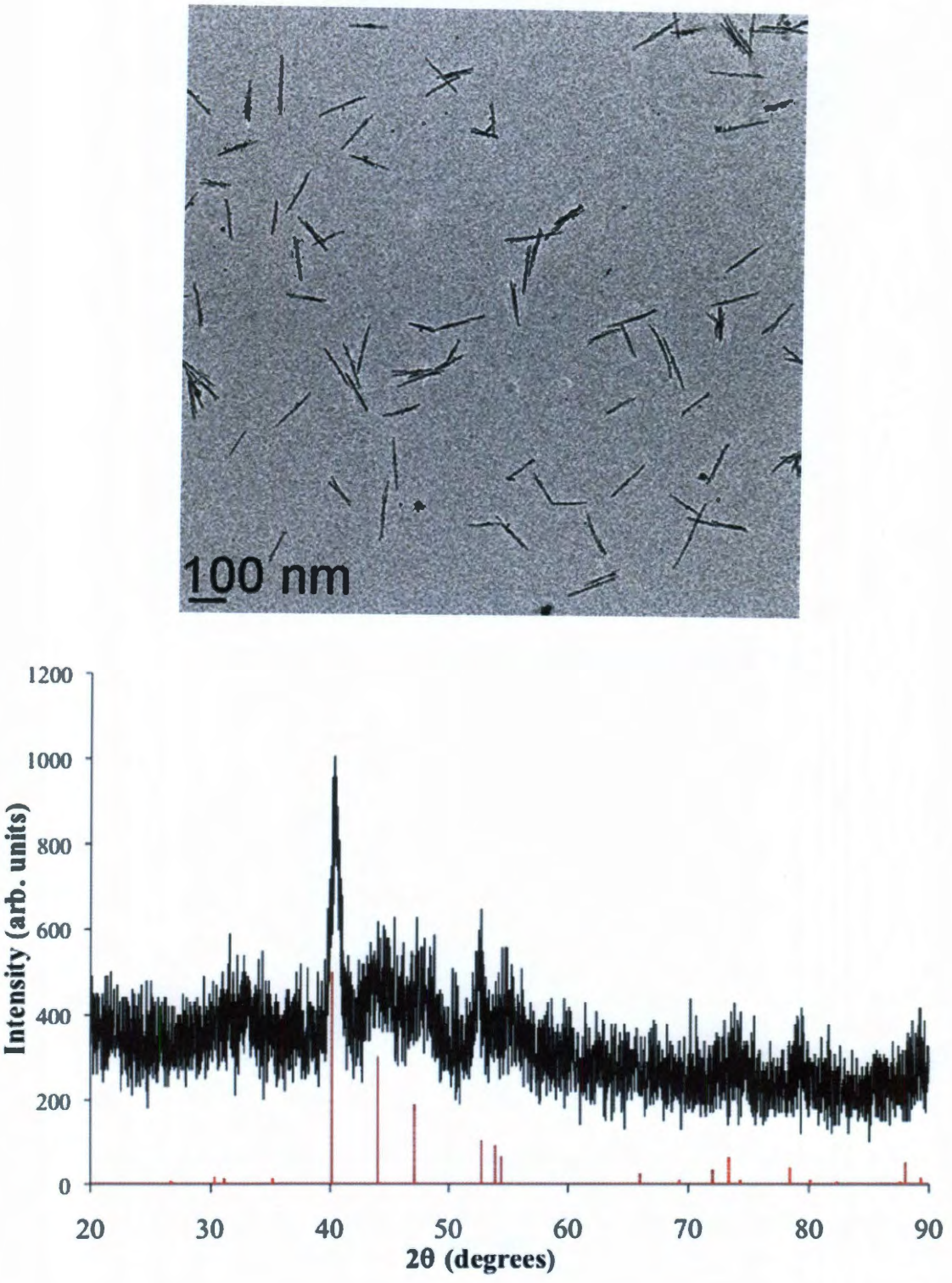

Figure 3.3 TEM micrograph and powder X-ray diffraction pattern of $Fe_{1.3}Mn_{0.7}P$ nanoparticles prepared by thermal decomposition of $FeMn(CO)_8(\mu\text{-}PH_2)$. The line diagram underlying the experimental PXRD data represents the diffraction pattern of the closely related phase $Fe_{1.4}Mn_{0.6}P$ (ICDD PDF # 002-7218).

The isolation of FeO and $Fe_{2-x}Mn_xP$ nanoparticles from the decomposition of $FeMn(CO)_8(\mu\text{-}PPh_2)$ and $FeMn(CO)_8(\mu\text{-}PH_2)$, respectively, suggests that the identity of the precursor is important in determining the final elemental composition of the nanoparticles. However, even though the $FeMn(CO)_8(\mu\text{-}PH_2)$ precursor yielded $Fe_{2-x}Mn_xP$ nanoparticles, the final elemental composition of the particles is not exactly the same as the precursor stoichiometry. In order to determine whether the disparity between precursor and nanomaterial composition was linked to the nature of the precursor itself or the solution-based method of synthesis, we carried out the thermal decomposition of $FeMn(CO)_8(\mu\text{-}PH_2)$ under an inert atmosphere in the absence of solvents or stabilizing agents. $FeMn(CO)_8(\mu\text{-}PH_2)$ was heated to 300 °C under an argon atmosphere for 2 hours, then allowed to cool to room temperature. During the course of the decomposition, the red-orange microcrystalline precursor became a dark black solid with a slightly metallic luster. A fraction of the black solid was immediately digested in concentrated nitric acid for ICP-OES analysis, and the remaining material was quickly analyzed by powder X-ray diffraction. Elemental analysis by ICP-OES indicated that the material was composed of Fe, Mn, and P in a 1:1:1 atomic ratio. PXRD analysis of the solid showed what appeared to be a hexagonal material, albeit with substantial peak broadening most likely attributed to small crystallite size (Figure 3.4). Application of the Scherrer formula to the full width at half-maximum of the peak centered at $2\theta = 39.82°$ indicates that the crystallite size is approximately 12 nm. The formation of hexagonal FeMnP was somewhat surprising considering that stoichiometric FeMnP is known to adopt the orthorhombic structure at temperatures lower than 1473 K.

However, it is known that FeMnP undergoes an orthorhombic to hexagonal phase transformation above 1473 K that is associated with the disordering of metal sites in the crystal.[123] It is therefore possible that the occurrence of hexagonal FeMnP under the present conditions is a result of metal disordering, the material behaving as a random substitutional solid owing to the kinetically controlled synthesis. One might expect this type of behavior to arise from a relatively low temperature synthesis in which the metal atoms do not have sufficient mobility to migrate to preferred sites. If hexagonal FeMnP behaves as a substitutional solid, one might further expect the material to behave according to Vegard's law, and one would expect that the lattice parameters and, by extension, the position of the PXRD reflections would lie somewhere between those of hexagonal Fe_2P and hexagonal Mn_2P. Observation of the most intense reflection in the PXRD pattern (inset, Figure 3.4) reveals that the presumed (111) reflection of the FeMnP material lies between the (111) reflection from Fe_2P and the (111) reflection of Mn_2P, as expected from Vegard's law. It should be noted that the (111) reflection is generally the most intense reflection arising in bulk hexagonal metal phosphides.

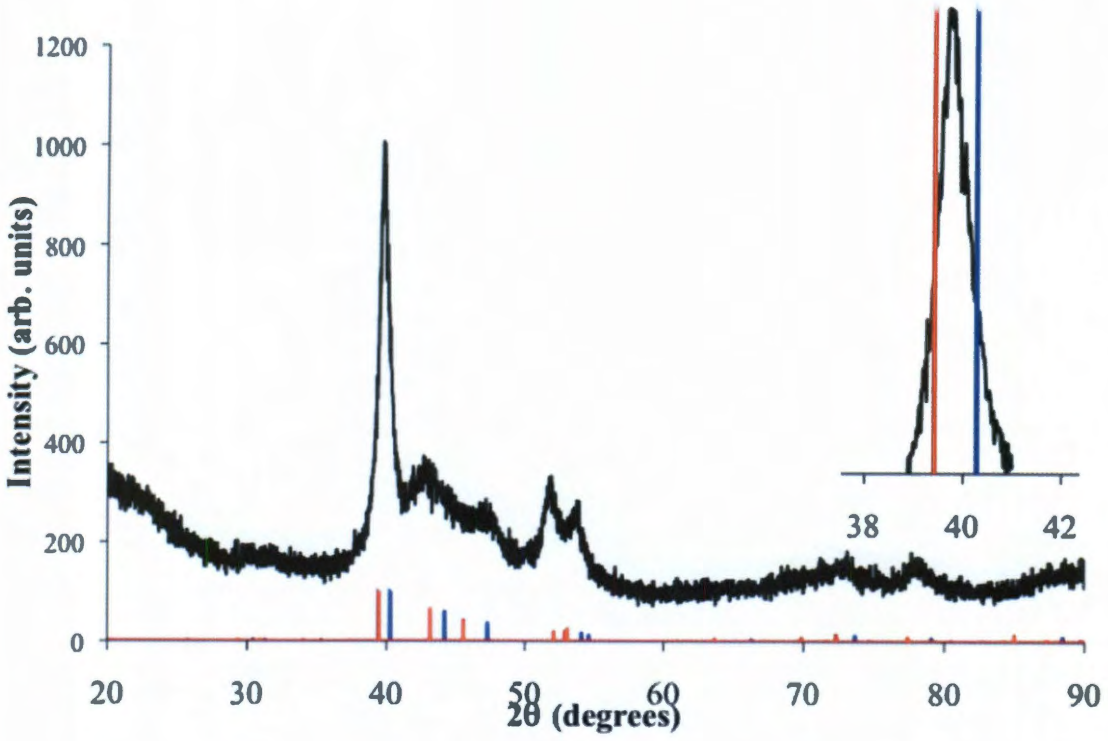

Figure 3.4 PXRD pattern of the FeMnP material produced *via* solventless decomposition of $FeMn(CO)_8(\mu\text{-}PH_2)$. The underlying red and blue lines represent the PXRD references for Mn_2P (ICDD PDF # 003-1864) and Fe_2P (ICDD PDF# 002-1837), respectively. *Inset:* Expanded view of the (111) reflection of FeMnP in relation to the (111) reflections of Mn_2P and Fe_2P.

In the absence of solvents or stabilizing agents, the FeMnP stoichiometry of the $FeMn(CO)_8(\mu\text{-}PH_2)$ precursor was conserved in the solid materials formed upon thermal decomposition. Based on this observation, we began to suspect that the formation of $Fe_{2-x}Mn_xP$ nanoparticles with compositions deviating from the ideal FeMnP stoichiometry was possibly caused by leaching or selective metal binding by the solvent or stabilizing agents present in solution. The solution-based method of nanoparticle formation used in this work employs a high-boiling organic solvent as well as one or more stabilizing agents. In principle, the role of the solvent is to provide a homogeneous environment of sufficient thermal energy to allow

precursor decomposition, while the role of the stabilizers is to prevent the agglomeration of newly formed nuclei and to control nanoparticle growth.[134] In this study, the most commonly used solvents were dioctyl ether and 1-octadecene, both of which are considered very weakly binding. In order to determine whether or not the solvent alone contributed to deviation from the FeMnP stoichiometry, $FeMn(CO)_8(\mu\text{-}PH_2)$ was subjected to thermal decomposition in neat dioctyl ether at 185 °C. In the absence of additional stabilizing agents, we expected that the decomposition of $FeMn(CO)_8(\mu\text{-}PH_2)$ in dioctyl ether would result in the formation of bulk aggregates, similar to those observed under solventless decomposition conditions. Instead, we observed the formation of discrete nanoparticles (≤ 5 nm, Figure 3.5). These particles were precipitated from the dioctyl ether solution, washed several times, and analyzed as before. Elemental analysis of the particles indicated that Fe, Mn, and P were present in equal atomic proportions. Unfortunately, the particles failed to yield PXRD or SAED patterns, either because of their small size or poor crystallinity. Similar results were obtained when $FeMn(CO)_8(\mu\text{-}PH_2)$ was decomposed in 1-octadecene at 220 °C in the absence of additional stabilizing agents (Figure 3.5). The particles prepared in 1-octadecene were also heated for an extended period at 315 °C in an attempt to improve crystallinity or induce agglomeration. However, the resulting particles did not yield PXRD or SAED patterns and only minor particle coalescence was observed (Figure 3.6). Attempts were also made to induce aggregative nanoparticle growth by adding tetrakis(decyl)ammonium bromide to a 1-octadecene solution containing the nanoparticles and heating for several hours in the manner described by Buhro and

coworkers, but the particles remained unchanged (Figure 3.7).[135] Similarly, addition of oleic acid to the particles shown in Figure 3.5 did not result in particle aggregation or growth. Introduction of additional $FeMn(CO)_8(\mu\text{-}PH_2)$ after the initial nucleation of particles failed to induce further particle growth, and the particles examined before and after introduction of additional $FeMn(CO)_8(\mu\text{-}PH_2)$ were indistinguishable from one another.

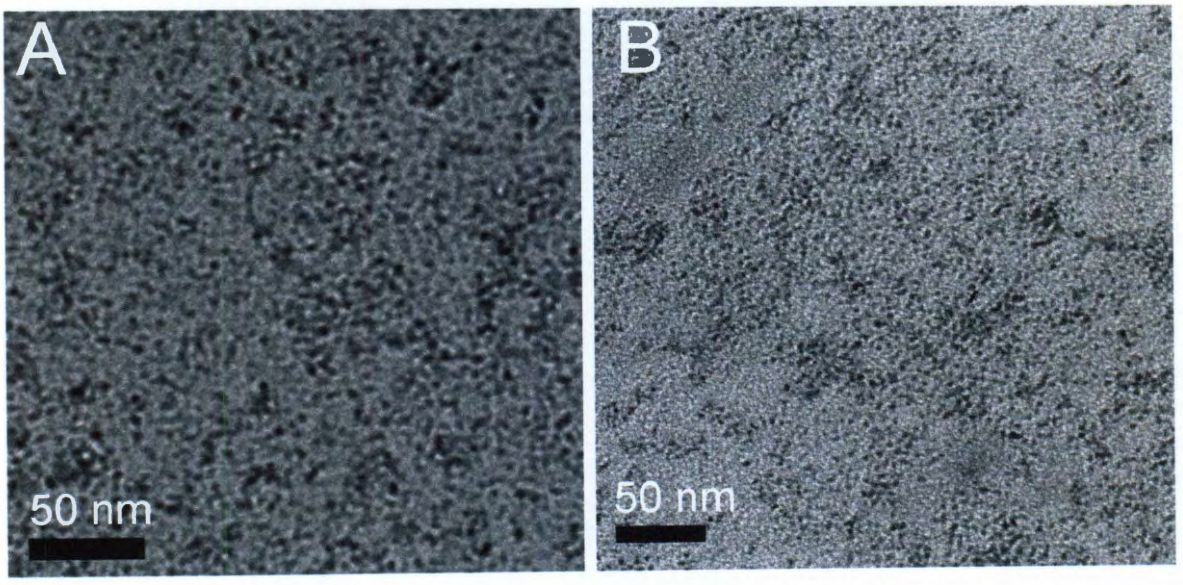

Figure 3.5 TEM images of nanoparticles formed *via* thermal decomposition of $FeMn(CO)_8(\mu\text{-}PH_2)$ in A) dioctyl ether at 185 °C and B) 1-octadecene at 220 °C.

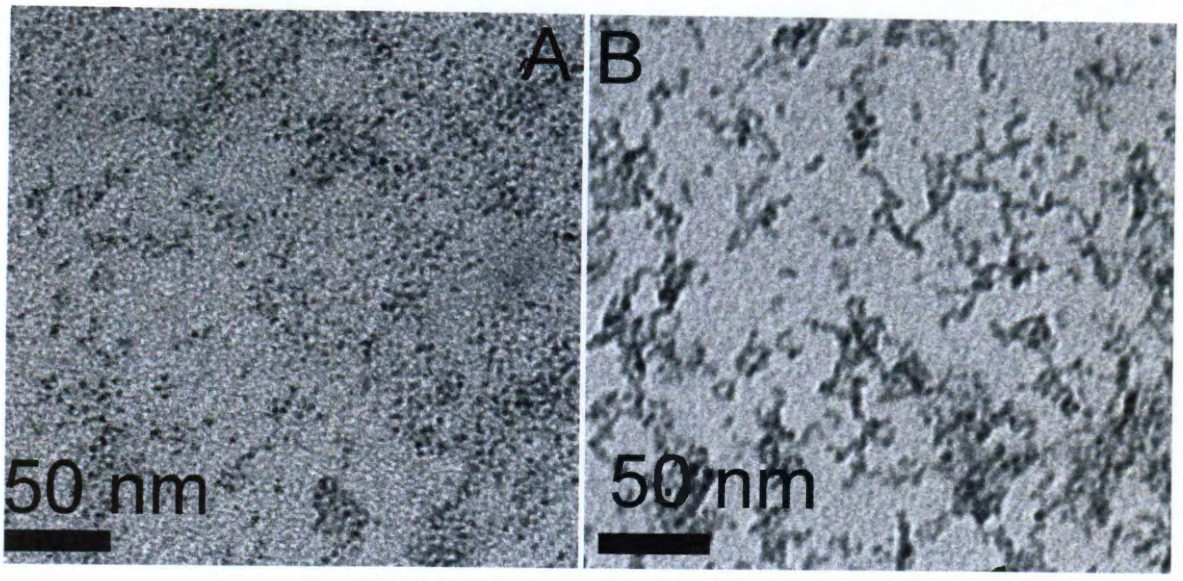

Figure 3.6 Nanoparticles prepared *via* decomposition of $FeMn(CO)_8(\mu\text{-}PH_2)$ at 220 °C in neat 1-octadecene a) before and b) after extended heating at 315 °C.

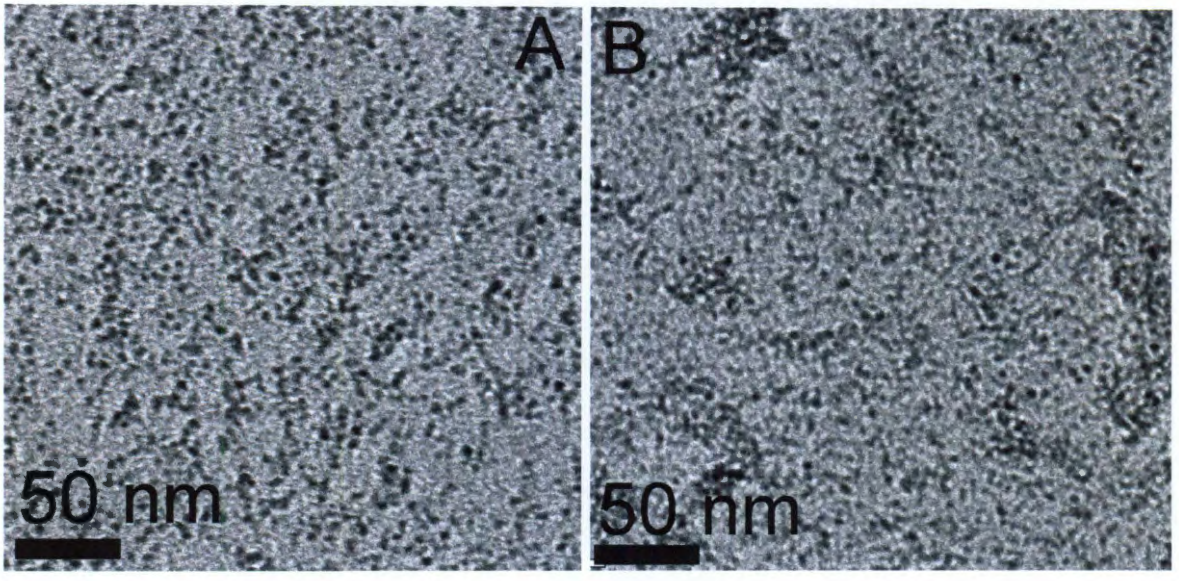

Figure 3.7 Nanoparticles prepared *via* decomposition of $FeMn(CO)_8(\mu\text{-}PH_2)$ at 220 °C in neat 1-octadecene a) before and b) after treatment with tetrakis(decyl)ammonium bromide.

After concluding that dioctyl ether and 1-octadecene were not responsible for the formation of iron-rich $Fe_{2-x}Mn_xP$ nanoparticles from $FeMn(CO)_8(\mu\text{-}PH_2)$, several experiments were performed to explore the effects of the individual stabilizing agents on nanoparticle composition. $FeMn(CO)_8(\mu\text{-}PH_2)$ was decomposed in dioctyl ether in the presence of 5 molar equivalents of hexadecylamine. TEM analysis indicates the formation of nanoparticles with morphologies that are very similar to those observed when $FeMn(CO)_8(\mu\text{-}PH_2)$ was decomposed in neat dioctyl ether or 1-octadecene (Figure 3.8). Again, the particles did not yield PXRD or SAED patterns and elemental analysis of the particles indicated that the FeMnP stoichiometry of the precursor was conserved in the particles. Additional experiments were performed using 15 and 30 molar equivalents of hexadecylamine, and in both cases the resulting particle morphologies and compositions were similar to those observed when 5 molar equivalents of hexadecylamine were used (Figure 3.8). These results suggest that hexadecylamine does not contribute significantly to nanoparticle growth and does not appear to be responsible for the apparent leaching or selective binding that leads to iron-rich $Fe_{2-x}Mn_xP$ nanoparticles.

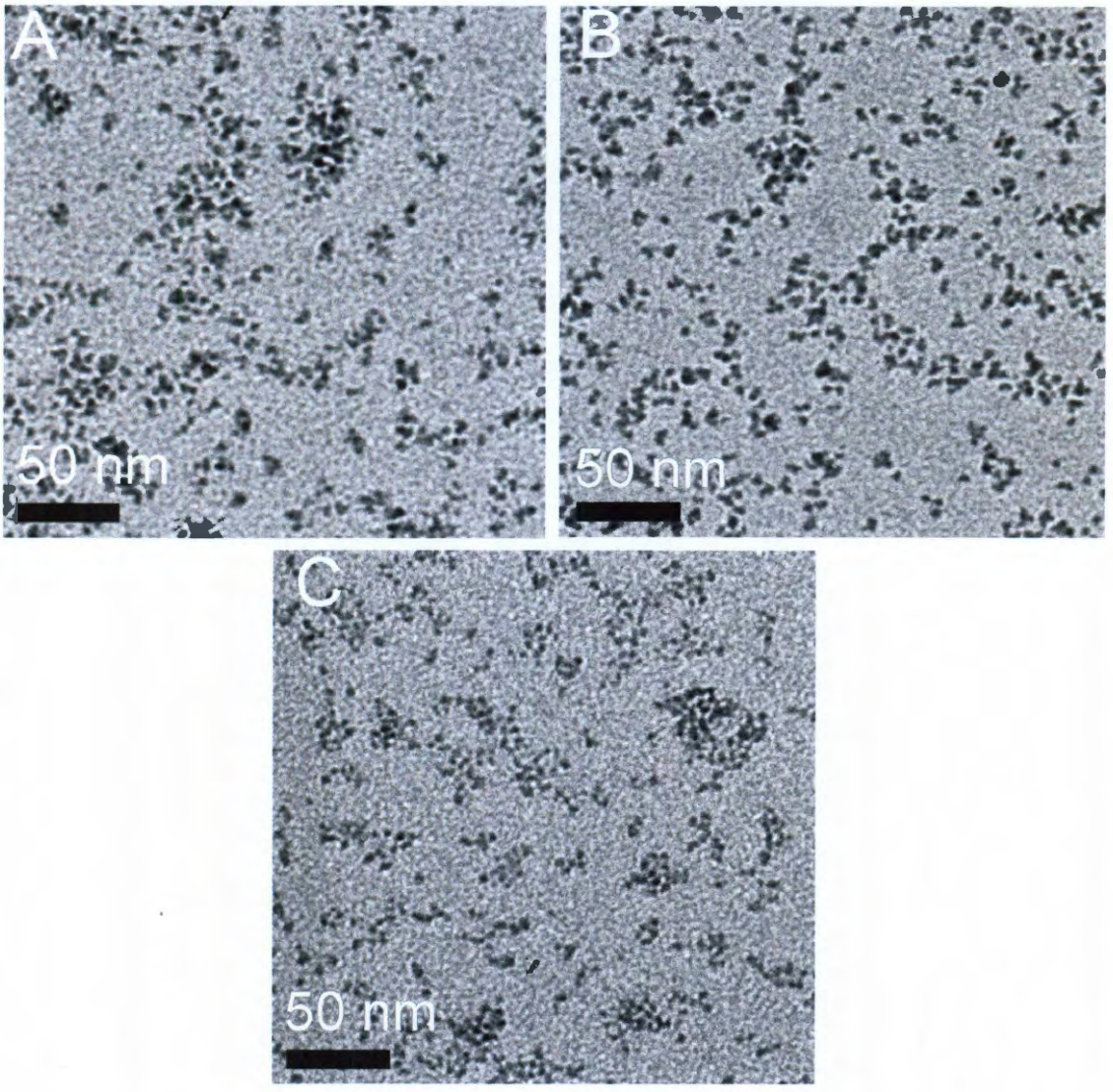

Figure 3.8 TEM images of nanoparticles prepared by thermal decomposition of $FeMn(CO)_8(\mu\text{-}PH_2)$ in dioctyl ether in the presence of A) 5 molar equivalents, B) 15 molar equivalents, and C) 30 molar equivalents of hexadecylamine.

The $FeMn(CO)_8(\mu\text{-}PH_2)$ precursor was then decomposed in dioctyl ether in the presence of 1 molar equivalent of oleic acid. These particles were found to be slightly larger than those formed in neat dioctyl ether (Figure 3.9) and also produced a PXRD pattern similar to that shown in Figure 3.3. Elemental analyses conducted on particles from several trials indicated that the elemental composition was $Fe_{2-x}Mn_xP$ ($0.15 \leq x \leq$

0.7), similar to what was observed for the particles prepared in the presence of 1 molar equivalent oleic acid and 5 equivalents of hexadecylamine. These observations suggest that the use of oleic acid as a stabilizing agent contributes to deviation from the ideal FeMnP stoichiometry. A further experiment was conducted in which $FeMn(CO)_8(\mu\text{-}PH_2)$ was decomposed in dioctyl ether in the presence of 10 molar equivalents of oleic acid. TEM analysis indicated the formation of aggregated clusters of particles (Figure 3.9). More importantly, PXRD data obtained from the clusters revealed that the predominant phase was FeP, demonstrating the preferential leaching of manganese in the presence of excess oleic acid. Experiments in which the amount of oleic acid was substantially decreased (0.25 molar equivalents relative to the $FeMn(CO)_8(\mu\text{-}PH_2)$ precursor) were also conducted, but the particles were poorly formed and exhibited manganese deficiencies comparable to those observed in previous experiments. It should be noted that others have employed oleic acid as a stabilizing agent in the synthesis of both MnP and Mn nanoparticles.[65, 136] Comparison of these reports with the present work implies that manganese leaching appears to be problematic for phase determination only when at least one other metal of differing oxophilicity is present, although nanoparticle yield is probably affected by the presence of acidic stabilizing agents.

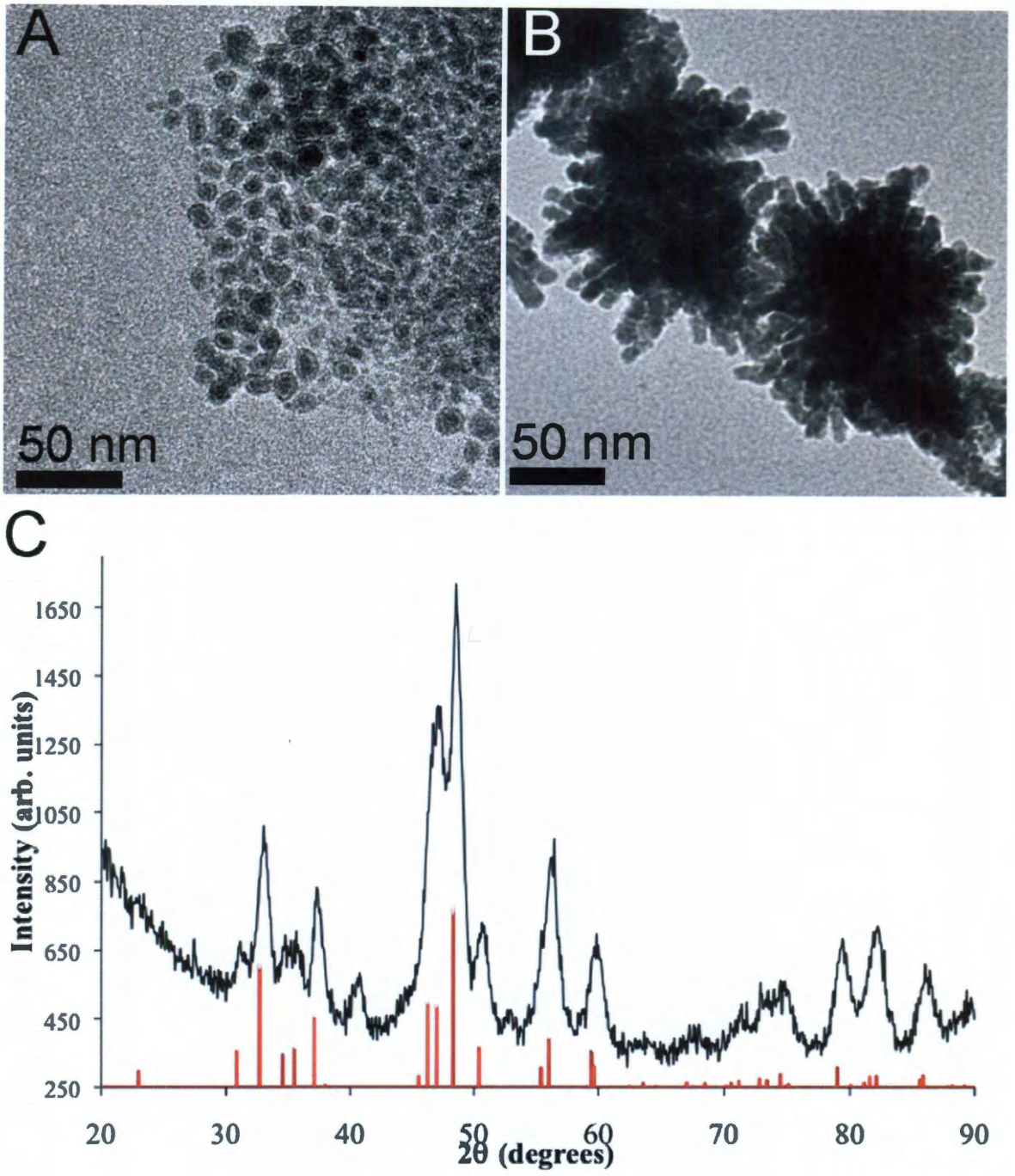

Figure 3.9 TEM images of nanoparticles formed from thermal decomposition of $FeMn(CO)_8(\mu\text{-}PH_2)$ in dioctyl ether in the presence of A) 1 molar equivalent and B) 10 molar equivalents of oleic acid. C) XRPD pattern of particles shown in B). The line diagram below the experimental data represents the diffraction pattern of FeP (ICDD PDF # 008-6293).

The preferential sequestration of manganese by oleic acid is believed to arise as a result of the relatively high oxophilicity of manganese. This conclusion is further substantiated by the results of a simple experiment carried out with the hexagonal FeMnP material prepared *via* solventless decomposition of $FeMn(CO)_8(\mu\text{-}PH_2)$. Hexagonal FeMnP was ground to a fine powder using a mortar and pestle, and the solid was exposed to the air. After several days, the solid was analyzed using PXRD. The PXRD pattern indicated that some of the FeMnP had been oxidized to form face-centered cubic MnO and orthorhombic FeP (Figure 3.10). No evidence of additional phases was observed.

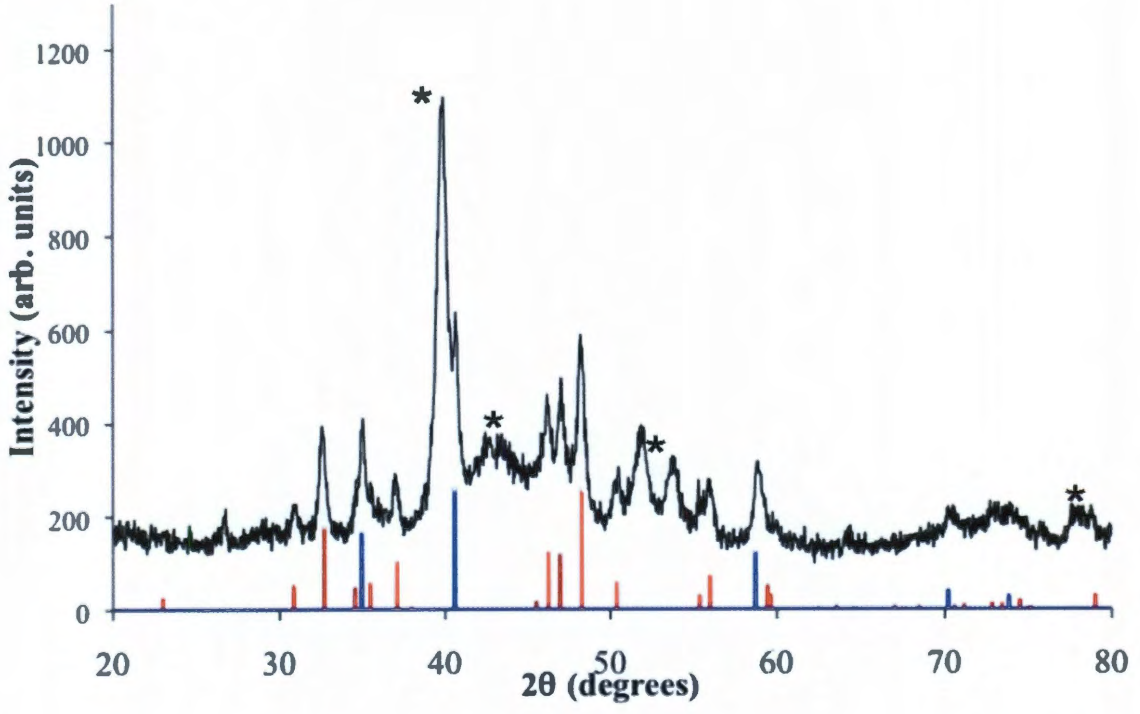

Figure 3.10 PXRD pattern of hexagonal FeMnP subjected to oxidation in air. The underlying red and blue lines represent the PXRD references for FeP (ICDD PDF # 008-6293) and MnO (ICDD PDF# 075-0626), respectively. Peaks indicated with (*) represent unoxidized FeMnP.

Surface analysis of the $Fe_{2-x}Mn_xP$ nanoparticles using X-ray photoelectron spectroscopy (XPS) also confirms that manganese is preferentially oxidized. The XPS spectra of Fe, Mn, and P are shown in Figure 3.11. The XPS spectrum of iron displays a prominent $2p_{3/2}$ peak at a binding energy (BE) of 707.1 eV, in close agreement with the binding energy reported for other iron phosphide phases.[137] A small shoulder is also observed at 710.5 eV, indicating the presence of a minor oxidized iron species, possibly FeO.[138] The XPS spectrum of manganese exhibited a single $2p_{3/2}$ peak at a BE of 641.3 eV, which differs substantially from the BE of 638.7 eV that was previously reported for the manganese phosphides.[137] The manganese BE of 641.3 eV corresponds well with the BE of an oxidized manganese species such as MnO or Mn_2O_3, signifying that the manganese atoms at the surface of the particles are predominantly oxidized.[139] The XPS spectrum of phosphorus contains two distinct 2p peaks at binding energies of 129.2 eV and 133.2 eV, indicating the presence of phosphorus in two different oxidation states. The peak at 129.2 eV is in agreement with the binding energies observed for phosphorus in iron and manganese phosphide materials, while the peak at 133.2 eV is consistent with an oxidized form of phosphorus, such as a phosphate.[137, 140] It is uncertain whether exposure to air or reaction with oleic acid is responsible for the oxidation of the surface metal and phosphorus atoms, but in either case manganese is decidedly more susceptible to oxidation than iron in this material. The phenomenon of selective oxidation of manganese in bimetallic systems has also been observed in the supported catalyst Co-Mn/SiO_2.[141]

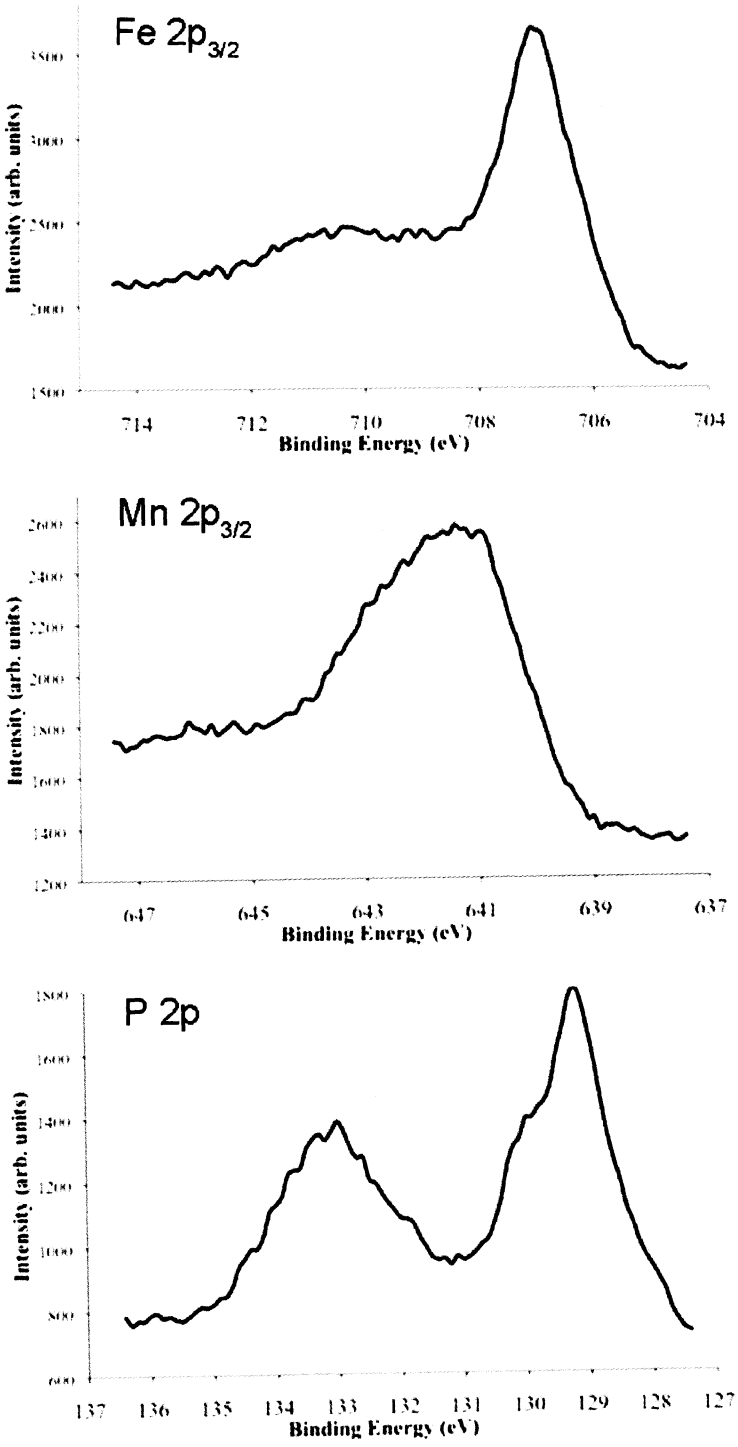

Figure 3.11 XPS spectra of Fe, Mn, and P obtained from $Fe_{2-x}Mn_xP$ nanoparticles.

After demonstrating that decomposition of $FeMn(CO)_8(\mu\text{-}PH_2)$ in the presence of oleic acid leads to the formation of manganese-deficient $Fe_{2-x}Mn_xP$ nanoparticles, alternative stabilizing agents were tested. The objective of these trials was to identify an additive that would induce nanoparticle growth beyond what was observed in neat dioctyl ether or 1-octadecene but would not result in manganese leaching. The results of several experiments using alternative additives are tabulated in Table 3.1 and TEM images from several experiments are shown in Figure 3.12.

Table 3.1 Results from the decomposition of $FeMn(CO)_8(\mu\text{-}PH_2)$ in the presence of various additives.

Additive	Induced Growth? (Yes/No)	Additive	Induced Growth? (Yes/No)
Polyvinylpyrrolidone	No	Triphenylphosphate	No
Perfluorononanoic acid	No	Hexadecylisocyanide	No
Triphenylphosphine	No	Trioctylphosphine Oxide	No
Butylated hydroxytoluene (BHT)	No	Quinoline	No
Hexadecanol	No	Stearonitrile	No
Methyl oleate	No	tetrakis(decyl)ammonium tetraphenylborate	No
Hexadecylphosphonic acid	No	Tetrakis(decyl)ammonium bromide	Yes

The additives listed in Table 3.1 may appear to have been randomly selected, but each was used for a specific purpose. Polyvinylpyrrolidone was used to determine whether or not the presence of a polymeric species would aid in nanoparticle growth, while perfluorononanoic acid was used to examine the effect of altering the electronic properties of the carboxylic acid used in nanoparticle synthesis. Triphenylphosphine and hexadecanol were selected because they contain heteroatoms that could potentially bind

to the particle surfaces. If the decomposition of $FeMn(CO)_8(\mu\text{-}PH_2)$ proceeds through a radical mechanism, the addition of a radical inhibitor such as butylated hydroxytoluene (BHT) might be expected to have some effect of the nanoparticle growth process. Methyl oleate, hexadecylphosphonic acid, and triphenylphosphate were tested as oxygen-containing alternatives to oleic acid. Hexadecylisocyanide and stearonitrile were employed based on their ability to participate in π-backbonding with low-valent transition metals. Quinoline was selected in order to observe the effect of using a strong σ-donor as a stabilizing agent in nanoparticle growth. Trioctylphosphine oxide (TOPO) was also employed in several trials as it has been an effective stabilizer in other metal phosphide nanoparticle syntheses.[60, 62, 69] Under each of these conditions, it was observed that the nanoparticles did not grow significantly larger than the nanoparticles formed during decomposition of the precursor in neat dioctyl ether or 1-octadecence.

Tetrakis(decyl)ammonium bromide (TDAB) was also used as a potential alternative stabilizer in order to examine the effect of a charged stabilizer on particle formation. As shown in Figure 3.12, TDAB was the only stabilizer other than oleic acid that seemed capable of inducing $Fe_{2-x}Mn_xP$ nanoparticle growth beyond that observed in neat dioctyl ether or 1-octadecene. Use of TDAB and oleylamine invariably produced a mixture of rod-like and spherical particles, regardless of changes in reaction temperature, precursor injection rate, or other experimental variables, and in spite of attempts to carry out size-selective precipitation. PXRD data and elemental analyses of the particles confirmed the manganese-deficient $Fe_{2-x}Mn_xP$ composition, and the analyses were similar to those obtained from particles prepared in the presence of oleic acid, suggesting that manganese leaching

also occurs in the presence of bromide ions. Substitution of the non-coordinating tetraphenylborate ion for bromide failed to induce growth in the nanoparticles, indicating that the coordinating ability of the bromide ion plays a role in promoting nanoparticle growth. Although detailed mechanistic data are not available, it is possible that oleic acid and bromide ions play a role in particle etching, which may in turn lead to ripening and nanoparticle growth. Addition of oleic acid or bromide ions to nanoparticles initially prepared in the absence of stabilizing agents (such as those shown in Figure 3.5) failed to promote additional growth, suggesting that oleic acid or bromide ions must be present at the time of precursor decomposition in order to facilitate ripening and growth.

Several attempts at preparing $Fe_{2-x}Mn_xP$ nanoparticles by co-decomposition of multiple reactive precursors were also carried out. In the first experiment, a procedure similar to that used by Brock and co-workers to prepare β-MnAs was employed.[69] $Fe(CO)_5$, $Mn_2(CO)_{10}$, and $P(SiMe_3)_3$ were dissolved in 1-octadecene and injected into hot TOPO at 350 °C. The isolated particles displayed non-uniform morphology and PXRD data indicated that MnP was the predominant phase (Figure 3.13). Additional experiments were carried out using the procedure used to prepare $Fe_{2-x}Mn_xP$ nanoparticles, but the single-source precursor was replaced by the separate precursors $Fe(CO)_5$, $Mn_2(CO)_{10}$, and $P(SiMe_3)_3$. This approach failed to reproduce the particles obtained using $FeMn(CO)_8(\mu\text{-}PH_2)$. Instead, nanoparticles less than 5 nm in size were observed. The particles could only be isolated as an oily precipitate and failed to yield X-ray or electron diffraction patterns. Because of these

limitations, the composition and the phase of these particles could not be accurately determined.

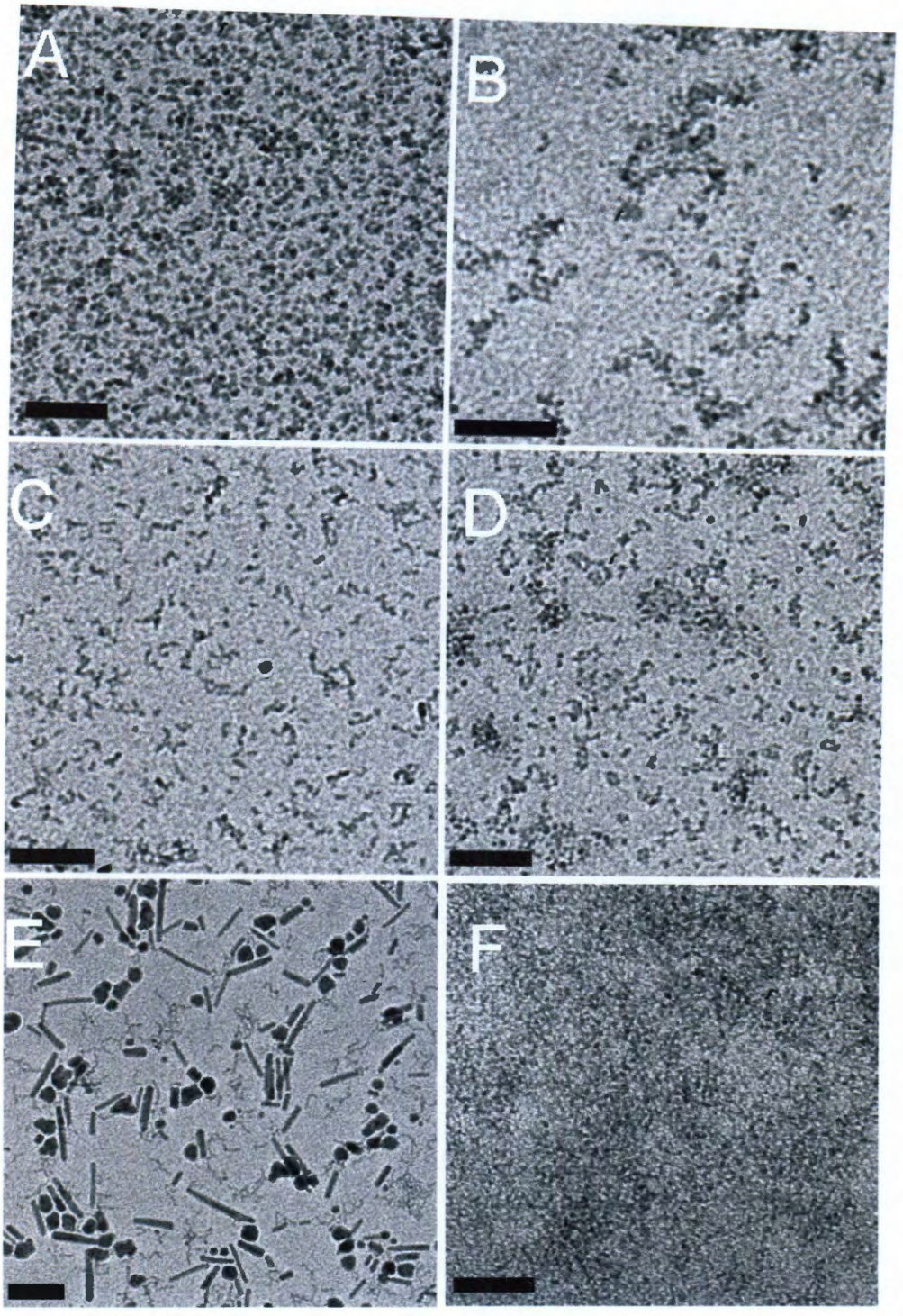

Figure 3.12 TEM images of nanoparticles prepared by decomposition of $FeMn(CO)_8(\mu\text{-}PH_2)$ in dioctyl ether in the presence of A) hexadecylisocyanide, B) trioctylphosphine oxide (TOPO), C) quinoline, D) stearonitrile, E) tetrakis(decyl)ammonium bromide and oleylamine, and F) tetrakis(decyl)ammonium tetraphenylborate and oleylamine. The scale bar = 50 nm for all images.

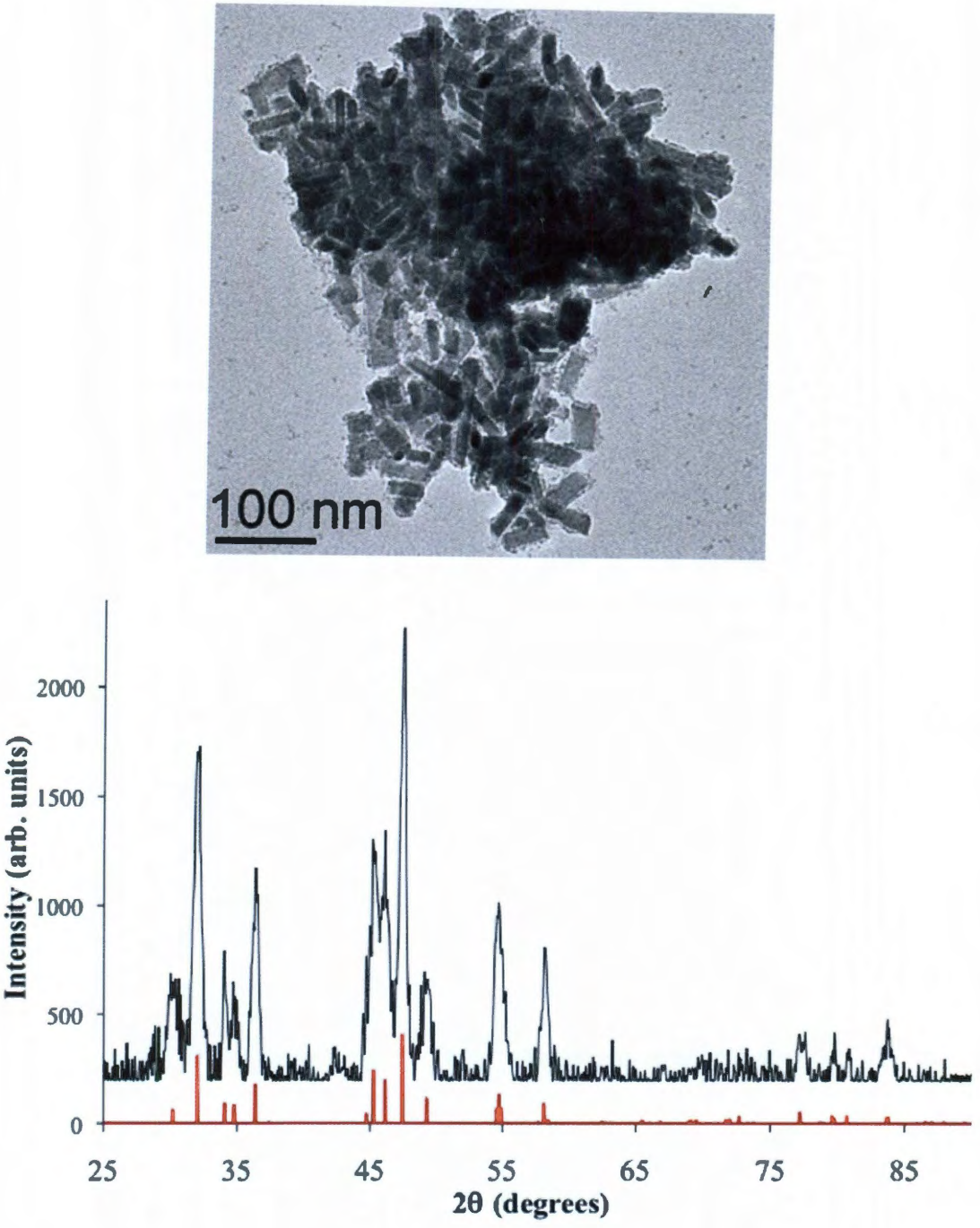

Figure 3.13 TEM micrograph and powder X-ray diffraction pattern of nanoparticles prepared by thermal decomposition of $Fe(CO)_5$, $Mn_2(CO)_{10}$, and $P(SiMe_3)_3$ in TOPO. The line diagram underlying the experimental PXRD data represents the diffraction pattern of MnP (ICDD PDF # 004-2973).

3.4 Conclusions

The formation of iron-rich heterometallic phosphide nanoparticles has been achieved *via* the thermal decomposition of the single-source molecular precursor $FeMn(CO)_8(\mu\text{-}PH_2)$. Thermal decomposition of the related precursor $FeMn(CO)_8(\mu\text{-}PPh_2)$ under similar conditions yielded FeO nanoparticles while decomposition of $FeMn(CO)_8(\mu\text{-}PPhH)$ did not yield useful results, demonstrating that the conversion from precursor to nanoparticles is sensitive to the functional group attached to the phosphorus atom in the precursor. The use of multiple-source precursors also failed to produce the desired FeMnP phase under similar conditions, suggesting that the intimate metal-metal and metal-phosphorus bonding present in the precursor facilitates the formation of the heterometallic material. Although solution-based synthesis of nanoparticles using $FeMn(CO)_8(\mu\text{-}PH_2)$ yielded iron-rich materials, decomposition of the precursor in the absence of solvents or stabilizing agents resulted in the formation of hexagonal FeMnP containing iron, manganese, and phosphorus in a 1:1:1 ratio. Empirical observations indicated that oleic acid, a stabilizing agent commonly employed in nanoparticle syntheses, was responsible for the preferential removal of manganese atoms leading to the formation of iron-rich $Fe_{2-x}Mn_xP$ particles, presumably due to the higher oxophilicity of manganese relative to iron. Various alternative stabilizers to oleic acid were tested, but only oleic acid and tetrakis(decyl)ammonium bromide were able to induce substantial crystalline nanoparticle growth. In both cases, iron-rich $Fe_{2-x}Mn_xP$ nanoparticles were isolated. This observation may have important implications in other bimetallic nanoparticle syntheses, especially in phases containing metals with substantially

differing affinities for stabilizing agents. This observation also suggests an explanation for why multiple-source precursors were not effective in the synthesis of the desired heterometallic material.

The bimetallic system studied in this work provides insight into the chemistry of nanoparticle formation that might not be available in a homometallic system, as leaching of the more soluble manganese atoms is readily detected *via* quantitative compositional analysis of the particles. By contrast, leaching of metal atoms from homometallic nanoparticles may be difficult to observe because the loss of metal atoms may manifest itself in a more subtle way, such as a lower-than-expected yield.

Considering that solventless decomposition of $FeMn(CO)_8(\mu\text{-}PH_2)$ led to the formation of stoichiometric hexagonal FeMnP, it may be possible to prepare advanced FeMnP materials by solventless routes such as metal-organic chemical vapor deposition (MOCVD) using $FeMn(CO)_8(\mu\text{-}PH_2)$ as a volatile precursor. Experimental work in this direction is described in Chapter 5 of this thesis.

Chapter 4. Synthesis of Ferromagnetic Fe_3P Films from Single-Source Molecular Precursors

4.1 Introduction

The preparation of advanced materials containing iron and phosphorus has interested the Whitmire research group for some time. As mentioned in Chapter 1, the series of metal pnictide phases containing iron and phosphorus is somewhat extensive, and includes Fe_3P, Fe_2P, FeP, FeP_2, and FeP_4.[45, 142-145] In the bulk, Fe_3P and Fe_2P are known to be ferromagnetic, with Curie temperatures of 716 K and 217 K, respectively.[24, 146] Intrigued by the prospect of preparing advanced metal pnictide materials with a relatively high ferromagnetic ordering temperature, Anna Kelly previously attempted the solution-based synthesis of Fe_3P nanoparticles via thermal decomposition of the single-source precursors $H_2Fe_3(CO)_9PR$ (R = ^{t}Bu or Ph).[58] These precursor molecules, first reported by Huttner and coworkers, seemed to be ideal candidates for single-source precursors owing to their modest volatilities, the relative lability of the CO ligands, and the intimate Fe-Fe and Fe-P bonding.[147] Based on the stoichiometry of the precursor, it was expected that Fe_3P nanoparticles would form. Surprisingly, the formation of Fe_2P nanoparticles was observed when the precursor was decomposed in the presence of oleic acid. Oleic acid was also implicated in the formation of manganese-deficient $Fe_{2-x}Mn_xP$ nanoparticles, as described in Chapter 3 of this work. The results from both studies

demonstrate that non-innocent interactions between the nanoparticles and stabilizing agents such as oleic acid can result in the formation of metal-deficient nanoparticles. While the decomposition of $H_2Fe_3(CO)_9PR$ (R = ^{t}Bu or Ph) in solution failed to yield the desired phase, bulk decomposition of the precursor was found to produce Fe_3P, suggesting that advanced materials of Fe_3P should be accessible under appropriate synthetic conditions. In this chapter, efforts to overcome the limitations of solution-based Fe_3P materials synthesis are described, and the preparation of ferromagnetic Fe_3P films prepared by rudimentary metal-organic chemical vapor deposition (MOCVD) is discussed. Films containing iron and phosphorus in a 3:1 ratio were readily deposited on quartz via thermal decomposition of volatilized $H_2Fe_3(CO)_9PR$ (R = ^{t}Bu or Ph) at 400 °C. The as-deposited films were amorphous, but could be annealed at higher temperatures in order to achieve sufficient crystallinity for characterization by X-ray analysis. The morphology of the films was studied by scanning electron and atomic force microscopy, and X-ray photoelectron spectroscopy was employed to examine the homogeneity of the films. Magnetic studies performed on the films confirm that the as-deposited and annealed films were both ferromagnetic, albeit with different properties.

4.2 Experimental

General Considerations: $H_2Fe_3(CO)_9PR$ (R = ^{t}Bu or Ph) was prepared according to literature procedures and was freshly crystallized and dried thoroughly under reduced pressure before use.[147] $H_2Fe_3(CO)_9PR$ (R = ^{t}Bu or Ph) can be weighed quickly in the air, but should be stored under inert gas below – 20 °C to avoid oxidation and decomposition. All films were kept under argon before and after all instrumental characterizations to prevent oxidation. The stainless steel heating stage used in all of the film syntheses was provided by the machinists at the Rice University machine shop and was fabricated from a 100 mm section of stainless steel rod (20 mm diameter). The rod was bisected along the long axis and beveled according to the dimensions shown in Figure 4.1. The surface of the stage was then polished prior to use.

Fe_3P Film Deposition: Quartz microscope slides were obtained from Ted Pella, Inc. and were cut into approximately 1.5 x 2.0 cm substrates. The substrates were cleaned with acetone and ethanol and dried under inert gas. Substrates were fixed to a stainless steel heating stage using silver paste (SPI Supplies). The paste was then dried by heating at 130 °C for three hours and cooling under vacuum. It is critical that the silver paste be allowed to dry completely before being subjected to reduced pressure to ensure adequate thermal conductivity between the heating stage and the quarts substrates. A rudimentary horizontal hot-wall MOCVD apparatus was used for all depositions, and a schematic of the device is shown in Figure 4.1. The apparatus consists of a 25 x 200 mm borosilicate glass tube (Corning) coupled to a 25 x 100 mm borosilicate glass spacer tube via a stainless

steel vacuum fitting (Ultra-Torr, Swagelok). The spacer tube was then coupled to a vacuum inlet using a second vacuum fitting. Prior to assembling the apparatus, 10 mg of $H_2Fe_3(CO)_9PR$ (R = ^{t}Bu or Ph) was loaded into the bottom of the tube, and the stainless steel heating stage was positioned as shown in the schematic. The apparatus was then connected to a high-vacuum manifold and evacuated until an attached cold-cathode ionization vacuum gauge stabilized at approximately 2×10^{-7} Torr. A 100-mm section of the apparatus (Zone 1 in Figure 4.1) was wrapped with fiberglass-insulated heating tape (Samox) connected to a variable transformer and embedded with a thermocouple probe. A 75 mm segment of the apparatus (Zone 2 in Figure 4.1) was prepared in a similar fashion, resulting in a two-zone heating system. Zone 1 was heated first, and after attaining the target temperature of 400 °C, Zone 2 was gradually heated to 125 °C. After approximately 25 minutes, the heating tapes were removed from Zones 1 and 2, and films with a metallic luster were found to have formed on the quartz substrates. The apparatus was immediately tilted into a vertical position and a 150 mm segment of the borosilicate tubing was flame sealed under high vacuum, isolating the heating stage and the attached substrates from the atmosphere. Selected samples were then annealed by placing the sealed tube in a muffle furnace and heating to 550 °C for 4 hours.

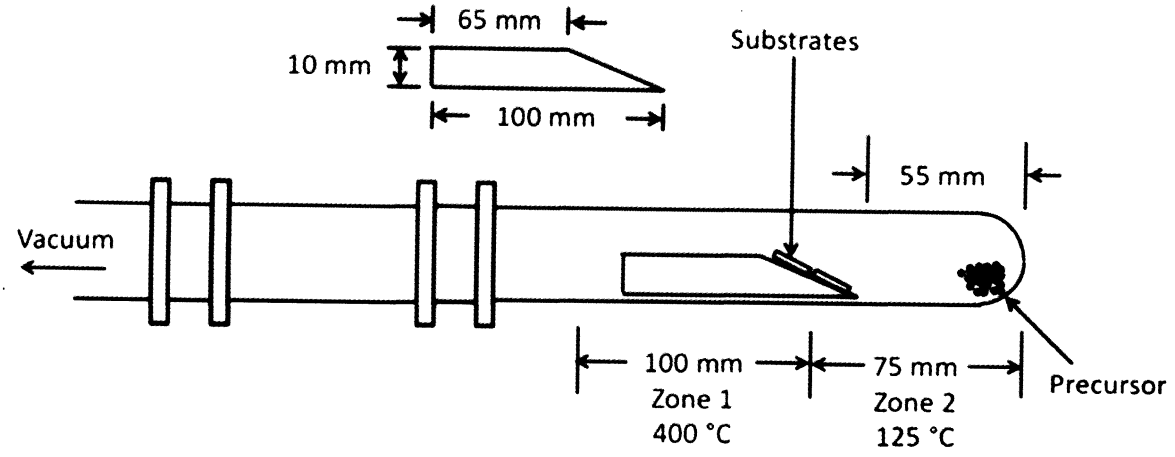

Figure 4.1 Schematic diagram of the home-built MOCVD apparatus employed in the deposition of Fe3P films.

Film Characterization: Quantitative elemental analyses of iron and phosphorus were carried out using inductively coupled plasma optical emission spectroscopy (ICP-OES) on a Perkin-Elmer instrument employing an internal yttrium standard. The spectral emission lines at 238.204 nm and 213.617 nm were selected for analysis of iron and phosphorus, respectively. Iron was analyzed by radial plasma viewing, while phosphorus was analyzed by axial plasma viewing. The films were digested in concentrated nitric acid with sonication and diluted to a suitable concentration prior to analysis.

X-ray photoelectron spectroscopy (XPS) was carried out using a Physical Electronics PHI Quantera SXM instrument using a monochromatic Al Kα source (1486.6 eV) operated at 40.7 W with a beam size of 200 μm and a take off angle of 45°. A band pass of 26 eV was used for the accurate determination of the iron $2p_{3/2}$ and phosphorus 2p binding energies and during depth profiling. The films were sputtered with an Ar^+ ion beam (4 keV) for 5 minutes prior to analysis to remove

any surface oxidation or contaminants. A 4 keV Ar^+ ion beam was also used for sputtering during depth profile studies. The peak positions were calibrated using the 1s peak from adventitious carbon (284.8 eV).

Scanning electron microscopy (SEM) was carried out on a FEI Quanta 400 FEG microscope operated in secondary electron mode at 30 kV. SEM images were obtained on the native films, as it was not necessary to sputter-coat the films prior to imaging. The film thicknesses were determined by analyzing the cross-section of selected films. Atomic force microscopy (AFM) images were obtained using a Digital Instrument Nanoscope IIIa microscope with a Si tip operated in tapping mode.

X-ray diffraction (XRD) data were collected on a Rigaku D/Max-2100PC powder diffractometer using unfiltered Cu Kα radiation (λ = 1.5406 Å) at 40 kV and 40 mA and a step size of 0.034°. Data processing was carried out using MDI's Jade 9.0. The powder diffraction file (PDF) for the Fe_3P phase (# 004-2129) was obtained from the International Centre for Diffraction Data (ICDD) and was used as a reference for phase identification and analysis.

The field-dependent magnetization data were collected by Chih-Wei Chen and Prof. Emilia Morosan using a Quantum Design Magnetic Property Measurement System (QD MPMS). Prior to analysis, the Fe_3P films on quartz were sectioned into pieces approximately 5.0 x 5.0 mm in size. Data from as-deposited samples were collected at 300 K, and data from annealed samples were collected at 300 and 4.2 K. After analysis, the samples were digested in concentrated nitric acid and the total iron and phosphorus content of each sample was quantitatively determined by ICP-

OES. The diamagnetic contribution from the quartz substrate was observed to be negligible, and no further corrections to the data were applied.

4.3 Results and Discussion

Using an independently controlled two-zone heating system (see Experimental section), solid $H_2Fe_3(CO)_9PR$ (R = ^{t}Bu or Ph) was sublimed at 125 °C under reduced pressure, and the gaseous material was carried through a second heating zone that had been preheated to 400 °C, whereupon the precursor underwent thermal decomposition and a metallic film was deposited on the sides of the borosilicate glass tube and onto the quartz substrates attached to the stainless steel heating stage. The ideal deposition temperature of Zone 1 (Figure 4.1) and the optimum position of the heating stage in the apparatus were determined empirically over several trials. Depositions carried out below 400 °C generally resulted in poor substrate coating, with the majority of the metallic material being deposited on the uppermost portion of the glass tube behind the location of the substrates (Figure 4.2). When the temperature of Zone 1 exceeded 450 °C, the metallic material was mostly deposited on the uppermost portion of glass tube above the quartz substrates, and any material deposited on the substrates exhibited poor adhesion and was prone to flaking (Figure 4.2). Film deposition at 400 °C resulted in good substrate coating with less material deposited on the uppermost portion of the glass tube than was observed at other temperatures (Figure 4.2). The films deposited at 400 °C were found to be very reproducible and exhibited good adhesion to the

quartz substrate, as determined by several applications of the Scotch tape test. It should be noted that identical deposition behavior was observed for both $H_2Fe_3(CO)_9PR$ (R = ^{t}Bu or Ph) precursors.

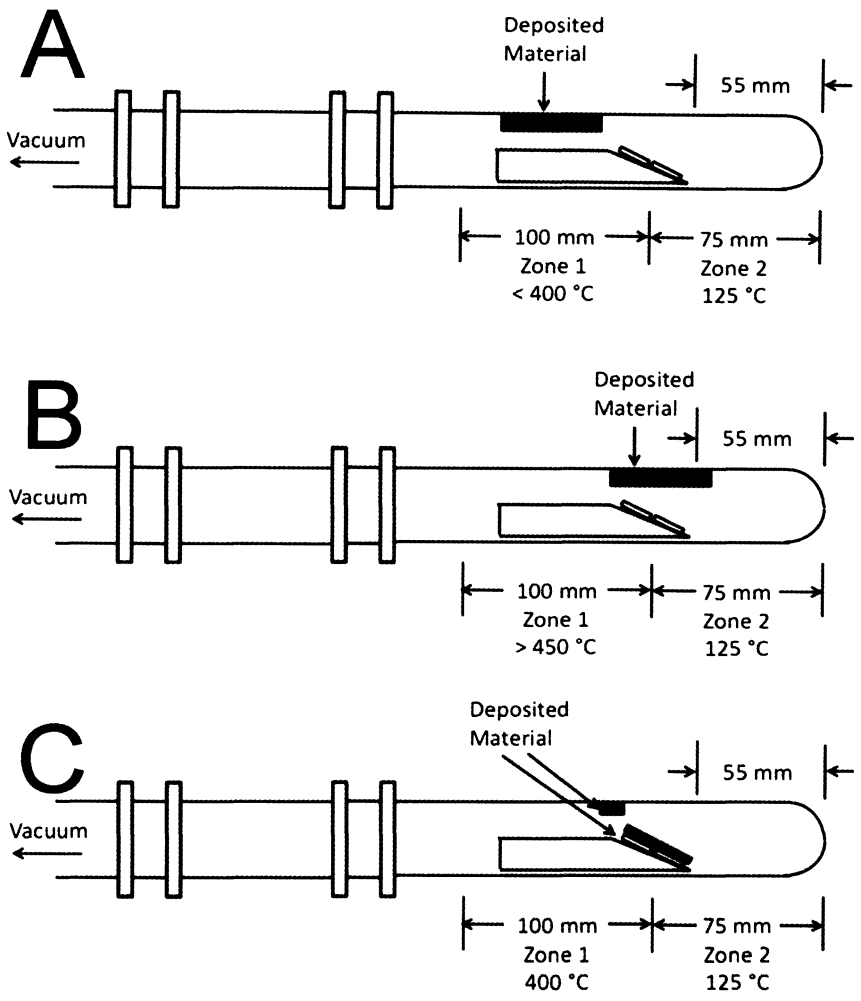

Figure 4.2 Location of deposited material at various Zone 1 temperatures. A) < 400 °C, B) > 450 °C, C) 400 °C.

X-ray diffraction experiments were performed on the films deposited at 400 °C, but no diffracted intensity was observed, indicating that the as-deposited material was amorphous. In order to improve crystallinity, the films were flame

sealed in an evacuated tube and annealed in a muffle furnace at 550 °C for four hours. Annealing in a sealed and evacuated tube was found to be more reliable than annealing under dynamic vacuum, as films annealed under dynamic vacuum often exhibited evidence of oxidation when analyzed by X-ray diffraction and X-ray photoelectron spectroscopy. X-ray diffraction patterns obtained from the films annealed in a sealed and evacuated tube closely match reference patterns obtained from bulk Fe_3P materials (Figure 4.3). The relative intensities of the reflections arising from the Fe_3P films are also similar to the intensities observed in bulk Fe_3P, suggesting that the crystallites in the film are randomly oriented with little or no preferred orientation. Unlike films prepared above 500 °C, the films that were prepared at 400 °C and annealed at 550 °C continued to exhibit good adhesion to the quartz substrates as determined by the Scotch tape test, although annealing for longer periods or at higher temperatures eventually resulted in poor adhesion and film flaking.

Attempts were also made to deposit Fe_3P films on crystalline silicon substrates. The initial deposition of the amorphous film was successful, but the annealing process resulted in poor film adhesion. Scanning electron microscopy of the Fe_3P films on silicon revealed unusual morphological features (*vide infra*).

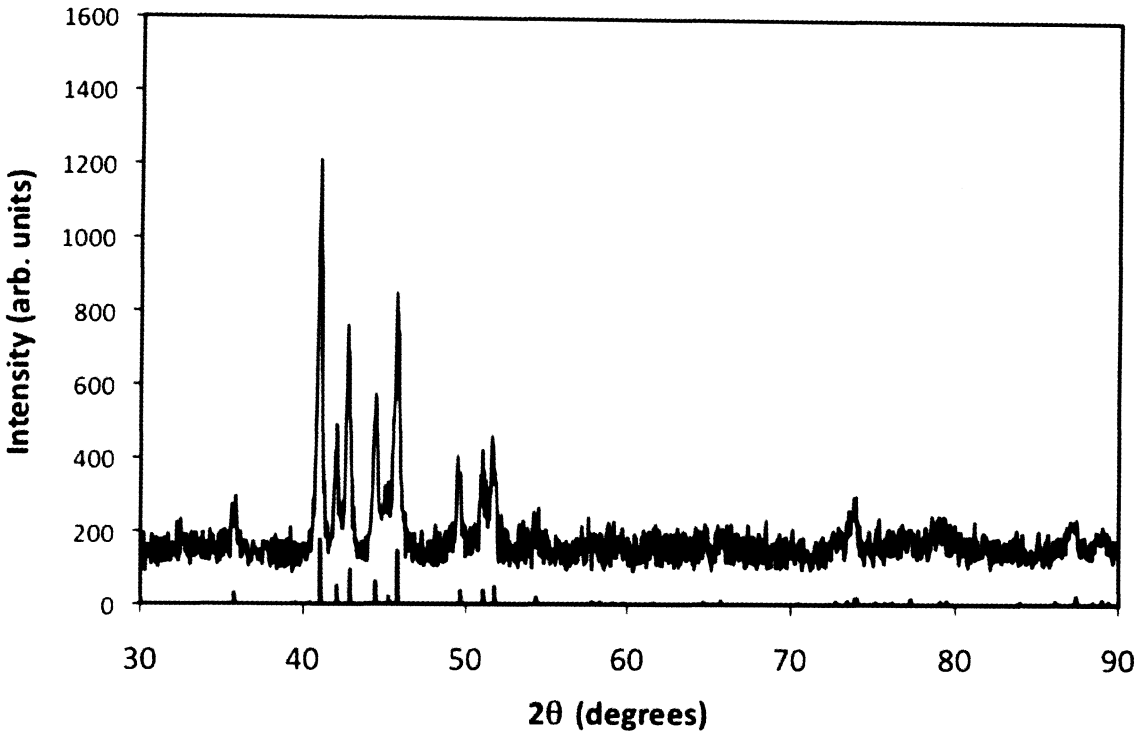

Figure 4.3 X-ray diffraction pattern of an annealed Fe_3P film. The underlying line diagram represents the diffraction pattern of bulk Fe_3P (ICDD PDF# 004-2129).

Annealed and as-deposited films prepared from $H_2Fe_3(CO)_9P^tBu$ and $H_2Fe_3(CO)_9PPh$ were digested in concentrated nitric acid and the relative amounts of iron and phosphorus were determined by ICP-OES analysis. In all cases, the iron to phosphorus ratio was found to be 3.0:1.0, indicating that both molecules were satisfactory precursors to Fe_3P materials. It should be noted that the use of $H_2Fe_3(CO)_9P^tBu$ over $H_2Fe_3(CO)_9PPh$ is preferred because the latter appears to undergo considerable decomposition when stored for extended periods of time.

The Fe_3P films were also studied by X-ray photoelectron spectroscopy (XPS), and the XPS spectra of iron and phosphorus are shown in Figure 4.4. Prior to the acquisition of the spectra, the film surfaces were sputtered with 4 keV Ar^+ ions to

remove oxidized material and surface-adsorbed contaminants. The XPS spectrum of iron shows a single $2p_{3/2}$ peak at a binding energy (BE) of 706.9 eV, in precise agreement with the value reported from a high-resolution XPS analysis of bulk Fe_3P[137]. The XPS spectrum of phosphorus contains a prominent $2p_{3/2}$ peak at a BE of 129.4 eV with a $2p_{1/2}$ shoulder at a slightly higher binding energy, in good agreement with the XPS spectrum of phosphorus obtained from bulk Fe_3P.[137] A slight carbon 1s peak was observed with a BE of 284.8 and was used as a calibration reference. Integration of the carbon 1s intensity indicated that carbon comprised less than 1% of the total atomic composition of the films. The XPS spectra obtained from annealed and as-deposited Fe_3P films were indistinguishable from one another.

An XPS depth-profile was carried out on the annealed Fe_3P films in order to assess the compositional homogeneity of the deposited material. The depth profile indicates that iron and phosphorus are present in a consistent 3:1 atomic ratio throughout the entirety of the film, with the iron and phosphorus compositions dropping to zero as Ar^+ sputtering penetrates to the underlying quartz substrate (Figure 4.5), demonstrating that the film is homogeneous and free of stratification. No significant deviation in the binding energies for iron and phosphorus were observed during the depth profile.

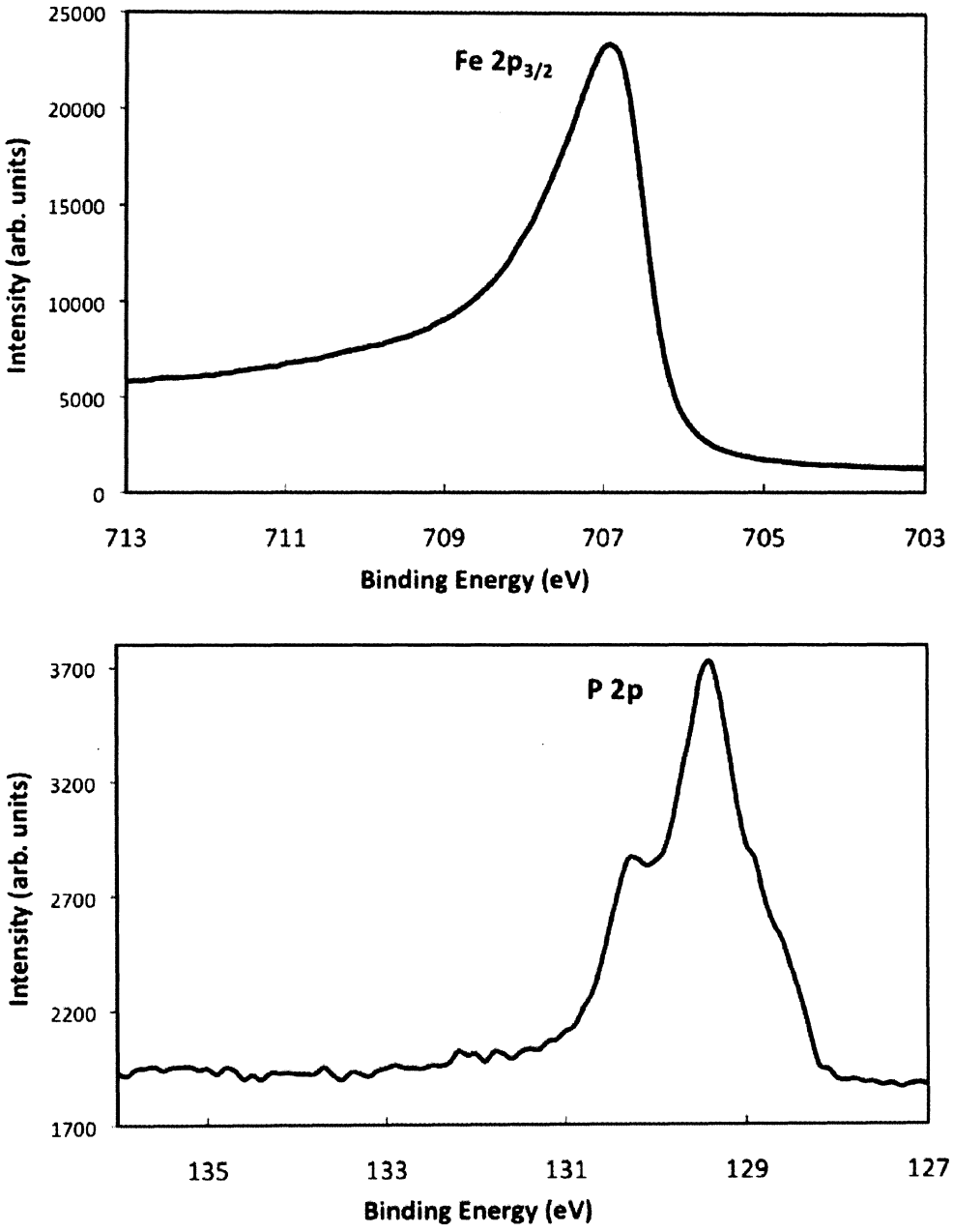

Figure 4.4 X-ray photoelectron spectra of Fe and P obtained from Fe_3P films.

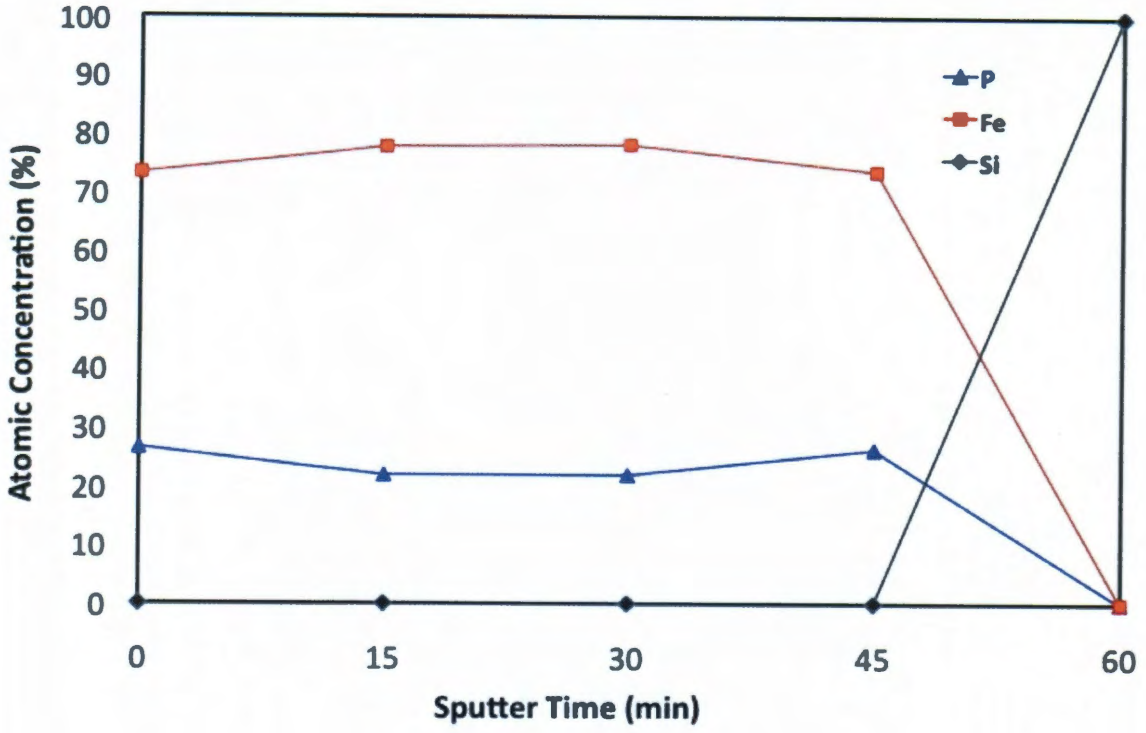

Figure 4.5 XPS depth profile for an annealed Fe_3P film.

The surface morphology and thickness of the films were analyzed by scanning electron microscopy (SEM) and atomic force microscopy (AFM). SEM analysis of the film surfaces revealed a granular texture, with irregularly shaped grains approximately 75-100 nm in size (Figure 4.6). The film texture is considerably smoother than the surface of the quartz substrate, and the film surface can easily be distinguished from the surface of the quartz substrate in SEM micrographs. Cross-sectional SEM analysis of several samples indicated that the films were between 350 and 500 nm in thickness (Figure 4.6). The granular texture was visible only at the surface of the films, the underlying material exhibiting a relatively featureless morphology.

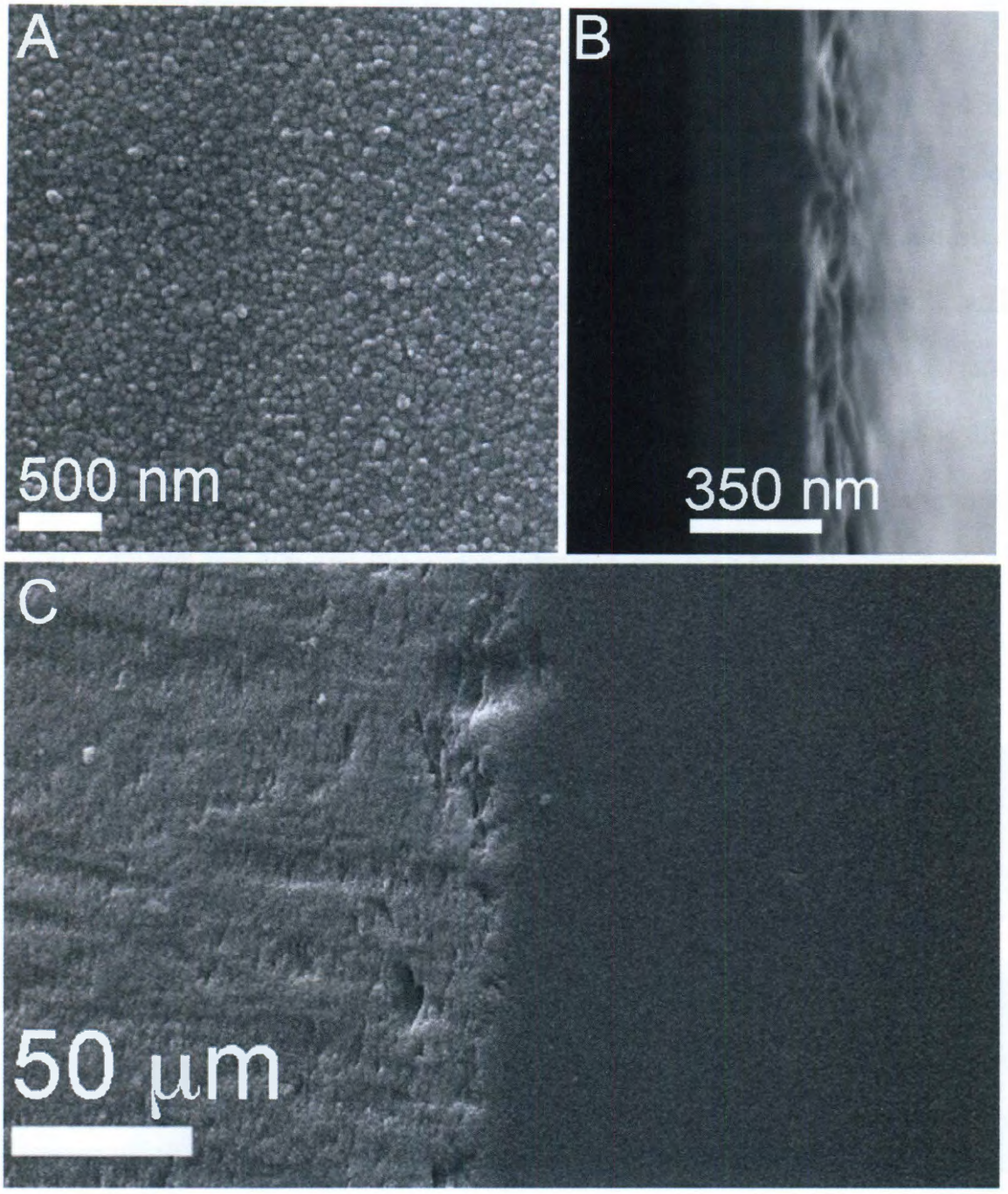

Figure 4.6 A) Surface and B) cross-sectional SEM micrographs obtained from an as-deposited Fe_3P film. C) Surface SEM micrograph highlighting the texture difference between the Fe_3P film (at right) and the quartz substrate (at left).

As mentioned previously, amorphous Fe_3P films were also deposited on crystalline silicon substrates, but attempts at annealing the films resulted in poor adhesion to the substrate. In order to investigate the causes of poor film adhesion, cross-sectional SEM analysis of an annealed Fe_3P film on silicon was performed. Dome-shaped cavities of up to 2 μm in size were observed on the silicon surface, and the hollow nature of the domes can be observed in Figure 4.7. The poor film adhesion observed upon annealing is most likely attributed to poor interfacial contact between the film and the silicon substrate resulting from the presence of these cavities.

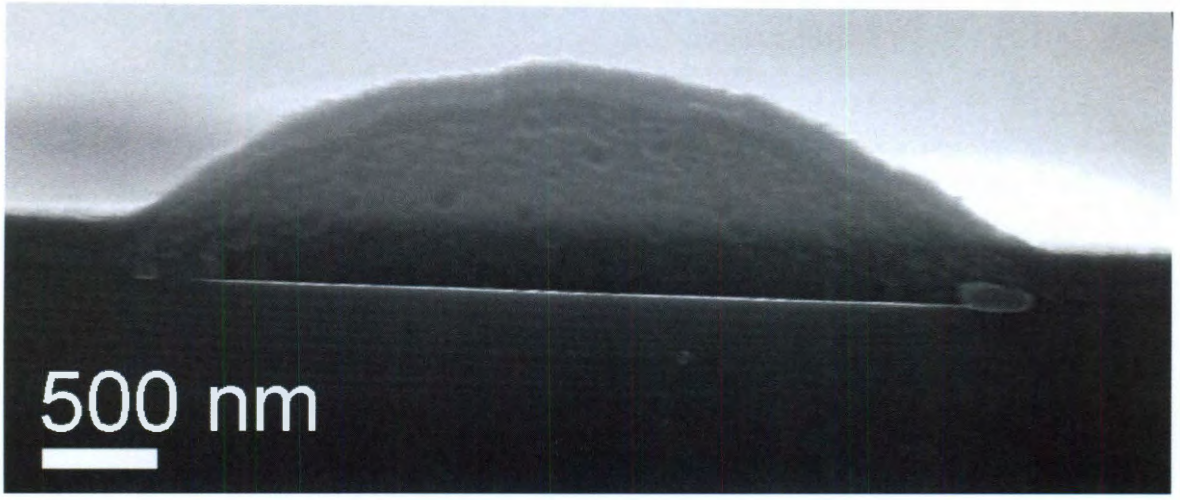

Figure 4.7 Cross-sectional SEM micrograph of an Fe_3P film deposited on silicon. The hollow cavity is prominent.

AFM analysis demonstrates that the films had a somewhat rough texture, with some grains protruding as much as 50 nm from the surface (Figure 4.8). The annealing process had practically no effect on the morphology of the films, and the

annealed and as-deposited films were virtually indistinguishable from one another based on microscopic analysis.

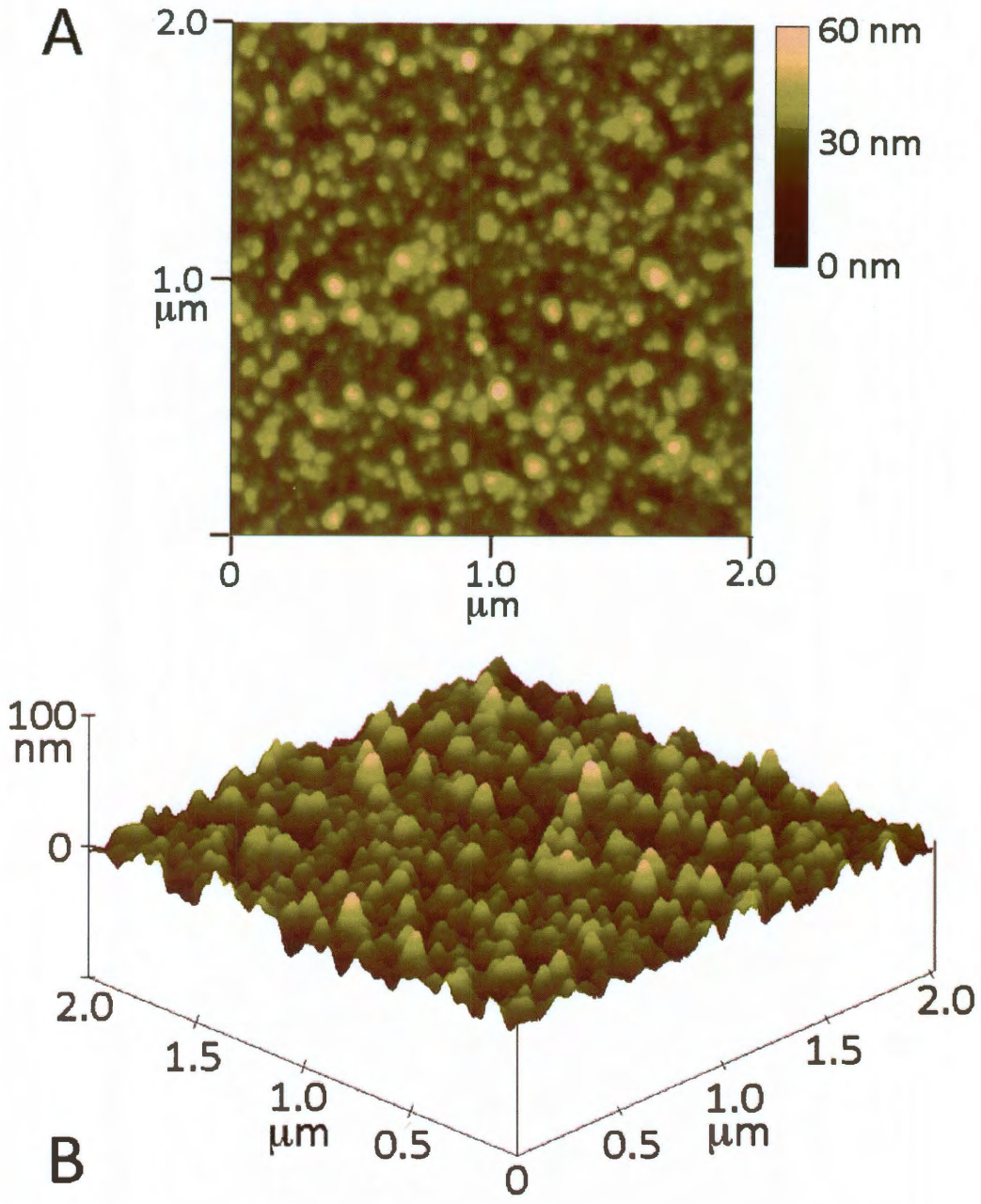

Figure 4.8 A) AFM micrograph and B) height profile (tilted 20° from surface normal) obtained from an as-deposited Fe_3P film.

The attraction of both the as-deposited and annealed films to a permanent neodymium magnet provided empirical evidence of the ferromagnetic nature of the deposited material. Additionally, quantitative magnetic measurements were performed on the as-deposited and annealed films, and a plot of magnetization versus applied field is presented in Figure 4.9. The as-deposited films demonstrated ferromagnetic behavior at 300 K, although no significant hysteresis was observed. By contrast, magnetic measurements carried out on an annealed sample at temperatures of 300 K and 4.2 K resulted in well-defined, symmetrical hysteresis loops, the latter exhibiting a wider loop than the former. The magnetization shown in Figure 4.9 is reported in units of emu $mole^{-1}$ iron, and the quantitative elemental analyses of the films were carried out spectroscopically using ICP-OES. The saturation magnetization of bulk Fe_3P at 4.2 K and 25 kOe was reported to be 155 emu g^{-1}.[146] This is in close agreement with the saturation magnetization of annealed Fe_3P films reported in this work, which was calculated to be 153 emu g^{-1}.

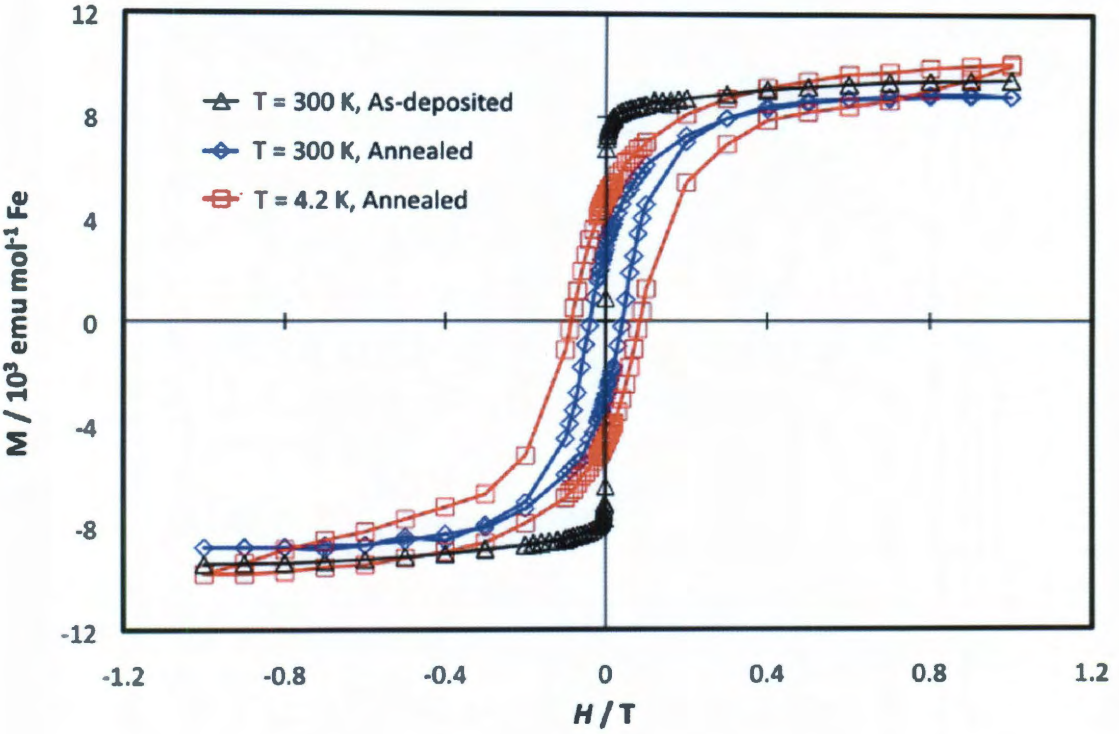

Figure 4.9 Magnetic hysteresis loops obtained from as-deposited and annealed Fe_3P films. (Raw data courtesy of Emilia Morosan and Chi-Wei Chen)

4.4 Conclusions

In this chapter, the facile preparation of Fe_3P films using the conveniently synthesized single-source molecular precursors $H_2Fe_3(CO)_9PR$ (R = ^{t}Bu or Ph) has been described. Characterization by ICP-OES, XRD, and XPS indicates that the films exhibit unprecedented phase-purity with no evidence of contaminant phosphide phases or metallic iron, unlike previously reported attempts at iron phosphide film synthesis.[148, 149]

Brock and coworkers have recently suggested that a critical study of the magnetic properties of metal phosphide materials provides a more complete

assessment of phase purity, arguing that techniques such as XRD can incorrectly imply phase purity in cases where impurities are present at low concentrations or are amorphous and undetectable by X-ray analysis.[57] In keeping with this expanded criterion for establishing phase purity, field-dependent magnetization studies were carried out on the Fe_3P films. The data obtained from annealed Fe_3P films were in close agreement with data obtained from bulk samples of Fe_3P, providing additional evidence of phase purity.

The use of single-source precursors has allowed us to prepare Fe_3P films using an extremely rudimentary MOCVD apparatus. By contrast, preparation of phase-pure Fe_3P films using separate sources of iron and phosphorus could require considerable engineering in order to achieve co-decomposition of precursors with the correct stoichiometries and avoid the formation of phases such as Fe_2P or FeP. The films reported in this work exhibit electronic, magnetic, and crystallographic properties similar to those observed in bulk Fe_3P. This is an interesting and potentially useful observation, as bulk Fe_3P has been identified as a possible component in the preparation of semiconductor spintronic materials.[52]

As discussed previously, Fe_3P is only one of several known iron phosphide phases. The directed synthesis of phase-pure Fe_3P films using a single-source molecular precursor represents a major advance in the preparation of functional metal pnictide materials. A logical extension of this work would be the preparation of ternary or quaternary metal pnictides by employing single-source precursor strategies, and investigations in this direction are the subject of the next chapter.

Chapter 5. Synthesis of Heterobimetallic Phosphide Films from Single-Source Molecular Precursors

5.1 Introduction

In Chapter 3 of this thesis, the preparation of $Fe_{2-x}Mn_xP$ nanoparticles using the single-source molecular precursor $FeMn(CO)_8(\mu\text{-}PH_2)$ was described. Although the particles contained iron, manganese, and phosphorus, the stoichiometric ratios of these elements were found to be inconsistent with the stoichiometry of the single-source precursor. Empirical evidence suggested that the oleic acid employed in the solution-based preparation of the nanoparticles was responsible for the formation of manganese-deficient materials. Furthermore, it was observed that most alternative stabilizers were ineffective at inducing nanoparticle growth, severely limiting the utility of solution-based methods of advanced $Fe_{2-x}Mn_xP$ materials processing.

As discussed previously, attempts at preparing Fe_3P nanoparticles *via* the thermal decomposition of the single-source precursors $H_2Fe_3(CO)_9PR$ (R = ^{t}Bu or Ph) in the presence of oleic acid resulted in the formation of iron-deficient Fe_2P nanoparticles.[58] In order to overcome the limitations of solution-based synthetic methods, the feasibility of preparing Fe_3P films by chemical vapor deposition was explored. As described in the previous chapter, phase-pure Fe_3P films were prepared using a simple, homebuilt, MOCVD apparatus under reduced pressure. Based on the successful preparation of Fe_3P films from a single-source molecular

precursor, it was reasoned that a similar synthetic strategy might be applied to prepare FeMnP films from $FeMn(CO)_8(\mu\text{-}PH_2)$.

In this chapter, progress toward the preparation of bimetallic FeMnP films is discussed. In general, $FeMn(CO)_8(\mu\text{-}PH_2)$ proved to be a suitable precursor for the deposition of films containing Fe, Mn, and P in a 1:1:1 stoichiometric ratio. By constrast, films prepared using $FeMn(CO)_8(\mu\text{-}PPh_2)$ were found to be phosphorus-deficient. X-ray diffraction patterns obtained from annealed films prepared from $FeMn(CO)_8(\mu\text{-}PH_2)$ are similar to patterns obtained from hexagonal FeMnP prepared *via* bulk decomposition of $FeMn(CO)_8(\mu\text{-}PH_2)$. Although elemental analyses and X-ray diffraction studies suggested a uniform film composition, depth profiles obtained using X-ray photoelectron spectroscopy demonstrated that the films were partially oxidized. Based on the X-ray diffraction and spectroscopic data, the film composition is believed to be a mixture of crystalline hexagonal FeMnP, amorphous FeP, and amorphous oxidized manganese material of the form Mn_xO_y.

5.2 Experimental

General Considerations $FeMn(CO)_8(\mu\text{-}PH_2)$ was prepared according to the methods described in Chapter 2 of this thesis. $FeMn(CO)_8(\mu\text{-}PPh_2)$ was prepared in the manner described by Yasafuku and Yamazaki.[89] $FeMn(CO)_8(\mu\text{-}PH_2)$ and $FeMn(CO)_8(\mu\text{-}PPh_2)$ can be handled in the air for short periods of time and are most easily weighed under ambient conditions. Before and after use, the precursors should be stored under inert gas below –20 °C to avoid oxidation and

decomposition. All films were kept under argon or nitrogen before and after all instrumental characterizations to prevent additional oxidation or absorption of atmospheric contaminants. The stainless steel heating stage used in all of the experiments was built to custom specifications by the machinists at the Rice University machine shop and was machined from a 100 mm section of stainless steel rod (20 mm diameter). The rod was cut lengthwise into halves, and beveled according to the dimensions shown in Figure 5.1. The surface of the stage was smoothed prior to use.

Film Depositions

General low-pressure deposition procedure: Standard glass microscope slides were cut into approximately 1.5 x 3.0 cm substrates. The substrates were cleaned with acetone and ethanol and dried under inert gas. Substrates were adhered to the stainless steel heating stage using colloidal silver paste (SPI Supplies) and dried at 130 °C in the air. The heating stage and attached substrates were heated for three hours and cooled under vacuum. A horizontal hot-wall MOCVD apparatus similar to that used in the deposition of Fe_3P films (Chapter 4) was used for all deposition experiments. Prior to assembling the apparatus, the single source precursor (6-8 mg $FeMn(CO)_8(\mu\text{-}PH_2)$ or 8-10 mg $FeMn(CO)_8(\mu\text{-}PPh_2)$) was loaded into the bottom of the tube, followed by the stainless steel heating stage. The apparatus was then connected to a vacuum manifold and evacuated, whereupon the vacuum inlet was closed and the apparatus was maintained under static vacuum. A section of the apparatus (Zone 1 in Figure 5.1A) 100-mm in length was wrapped with insulated heating tape (Samox) connected to a variable voltage transformer and embedded

with a K-type thermocouple probe. Zone 1 was then heated to the desired temperature, after which a 75 mm segment of the apparatus (Zone 2 in Figure 5.1A) was either wrapped in insulating glass wool and aluminum foil or a second heating tape. The vacuum inlet was then opened for approximately 30 minutes, after which the apparatus was allowed to cool to room temperature. Films with a metallic appearance were found to have formed on the glass substrates and on the sidewalls of the apparatus.

High-vacuum deposition using $FeMn(CO)_8(\mu\text{-}PH_2)$: The deposition apparatus was assembled according to the general procedure and was evacuated using a high-vacuum manifold until an attached cold-cathode ionization vacuum gauge stabilized at approximately 2 x 10^{-7} Torr. The position of the heating stage in the apparatus was adjusted to achieve optimum substrate coverage (Figure 5.1A). Zone 1 of the apparatus was heated to 350 °C prior to deposition, and Zone 2 was wrapped with glass wool and aluminum foil. Upon deposition, the apparatus was immediately tilted into a vertical position and a 150 mm segment of the borosilicate tubing was flame sealed under high vacuum, isolating the heating stage and the attached substrates from the atmosphere. Selected samples were then annealed by placing the sealed tube in a muffle furnace and heating to 450 °C for 4 hours.

Medium-vacuum deposition using $FeMn(CO)_8(\mu\text{-}PH_2)$ performed in the glovebox: Prior to conducting deposition experiments, a medium-vacuum source was plumbed into the inert atmosphere glovebox. The deposition apparatus described above was then assembled inside of the nitrogen-filled glovebox and evacuated until an ultimate pressure of approximately 10 mTorr was achieved. The

heating stage was positioned in the apparatus according to Figure 5.1A. The films were annealed under static vacuum in the glovebox at 450 °C for 4 hours.

Attempted atmospheric pressure deposition using $FeMn(CO)_8(\mu\text{-}PH_2)$: A deposition apparatus similar to the apparatus employed for low-pressure deposition experiments was constructed, but was modified with an inert gas inlet and outlet (Figure 5.1B). $FeMn(CO)_8(\mu\text{-}PH_2)$ (15 mg) was placed in a small aluminum foil boat and loaded into the apparatus. The heating stage and attached substrates were then loaded and the entire apparatus was purged with a flow of argon gas for 20 minutes. Under a continuous flow of argon, Zone 1 was heated to 350 °C, after which Zone 2 was slowly heated to 50 °C. No deposition was observed after 1 hour, and Zone 2 was subsequently heated to 100 °C. After an additional hour, no film deposition was observed, and the precursor had begun to melt. The temperature was raised to 150 °C, whereupon the precursor decomposed with little or no volatilization. No film deposition was observed, and no further attempts at atmospheric pressure deposition were made.

High-vacuum deposition using $FeMn(CO)_8(\mu\text{-}PPh_2)$: The procedure used for high-vacuum deposition using $FeMn(CO)_8(\mu\text{-}PH_2)$ was employed for the high-vacuum deposition of $FeMn(CO)_8(\mu\text{-}PPh_2)$. Zone 1 was heated to 400 °C prior to deposition, and Zone 2 was wrapped with a second heating tape and heated to 125 °C in order to volatilize the precursor (Figure 5.1A).

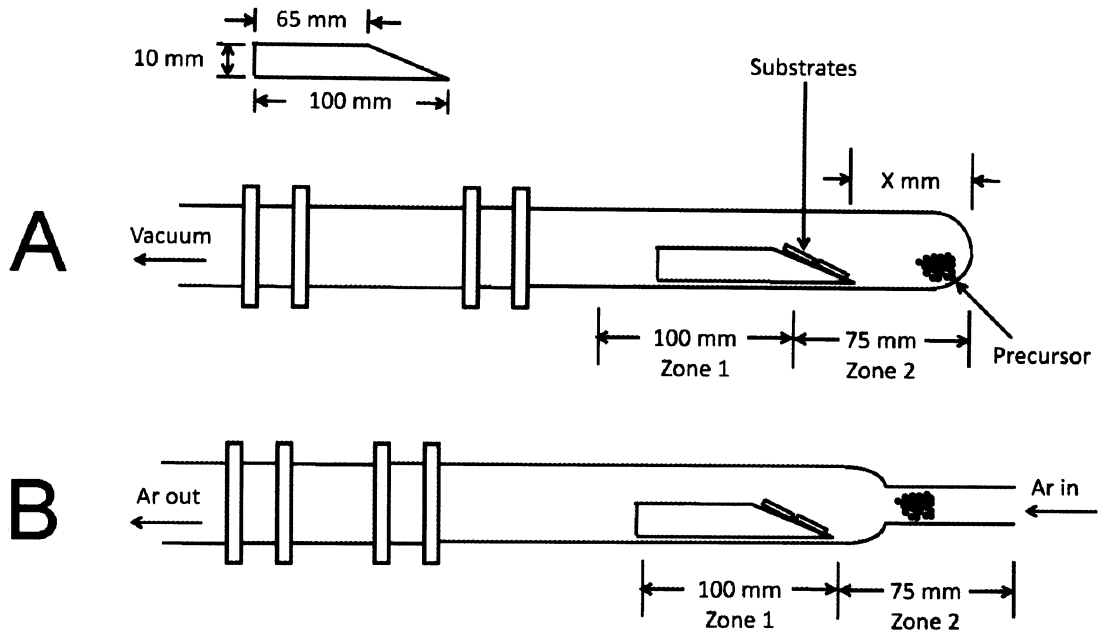

Figure 5.1 Schematic diagram of the home-built MOCVD apparatuses. A) High-vacuum deposition using $FeMn(CO)_8(\mu\text{-}PH_2)$: X = 55 mm, Zone 1 = 350 °C; Medium-vacuum deposition using $FeMn(CO)_8(\mu\text{-}PH_2)$ performed in the glovebox: X = 45 mm, Zone 1 = 350 °C; High-vacuum deposition using $FeMn(CO)_8(\mu\text{-}PPh_2)$: X = 55 mm, Zone 1 = 400 °C, Zone 2 = 125 °C. B) Atmospheric pressure deposition using $FeMn(CO)_8(\mu\text{-}PH_2)$: Zone 1 = 350 °C, Zone 2 = 50 – 150 °C.

Film Characterization: Quantitative elemental analyses of iron, manganese, and phosphorus were carried out by inductively coupled plasma optical emission spectroscopy (ICP-OES) on an instrument employing an internal yttrium standard (Perkin-Elmer). The spectral emission lines at 238.204 nm, 257.610 nm, and 213.617 nm were selected for analysis of iron, manganese, and phosphorus, respectively. Iron and manganese were analyzed by radial plasma viewing, while phosphorus was analyzed by axial plasma viewing. Prior to ICP-OES analysis, the films were digested in concentrated nitric acid with sonication and diluted to a suitable concentration.

X-ray photoelectron spectroscopy (XPS) was carried out on a Physical Electronics PHI Quantera SXM instrument using a monochromatic Al Kα source (1486.6 eV) operated at 40.7 W with a beam size of 200 μm and a take off angle of 45°. A band pass of 26 eV was used for the accurate determination of the iron $2p_{3/2}$, manganese $2p_{3/2}$, and phosphorus 2p binding energies (BE's). During depth profiling, the entire BE range from 1100 to 0 eV was surveyed with a band pass of 140 eV. The films were sputtered with an Ar^+ ion beam (3 keV) for 3-5 minutes prior to analysis to remove any surface oxidation or contaminants. A 2 or 3 keV Ar^+ ion beam was used for all sputtering during depth profile studies. The peak positions were calibrated using the 1s peak from adventitious carbon (284.8 eV).

Scanning electron microscopy (SEM) was carried out on a FEI Quanta 400 FEG microscope operated in secondary electron mode at 30 kV. SEM images were obtained on the native films, as it was not necessary to sputter-coat the films prior to imaging. The film thicknesses were determined by analyzing the cross-section of selected films.

X-ray diffraction (XRD) data were collected on a Rigaku D/Max-2100PC powder diffractometer using unfiltered Cu Kα radiation (λ = 1.5406 Å) at 40 kV and 40 mA and a step size of 0.034°. Data processing was carried out using MDI's Jade 9.0.

5.3 Results and Discussion

The molecular species $FeMn(CO)_8(\mu\text{-}PPh_2)$ and $FeMn(CO)_8(\mu\text{-}PH_2)$ were examined as possible single-source precursors to FeMnP films. Initial experiments were carried using $FeMn(CO)_8(\mu\text{-}PPh_2)$, as this precursor is synthetically accessible using commercially available starting materials that are relatively inexpensive. As described in the Experimental section of this chapter, a low-pressure MOCVD apparatus with an independently controlled two-zone heating system was used to volatilize and decompose $FeMn(CO)_8(\mu\text{-}PPh_2)$ at temperatures of 125 °C and 400 °C, respectively. A film with a metallic appearance was deposited on the walls of the apparatus as well as on the glass substrates attached to the heating stage. Fortuitously, the temperatures of Zones 1 and 2 and the position of the heating stage used in the deposition of Fe_3P films yielded films with acceptable substrate coating and adhesion. Thus, optimization of experimental parameters was not necessary.

The films deposited using $FeMn(CO)_8(\mu\text{-}PPh_2)$ were digested in concentrated nitric acid and elemental analyses for iron, manganese, and phosphorus were performed by ICP-OES. All three elements were observed to be present in the films, but the 1:1:1 stoichiometric ratio of iron, manganese, and phosphorus present in the precursor was not conserved in the deposited film. Rather, the films were found to be phosphorus-deficient with an elemental composition of $Fe_{1.5}Mn_{1.5}P$. After deposition of these films, a film of white waxy solid was observed to have collected on the cool sidewalls near the vacuum outlet of the apparatus. The solid was removed and analyzed by gas chromatography-mass spectrometry (GC-MS). The data obtained from the mass spectrometry experiments indicated that the solid was

composed of a mixture of triphenylphosphine and triphenylphopshine oxide. These data indicate that the formation of phosphorus-deficient films results from the fragmentation of the organometallic precursor, possibly *via* homolytic cleavage of phosphorus-carbon and phosphorus-metal bonds. When the temperature of Zone 1 was changed from 400 °C to 300 °C, films with even lower phosphorus content were obtained ($Fe_{3.0}Mn_{3.1}P$). At deposition temperatures above 400 °C, the films exhibit poor adhesion to the substrate surface. Additional experiments using $FeMn(CO)_8(\mu\text{-}PPh_2)$ as a single-source precursor were subsequently abandoned.

The failure of the $FeMn(CO)_8(\mu\text{-}PPh_2)$ precursor to yield stoichiometric FeMnP films prompted us to investigate $FeMn(CO)_8(\mu\text{-}PH_2)$ as an alternative precursor. The low-pressure CVD apparatus described for the previous experiments was again employed, but the temperature of Zone 1 was reduced from 400 °C to 350 °C in order to achieve better substrate coverage. $FeMn(CO)_8(\mu\text{-}PH_2)$ was found to be more volatile than $FeMn(CO)_8(\mu\text{-}PPh_2)$ and did not require heating to achieve sublimation at reduced pressures. Instead, Zone 2 of the deposition apparatus was simply wrapped in glass wool and aluminum foil to provide thermal insulation and prevent condensation of the sublimed precursor onto the glass sidewalls. At the conclusion of the deposition process, a film similar in appearance to the film prepared using $FeMn(CO)_8(\mu\text{-}PPh_2)$ was observed to have been deposited on the sidewalls of the apparatus and on the glass substrates.

The films prepared using the $FeMn(CO)_8(\mu\text{-}PH_2)$ precursor were also digested in concentrated nitric acid and analyzed by ICP-OES. Unlike the films prepared from $FeMn(CO)_8(\mu\text{-}PPh_2)$, the films deposited using $FeMn(CO)_8(\mu\text{-}PH_2)$

contained iron, manganese, and phosphorus in a 1:1:1 ratio, the Fe:Mn:P stoichiometry of the precursor being conserved in the films. The complete incorporation of phosphorus into the films can most likely be attributed to the more labile nature and more facile thermal cleavage of the P-H bonds of $FeMn(CO)_8(\mu\text{-}PH_2)$ relative to the P-C bonds of $FeMn(CO)_8(\mu\text{-}PPh_2)$.

The thickness and morphology of the films were studied using scanning electron microscopy. The film surfaces were generally featureless, with no indication of fragmentation or cracking. Cross-sectional SEM analysis indicated that the films were between 500 and 650 nm in thickness (Figure 5.2).

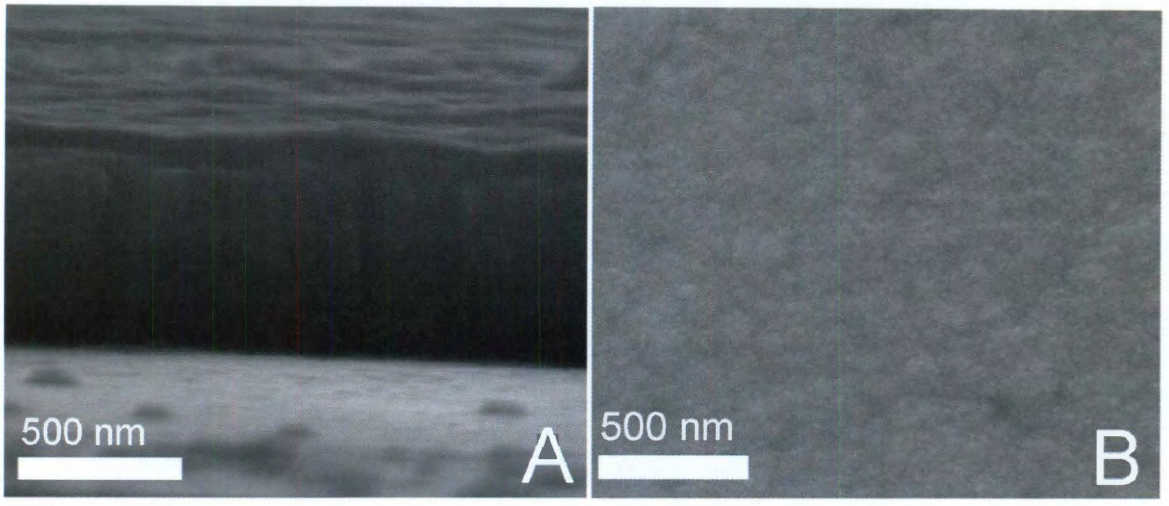

Figure 5.2 A) Cross-sectional and B) surface SEM micrographs of films deposited using the single-source molecular precursor $FeMn(CO)_8(\mu\text{-}PH_2)$.

X-ray diffraction experiments were carried out on the as-deposited films, but no diffracted intensity was observed. Selected films were annealed at 450 °C for four hours after initial deposition, and X-ray diffraction experiments yielded a simple diffraction pattern, as shown in Figure 5.3. This diffraction pattern is not consistent

with the diffraction pattern obtained from either the orthorhombic or hexagonal FeMnP phases.

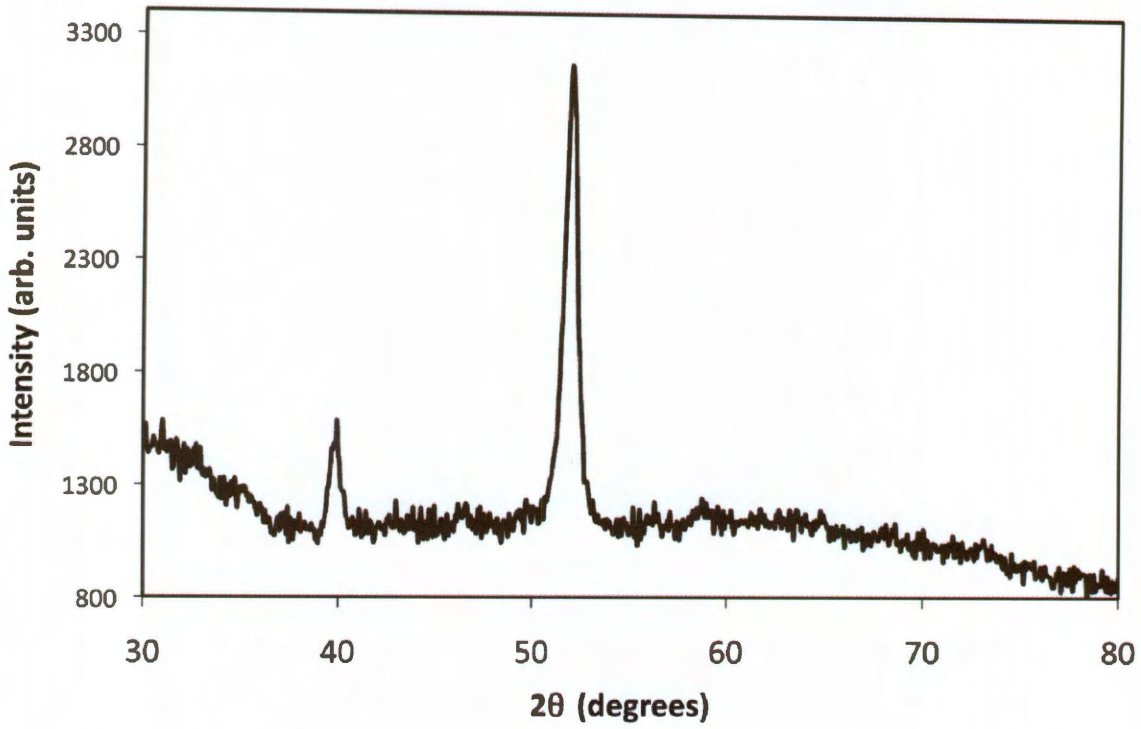

Figure 5.3 X-ray diffraction pattern of an annealed film deposited under high-vacuum conditions using the precursor $FeMn(CO)_8(\mu\text{-}PH_2)$.

Furthermore, the diffraction pattern is inconsistent with any entry from the International Centre for Diffraction Data (ICDD) database, including mono-and bimetallic oxides or metal phosphates. XPS depth profiling was carried out on the as-deposited and annealed films in order to assess the elemental composition and homogeneity of the deposited material. The depth profile of the as-deposited film indicated that the atomic percentages of iron, manganese, and phosphorus were relatively constant throughout the thickness of the film (Figure 5.4).

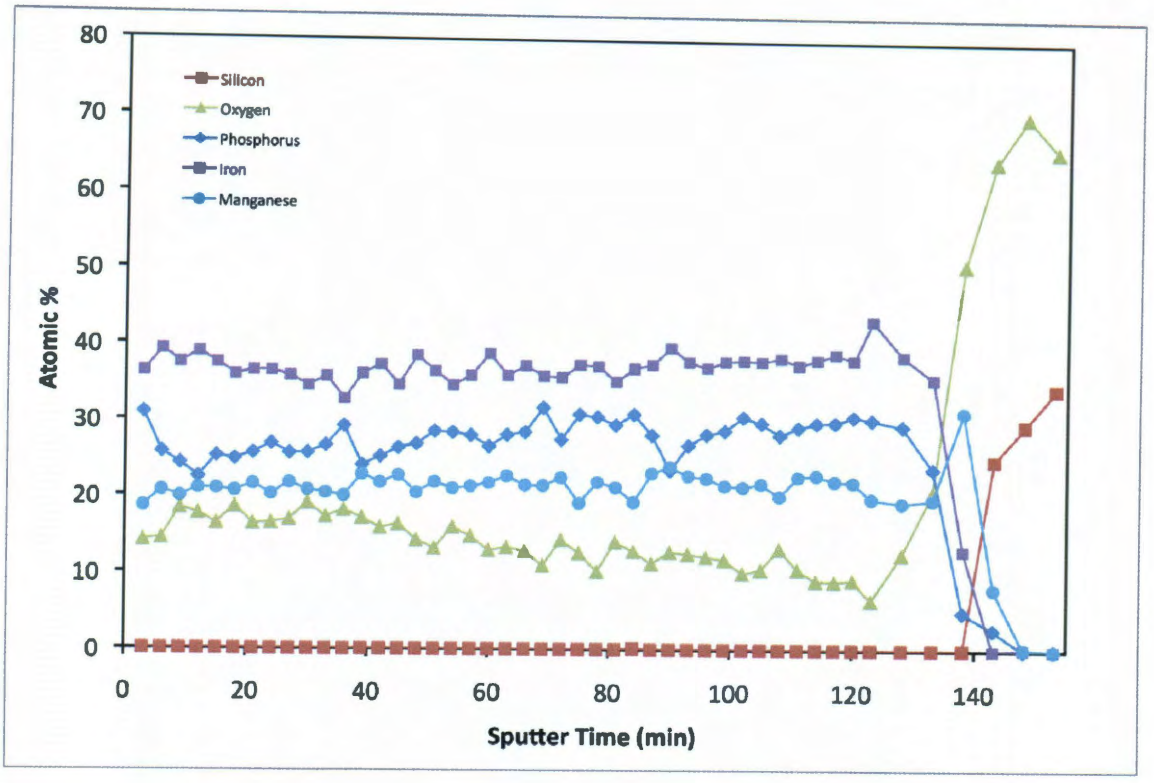

Figure 5.4 XPS depth profile of an as-deposited film prepared using $FeMn(CO)_8(\mu\text{-}PH_2)$ under high-vacuum conditions sputtered with a 2 keV Ar^+ ion beam.

It should be noted that the XPS data suggest that iron, manganese, and phosphorus are present in an atomic ratio of Fe(1.33):Mn(0.78):P(1.00). This elemental composition is inconsistent with the results of the bulk elemental analysis performed by ICP-OES, which found that iron, manganese, and phosphorus were present in a 1:1:1 ratio. This apparent discrepancy can be explained by considering the well-known phenomenon of preferential sputtering. When a material is bombarded by reactive ions such as Ar^+, the constituent atoms are ejected from the surface of the material by a process known as sputtering. The number of surface atoms sputtered by an incident ion is known as the sputter yield, and the sputter yields of different elements can vary considerably.[150] In alloys or compounds

containing multiple elements, differences in the sputter yields of the constituent elements can lead to the disproportionate ejection of atoms with higher sputter yields and subsequent surface enrichment of atoms with lower sputter yields until an equilibrium condition is reached, the end result being a surface composition that does not represent the bulk composition of the material.[151-155] For bimetallic alloys in which the sputter yield of the constituent elements is relatively constant and unaffected by composition, the following equation can be used to estimate the actual bulk composition of the material:

$$\frac{C^{A}_{Surface}}{C^{B}_{Surface}} = \frac{C^{A}_{Bulk}}{C^{B}_{Bulk}} \frac{S^{B}}{S^{A}}$$

where $C^{A}_{Surface}$, $C^{B}_{Surface}$, C^{A}_{Bulk}, and C^{B}_{Bulk} represent the surface and bulk concentrations of elements A and B and S^{A} and S^{B} denote the sputter yields of the elements. As the sputter yield of component A approaches that of component B, the surface composition of the material more closely resembles the bulk composition. Using the data obtained from the XPS depth profile (Figure 5.4) and tabulated sputter yields, the corrected ratio of Fe:Mn in the as-deposited films was calculated to be 1.02 : 1.00, in good agreement with the data obtained from ICP-OES analysis. It is worth noting, however, that the process of preferential sputtering is a complex one, and corrections of the type just described should only be applied when other experimental data are available to corroborate the corrections.

The XPS depth profile shown in Figure 5.4 also indicates that oxygen is present throughout the as-deposited films. According to the XPS data, the observed oxygen content in the films is approximately 14 atomic percent, but the actual atomic contribution could be different depending on whether or not oxygen experiences any anomalous depletion or enrichment due to preferential sputtering. In any event, the not-insignificant amount of oxygen observed in the films indicates that the constituent elements may be partially oxidized, and XPS spectra of iron, manganese, and phosphorus were obtained in order to assess the extent of film oxidation (Figure 5.5). The XPS spectra of iron and phosphorus display prominent peaks at binding energies (BE) of 706.8 eV and 129.3 eV, respectively, in agreement with the binding energies reported for iron and phosphorus in Fe_xP (x = 1, 2, or 3) phases.[137] These data indicate that iron and phosphorus are either completely free from oxidation or that the relative amounts of oxidized iron and phosphorus are so small as to be undetectable. XPS spectra of iron and phosphorus obtained after various sputtering times exhibited no deviation in binding energy or evidence of oxidation.

Although the atomic percentage of manganese remains relatively constant throughout the thickness of the film, fluctuations were observed in the binding energies, suggesting that the oxidation state and bonding environment of manganese is not uniform throughout the film. Representative XPS spectra of manganese obtained during depth profiling are shown in Figure 5.5. The peak centered around 638.7 eV corresponds well with the binding energies reported for Mn_xP (x = 1, 2, or 3) phases, but the peaks centered around 641.3 to 641.9 eV are

consistent with the binding energies observed in oxidized manganese species such as MnO or Mn_2O_3.[137, 139] The peak broadening and shoulders observed in the manganese XPS spectra likely signify that manganese is present in both oxide and phosphide bonding environments and that the relative contribution from each fluctuates throughout the film. Because the XPS spectra of iron and phosphorus give no indication of oxidation, it is reasonable to conclude that the oxygen present in the film is exclusively bound to manganese. The selective oxidation of manganese in advanced bimetallic phosphide materials was also described in Chapter 3 of this thesis.

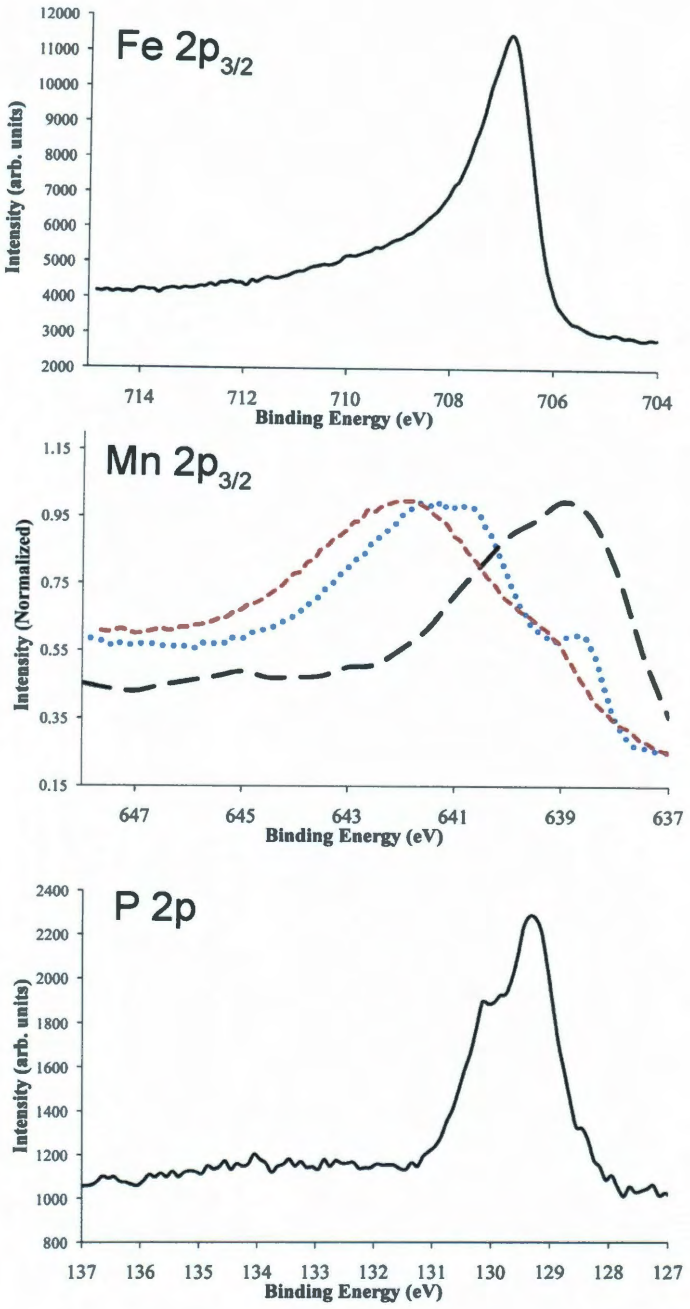

Figure 5.5 XPS spectra of Fe, Mn, and P obtained from films deposited using $FeMn(CO)_8(\mu\text{-}PH_2)$ under high-vacuum conditions. The spectral variations observed for Mn are shown.

XPS depth profiling was also carried out on annealed films deposited using $FeMn(CO)_8(\mu\text{-}PH_2)$ under high-vacuum conditions. As shown in Figure 5.6, the depth

profile obtained from the annealed films differs considerably from the depth profile obtained from the as-deposited films. The most striking difference between the two depth profiles is the notable absence of iron and phosphorus from XPS surveys obtained during the first 20 minutes of film sputtering, during which time only manganese and oxygen were detected. After approximately 20 minutes of sputtering, the amount of iron and phosphorus increased, eventually stabilizing after about 50 minutes of sputter time. These results indicate that the film composition is not homogeneous throughout the thickness of the film. Rather, it appears that annealing results in phase segregation, with oxidized manganese species of the general form Mn_xO_y migrating to the surface of the film. This layer of Mn_xO_y appears to be amorphous, as the X-ray diffraction pattern of the annealed film (Figure 5.3) exhibits no diffraction peaks consistent with known manganese oxide phases. Curiously, the migration of Mn_xO_y appears to occur only toward the surface of the film, possibly due to the lower density of Mn_xO_y phases relative to the $Fe_{2-x}Mn_xP$ phases. After approximately 50 minutes of sputter time, the atomic percentages of iron, manganese, phosphorus, and oxygen remained relatively constant throughout the remainder of the film thickness. Using tabulated sputter rates to correct for preferential sputtering, the average Fe:Mn ratio was calculated to be 1.69:1.00, suggesting that up to 41% of the manganese present in the film had migrated to the surface.

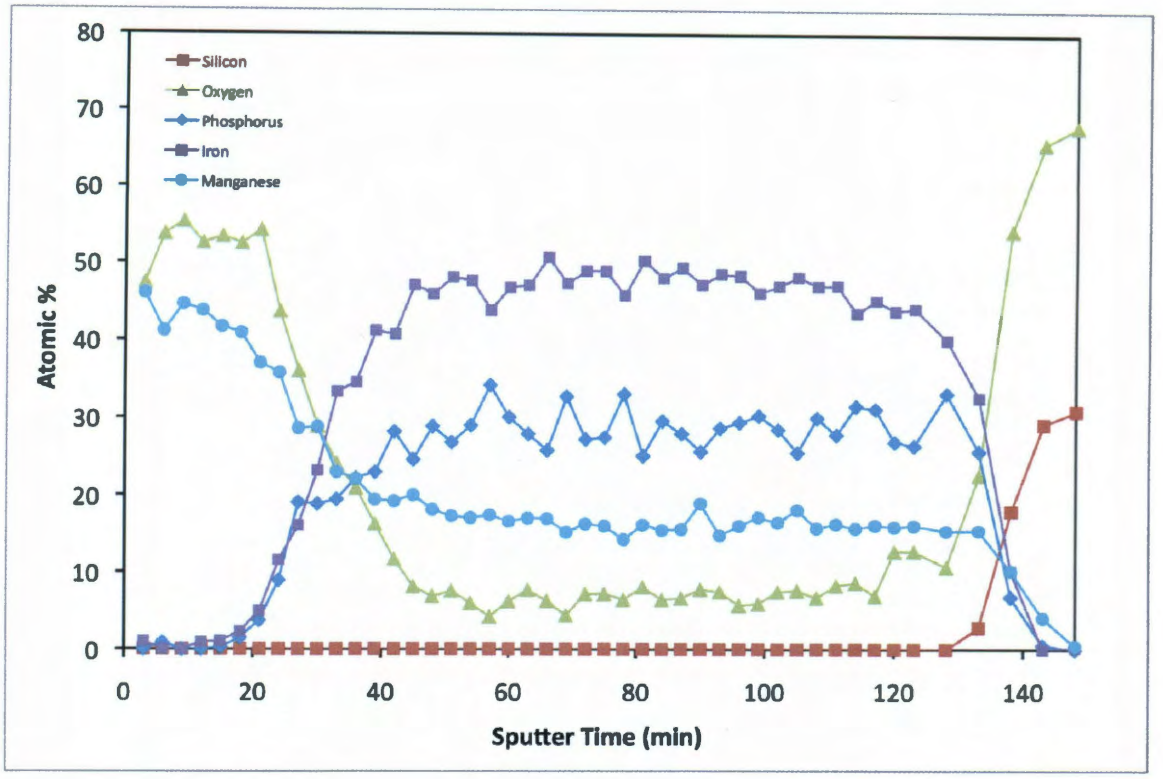

Figure 5.6 XPS depth profile of an annealed film prepared using $FeMn(CO)_8(\mu\text{-}PH_2)$ under high-vacuum conditions sputtered with a 2 keV Ar^+ ion beam.

The XPS data presented above provide strong evidence that oxygen is present throughout the thickness of the as-deposited and annealed films and that manganese atoms are selectively oxidized. Although the exact source of this oxygen contamination remains unknown, a logical possibility is the very small partial pressure of oxygen in the deposition apparatus. Under dynamic vacuum conditions, any oxygen molecules that might react with the film surface would be replaced by the very slight influx of atmospheric gases into the apparatus. In an attempt to prevent the incorporation of oxygen into the films, the deposition apparatus was

assembled inside of a nitrogen-filled glovebox and film depositions were carried out under medium-vacuum conditions of approximately 10 mTorr.

The film compositions were analyzed using ICP-OES and XPS depth profiling techniques. The ICP-OES data confirmed that the films contained iron, manganese, and phosphorus in a 1:1:1 atomic ratio. The XPS depth profile of the as-deposited film was very similar to the depth profile obtained on as-deposited films prepared under high-vacuum conditions. As shown in Figure 5.7, the elemental composition is consistent throughout the thickness of the film with no indication of stratification or phase separation. The XPS data also indicate that oxygen is uniformly distributed throughout the film.

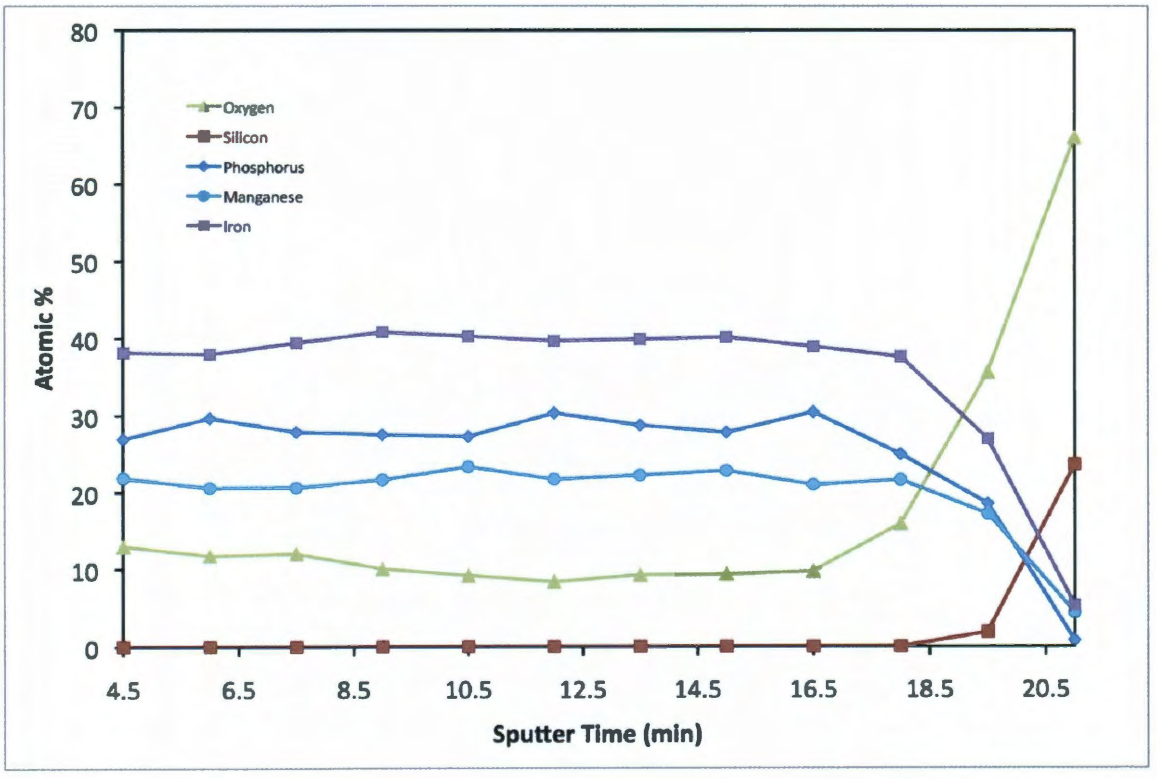

Figure 5.7 XPS depth profile of an as-deposited film prepared using $FeMn(CO)_8(\mu\text{-}PH_2)$ under medium-vacuum conditions in a nitrogen-filled glovebox. The film was sputtered with a 3 keV Ar^+ ion beam.

The XPS spectra of iron, manganese, and phosphorus are presented in Figure 5.8. The XPS spectra of iron and phosphorus are identical to those obtained from the films deposited under high-vacuum conditions and are in agreement with data obtained from Fe_xP (x = 1, 2, or 3) phases.[137] Unlike the spectra obtained from films deposited under high-vacuum conditions, the XPS spectra of manganese did not fluctuate during the depth profiling process. The Mn $2p_{3/2}$ peak is located at a binding energy of 638.7 eV and is in good agreement with Mn $2p_{3/2}$ energies reported for Mn_xP (x = 1, 2, or 3) phases.[137] The unusual peak shape and breadth suggests that the spectrum represents a superposition of peaks, the major component arising from phosphide-bound manganese atoms and the minor component arising from oxygen-bound manganese atoms. As the XPS spectra of iron and phosphorus present no indication of oxidation, it can be concluded that all of the oxygen present in the film is associated with manganese atoms. Surprisingly, deposition of the films inside a nitrogen-filled glovebox did not significantly reduce the amount of oxygen incorporated into the films.

XPS depth profiling was also conducted on annealed films deposited using $FeMn(CO)_8(\mu\text{-}PH_2)$ under medium-vacuum conditions in the nitrogen-filled glovebox. As shown in Figure 5.9, the depth profile data indicate that the uppermost surface of the film is composed mainly of manganese and oxygen, again implying a thermally induced migration of Mn_xO_y to the film surface. However, comparison of depth profile data shown in Figures 5.6 and 5.9 demonstrates that the Mn_xO_y layer of the films deposited and annealed in the glovebox is not as thick as the Mn_xO_y layer of the films prepared and annealed under high-vacuum conditions. Aside from the

difference in the thickness of the Mn_xO_y surface layer, the composition and elemental distribution of the two types of films are quite similar.

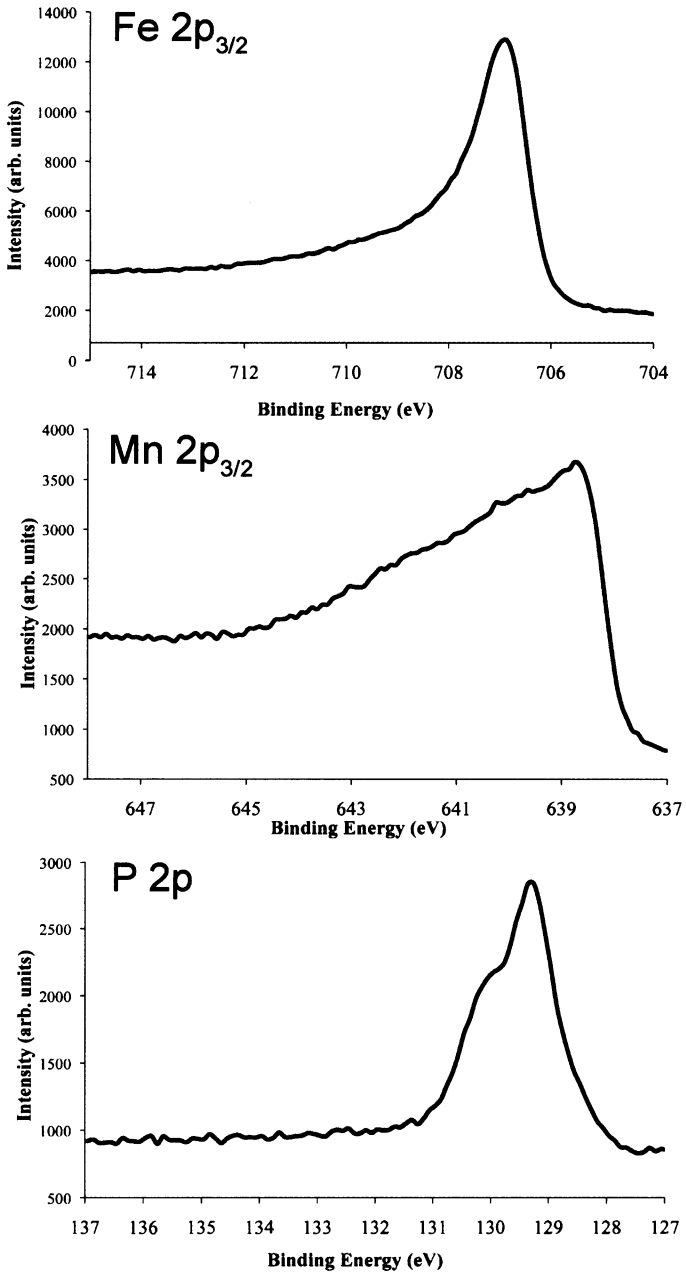

Figure 5.8 XPS spectra of Fe, Mn, and P obtained from films deposited using $FeMn(CO)_8(\mu\text{-}PH_2)$ under medium-vacuum conditions in a nitrogen-filled glovebox.

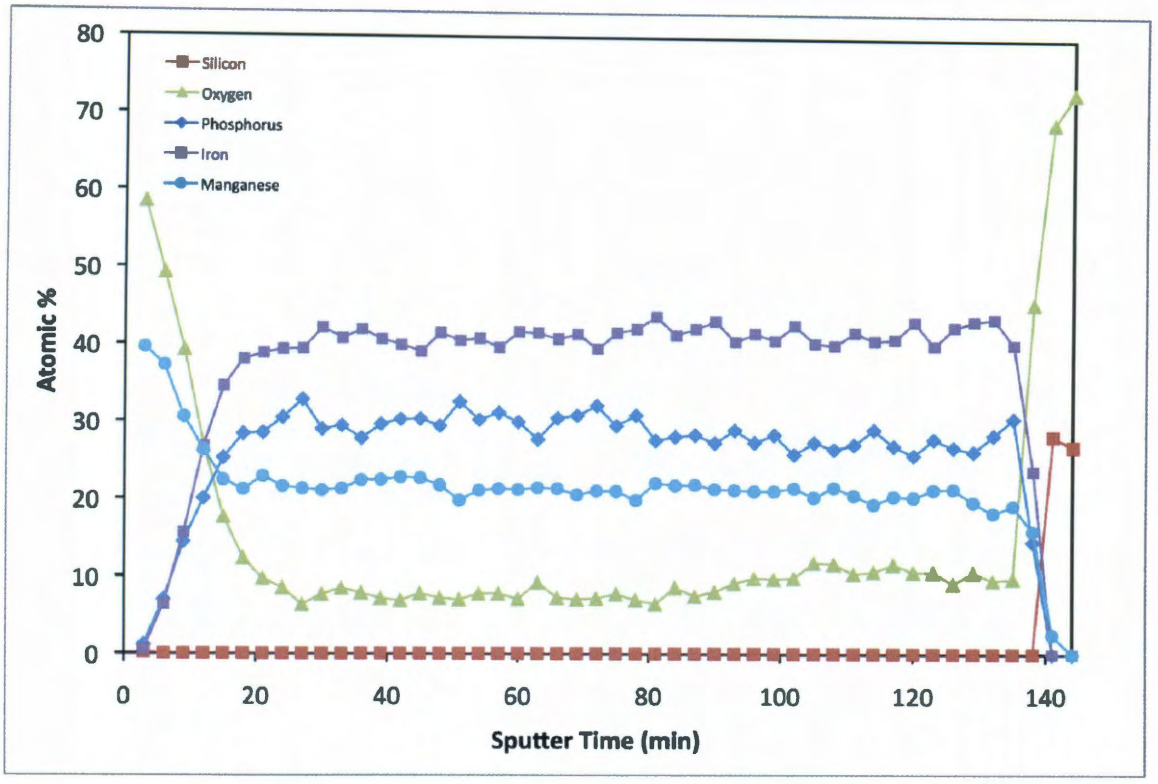

Figure 5.9 XPS depth profile of an annealed film prepared using $FeMn(CO)_8(\mu\text{-}PH_2)$ under medium-vacuum conditions in a nitrogen-filled glovebox. The film was sputtered with a 2 keV Ar^+ ion beam.

X-ray diffraction experiments performed on the as-deposited films prepared in the nitrogen-filled glovebox failed to yield diffraction patterns, signifying that the films were amorphous. Films annealed at 450 °C for four hours gave rise to the X-ray diffraction pattern shown in Figure 5.10. Although the XPS data indicate that one or more manganese oxide species may be present in the films, the X-ray diffraction pattern displays no evidence of Mn_xO_y phases, suggesting that any Mn_xO_y components are amorphous. Furthermore, the diffraction pattern presented in Figure 5.10 is not consistent with the orthorhombic crystal structure usually observed for FeMnP below 1200 °C.[123]

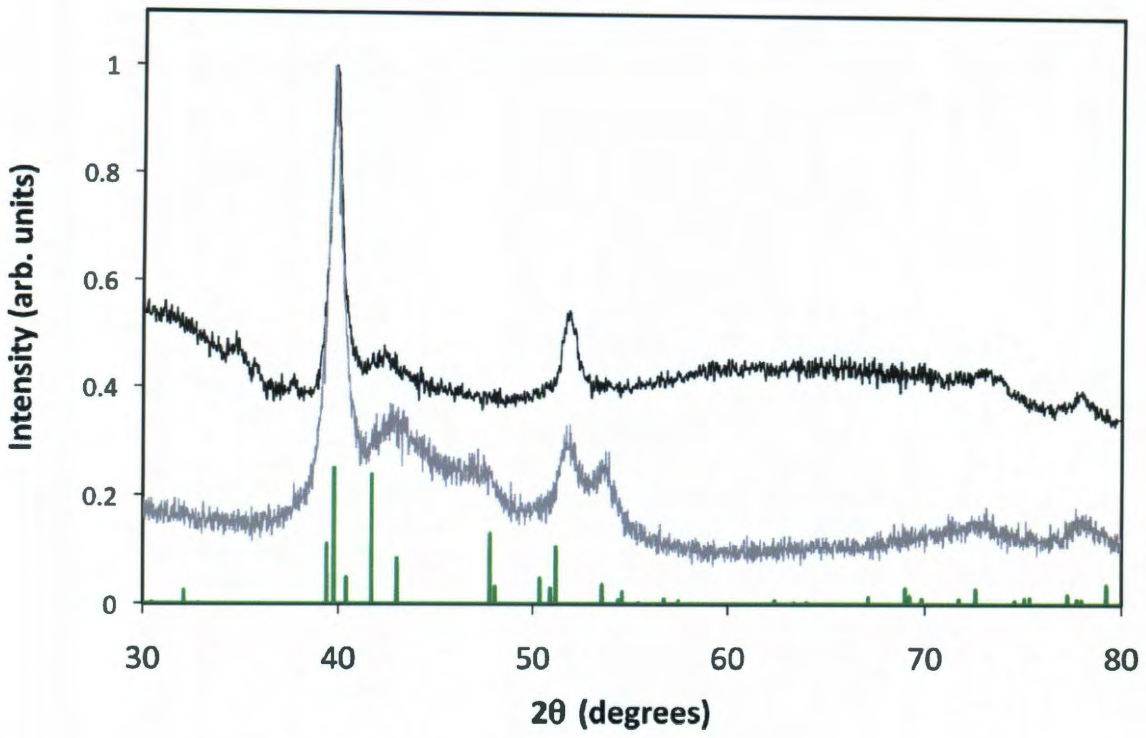

Figure 5.10 X-ray diffraction patterns of an annealed film prepared using $FeMn(CO)_8(\mu\text{-}PH_2)$ under medium-vacuum conditions in a nitrogen-filled glovebox (top) and hexagonal FeMnP prepared by bulk decomposition of $FeMn(CO)_8(\mu\text{-}PH_2)$ (bottom). The underlying line diagram represents the diffraction pattern of bulk orthorhombic FeMnP (ICDD PDF# 001-4554).

Recently, our research group reported that bulk decomposition of $FeMn(CO)_8(\mu\text{-}PH_2)$ at 300 °C resulted in the formation of hexagonal FeMnP, a structure generally formed at temperatures above 1200 °C.[156] In the orthorhombic FeMnP structure, the metal atoms are surrounded by phosphorus in either a tetrahedral or a square pyramidal fashion, the manganese atoms occupying the square pyramidal sites and the iron atoms occupying tetrahedral sites.[47] The orthorhombic to hexagonal phase transition that occurs at 1200 °C is attributed to the disordering of these metal sites. During the relatively "soft" synthesis of FeMnP from $FeMn(CO)_8(\mu\text{-}PH_2)$ at 300 °C, the material might be expected to form as a

random substitutional solid with disordered metal sites, in which case the hexagonal structure would be favored, and higher temperatures might be required to allow the metal atoms to migrate to preferred sites. Experimentally, the transition of rapidly-quenched hexagonal FeMnP to orthorhombic FeMnP has been observed to occur above 625 °C, a temperature well above that used for film deposition and annealing.[157] As demonstrated in Figure 5.10, the X-ray diffraction pattern of the annealed films prepared in the inert-atmosphere glovebox appears very similar to the pattern obtained from hexagonal FeMnP prepared *via* bulk decomposition of $FeMn(CO)_8(\mu\text{-}PH_2)$ at 300 °C. The overlapping reflections at $2\theta = 39.82$ ° and at $2\theta = 51.72$ °, respectively believed to be the (111) and the (002) reflections, indicate identical *d*-spacings between lattice planes. Several of the reflections observed in the diffraction pattern of hexagonal FeMnP obtained from bulk decomposition of $FeMn(CO)_8(\mu\text{-}PH_2)$ appear to be absent in the diffraction pattern obtained from the annealed film. This apparent anomaly may simply be the result of crystallite orientation, as the material obtained from the bulk decomposition of $FeMn(CO)_8(\mu\text{-}PH_2)$ was ground into a randomly-oriented powder prior to analysis. The annealed films, on the other hand, are fixed to the surface of the substrate and the crystallites may not be completely randomized. The non-random orientation of crystallites in the annealed films may also explain the unusual X-ray diffraction pattern obtained from films that were prepared and annealed under high-vacuum conditions (Figure 5.3). Overlaying the diffraction patterns of the annealed films prepared under high-vacuum and medium-vacuum conditions, it is observed that the reflections are centered about identical values of 2θ, the diffraction patterns

differing only in the relative intensities of the reflections (Figure 5.11). Based on the similarities observed in the elemental analyses and XPS depth profiles, it is likely that the diffraction patterns obtained in both sample types arise from the same crystalline material, but the differences in preparative methods have resulted in different preferred crystallite orientations.

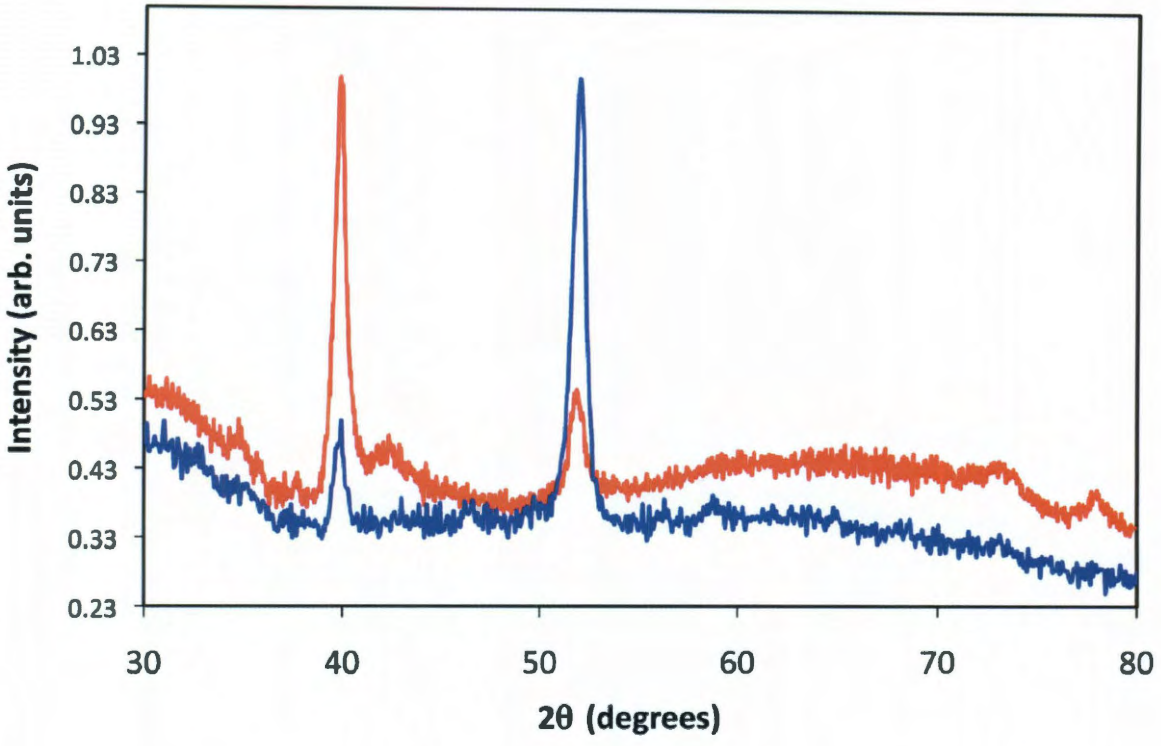

Figure 5.11 X-ray diffraction patterns of annealed films prepared using $FeMn(CO)_8(\mu\text{-}PH_2)$ under medium-vacuum conditions in a nitrogen-filled glovebox (red) and under high-vacuum conditions (blue).

Based on the data provided by X-ray diffraction experiments, ICP-OES elemental analysis, and XPS depth profiling and spectral analysis, a model describing the composition of films prepared using the single-source precursor $FeMn(CO)_8(\mu\text{-}PH_2)$ can be proposed (Figure 5.12).

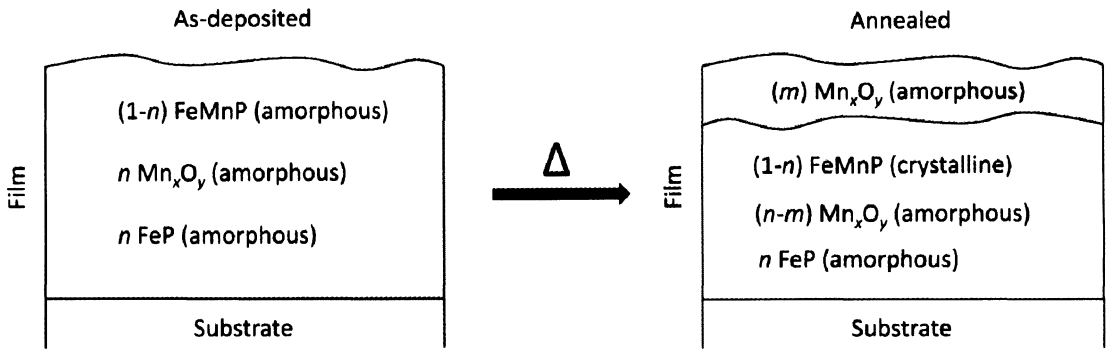

Figure 5.12 Proposed composition of as-deposited and annealed films prepared using the single-source precursor $FeMn(CO)_8(\mu\text{-}PH_2)$.

As summarized in Figure 5.12, the as-deposited films are composed of iron, manganese, and phosphorus in a 1:1:1 ratio, but XPS data suggest that a fraction *n* of the manganese atoms have been oxidized. Previously reported X-ray diffraction studies have revealed that the oxidation of hexagonal FeMnP results in the formation of MnO and FeP (Chapter 3). Based on this observation, it is reasonable to assume that for every fraction *n* of manganese atoms oxidized in the films, an equal amount of FeP is also present. XPS depth profiling experiments clearly indicate that all of the phases are equally distributed throughout the thickness of the film. During annealing of the as-deposited films, a fraction *m* of the Mn_xO_y species migrates to the surface of the films, forming a layer of oxidized manganese material. Beneath this layer of oxidized manganese is believed to be a heterogeneous mixture of FeMnP, Mn_xO_y, and FeP. According to the results of X-ray diffraction studies, the only crystalline component of the films is hexagonal FeMnP.

The source of the oxygen observed in the films has not been identified definitively, but several possibilities can be suggested. First, the oxygen atoms of the

carbonyl ligands may contribute to the oxygen content of the films. Second, oxygen contamination may result from post-synthetic oxidation as the films are exposed to the atmosphere after preparation. Finally, the very small partial pressure of oxygen present in the apparatus under high- or medium-vacuum conditions might be responsible for manganese oxidation in the films. If the oxygen originated from the CO ligands, the observation of an approximately equal amount of carbon in the XPS depth profiling experiments would have been expected. However, a significant carbon presence was not observed experimentally. The migration of Mn_xO_y species to the surface of the films during annealing provides evidence that oxidation occurs prior to the exposure of the films to atmospheric oxygen. At present, the selective oxidation of manganese by trace amounts of residual oxygen in the deposition apparatus appears to be the most likely source of oxygen inclusion into the films.

5.4 Conclusions

The feasibility of employing single-source precursors in the preparation of bimetallic phosphide films containing iron, manganese, and phosphorus has been explored. Films prepared using the molecular precursor $FeMn(CO)_8(\mu\text{-}PPh_2)$ were found to be phosphorus-deficient relative to the stoichiometry of precursor. This phosphorus deficiency was attributed to the formation of stable phosphorus-containing molecular species such as triphenylphosphine and triphenylphosphine oxide during precursor decomposition. Elemental analysis of films prepared using $FeMn(CO)_8(\mu\text{-}PH_2)$ revealed that iron, manganese, and phosphorus were present in 1:1:1 stoichiometric ratio. X-ray diffraction patterns obtained from annealed films indicate that crystalline hexagonal FeMnP is present in the films. Based solely on

elemental analysis and X-ray diffraction experiments, one might conclude that the films consisted of phase pure FeMnP. However, XPS data obtained from depth profiling experiments indicate that oxygen was also present throughout the thickness of the films. The XPS spectra of iron and phosphorus are consistent with Fe_xP (x = 1, 2, or 3) phases, but the XPS spectra of manganese suggest that manganese exists in both phosphide and oxide bonding environments, indicating that manganese is subject to selective partial oxidation. The preferential oxidation of manganese over iron is consistent with the electrochemical oxidation potentials of the two metals. Based on the analytical data, the film composition is believed to be a mixture of crystalline hexagonal FeMnP, amorphous FeP, and amorphous Mn_xO_y.

Although the films described in this work invariably exhibited evidence of partial oxidation, it is worth reiterating that the single-source precursor $FeMn(CO)_8(\mu\text{-}PH_2)$ performed the intended function of delivering Fe, Mn, and P in a 1:1:1 stoichiometric ratio remarkably well. The use of a single-source precursor has allowed us to prepare bimetallic phosphide films using an extremely rudimentary MOCVD apparatus. By contrast, preparation of bimetallic phosphide films using separate sources of iron, manganese, and phosphorus could require considerable engineering in order to achieve co-decomposition of precursors with the targeted stoichiometries. The pronounced sensitivity to oxygen exhibited by manganese in the films appears to be a general property of the material, and it may be possible to eliminate oxygen incorporation by carrying out depositions using more advanced ultra-high vacuum (UHV) MOCVD techniques. The development of UHV methods of preparing bimetallic phosphide films as well as the extension of single-source

precursor strategies to prepare quaternary transition metal pnictide films are the objects of ongoing research in our group.

Chapter 6. Conclusions and Outlook

The purpose of the experimental work described in this thesis was to examine the feasibility of employing organometallic single-source precursors in the preparation of advanced transition metal pnictide materials such as colloidal nanoparticles and films. In particular, the ternary FeMnP phase was targeted as a model for preparing advanced heterobimetallic phosphide materials, and the iron-rich Fe_3P phase was targeted due to its ferromagnetic properties as well as the fact that previous efforts to prepare well-defined advanced Fe_3P materials have generally been unsuccessful.

Progress towards the synthesis of advanced $Fe_{2-x}Mn_xP$ nanomaterials and films was described in detail in Chapters 3 and 5. Iron rich $Fe_{2-x}Mn_xP$ nanoparticles were obtained by thermal decomposition of the novel single-source precursor $FeMn(CO)_8(\mu\text{-}PH_2)$, and empirical evidence suggested that oleic acid was responsible for manganese sequestration. Films containing Fe, Mn, and P with the desired stoichiometric ratio of 1:1:1 were prepared using $FeMn(CO)_8(\mu\text{-}PH_2)$ in a simple low-pressure MOCVD apparatus. Although the elemental composition of the precursor was conserved in the deposited film material, spectroscopic evidence indicated that the films were not composed of pure-phase FeMnP, but were actually mixtures of crystalline FeMnP and amorphous FeP and Mn_xO_y.

In considering the efficacy of employing $FeMn(CO)_8(\mu\text{-}PH_2)$ as a single-source precursor to FeMnP materials, it is worth noting that bulk decomposition or MOCVD

deposition of $FeMn(CO)_8(\mu\text{-}PH_2)$ yielded materials containing Fe, Mn, and P in a 1:1:1 stoichiometric ratio, indicating that the precursor successfully performed the intended function of delivering predetermined amounts of constituent elements. However, spectroscopic evidence obtained from the nanoparticles and films demonstrated that manganese undergoes selective oxidation when exposed to molecular oxygen or oxygen-containing agents such as oleic acid. It is the pronounced oxophilicity of manganese in FeMnP that is responsible for the formation of manganese-deficient $Fe_{2-x}Mn_xP$ nanoparticles and partially oxidized FeMnP films, and appears to be a limitation of the solid-state material rather than of the precursor. The selective oxidation of manganese in the FeMnP materials may be related to the substantial difference in standard electrochemical oxidation potentials between Fe and Mn. By extension, the preparation of bimetallic phosphide materials containing metals with more similar redox properties (such as FeCoP or FeNiP) may be expected to proceed in a more straightforward manner.

Unlike the bimetallic phosphide films containing iron and manganese, Fe_3P films prepared from the single-source precursors $H_2Fe_3(CO)_9PR$ (R = ^{t}Bu or Ph) exhibited high phase-purity with negligible oxygen contamination. The ability to prepare films of such high phase-purity using a rudimentary MOCVD device is a testament to the utility of the precursor molecules. However, it is worth recalling that the attempted solution-based synthesis of Fe_3P nanoparticles using identical precursors resulted in the formation of Fe_2P particles in the presence of oleic acid. Once again, it can be concluded that the chemical properties of the solid-state

material impose certain limits on the extent to which the precursor can be effectively employed in the preparation of advanced materials.

In summary, the rational design and use of organometallic single-source precursors in the synthesis of advanced metal pnictide materials has been examined. In general, the precursors explored in this thesis have proven to be effective at delivering pre-defined stoichiometric quantities of constituent elements to form the desired metal pnictide phases. However, it has also been shown that the interactions of the newly formed solid-state materials with additives, stabilizers, or other species present in the synthetic environment can result in unfavorable or unwanted side-reactions, including leaching and selective oxidation. Thus, the chemistry of the solid-state materials of interest must also be taken into consideration. In future experiments evolving from this work, it is advisable that genuine bulk samples of the target phases be obtained and subjected to synthetic conditions identical to those used in the preparation of advanced materials such as nanoparticles or films. Analysis of the bulk materials before and after should give some indication about whether or not the materials have been adversely affected by processing, and the bulk materials would serve as primary reference standards for crystallographic, spectroscopic, and magnetic measurements.

Appendix I: Infrared Spectra of $FeMn(CO)_8(\mu\text{-}PH_2)$, $FeMn(CO)_8(\mu\text{-}PPhH_2)$, $FeMn(CO)_8[\mu\text{-}PPh(Mn(CO)_5)]$, $FeMn(CO)_8[\mu\text{-}PPh(AuPPh_3)]$, and important intermediates

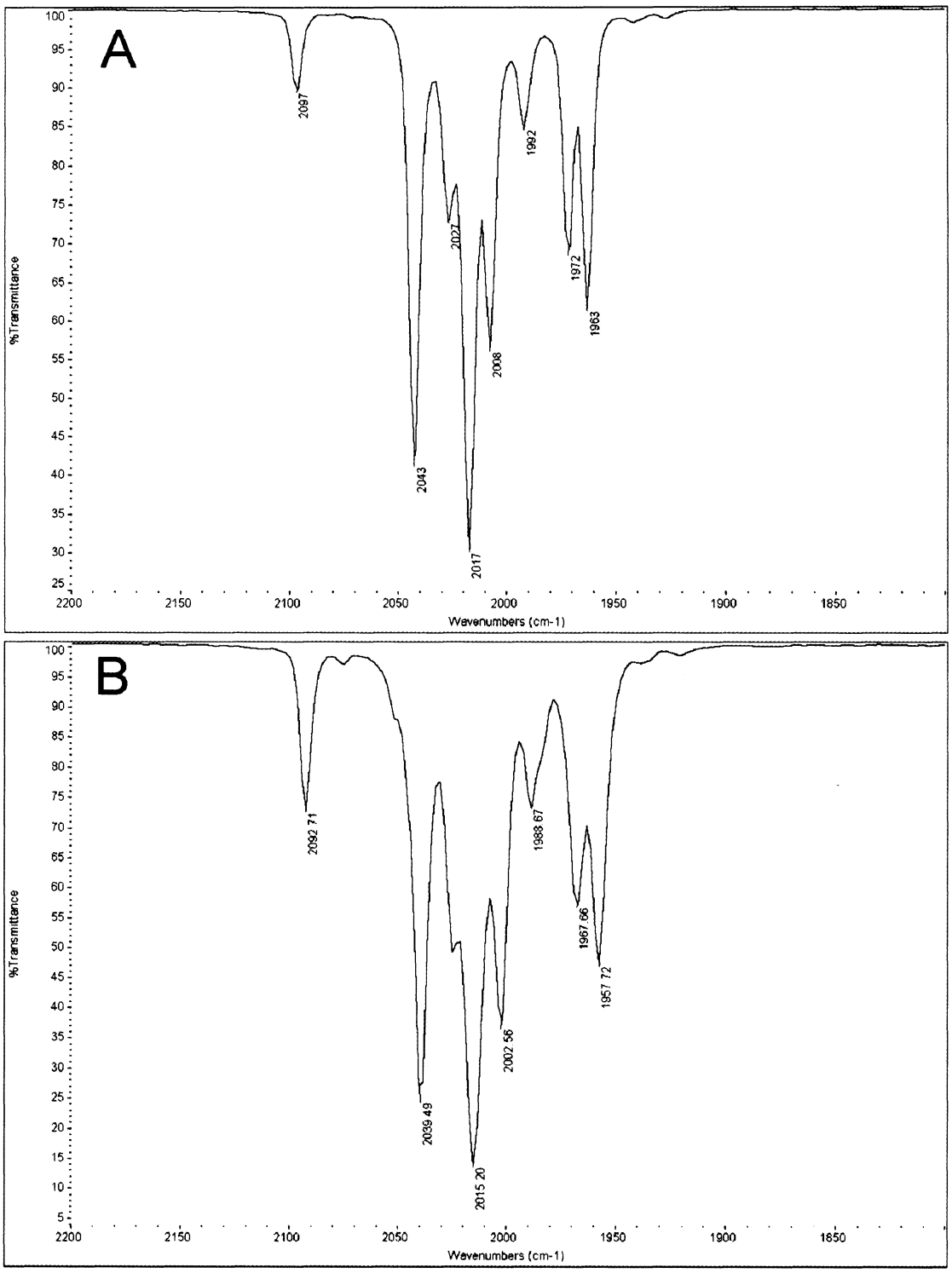

Figure A I. 1 Infrared spectra of A) $FeMn(CO)_8(\mu\text{-}PH_2)$ and B) $FeMn(CO)_8(\mu\text{-}PPhH_2)$ in hexanes.

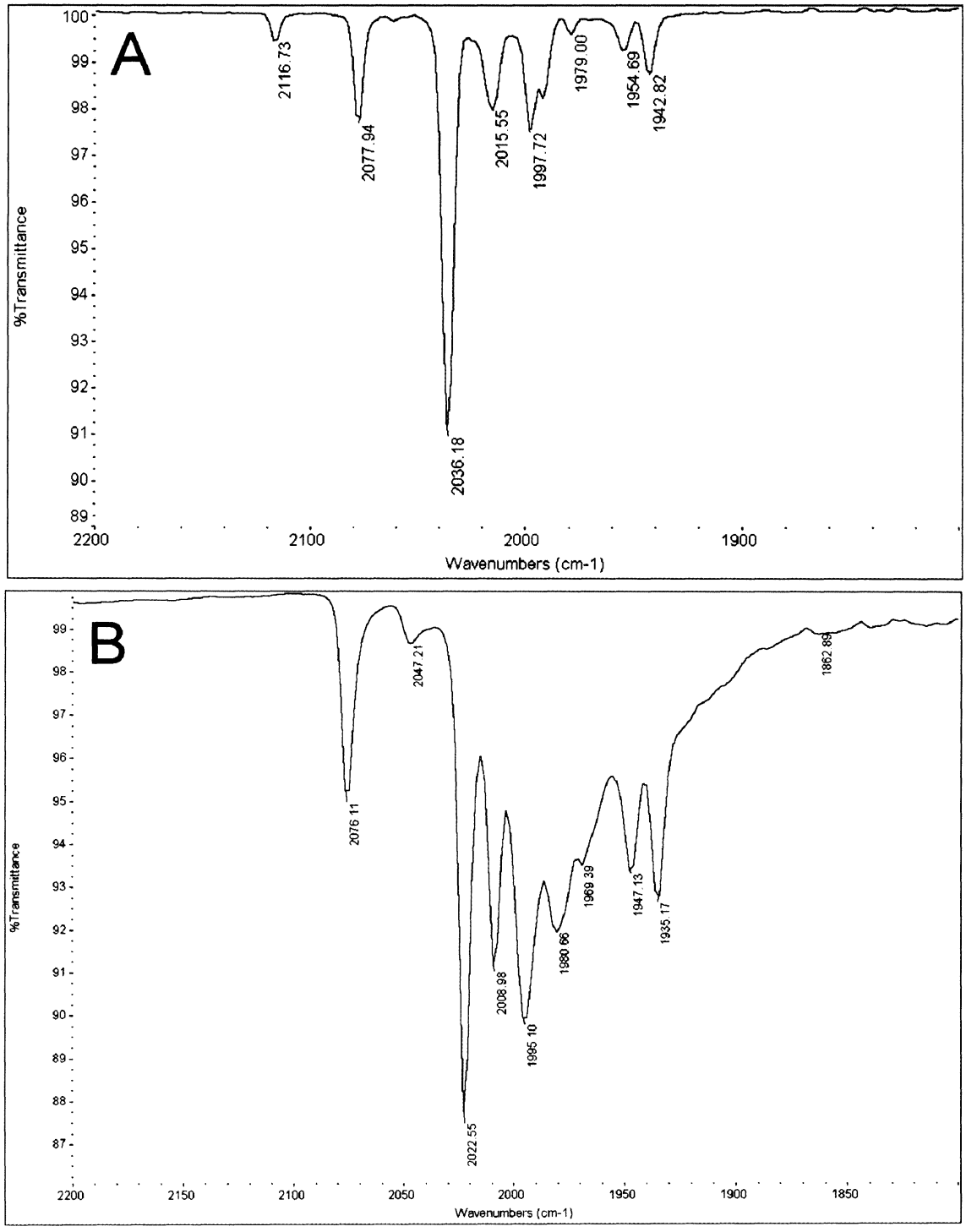

Figure A I. 2 Infrared spectra of A) $FeMn(CO)_8[\mu\text{-}PPh(Mn(CO)_5)]$ and B) $FeMn(CO)_8[\mu\text{-}PPh(AuPPh_3)]$ in hexanes.

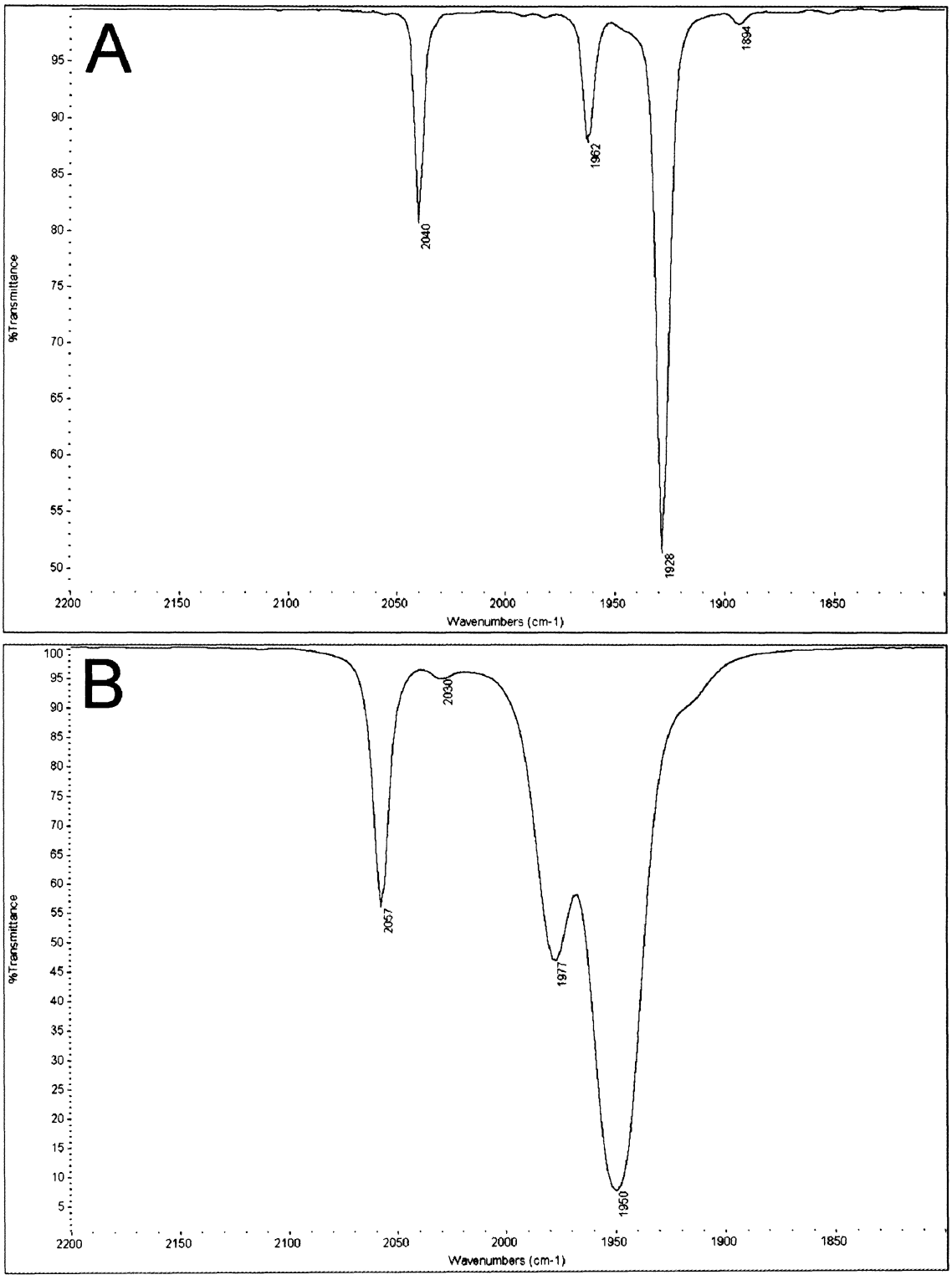

Figure A I. 3 Infrared spectra of A) $Fe(CO)_4P(TMS)_3$ in hexanes and B) $Fe(CO)_4PH_3$ in THF.

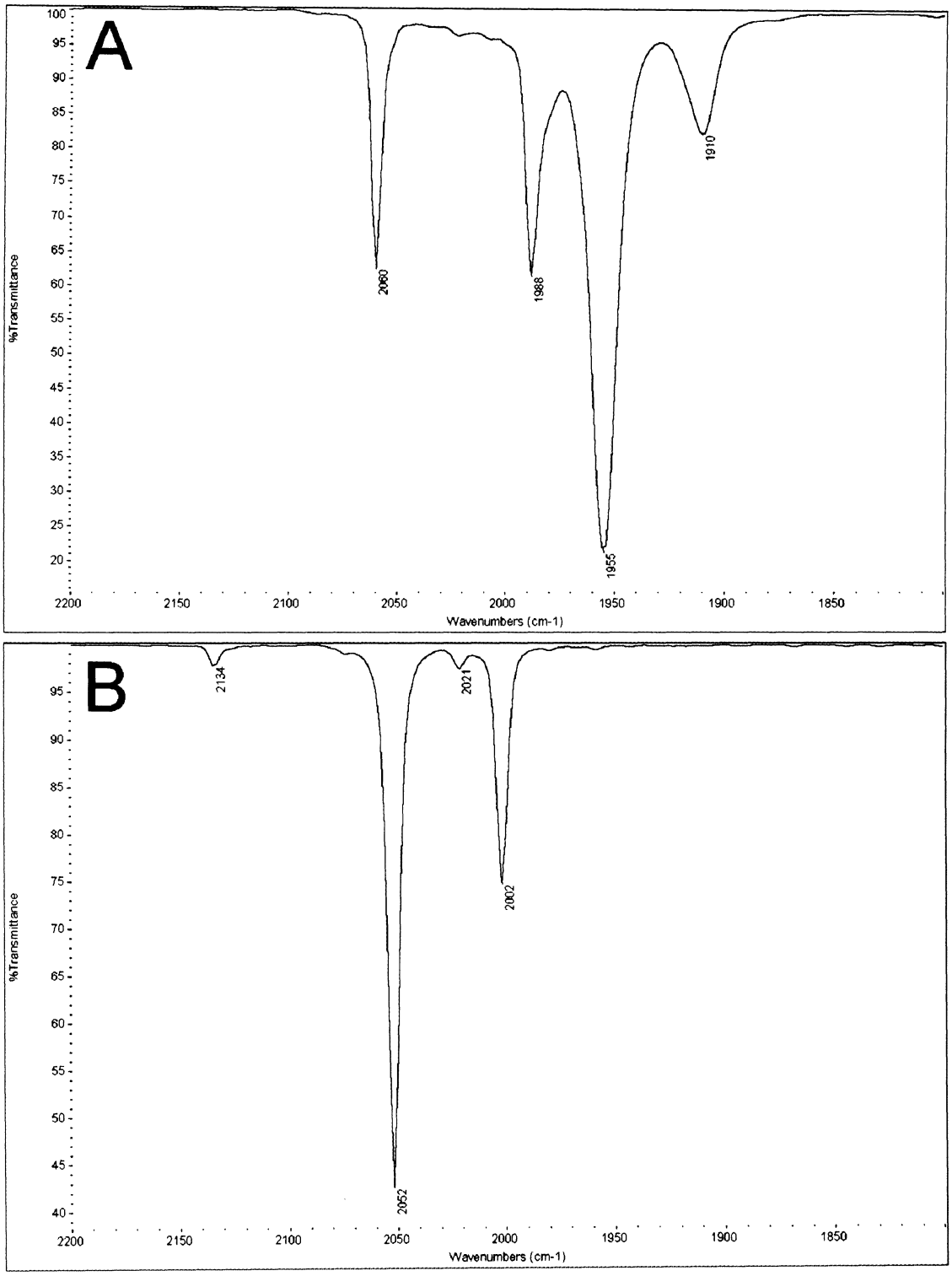

Figure A I. 4 Infrared spectra of A) $Fe(CO)_4PPhH_2$ in THF and B) $Mn(CO)_5Br$ in hexanes.

Appendix II: ^{1}H and ^{31}P NMR spectra of $FeMn(CO)_8(\mu\text{-}PH_2)$, $FeMn(CO)_8(\mu\text{-}PPhH_2)$, $FeMn(CO)_8[\mu\text{-}PPh(Mn(CO)_5)]$, and $FeMn(CO)_8[\mu\text{-}PPh(AuPPh_3)]$

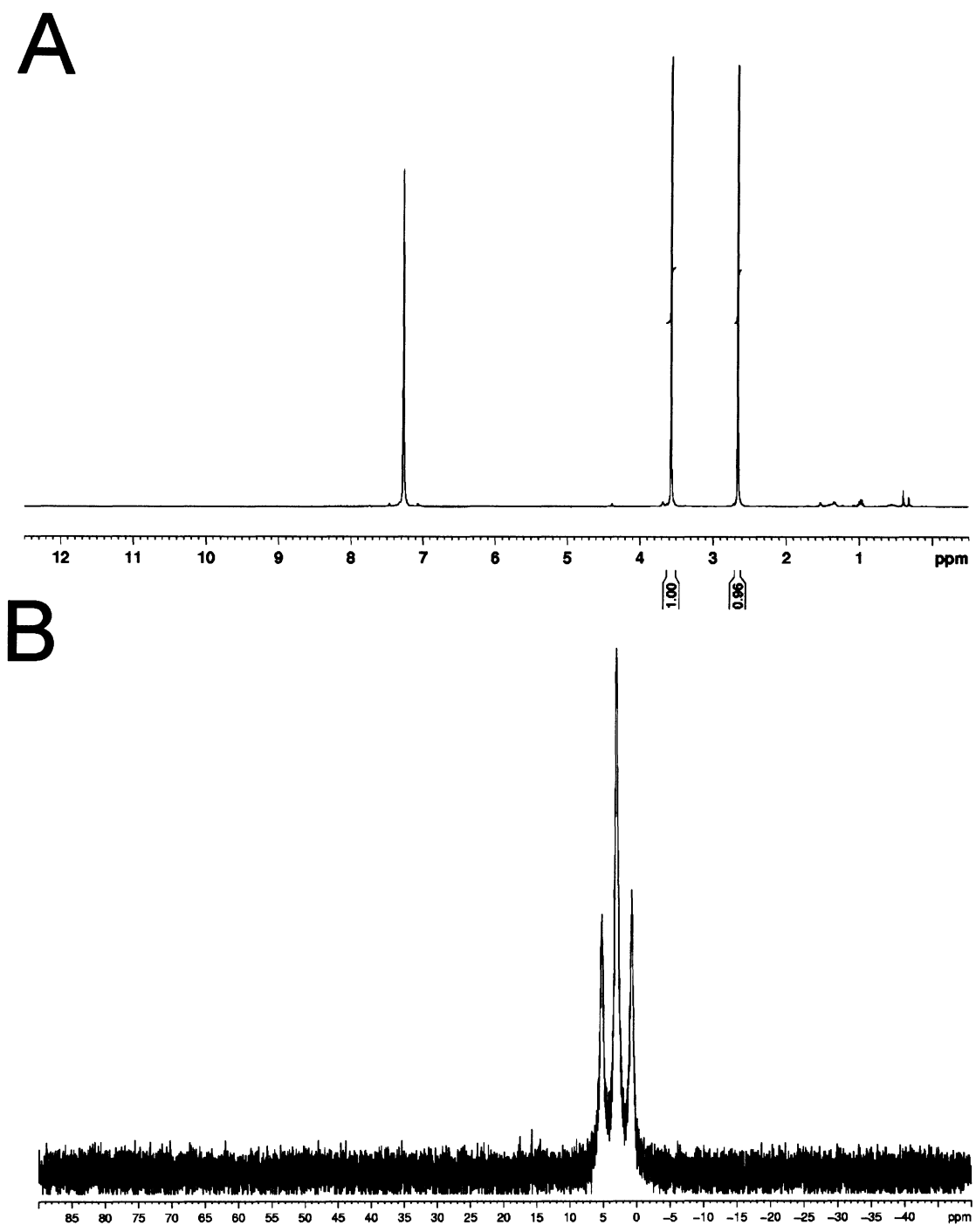

Figure A II. 1 A) ^{1}H and B) ^{31}P NMR spectra of $FeMn(CO)_8(\mu\text{-}PH_2)$.

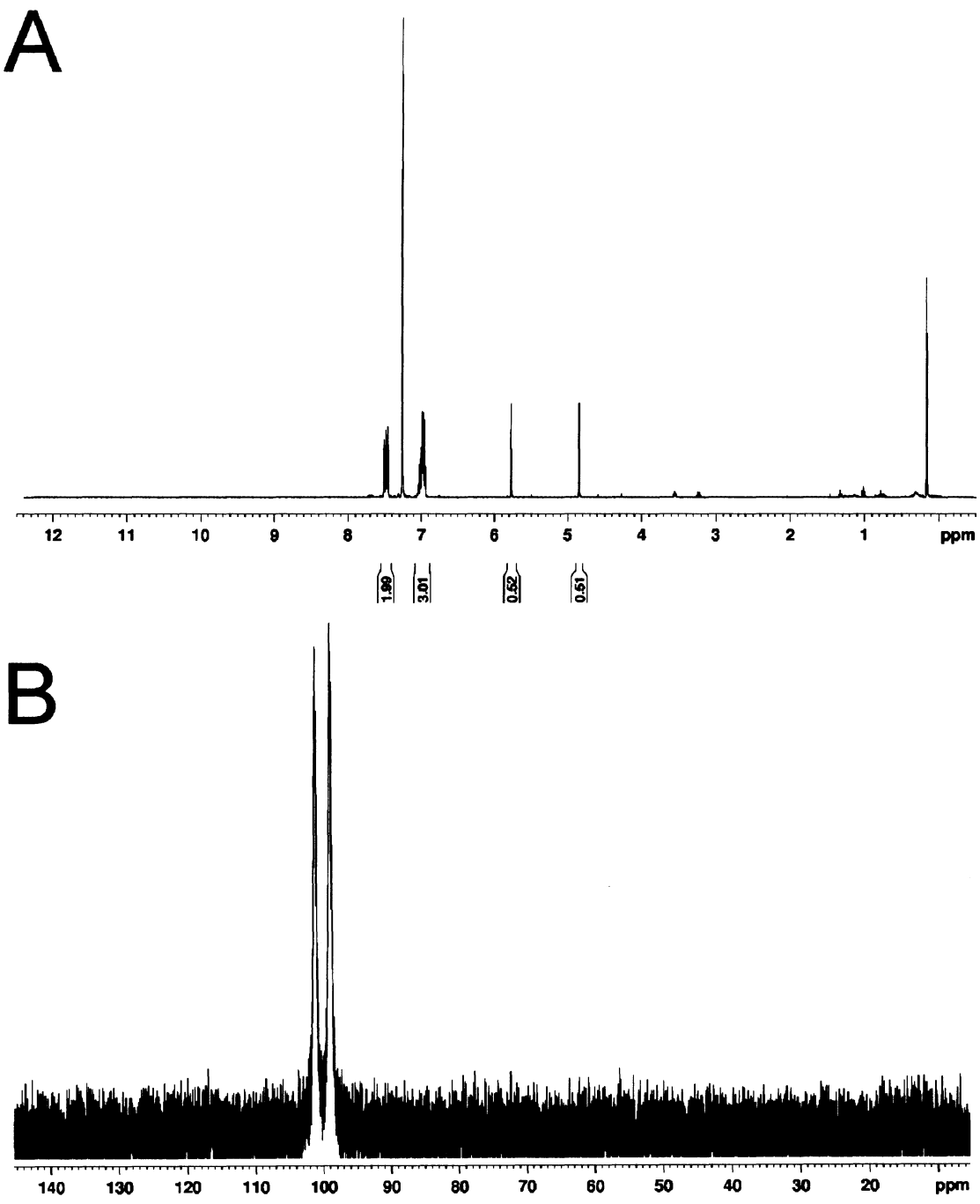

Figure A II. 2 A) ^{1}H and B) ^{31}P NMR spectra of $FeMn(CO)_8(\mu\text{-}PPh_2)$.

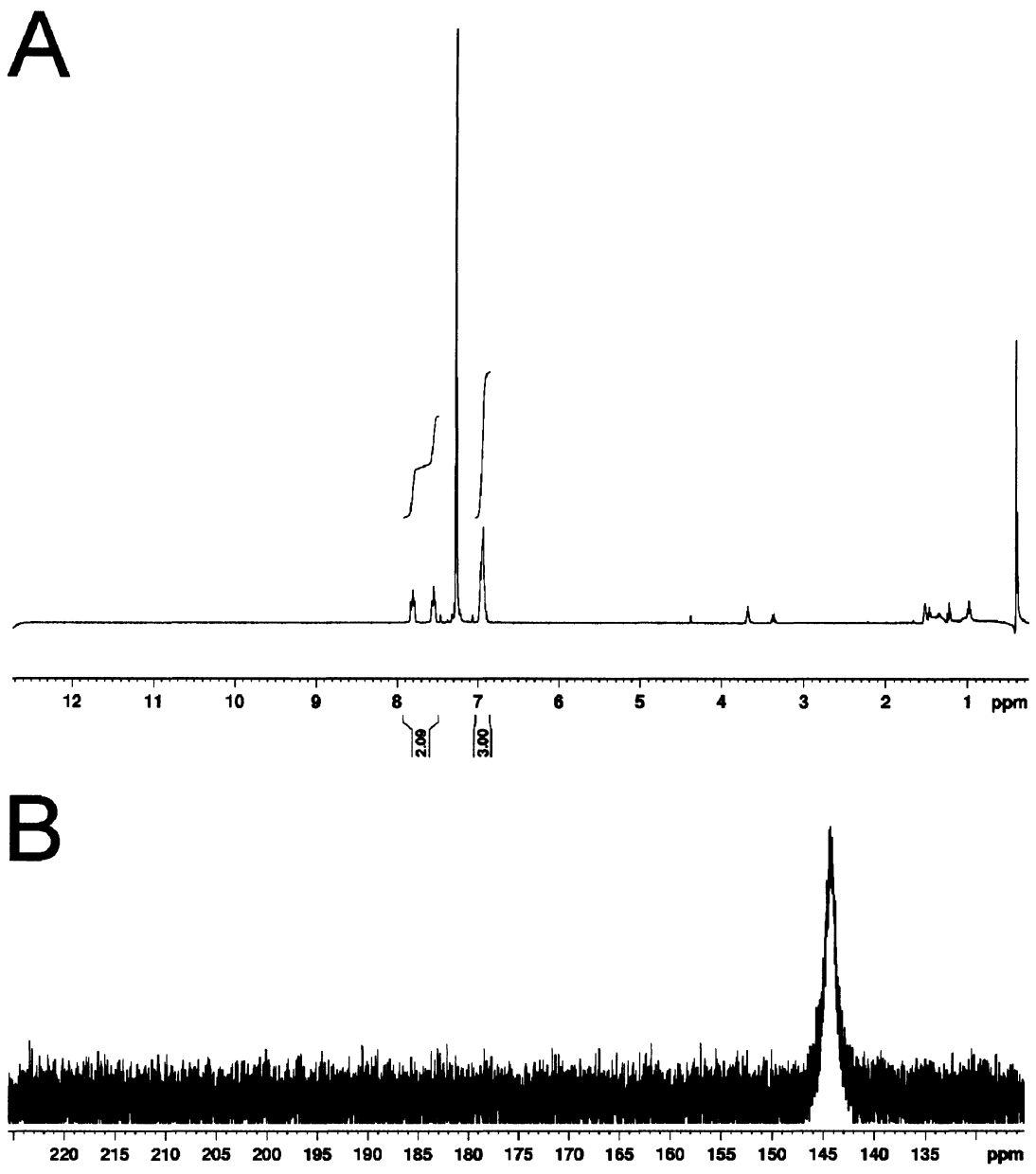

Figure A II. 3 A) ^{1}H and B) ^{31}P NMR spectra of $FeMn(CO)_8[\mu\text{-}PPh(Mn(CO)_5)]$.

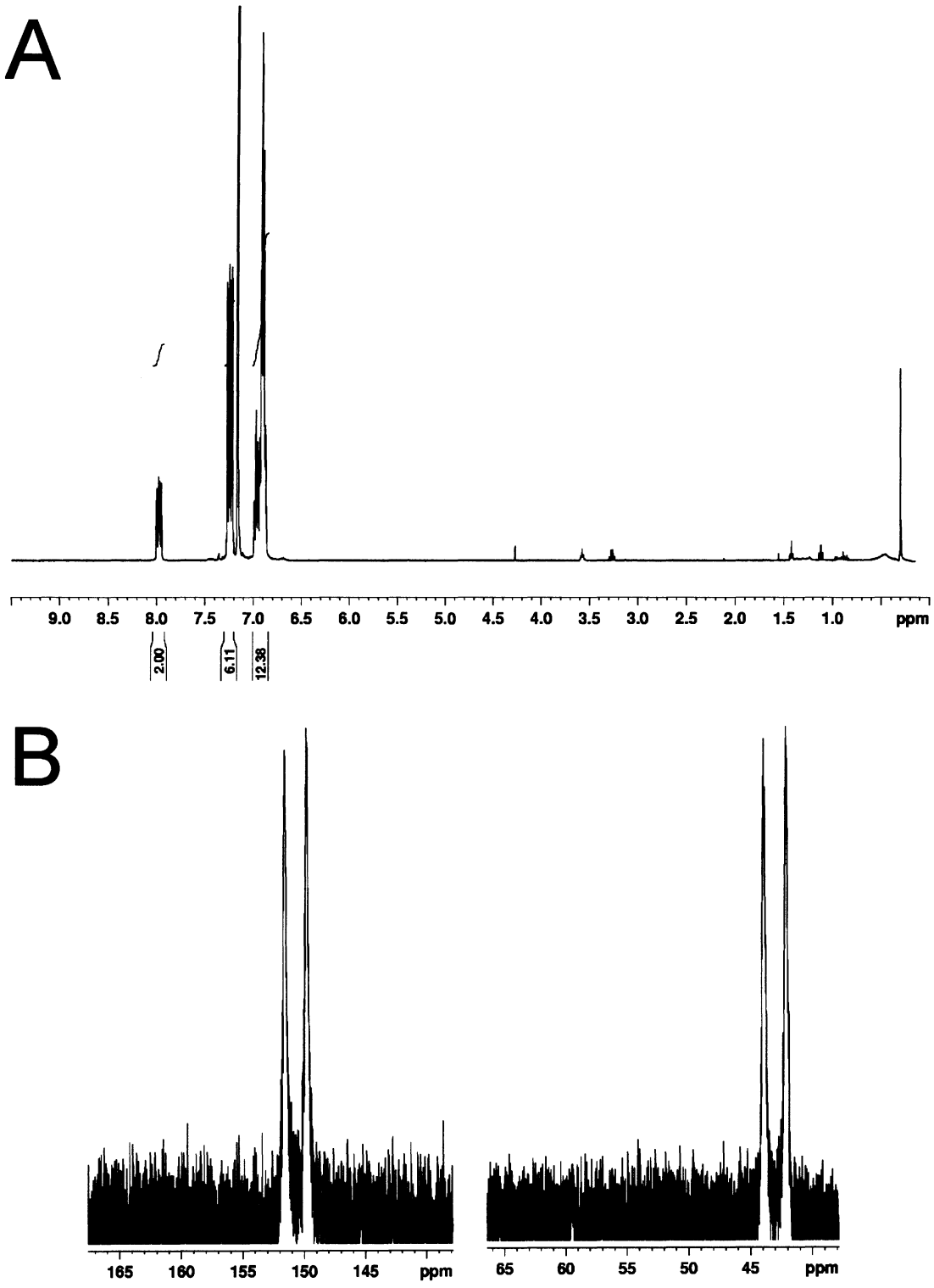

Figure A II. 4 A) ^{1}H and B) ^{31}P NMR spectra of $FeMn(CO)_8[\mu\text{-}PPh(AuPPh_3)]$.

Appendix III: EI mass spectrometry data for $FeMn(CO)_8(\mu\text{-}PH_2)$, $FeMn(CO)_8(\mu\text{-}PPhH_2)$, $FeMn(CO)_8[\mu\text{-}PPh(Mn(CO)_5)]$, and $FeMn(CO)_8[\mu\text{-}PPh(AuPPh_3)]$

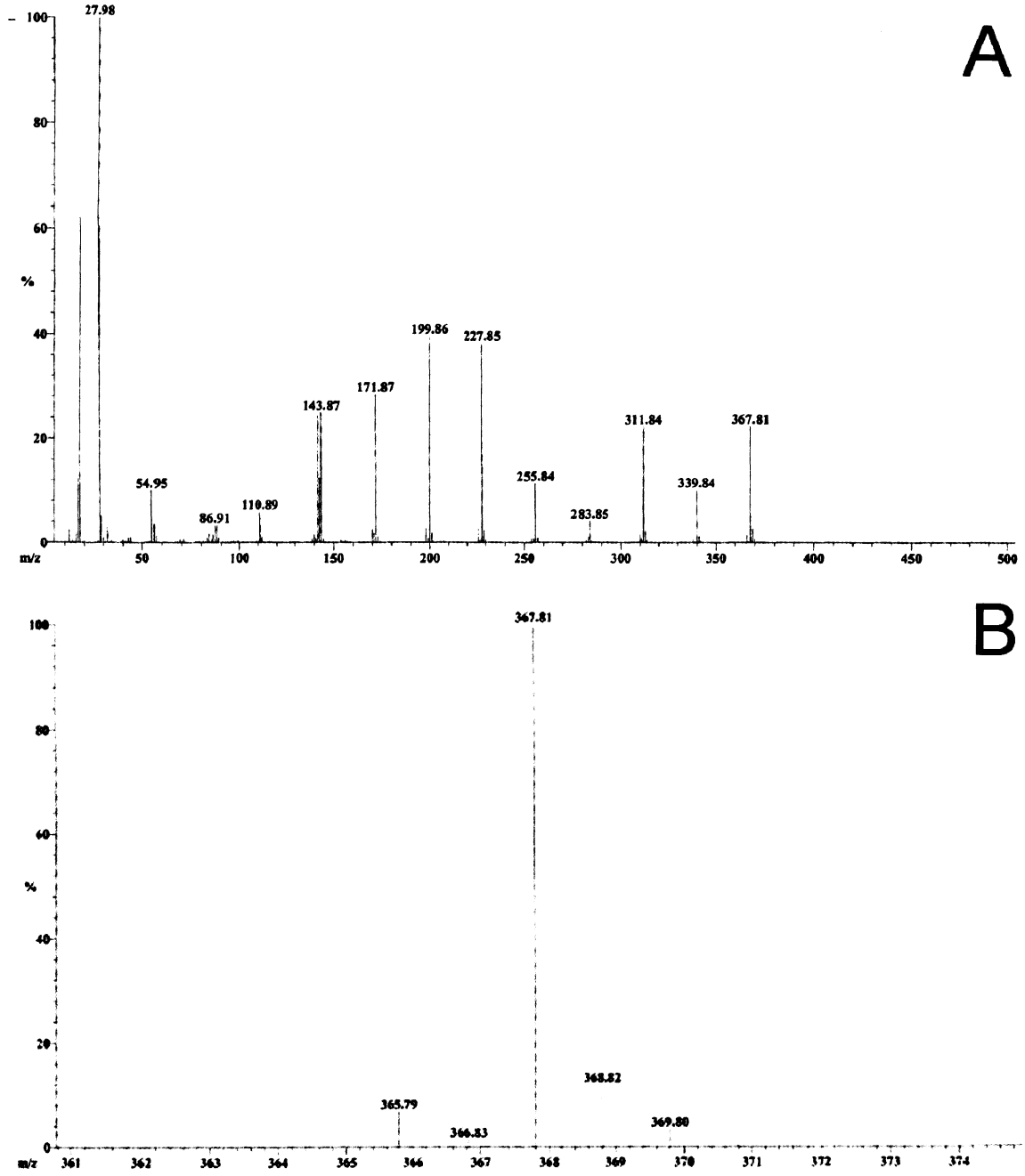

Figure A III. 1 EI mass spectrometry data showing A) the fragmentation pattern and B) M^+ ion for $FeMn(CO)_8(\mu\text{-}PH_2)$.

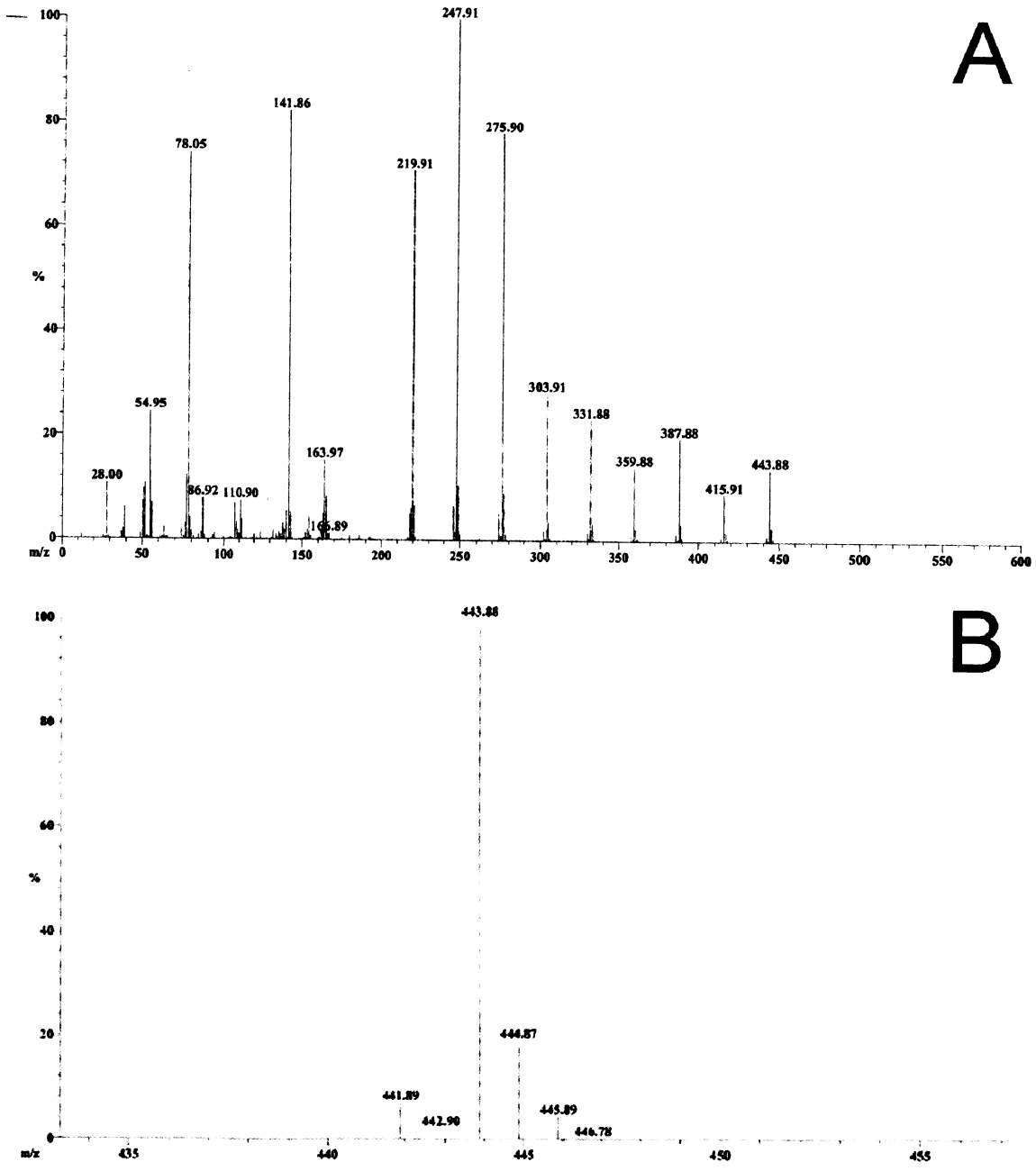

Figure A III. 2 EI mass spectrometry data showing A) the fragmentation pattern and B) M^+ ion for $FeMn(CO)_8(\mu\text{-}PPhH)$.

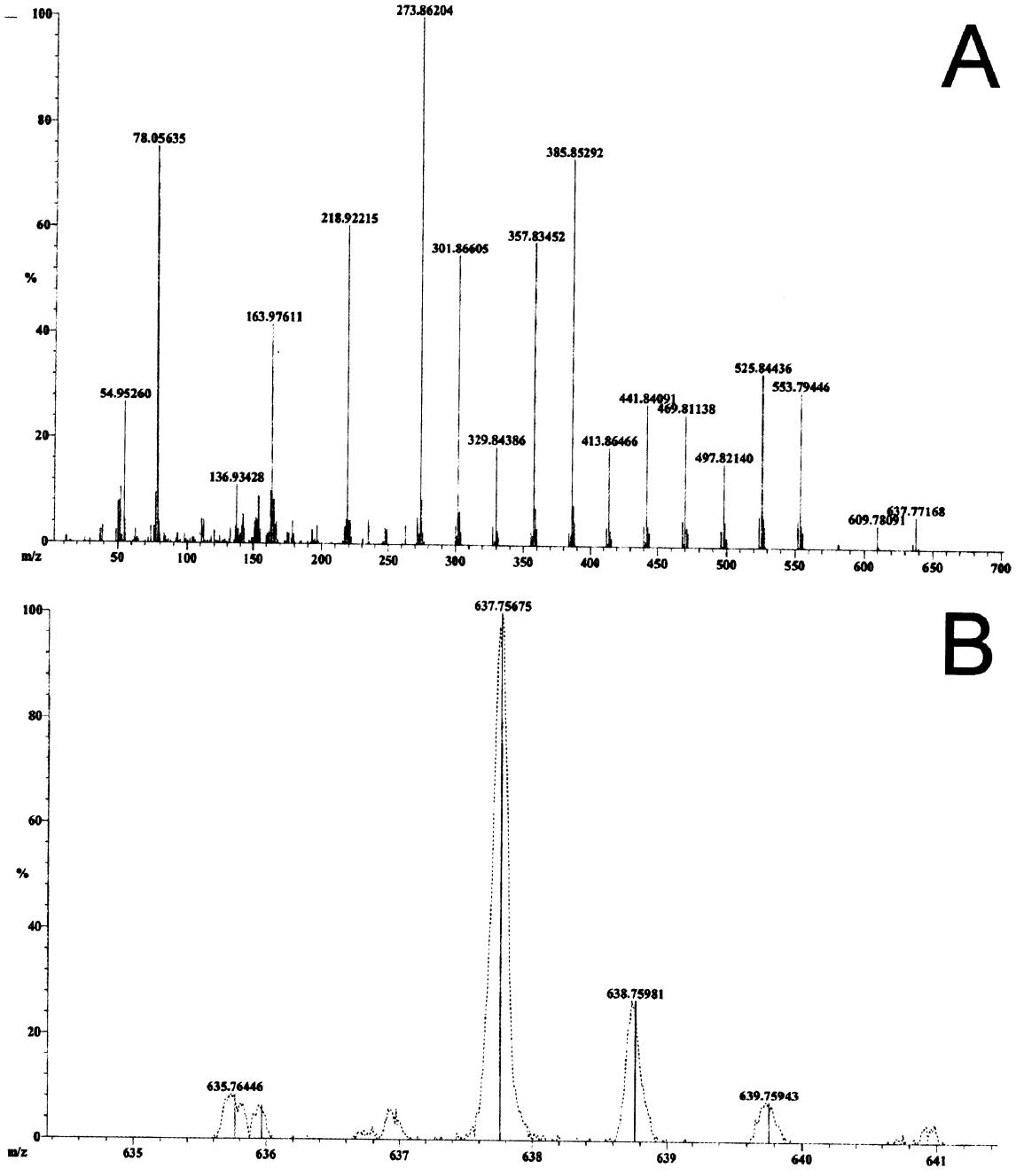

Figure A III. 3 EI mass spectrometry data showing A) the fragmentation pattern and B) M^+ ion for $FeMn(CO)_8[\mu\text{-}PPh(Mn(CO)_5)]$.

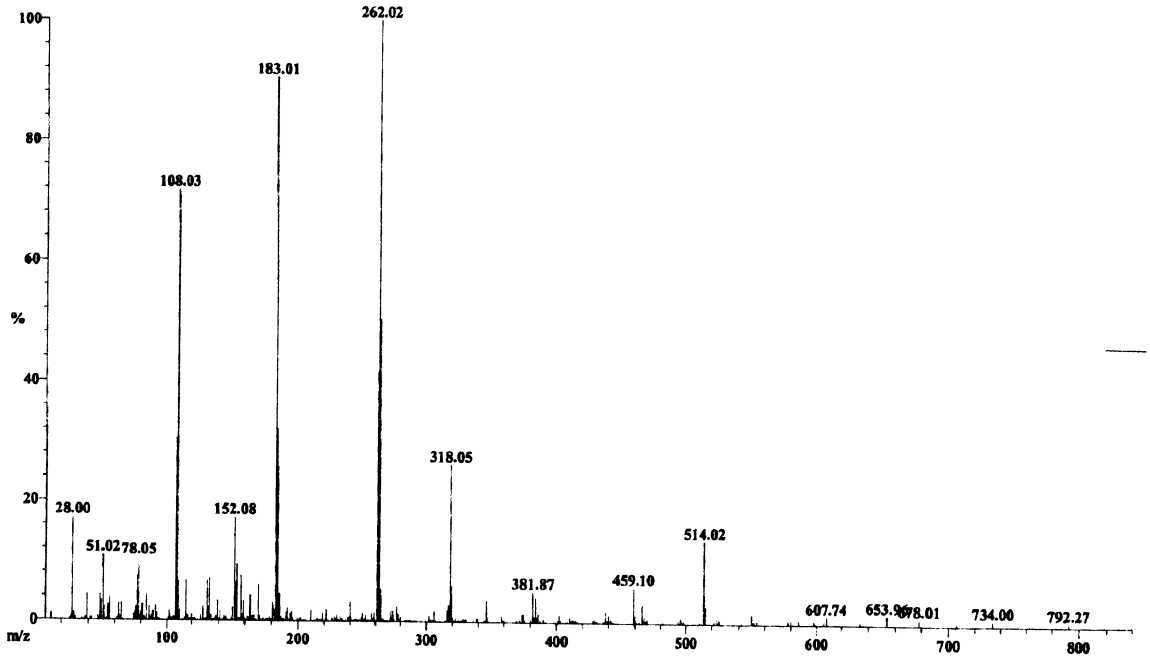

Figure A III. 4 EI mass spectrometry data showing the fragmentation pattern for $FeMn(CO)_8[\mu\text{-}PPh(AuPPh_3)]$. The M^+ ion was not observed.

Appendix IV: Supplemental X-ray diffraction data for $FeMn(CO)_8(\mu\text{-}PH_2)$

Table A IV. 1 Atomic coordinates [× 10^4] and equivalent isotropic displacement parameters [$Å^2$ × 10^3] for $FeMn(CO)_8(\mu\text{-}PH_2)$. U(eq) is defined as one third of the trace of the orthogonalized U_{ij} tensor.

	x	y	z	U(eq)
Fe(1)	1664(1)	3835(1)	2785(1)	26(1)
Mn(1)	1664(1)	3835(1)	2785(1)	26(1)
Fe(2)	2936(1)	1311(1)	2554(1)	26(1)
Mn(2)	2936(1)	1311(1)	2554(1)	26(1)
P(3)	1368(1)	2164(1)	965(1)	30(1)
C(13)	627(4)	5216(4)	2257(4)	39(1)
C(11)	-487(4)	2568(4)	3453(3)	35(1)
C(12)	3777(4)	5105(3)	2052(3)	31(1)
C(14)	2507(4)	4424(3)	4590(3)	33(1)
C(22)	5067(4)	2568(4)	1806(3)	31(1)
C(21)	798(4)	-56(4)	3143(3)	34(1)
C(23)	3476(5)	-279(4)	1818(3)	39(1)
C(24)	3941(4)	1598(3)	4354(3)	32(1)
O(13)	12(3)	6103(3)	1919(3)	60(1)
O(11)	-1838(3)	1827(3)	3870(3)	54(1)
O(12)	5041(3)	5934(3)	1587(3)	45(1)
O(14)	3031(3)	4808(3)	5724(2)	52(1)
O(22)	6414(3)	3253(3)	1343(2)	43(1)
O(21)	-510(3)	-961(3)	3471(3)	51(1)
O(23)	3844(4)	-1269(3)	1342(3)	60(1)
O(24)	4580(3)	1762(3)	5466(2)	48(1)

Table A IV. 2 Bond lengths [Å] and angles [degrees] for $FeMn(CO)_8(\mu\text{-}PH_2)$.

Fe(1)-C(13)	1.802(3)	C(13)-Fe(1)-Fe(2)	158.80(11)
Fe(1)-C(14)	1.809(3)	C(14)-Fe(1)-Fe(2)	96.58(9)
Fe(1)-C(11)	1.825(3)	C(11)-Fe(1)-Fe(2)	90.65(8)
Fe(1)-C(12)	1.829(3)	C(12)-Fe(1)-Fe(2)	89.92(8)
Fe(1)-P(3)	2.2329(9)	P(3)-Fe(1)-Fe(2)	50.56(2)
Fe(1)-Fe(2)	2.8375(6)	C(23)-Fe(2)-C(24)	104.45(13)
Fe(2)-C(23)	1.792(3)	C(23)-Fe(2)-C(21)	88.88(14)
Fe(2)-C(24)	1.824(3)	C(24)-Fe(2)-C(21)	92.68(14)
Fe(2)-C(21)	1.825(4)	C(23)-Fe(2)-C(22)	86.64(14)
Fe(2)-C(22)	1.840(3)	C(24)-Fe(2)-C(22)	91.56(13)
Fe(2)-P(3)	2.2334(8)	C(21)-Fe(2)-C(22)	174.48(13)
P(3)-H(2)	1.35(3)	C(23)-Fe(2)-P(3)	110.74(11)
P(3)-H(1)	1.23(3)	C(24)-Fe(2)-P(3)	144.81(9)
C(13)-O(13)	1.131(4)	C(21)-Fe(2)-P(3)	88.52(9)
C(11)-O(11)	1.130(4)	C(22)-Fe(2)-P(3)	90.06(9)
C(12)-O(12)	1.127(4)	C(23)-Fe(2)-Fe(1)	161.15(10)
C(14)-O(14)	1.138(4)	C(24)-Fe(2)-Fe(1)	94.27(9)
C(22)-O(22)	1.131(4)	C(21)-Fe(2)-Fe(1)	92.46(8)
C(21)-O(21)	1.132(4)	C(22)-Fe(2)-Fe(1)	90.75(8)
C(23)-O(23)	1.135(3)	P(3)-Fe(2)-Fe(1)	50.55(2)
C(24)-O(24)	1.133(4)	Fe(1)-P(3)-Fe(2)	78.89(3)
		Fe(1)-P(3)-H(2)	117.7(12)
C(13)-Fe(1)-C(14)	104.57(14)	Fe(2)-P(3)-H(2)	119.8(13)
C(13)-Fe(1)-C(11)	90.61(13)	Fe(1)-P(3)-H(1)	119.1(15)
C(14)-Fe(1)-C(11)	90.74(14)	Fe(2)-P(3)-H(1)	120.9(14)
C(13)-Fe(1)-C(12)	88.11(13)	H(2)-P(3)-H(1)	101(2)
C(14)-Fe(1)-C(12)	91.24(13)	O(13)-C(13)-Fe(1)	178.5(3)
C(11)-Fe(1)-C(12)	177.87(14)	O(11)-C(11)-Fe(1)	177.6(3)
C(13)-Fe(1)-P(3)	108.30(11)	O(12)-C(12)-Fe(1)	176.9(2)
C(14)-Fe(1)-P(3)	147.13(9)	O(14)-C(14)-Fe(1)	179.3(3)
C(11)-Fe(1)-P(3)	89.04(10)	O(22)-C(22)-Fe(2)	175.2(2)
C(12)-Fe(1)-P(3)	89.73(10)	O(21)-C(21)-Fe(2)	176.5(3)
		O(23)-C(23)-Fe(2)	178.9(3)
		O(24)-C(24)-Fe(2)	178.9(3)

Table A IV. 3 Anisotropic displacement parameters ($Å^2 \times 10^3$) for $FeMn(CO)_8(\mu\text{-}PH_2)$. The anisotropic displacement factor exponent takes the form: $-2\pi^2[(ha^*)^2U_{11} + ... + 2\ h\ k\ a^*b^*U_{12}]$

	U11	U22	U23	U23	U13	U12
Fe(1)	25(1)	25(1)	27(1)	1(1)	1(1)	6(1)
Mn(1)	25(1)	25(1)	27(1)	1(1)	1(1)	6(1)
Fe(2)	27(1)	27(1)	24(1)	0(1)	1(1)	8(1)
Mn(2)	27(1)	27(1)	24(1)	0(1)	1(1)	8(1)
P(3)	29(1)	33(1)	25(1)	-1(1)	-4(1)	7(1)
C(13)	30(2)	33(2)	49(2)	3(2)	2(2)	7(2)
C(11)	33(2)	34(2)	40(2)	6(1)	3(1)	16(2)
C(12)	35(2)	29(2)	29(2)	2(1)	2(1)	12(2)
C(14)	26(2)	33(2)	38(2)	2(1)	7(1)	6(2)
C(22)	39(2)	35(2)	23(1)	-2(1)	-2(1)	17(2)
C(21)	38(2)	30(2)	34(2)	1(1)	3(1)	12(2)
C(23)	42(2)	39(2)	37(2)	2(2)	2(2)	13(2)
C(24)	32(2)	33(2)	30(2)	3(1)	8(1)	8(2)
O(13)	54(2)	45(2)	90(2)	20(1)	5(2)	27(2)
O(11)	30(1)	53(2)	80(2)	22(1)	18(1)	12(1)
O(12)	40(1)	41(1)	51(2)	11(1)	12(1)	8(1)
O(14)	49(2)	65(2)	31(1)	-7(1)	-2(1)	7(2)
O(22)	31(1)	51(2)	40(1)	1(1)	6(1)	5(1)
O(21)	42(2)	37(1)	63(2)	3(1)	15(1)	0(1)
O(23)	82(2)	46(2)	62(2)	-11(1)	12(2)	33(2)
O(24)	47(2)	62(2)	29(1)	3(1)	-3(1)	10(1)

Table A IV. 4 Hydrogen coordinates ($\times 10^4$) and isotropic displacement parameters ($Å^2 \times 10^3$) for $FeMn(CO)_8(\mu\text{-}PH_2)$.

	x	y	z	U(eq)
H(2)	-320(40)	1260(40)	550(30)	41(9)
H(1)	2010(40)	2650(40)	-190(40)	47(9)

Appendix V: Supplemental X-ray diffraction data for $FeMn(CO)_8(\mu\text{-}PPhH)$

Table A V. 1 Atomic coordinates [× 10^4] and equivalent isotropic displacement parameters [$Å^2$ × 10^3] for $FeMn(CO)_8(\mu\text{-}PPhH)$. U(eq) is defined as one third of the trace of the orthogonalized U_{ij} tensor.

	x	y	z	U(eq)
Mn(2)	7800(1)	303(1)	6624(1)	61(1)
Fe(2)	7800(1)	303(1)	6624(1)	61(1)
Fe(1)	6132(1)	1272(1)	7945(1)	52(1)
Mn(1)	6132(1)	1272(1)	7945(1)	52(1)
P(1)	8117(2)	604(1)	8471(2)	52(1)
C(1)	8206(6)	-238(4)	9629(5)	48(2)
C(2)	8128(6)	76(5)	10701(6)	65(2)
C(3)	8131(7)	-552(7)	11588(7)	78(2)
C(4)	8181(7)	-1480(7)	11401(7)	79(2)
C(5)	8293(7)	-1814(5)	10337(8)	78(2)
C(6)	8325(7)	-1205(5)	9451(6)	71(2)
C(11)	6938(7)	2325(6)	7600(6)	71(2)
C(12)	5404(6)	193(5)	8316(6)	60(2)
C(13)	5738(7)	1823(5)	9183(7)	66(2)
C(14)	4725(8)	1491(5)	6886(7)	71(2)
C(21)	8795(8)	1340(6)	6396(6)	70(2)
C(22)	6885(7)	-775(5)	6758(6)	63(2)
C(23)	9129(8)	-416(5)	6322(6)	74(2)
C(24)	6866(8)	485(5)	5227(8)	82(2)
O(11)	7443(6)	3030(4)	7437(5)	101(2)
O(12)	4917(5)	-492(4)	8589(5)	89(2)
O(13)	5543(6)	2187(4)	10003(5)	106(2)
O(14)	3811(6)	1615(4)	6248(5)	108(2)
O(21)	9457(6)	1959(4)	6239(5)	111(2)
O(22)	6350(5)	-1486(4)	6815(5)	86(2)
O(23)	10004(6)	-852(5)	6109(6)	120(2)
O(24)	6297(7)	600(4)	4355(5)	126(3)

Table A V. 2 Bond lengths [Å] and angles [degrees] for $FeMn(CO)_8(\mu\text{-}PPhH)$.

Mn(2)-C(23)	1.777(8)	P(1)-Mn(2)-Fe(1)	51.12(6)
Mn(2)-C(22)	1.813(8)	C(13)-Fe(1)-C(11)	89.3(3)
Mn(2)-C(24)	1.823(10)	C(13)-Fe(1)-C(12)	91.2(3)
Mn(2)-C(21)	1.831(9)	C(11)-Fe(1)-C(12)	177.1(3)
Mn(2)-P(1)	2.225(2)	C(13)-Fe(1)-C(14)	104.9(3)
Mn(2)-Fe(1)	2.8361(15)	C(11)-Fe(1)-C(14)	92.5(3)
Fe(1)-C(13)	1.767(8)	C(12)-Fe(1)-C(14)	90.0(3)
Fe(1)-C(11)	1.784(8)	C(13)-Fe(1)-P(1)	104.8(2)
Fe(1)-C(12)	1.785(8)	C(11)-Fe(1)-P(1)	89.3(2)
Fe(1)-C(14)	1.808(10)	C(12)-Fe(1)-P(1)	87.8(2)
Fe(1)-P(1)	2.252(2)	C(14)-Fe(1)-P(1)	150.3(2)
P(1)-C(1)	1.820(6)	C(13)-Fe(1)-Mn(2)	154.7(2)
P(1)-H(1)	1.16(5)	C(11)-Fe(1)-Mn(2)	86.8(2)
C(1)-C(2)	1.368(8)	C(12)-Fe(1)-Mn(2)	91.5(2)
C(1)-C(6)	1.397(8)	C(14)-Fe(1)-Mn(2)	100.2(2)
C(2)-C(3)	1.383(9)	P(1)-Fe(1)-Mn(2)	50.28(6)
C(2)-H(6A)	0.93	C(1)-P(1)-Mn(2)	127.7(2)
C(3)-C(4)	1.339(10)	C(1)-P(1)-Fe(1)	115.9(2)
C(3)-H(1A)	0.93	Mn(2)-P(1)-Fe(1)	78.60(7)
C(4)-C(5)	1.375(10)	C(1)-P(1)-H(1)	102(2)
C(4)-H(2A)	0.93	Mn(2)-P(1)-H(1)	121(2)
C(5)-C(6)	1.370(9)	Fe(1)-P(1)-H(1)	108(2)
C(5)-H(3A)	0.93	C(2)-C(1)-C(6)	118.7(6)
C(6)-H(4A)	0.93	C(2)-C(1)-P(1)	119.5(5)
C(11)-O(11)	1.155(8)	C(6)-C(1)-P(1)	121.8(5)
C(12)-O(12)	1.160(7)	C(1)-C(2)-C(3)	120.8(7)
C(13)-O(13)	1.148(7)	C(1)-C(2)-H(6A)	119.6
C(14)-O(14)	1.136(8)	C(3)-C(2)-H(6A)	119.6
C(21)-O(21)	1.141(8)	C(4)-C(3)-C(2)	120.2(8)
C(22)-O(22)	1.155(7)	C(4)-C(3)-H(1A)	119.9
C(23)-O(23)	1.146(8)	C(2)-C(3)-H(1A)	119.9
C(24)-O(24)	1.132(8)	C(3)-C(4)-C(5)	120.2(7)
		C(3)-C(4)-H(2A)	119.9
C(23)-Mn(2)-C(22)	87.3(3)	C(5)-C(4)-H(2A)	119.9
C(23)-Mn(2)-C(24)	102.5(4)	C(6)-C(5)-C(4)	120.6(7)
C(22)-Mn(2)-C(24)	89.3(3)	C(6)-C(5)-H(3A)	119.7
C(23)-Mn(2)-C(21)	88.5(3)	C(4)-C(5)-H(3A)	119.7
C(22)-Mn(2)-C(21)	175.1(3)	C(5)-C(6)-C(1)	119.4(7)
C(24)-Mn(2)-C(21)	89.0(3)	C(5)-C(6)-H(4A)	120.3
C(23)-Mn(2)-P(1)	107.5(2)	C(1)-C(6)-H(4A)	120.3
C(22)-Mn(2)-P(1)	94.7(2)	O(11)-C(11)-Fe(1)	175.9(7)

C(24)-Mn(2)-P(1)	149.9(3)	O(12)-C(12)-Fe(1)	177.7(6)
C(21)-Mn(2)-P(1)	89.1(2)	O(13)-C(13)-Fe(1)	176.8(7)
C(23)-Mn(2)-Fe(1)	158.1(2)	O(14)-C(14)-Fe(1)	177.4(7)
C(22)-Mn(2)-Fe(1)	90.1(2)	O(21)-C(21)-Mn(2)	176.8(7)
C(24)-Mn(2)-Fe(1)	99.2(3)	O(22)-C(22)-Mn(2)	176.4(6)
C(21)-Mn(2)-Fe(1)	94.8(2)	O(23)-C(23)-Mn(2)	177.5(8)
		O(24)-C(24)-Mn(2)	179.3(8)

Table A V. 3 Anisotropic displacement parameters ($Å^2 \times 10^3$) for $FeMn(CO)_8(\mu\text{-}PPhH)$. The anisotropic displacement factor exponent takes the form: $-2\pi^2[(ha^*)^2U_{11} + ... + 2\ h\ k\ a^*b^*U_{12}]$

	U11	U22	U33	U23	U13	U12
Mn(2)	66(1)	67(1)	53(1)	-4(1)	15(1)	-3(1)
Fe(2)	66(1)	67(1)	53(1)	-4(1)	15(1)	-3(1)
Fe(1)	59(1)	49(1)	50(1)	3(1)	13(1)	3(1)
Mn(1)	59(1)	49(1)	50(1)	3(1)	13(1)	3(1)
P(1)	52(1)	55(1)	49(1)	-4(1)	10(1)	-7(1)
C(1)	42(4)	56(4)	45(4)	-4(3)	4(3)	-4(3)
C(2)	63(5)	76(5)	58(5)	-3(4)	16(4)	7(4)
C(3)	67(5)	107(7)	61(6)	2(5)	11(4)	4(5)
C(4)	61(5)	104(7)	71(6)	22(5)	2(4)	-17(5)
C(5)	83(6)	66(5)	79(6)	17(5)	-10(5)	-13(4)
C(6)	76(5)	76(5)	58(5)	-1(4)	-6(4)	-3(4)
C(11)	71(5)	76(6)	65(5)	4(4)	7(4)	7(5)
C(12)	43(4)	72(5)	65(5)	6(4)	7(4)	9(4)
C(13)	83(5)	41(4)	75(6)	9(4)	10(4)	9(4)
C(14)	70(6)	73(5)	75(6)	27(4)	28(5)	-4(4)
C(21)	76(5)	87(6)	51(4)	-10(4)	24(4)	-1(5)
C(22)	65(5)	66(5)	56(5)	-2(4)	2(4)	0(4)
C(23)	77(6)	84(6)	64(5)	-14(4)	20(4)	-3(5)
C(24)	86(6)	82(6)	76(6)	4(5)	4(5)	-4(5)
O(11)	122(5)	71(4)	115(5)	9(4)	32(4)	-20(3)
O(12)	76(4)	77(4)	118(5)	28(3)	29(3)	-9(3)
O(13)	168(6)	85(4)	69(4)	-11(3)	34(4)	32(4)
O(14)	86(5)	136(5)	95(5)	35(4)	-17(4)	-4(4)
O(21)	123(5)	108(5)	111(5)	-6(4)	50(4)	-55(4)
O(22)	94(4)	62(3)	100(4)	-8(3)	11(3)	-16(3)
O(23)	97(5)	135(5)	133(5)	-36(4)	38(4)	20(4)
O(24)	156(6)	129(6)	79(5)	17(4)	-35(4)	-18(4)

Table A V. 4 Hydrogen coordinates (× 10^4) and isotropic displacement parameters (Å^2 × 10^3) for $FeMn(CO)_8(\mu\text{-}PPhH)$.

	x	y	z	U(eq)
H(6A)	8072	719	10835	78
H(1A)	8099	-328	12316	94
H(2A)	8139	-1901	11993	95
H(3A)	8348	-2460	10218	94
H(4A)	8425	-1434	8737	85
H(1)	8840(50)	1180(30)	8850(40)	53(15)

Appendix VI: Supplemental X-ray diffraction data for $FeMn(CO)_8[\mu\text{-}PPh(Mn(CO)_5)]$

Table A VI. 1 Atomic coordinates [× 10^4] and equivalent isotropic displacement parameters [$Å^2$ × 10^3] for $FeMn(CO)_8[\mu\text{-}PPh(Mn(CO)_5)]$. U(eq) is defined as one third of the trace of the orthogonalized U_{ij} tensor.

	x	y	z	U(eq)
Fe(1A)	2773(1)	9625(1)	2524(1)	27(1)
Mn(1A)	2773(1)	9625(1)	2524(1)	27(1)
Fe(1B)	2266(1)	8363(1)	3532(1)	33(1)
Mn(1B)	2266(1)	8363(1)	3532(1)	33(1)
Mn(3A)	-730(1)	9516(1)	2406(1)	29(1)
Fe(2A)	-3596(1)	12942(1)	1381(1)	30(1)
Mn(2A)	-3596(1)	12942(1)	1381(1)	30(1)
Fe(2B)	-2217(1)	13832(1)	3374(1)	31(1)
Mn(2B)	-2217(1)	13832(1)	3374(1)	31(1)
Mn(3B)	-4105(1)	15973(1)	2616(1)	28(1)
P(1)	988(1)	8764(1)	2327(1)	24(1)
P(2)	-3895(1)	14248(1)	2588(1)	23(1)
O(111)	2530(2)	11393(2)	4061(2)	57(1)
O(112)	3229(2)	7839(2)	1170(2)	49(1)
O(113)	2335(2)	10560(2)	985(2)	51(1)
O(114)	5303(2)	10202(2)	3479(2)	52(1)
O(121)	2185(2)	10032(2)	5275(2)	61(1)
O(122)	2321(2)	6413(2)	2074(2)	59(1)
O(123)	1037(2)	7130(2)	4349(2)	67(1)
O(124)	4729(2)	8447(2)	4554(2)	58(1)
O(131)	-2834(2)	10365(2)	2438(2)	68(1)
O(132)	-2157(2)	8115(2)	364(2)	54(1)
O(133)	-1228(2)	7960(2)	3286(2)	50(1)
O(134)	200(2)	10919(2)	1525(2)	64(1)
O(135)	306(2)	11017(2)	4468(2)	61(1)
O(211)	-2147(2)	14163(2)	689(2)	53(1)
O(212)	-5043(2)	11409(2)	1750(2)	52(1)
O(213)	-5452(2)	12678(2)	-454(2)	64(1)
O(214)	-2331(2)	11313(2)	799(2)	54(1)
O(221)	-870(2)	15349(2)	2911(2)	57(1)
O(222)	-3481(2)	12342(2)	3923(2)	63(1)
O(223)	-1307(2)	15084(2)	5480(2)	63(1)
O(224)	-490(2)	12553(2)	3194(2)	70(1)
O(231)	-4298(2)	18068(2)	2703(2)	58(1)
O(232)	-5834(2)	16017(2)	3694(2)	51(1)
O(233)	-2113(2)	16707(2)	4512(2)	42(1)
O(234)	-5993(2)	14961(2)	681(2)	67(1)
O(235)	-2545(2)	16160(2)	1442(2)	44(1)
C(111)	2597(3)	10690(3)	3476(3)	38(1)

C(112)	3010(3)	8500(3)	1694(3)	36(1)
C(113)	2506(3)	10209(3)	1593(3)	36(1)
C(114)	4315(3)	9979(2)	3119(3)	35(1)
C(121)	2218(3)	9443(3)	4576(3)	37(1)
C(122)	2296(3)	7183(3)	2595(3)	42(1)
C(123)	1505(3)	7597(3)	4015(3)	45(1)
C(124)	3785(3)	8438(3)	4188(2)	40(1)
C(131)	-2036(3)	10042(3)	2435(3)	42(1)
C(132)	-1591(3)	8622(3)	1128(3)	36(1)
C(133)	-1047(3)	8555(3)	2954(2)	35(1)
C(134)	-155(3)	10390(3)	1854(3)	40(1)
C(135)	-22(3)	10439(3)	3687(3)	37(1)
C(141)	404(2)	7729(2)	1123(2)	25(1)
C(142)	474(2)	7851(2)	239(2)	28(1)
C(143)	18(3)	7079(3)	-648(2)	34(1)
C(144)	-547(3)	6166(3)	-704(3)	38(1)
C(145)	-651(3)	6031(2)	145(3)	37(1)
C(146)	-168(3)	6792(2)	1043(2)	31(1)
C(211)	-2679(3)	13745(2)	1012(2)	35(1)
C(212)	-4490(3)	12028(3)	1655(2)	32(1)
C(213)	-4734(3)	12774(3)	265(3)	42(1)
C(214)	-2810(3)	11955(3)	1025(2)	35(1)
C(221)	-1403(3)	14755(3)	3060(3)	39(1)
C(222)	-3033(3)	12908(3)	3673(3)	37(1)
C(223)	-1679(3)	14610(3)	4661(3)	42(1)
C(224)	-1171(3)	13048(3)	3252(3)	44(1)
C(231)	-4242(3)	17257(3)	2664(2)	38(1)
C(232)	-5172(3)	15971(2)	3303(3)	35(1)
C(233)	-2878(3)	16424(2)	3790(2)	30(1)
C(234)	-5286(3)	15341(3)	1420(3)	38(1)
C(235)	-3110(3)	16037(2)	1888(2)	31(1)
C(241)	-5179(2)	13824(2)	2874(2)	26(1)
C(242)	-6222(2)	13408(2)	2126(2)	34(1)
C(243)	-7217(3)	13117(3)	2313(3)	38(1)
C(244)	-7170(3)	13247(3)	3272(3)	46(1)
C(245)	-6152(3)	13659(3)	4021(3)	51(1)
C(246)	-5147(3)	13953(3)	3850(2)	38(1)

Table A VI. 2 Bond lengths [Å] and angles [degrees] for $FeMn(CO)_8[\mu\text{-}PPh(Mn(CO)_5)]$.

Fe(1A)-C(113)	1.795(4)	O(123)-C(123)	1.144(4)
Fe(1A)-C(114)	1.801(4)	O(124)-C(124)	1.135(4)
Fe(1A)-C(112)	1.809(4)	O(131)-C(131)	1.125(4)
Fe(1A)-C(111)	1.815(4)	O(132)-C(132)	1.124(4)
Fe(1A)-P(1)	2.3067(10)	O(133)-C(133)	1.135(4)
Fe(1A)-Fe(1B)	2.7955(8)	O(134)-C(134)	1.130(4)
Fe(1B)-C(123)	1.801(4)	O(135)-C(135)	1.134(4)
Fe(1B)-C(124)	1.827(4)	O(211)-C(211)	1.137(3)
Fe(1B)-C(122)	1.841(4)	O(212)-C(212)	1.127(4)
Fe(1B)-C(121)	1.847(4)	O(213)-C(213)	1.142(4)
Fe(1B)-P(1)	2.2891(9)	O(214)-C(214)	1.151(4)
Mn(3A)-C(131)	1.845(4)	O(221)-C(221)	1.132(4)
Mn(3A)-C(133)	1.853(4)	O(222)-C(222)	1.142(4)
Mn(3A)-C(135)	1.859(4)	O(223)-C(223)	1.133(4)
Mn(3A)-C(134)	1.872(4)	O(224)-C(224)	1.151(4)
Mn(3A)-C(132)	1.874(4)	O(231)-C(231)	1.146(4)
Mn(3A)-P(1)	2.4775(10)	O(232)-C(232)	1.125(4)
Fe(2A)-C(213)	1.783(4)	O(233)-C(233)	1.142(4)
Fe(2A)-C(214)	1.814(4)	O(234)-C(234)	1.128(4)
Fe(2A)-C(211)	1.834(3)	O(235)-C(235)	1.126(3)
Fe(2A)-C(212)	1.834(3)	C(141)-C(146)	1.399(4)
Fe(2A)-P(2)	2.3030(10)	C(141)-C(142)	1.406(4)
Fe(2A)-Fe(2B)	2.7918(8)	C(142)-C(143)	1.362(4)
Fe(2B)-C(223)	1.791(4)	C(142)-H(14A)	0.94
Fe(2B)-C(224)	1.795(4)	C(143)-C(144)	1.379(4)
Fe(2B)-C(222)	1.811(4)	C(143)-H(14B)	0.94
Fe(2B)-C(221)	1.825(4)	C(144)-C(145)	1.376(4)
Fe(2B)-P(2)	2.2997(9)	C(144)-H(14C)	0.94
Mn(3B)-C(231)	1.830(4)	C(145)-C(146)	1.367(4)
Mn(3B)-C(233)	1.845(3)	C(145)-H(14D)	0.94
Mn(3B)-C(234)	1.850(4)	C(146)-H(14E)	0.94
Mn(3B)-C(235)	1.866(3)	C(241)-C(242)	1.376(4)
Mn(3B)-C(232)	1.882(4)	C(241)-C(246)	1.401(4)
Mn(3B)-P(2)	2.4777(10)	C(242)-C(243)	1.384(4)
P(1)-C(141)	1.837(3)	C(242)-H(24A)	0.94
P(2)-C(241)	1.845(3)	C(243)-C(244)	1.371(5)
O(111)-C(111)	1.138(4)	C(243)-H(24B)	0.94
O(112)-C(112)	1.136(4)	C(244)-C(245)	1.356(5)
O(113)-C(113)	1.141(4)	C(244)-H(24C)	0.94
O(114)-C(114)	1.152(4)	C(245)-C(246)	1.384(4)
O(121)-C(121)	1.136(4)	C(245)-H(24D)	0.94
O(122)-C(122)	1.143(4)	C(246)-H(24E)	0.94

C(113)-Fe(1A)-C(114)	103.67(14)	C(132)-Mn(3A)-P(1)	90.87(10)
C(113)-Fe(1A)-C(112)	92.41(15)	C(213)-Fe(2A)-C(214)	104.45(15)
C(114)-Fe(1A)-C(112)	87.54(14)	C(213)-Fe(2A)-C(211)	88.44(15)
C(113)-Fe(1A)-C(111)	94.53(15)	C(214)-Fe(2A)-C(211)	88.20(14)
C(114)-Fe(1A)-C(111)	89.79(15)	C(213)-Fe(2A)-C(212)	90.16(15)
C(112)-Fe(1A)-C(111)	172.99(15)	C(214)-Fe(2A)-C(212)	86.60(14)
C(113)-Fe(1A)-P(1)	105.02(10)	C(211)-Fe(2A)-C(212)	174.10(14)
C(114)-Fe(1A)-P(1)	151.27(11)	C(213)-Fe(2A)-P(2)	105.25(11)
C(112)-Fe(1A)-P(1)	89.64(10)	C(214)-Fe(2A)-P(2)	150.16(11)
C(111)-Fe(1A)-P(1)	89.59(10)	C(211)-Fe(2A)-P(2)	95.43(10)
C(113)-Fe(1A)-Fe(1B)	156.95(10)	C(212)-Fe(2A)-P(2)	90.47(10)
C(114)-Fe(1A)-Fe(1B)	99.02(11)	C(213)-Fe(2A)-Fe(2B)	157.71(11)
C(112)-Fe(1A)-Fe(1B)	84.48(11)	C(214)-Fe(2A)-Fe(2B)	97.81(11)
C(111)-Fe(1A)-Fe(1B)	89.54(11)	C(211)-Fe(2A)-Fe(2B)	91.15(11)
P(1)-Fe(1A)-Fe(1B)	52.25(2)	C(212)-Fe(2A)-Fe(2B)	92.32(10)
C(123)-Fe(1B)-C(124)	103.69(16)	P(2)-Fe(2A)-Fe(2B)	52.60(3)
C(123)-Fe(1B)-C(122)	87.22(17)	C(223)-Fe(2B)-C(224)	103.49(16)
C(124)-Fe(1B)-C(122)	88.37(15)	C(223)-Fe(2B)-C(222)	89.91(16)
C(123)-Fe(1B)-C(121)	85.76(16)	C(224)-Fe(2B)-C(222)	89.99(16)
C(124)-Fe(1B)-C(121)	90.19(15)	C(223)-Fe(2B)-C(221)	90.65(16)
C(122)-Fe(1B)-C(121)	172.29(15)	C(224)-Fe(2B)-C(221)	90.00(15)
C(123)-Fe(1B)-P(1)	110.26(11)	C(222)-Fe(2B)-C(221)	179.43(16)
C(124)-Fe(1B)-P(1)	145.93(11)	C(223)-Fe(2B)-P(2)	109.86(11)
C(122)-Fe(1B)-P(1)	90.40(11)	C(224)-Fe(2B)-P(2)	146.64(12)
C(121)-Fe(1B)-P(1)	95.01(10)	C(222)-Fe(2B)-P(2)	90.57(11)
C(123)-Fe(1B)-Fe(1A)	162.68(11)	C(221)-Fe(2B)-P(2)	89.12(11)
C(124)-Fe(1B)-Fe(1A)	93.45(11)	C(223)-Fe(2B)-Fe(2A)	162.54(11)
C(122)-Fe(1B)-Fe(1A)	95.86(11)	C(224)-Fe(2B)-Fe(2A)	93.94(12)
C(121)-Fe(1B)-Fe(1A)	91.78(11)	C(222)-Fe(2B)-Fe(2A)	89.30(11)
P(1)-Fe(1B)-Fe(1A)	52.82(3)	C(221)-Fe(2B)-Fe(2A)	90.13(11)
C(131)-Mn(3A)-C(133)	95.58(15)	P(2)-Fe(2B)-Fe(2A)	52.71(2)
C(131)-Mn(3A)-C(135)	86.56(15)	C(231)-Mn(3B)-C(233)	92.44(14)
C(133)-Mn(3A)-C(135)	88.80(15)	C(231)-Mn(3B)-C(234)	95.51(15)
C(131)-Mn(3A)-C(134)	95.30(14)	C(233)-Mn(3B)-C(234)	171.92(14)
C(133)-Mn(3A)-C(134)	169.12(14)	C(231)-Mn(3B)-C(235)	86.85(14)
C(135)-Mn(3A)-C(134)	91.56(15)	C(233)-Mn(3B)-C(235)	90.98(13)
C(131)-Mn(3A)-C(132)	87.50(15)	C(234)-Mn(3B)-C(235)	88.03(14)
C(133)-Mn(3A)-C(132)	90.70(14)	C(231)-Mn(3B)-C(232)	89.41(14)
C(135)-Mn(3A)-C(132)	173.96(14)	C(233)-Mn(3B)-C(232)	91.63(14)
C(134)-Mn(3A)-C(132)	90.06(15)	C(234)-Mn(3B)-C(232)	89.89(15)
C(131)-Mn(3A)-P(1)	178.29(12)	C(235)-Mn(3B)-C(232)	175.53(14)
C(133)-Mn(3A)-P(1)	83.92(10)	C(231)-Mn(3B)-P(2)	178.84(11)
C(135)-Mn(3A)-P(1)	95.06(10)	C(233)-Mn(3B)-P(2)	86.44(10)
C(134)-Mn(3A)-P(1)	85.22(10)	C(234)-Mn(3B)-P(2)	85.62(11)

C(235)-Mn(3B)-P(2)	93.48(10)	C(141)-C(146)-H(14E)	119.2
C(232)-Mn(3B)-P(2)	90.31(10)	O(211)-C(211)-Fe(2A)	172.8(3)
C(141)-P(1)-Fe(1B)	113.70(10)	O(212)-C(212)-Fe(2A)	174.2(3)
C(141)-P(1)-Fe(1A)	111.32(10)	O(213)-C(213)-Fe(2A)	178.9(4)
Fe(1B)-P(1)-Fe(1A)	74.93(3)	O(214)-C(214)-Fe(2A)	178.5(3)
C(141)-P(1)-Mn(3A)	101.45(9)	O(221)-C(221)-Fe(2B)	176.8(3)
Fe(1B)-P(1)-Mn(3A)	128.73(4)	O(222)-C(222)-Fe(2B)	175.0(3)
Fe(1A)-P(1)-Mn(3A)	125.66(4)	O(223)-C(223)-Fe(2B)	177.5(3)
C(241)-P(2)-Fe(2B)	115.43(10)	O(224)-C(224)-Fe(2B)	178.6(4)
C(241)-P(2)-Fe(2A)	109.75(10)	O(231)-C(231)-Mn(3B)	178.2(3)
Fe(2B)-P(2)-Fe(2A)	74.68(3)	O(232)-C(232)-Mn(3B)	175.8(3)
C(241)-P(2)-Mn(3B)	101.91(10)	O(233)-C(233)-Mn(3B)	179.5(3)
Fe(2B)-P(2)-Mn(3B)	124.66(4)	O(234)-C(234)-Mn(3B)	178.7(3)
Fe(2A)-P(2)-Mn(3B)	129.47(4)	O(235)-C(235)-Mn(3B)	173.2(3)
O(111)-C(111)-Fe(1A)	176.0(3)	C(242)-C(241)-C(246)	117.8(3)
O(112)-C(112)-Fe(1A)	174.7(3)	C(242)-C(241)-P(2)	120.3(2)
O(113)-C(113)-Fe(1A)	178.4(3)	C(246)-C(241)-P(2)	121.9(2)
O(114)-C(114)-Fe(1A)	178.5(3)	C(241)-C(242)-C(243)	122.1(3)
O(121)-C(121)-Fe(1B)	172.1(3)	C(241)-C(242)-H(24A)	118.9
O(122)-C(122)-Fe(1B)	174.2(3)	C(243)-C(242)-H(24A)	118.9
O(123)-C(123)-Fe(1B)	178.1(4)	C(244)-C(243)-C(242)	119.4(3)
O(124)-C(124)-Fe(1B)	176.5(3)	C(244)-C(243)-H(24B)	120.3
O(131)-C(131)-Mn(3A)	178.8(3)	C(242)-C(243)-H(24B)	120.3
O(132)-C(132)-Mn(3A)	176.0(3)	C(245)-C(244)-C(243)	119.4(3)
O(133)-C(133)-Mn(3A)	179.0(3)	C(245)-C(244)-H(24C)	120.3
O(134)-C(134)-Mn(3A)	179.5(3)	C(243)-C(244)-H(24C)	120.3
O(135)-C(135)-Mn(3A)	173.3(3)	C(244)-C(245)-C(246)	122.2(3)
C(146)-C(141)-C(142)	117.0(3)	C(244)-C(245)-H(24D)	118.9
C(146)-C(141)-P(1)	121.1(2)	C(246)-C(245)-H(24D)	118.9
C(142)-C(141)-P(1)	121.8(2)	C(245)-C(246)-C(241)	119.1(3)
C(143)-C(142)-C(141)	120.9(3)	C(245)-C(246)-H(24E)	120.4
C(143)-C(142)-H(14A)	119.6	C(241)-C(246)-H(24E)	120.4
C(141)-C(142)-H(14A)	119.6		
C(142)-C(143)-C(144)	120.7(3)		
C(142)-C(143)-H(14B)	119.6		
C(144)-C(143)-H(14B)	119.6		
C(145)-C(144)-C(143)	119.7(3)		
C(145)-C(144)-H(14C)	120.1		
C(143)-C(144)-H(14C)	120.1		
C(146)-C(145)-C(144)	120.0(3)		
C(146)-C(145)-H(14D)	120		
C(144)-C(145)-H(14D)	120		
C(145)-C(146)-C(141)	121.6(3)		
C(145)-C(146)-H(14E)	119.2		

Table A VI. 3 Anisotropic displacement parameters ($Å^2 \times 10^3$) for $FeMn(CO)_8[\mu\text{-}PPh(Mn(CO)_5)]$. The anisotropic displacement factor exponent takes the form: $-2\pi^2[(ha^*)^2U_{11} + ... + 2\ h\ k\ a^*b^*U_{12}]$

	U11	U22	U33	U23	U13	U12
Fe(1A)	22(1)	25(1)	28(1)	3(1)	10(1)	3(1)
Mn(1A)	22(1)	25(1)	28(1)	3(1)	10(1)	3(1)
Fe(1B)	34(1)	36(1)	27(1)	10(1)	6(1)	11(1)
Mn(1B)	34(1)	36(1)	27(1)	10(1)	6(1)	11(1)
Mn(3A)	27(1)	32(1)	32(1)	12(1)	14(1)	11(1)
Fe(2A)	30(1)	30(1)	30(1)	8(1)	15(1)	7(1)
Mn(2A)	30(1)	30(1)	30(1)	8(1)	15(1)	7(1)
Fe(2B)	23(1)	31(1)	37(1)	13(1)	2(1)	5(1)
Mn(2B)	23(1)	31(1)	37(1)	13(1)	2(1)	5(1)
Mn(3B)	29(1)	29(1)	26(1)	10(1)	10(1)	10(1)
P(1)	23(1)	25(1)	24(1)	8(1)	8(1)	6(1)
P(2)	21(1)	26(1)	22(1)	8(1)	7(1)	4(1)
O(111)	74(2)	36(2)	60(2)	1(2)	38(2)	11(1)
O(112)	45(2)	47(2)	41(2)	-6(1)	13(1)	14(1)
O(113)	55(2)	53(2)	53(2)	27(2)	21(1)	9(1)
O(114)	33(1)	48(2)	55(2)	-1(1)	7(1)	2(1)
O(121)	78(2)	65(2)	40(2)	9(2)	21(2)	33(2)
O(122)	70(2)	43(2)	51(2)	2(2)	8(2)	27(2)
O(123)	71(2)	69(2)	66(2)	44(2)	13(2)	-4(2)
O(124)	39(2)	85(2)	38(2)	10(2)	5(1)	24(2)
O(131)	51(2)	101(2)	88(2)	52(2)	44(2)	50(2)
O(132)	37(2)	77(2)	38(2)	11(2)	3(1)	14(1)
O(133)	62(2)	49(2)	45(2)	22(1)	25(1)	1(1)
O(134)	64(2)	70(2)	105(2)	67(2)	52(2)	37(2)
O(135)	61(2)	59(2)	47(2)	-6(2)	18(2)	14(2)
O(211)	65(2)	41(2)	64(2)	19(2)	39(2)	6(1)
O(212)	44(2)	46(2)	72(2)	24(2)	26(2)	2(1)
O(213)	49(2)	98(2)	38(2)	18(2)	10(1)	16(2)
O(214)	64(2)	51(2)	66(2)	22(2)	40(2)	29(2)
O(221)	43(2)	59(2)	67(2)	34(2)	9(1)	-5(1)
O(222)	69(2)	49(2)	62(2)	30(2)	6(2)	-7(2)
O(223)	73(2)	54(2)	43(2)	10(2)	-4(2)	12(2)
O(224)	64(2)	56(2)	89(2)	15(2)	24(2)	32(2)
O(231)	90(2)	35(2)	55(2)	17(2)	26(2)	26(2)
O(232)	50(2)	63(2)	61(2)	31(2)	33(2)	29(2)
O(233)	44(2)	41(2)	33(1)	9(1)	6(1)	3(1)
O(234)	61(2)	74(2)	43(2)	15(2)	-12(2)	6(2)
O(235)	45(2)	50(2)	42(2)	14(1)	22(1)	9(1)
C(111)	34(2)	35(2)	43(2)	12(2)	15(2)	1(2)

C(112)	27(2)	39(2)	33(2)	6(2)	6(2)	4(2)
C(113)	25(2)	36(2)	45(2)	10(2)	14(2)	2(2)
C(114)	40(2)	27(2)	34(2)	3(2)	14(2)	5(2)
C(121)	38(2)	40(2)	33(2)	15(2)	6(2)	12(2)
C(122)	41(2)	45(2)	36(2)	17(2)	1(2)	16(2)
C(123)	49(2)	46(2)	38(2)	20(2)	2(2)	15(2)
C(124)	39(2)	45(2)	29(2)	4(2)	8(2)	9(2)
C(131)	41(2)	51(2)	45(2)	22(2)	22(2)	20(2)
C(132)	28(2)	45(2)	41(2)	19(2)	12(2)	14(2)
C(133)	37(2)	39(2)	27(2)	5(2)	15(2)	8(2)
C(134)	36(2)	47(2)	50(2)	25(2)	21(2)	27(2)
C(135)	32(2)	34(2)	50(2)	15(2)	19(2)	12(2)
C(141)	19(2)	24(2)	28(2)	7(2)	5(1)	5(1)
C(142)	25(2)	31(2)	30(2)	13(2)	8(1)	6(2)
C(143)	29(2)	45(2)	25(2)	8(2)	7(2)	8(2)
C(144)	35(2)	34(2)	32(2)	3(2)	4(2)	6(2)
C(145)	30(2)	24(2)	48(2)	9(2)	7(2)	-1(2)
C(146)	29(2)	33(2)	32(2)	11(2)	10(2)	7(2)
C(211)	42(2)	26(2)	37(2)	7(2)	17(2)	10(2)
C(212)	29(2)	35(2)	31(2)	8(2)	10(2)	10(2)
C(213)	35(2)	61(3)	30(2)	9(2)	18(2)	12(2)
C(214)	36(2)	40(2)	33(2)	14(2)	17(2)	9(2)
C(221)	32(2)	36(2)	40(2)	10(2)	4(2)	9(2)
C(222)	38(2)	30(2)	35(2)	14(2)	-3(2)	1(2)
C(223)	37(2)	33(2)	44(2)	13(2)	-4(2)	5(2)
C(224)	41(2)	34(2)	44(2)	6(2)	3(2)	7(2)
C(231)	42(2)	45(2)	30(2)	10(2)	18(2)	14(2)
C(232)	37(2)	33(2)	38(2)	14(2)	13(2)	16(2)
C(233)	35(2)	26(2)	33(2)	9(2)	18(2)	7(2)
C(234)	39(2)	41(2)	36(2)	18(2)	8(2)	12(2)
C(235)	39(2)	25(2)	27(2)	8(2)	9(2)	10(2)
C(241)	23(2)	23(2)	32(2)	8(2)	11(1)	5(1)
C(242)	26(2)	43(2)	29(2)	9(2)	7(2)	10(2)
C(243)	20(2)	44(2)	48(2)	15(2)	7(2)	6(2)
C(244)	38(2)	51(2)	62(3)	25(2)	29(2)	14(2)
C(245)	50(2)	70(3)	38(2)	22(2)	24(2)	4(2)
C(246)	33(2)	48(2)	28(2)	11(2)	8(2)	-1(2)

Table A VI. 4 Hydrogen coordinates (× 10^4) and isotropic displacement parameters ($Å^2$ × 10^3) for $FeMn(CO)_8[\mu\text{-}PPh(Mn(CO)_5)]$.

	x	y	z	U(eq)
H(14A)	841	8473	261	33
H(14B)	90	7170	-1229	40
H(14C)	-860	5637	-1320	45
H(14D)	-1054	5417	107	44
H(14E)	-221	6683	1621	37
H(24A)	-6261	13318	1467	41
H(24B)	-7918	12833	1787	46
H(24C)	-7839	13052	3410	55
H(24D)	-6127	13749	4677	61
H(24E)	-4451	14235	4383	45

Appendix VII: Supplemental X-ray diffraction data for $FeMn(CO)_8[\mu\text{-}PPh(AuPPh_3)]$

[38] I. E. Zanin, K. B. Aleinikova, M. M. Afanasiev, M. Y. Antipin, *J. Struct. Chem.* **2004**, *45*, 844-848.

[39] M. Rubenstein, P. J. Dean, *J. Appl. Phys.* **1970**, *41*, 1777-1786.

[40] A. Dommann, R. E. Marsh, F. Hulliger, *J. Less-Common Met.* **1989**, *152*, 1-6.

[41] K. Sierański, J. Szatkowski, J. Misiewicz, *Phys. Rev. B: Condens. Matter* **1994**, *50*, 7331.

[42] M. E. Senko, H. M. Dunn, J. Neidenborner, H. Cole, *Acta Crystallogr.* **1959**, *12*, 76.

[43] E. Brück, O. Tegus, X. W. Li, F. R. de Boer, K. H. J. Buschow, *Physica B* **2003**, *327*, 431-437.

[44] L. Häggström, A. Narayanasamy, *J. Magn. Magn. Mater.* **1982**, *30*, 249-256.

[45] F. Hulliger, *Struct. Bond.* **1968**, *4*, 83-229.

[46] S. Ishida, et al., *J. Phys. F: Met. Phys.* **1987**, *17*, 475.

[47] T. Suzuki, Y. Yamaguchi, H. Yamamoto, H. Watanabe, *J. Phys. Soc. Jpn.* **1973**, *34*, 911.

[48] S. Yoshii, H. Katsuraki, *J. Phys. Soc. Jpn.* **1966**, *21*, 205.

[49] R. Zach, M. Guillot, R. Fruchart, *J. Magn. Magn. Mater.* **1990**, *89*, 221-228.

[50] V. A. Chernenko, L. Wee, P. G. McCormick, R. Street, *J. Appl. Phys.* **1999**, *85*, 7833-7837.

[51] O. Tegus, E. Brück, K. H. J. Buschow, F. R. de Boer, *Nature* **2002**, *415*, 150-152.

[52] S. J. Pearton, C. R. Abernathy, D. P. Norton, A. F. Hebard, Y. D. Park, L. A. Boatner, J. D. Budai, *Mater. Sci. Eng., R* **2003**, *40*, 137-168.

[53] S. T. Oyama, *J. Catal.* **2003**, *216*, 343-352.

[54] A. W. Burns, A. F. Gaudette, M. E. Bussell, *J. Catal.* **2008**, *260*, 262-269.

[55] R. Fruchart, A. Roger, J. P. Senateur, *J. Appl. Phys.* **1969**, *40*, 1250-1257.

[56] M. Bacmann, J.-L. Soubeyroux, R. Barrett, D. Fruchart, R. Zach, S. Niziol, R. Fruchart, *J. Magn. Magn. Mater.* **1994**, *134*, 59-67.

[73] T. Thomas, C. S. Blackman, I. P. Parkin, C. J. Carmalt, *Eur. J. Inorg. Chem.* **2010**, *2010*, 5629-5634.

[74] C. S. Blackman, C. J. Carmalt, S. A. O'Neill, I. P. Parkin, L. Apostolico, K. C. Molloy, *Chem. Mater.* **2004**, *16*, 1120-1125.

[75] C. S. Blackman, C. J. Carmalt, S. A. O'Neill, I. P. Parkin, K. C. Molloy, L. Apostolico, *J. Mater. Chem.* **2003**, *13*, 1930-1935.

[76] J. T. Scheper, K. C. Jayaratne, L. M. Liable-Sands, G. P. A. Yap, A. L. Rheingold, C. H. Winter, *Inorg. Chem.* **1999**, *38*, 4354-4360.

[77] I. M. Watson, J. A. Connor, R. Whyman, *Thin Solid Films* **1991**, *196*, L21-L24.

[78] C. S. Blackman, C. J. Carmalt, T. D. Manning, I. P. Parkin, L. Apostolico, K. C. Molloy, *Appl. Surf. Sci.* **2004**, *233*, 24-28.

[79] C. S. Blackman, C. J. Carmalt, T. D. Manning, S. A. O'Neill, I. P. Parkin, L. Apostolico, K. C. Molloy, *Chem. Vap. Deposition* **2003**, *9*, 10-13.

[80] S. Motojima, T. Wakamatsu, K. Sugiyama, *J. Less-Common Met.* **1981**, *82*, 379-383.

[81] J. Choi, S. Choi, M. H. Sohn, H. Park, Y. Park, H.-M. Park, S. C. Hong, S. Cho, *J. Magn. Magn. Mater.* **2006**, *304*, e112-e114.

[82] M. Solzi, C. Pernechele, M. Ghidini, M. Natali, M. Bolzan, *J. Magn. Magn. Mater.* **2010**, *322*, 1565-1568.

[83] P. J. Walsh, N. Bottka, *J. Electrochem. Soc.* **1984**, *131*, 444-446.

[84] J. Shin, A. Waheed, K. Agapiou, W. A. Winkenwerder, H.-W. Kim, R. A. Jones, G. S. Hwang, J. G. Ekerdt, *J. Am. Chem. Soc.* **2006**, *128*, 16510-16511.

[85] A. Panneerselvam, C. Q. Nguyen, J. Waters, M. A. Malik, P. O'Brien, J. Raftery, M. Helliwell, *Dalton Trans.* **2008**, 4499-4506.

[86] F.-R. Klingan, A. Miehr, R. A. Fischer, W. A. Herrmann, *Appl. Phys. Lett.* **1995**, *67*, 822-824.

[87] A. Panneerselvam, M. A. Malik, M. Afzaal, P. O'Brien, M. Helliwell, *J. Am. Chem. Soc.* **2008**, *130*, 2420-2421.

[88] J. A. Glass Jr, J. T. Spencer, *Thin Solid Films* **1998**, *322*, 138-142.

[89] K. Yasufuku, H. Yamazaki, *J. Organomet. Chem.* **1971**, *28*, 415-421.

Table A VII. 1 Atomic coordinates [× 10^4] and equivalent isotropic displacement parameters [$Å^2$ × 10^3] for $FeMn(CO)_8[\mu\text{-}PPh(AuPPh_3)]$. U(eq) is defined as one third of the trace of the orthogonalized U_{ij} tensor.

	x	y	z	U(eq)
Au(1)	-1(1)	7659(1)	1425(1)	24(1)
Mn(1)	1633(1)	8971(1)	773(1)	25(1)
Fe(1)	1633(1)	8971(1)	773(1)	25(1)
Mn(2)	755(1)	10616(1)	1098(1)	33(1)
Fe(2)	755(1)	10616(1)	1098(1)	33(1)
P(1)	874(1)	8968(1)	1418(1)	24(1)
P(2)	-788(1)	6251(1)	1378(1)	23(1)
C(111)	868(2)	8649(3)	399(1)	38(1)
C(112)	2391(2)	9395(3)	1136(1)	38(1)
C(113)	1921(2)	7622(3)	763(2)	42(1)
C(114)	2080(2)	9560(3)	266(1)	40(1)
C(121)	-68(2)	10145(3)	807(2)	45(1)
C(122)	1493(2)	11068(3)	1472(2)	47(1)
C(123)	187(2)	11471(4)	1426(2)	61(1)
C(124)	1066(2)	11394(3)	595(2)	47(1)
C(141)	-476(2)	5304(2)	940(1)	25(1)
C(142)	258(2)	5052(3)	929(1)	35(1)
C(152)	-894(2)	4399(3)	1918(1)	39(1)
C(143)	505(2)	4292(3)	619(1)	44(1)
C(153)	-971(2)	3857(3)	2342(2)	53(1)
C(145)	-685(2)	4047(3)	314(1)	39(1)
C(146)	-947(2)	4799(3)	630(1)	33(1)
C(151)	-880(2)	5496(2)	1918(1)	25(1)
C(155)	-1033(2)	5491(4)	2760(1)	48(1)
C(156)	-942(2)	6039(3)	2342(1)	36(1)
C(161)	-1701(2)	6618(2)	1205(1)	27(1)
C(162)	-2304(2)	6170(3)	1412(2)	46(1)
C(163)	-2987(2)	6483(4)	1271(2)	63(1)
C(164)	-3075(2)	7220(4)	920(2)	58(1)
C(165)	-2481(2)	7662(3)	709(2)	54(1)
C(166)	-1793(2)	7378(3)	852(1)	39(1)
O(111)	410(2)	8409(3)	151(1)	65(1)
O(112)	2896(2)	9619(3)	1341(1)	68(1)
O(113)	2086(2)	6755(2)	749(1)	74(1)
O(114)	2375(2)	9922(3)	-51(1)	66(1)
O(121)	-612(2)	9894(3)	653(1)	70(1)
O(123)	-177(2)	12015(4)	1644(2)	108(2)
O(124)	1267(2)	11879(3)	283(1)	69(1)
C(144)	39(2)	3794(3)	309(1)	39(1)

C(131)	1292(2)	8895(3)	2005(1)	31(1)
O(122)	1911(2)	11403(3)	1728(1)	85(1)
C(132)	1867(2)	8234(4)	2102(1)	48(1)
C(154)	-1038(2)	4404(4)	2760(1)	51(1)
C(136)	1002(3)	9462(4)	2379(2)	64(1)
C(133)	2149(3)	8163(5)	2555(2)	70(2)
C(134)	1865(3)	8745(5)	2916(2)	77(2)
C(135)	1295(4)	9375(5)	2831(2)	85(2)

Table A VII. 2 Bond lengths [Å] and angles [degrees] for $FeMn(CO)_8[\mu\text{-}PPh(AuPPh_3)]$.

Au(1)-P(2)	2.3009(8)	C(155)-H(15C)	0.93
Au(1)-P(1)	2.3125(8)	C(156)-H(15D)	0.93
Mn(1)-C(113)	1.785(4)	C(161)-C(162)	1.378(5)
Mn(1)-C(111)	1.810(4)	C(161)-C(166)	1.392(5)
Mn(1)-C(114)	1.812(4)	C(162)-C(163)	1.382(5)
Mn(1)-C(112)	1.817(4)	C(162)-H(16A)	0.93
Mn(1)-P(1)	2.2970(9)	C(163)-C(164)	1.370(6)
Mn(1)-Mn(2)	2.7895(7)	C(163)-H(16B)	0.93
Mn(2)-C(123)	1.769(4)	C(164)-C(165)	1.367(6)
Mn(2)-C(122)	1.817(4)	C(164)-H(16C)	0.93
Mn(2)-C(124)	1.818(5)	C(165)-C(166)	1.381(6)
Mn(2)-C(121)	1.827(4)	C(165)-H(16D)	0.93
Mn(2)-P(1)	2.2784(10)	C(166)-H(16E)	0.93
P(1)-C(131)	1.830(3)	C(144)-H(14E)	0.93
P(2)-C(151)	1.806(3)	C(131)-C(132)	1.378(5)
P(2)-C(141)	1.813(3)	C(131)-C(136)	1.383(5)
P(2)-C(161)	1.817(3)	C(132)-C(133)	1.381(6)
C(111)-O(111)	1.139(4)	C(132)-H(13A)	0.93
C(112)-O(112)	1.133(4)	C(154)-H(15E)	0.93
C(113)-O(113)	1.136(5)	C(136)-C(135)	1.389(7)
C(114)-O(114)	1.141(4)	C(136)-H(13B)	0.93
C(121)-O(121)	1.140(5)	C(133)-C(134)	1.360(8)
C(122)-O(122)	1.137(5)	C(133)-H(13C)	0.93
C(123)-O(123)	1.142(5)	C(134)-C(135)	1.341(9)
C(124)-O(124)	1.135(5)	C(134)-H(13D)	0.93
C(141)-C(146)	1.387(4)	C(135)-H(13E)	0.93
C(141)-C(142)	1.393(5)		
C(142)-C(143)	1.376(5)		
C(142)-H(14A)	0.93		
C(152)-C(153)	1.385(5)		
C(152)-C(151)	1.386(5)		
C(152)-H(15A)	0.93		
C(143)-C(144)	1.379(5)		
C(143)-H(14B)	0.93		
C(153)-C(154)	1.371(6)		
C(153)-H(15B)	0.93		
C(145)-C(144)	1.375(5)		
C(145)-C(146)	1.391(5)		
C(145)-H(14C)	0.93		
C(146)-H(14D)	0.93		
C(151)-C(156)	1.383(5)		
C(155)-C(154)	1.373(6)		
C(155)-C(156)	1.378(5)		

P(2)-Au(1)-P(1)	173.70(3)	O(112)-C(112)-Mn(1)	175.0(4)
C(113)-Mn(1)-C(111)	90.55(17)	O(113)-C(113)-Mn(1)	177.9(4)
C(113)-Mn(1)-C(114)	104.12(18)	O(114)-C(114)-Mn(1)	178.6(4)
C(111)-Mn(1)-C(114)	89.35(18)	O(121)-C(121)-Mn(2)	174.5(4)
C(113)-Mn(1)-C(112)	93.44(18)	O(122)-C(122)-Mn(2)	174.0(4)
C(111)-Mn(1)-C(112)	175.79(17)	O(123)-C(123)-Mn(2)	179.1(6)
C(114)-Mn(1)-C(112)	88.37(17)	O(124)-C(124)-Mn(2)	179.3(4)
C(113)-Mn(1)-P(1)	101.11(14)	C(146)-C(141)-C(142)	119.4(3)
C(111)-Mn(1)-P(1)	89.12(12)	C(146)-C(141)-P(2)	122.2(3)
C(114)-Mn(1)-P(1)	154.73(12)	C(142)-C(141)-P(2)	118.3(2)
C(112)-Mn(1)-P(1)	91.43(12)	C(143)-C(142)-C(141)	119.8(3)
C(113)-Mn(1)-Mn(2)	152.73(14)	C(143)-C(142)-H(14A)	120.1
C(111)-Mn(1)-Mn(2)	84.54(11)	C(141)-C(142)-H(14A)	120.1
C(114)-Mn(1)-Mn(2)	102.63(12)	C(153)-C(152)-C(151)	119.7(4)
C(112)-Mn(1)-Mn(2)	92.50(12)	C(153)-C(152)-H(15A)	120.1
P(1)-Mn(1)-Mn(2)	52.13(3)	C(151)-C(152)-H(15A)	120.1
C(123)-Mn(2)-C(122)	87.0(2)	C(142)-C(143)-C(144)	120.8(4)
C(123)-Mn(2)-C(124)	105.4(2)	C(142)-C(143)-H(14B)	119.6
C(122)-Mn(2)-C(124)	92.67(19)	C(144)-C(143)-H(14B)	119.6
C(123)-Mn(2)-C(121)	86.5(2)	C(154)-C(153)-C(152)	120.1(4)
C(122)-Mn(2)-C(121)	171.0(2)	C(154)-C(153)-H(15B)	119.9
C(124)-Mn(2)-C(121)	95.1(2)	C(152)-C(153)-H(15B)	119.9
C(123)-Mn(2)-P(1)	114.00(18)	C(144)-C(145)-C(146)	120.2(3)
C(122)-Mn(2)-P(1)	89.12(14)	C(144)-C(145)-H(14C)	119.9
C(124)-Mn(2)-P(1)	140.57(13)	C(146)-C(145)-H(14C)	119.9
C(121)-Mn(2)-P(1)	87.76(13)	C(141)-C(146)-C(145)	119.9(3)
C(123)-Mn(2)-Mn(1)	166.36(18)	C(141)-C(146)-H(14D)	120
C(122)-Mn(2)-Mn(1)	89.40(13)	C(145)-C(146)-H(14D)	120
C(124)-Mn(2)-Mn(1)	87.88(13)	C(156)-C(151)-C(152)	119.6(3)
C(121)-Mn(2)-Mn(1)	95.43(12)	C(156)-C(151)-P(2)	118.4(3)
P(1)-Mn(2)-Mn(1)	52.74(2)	C(152)-C(151)-P(2)	122.0(3)
C(131)-P(1)-Mn(2)	116.48(11)	C(154)-C(155)-C(156)	120.2(4)
C(131)-P(1)-Mn(1)	117.33(11)	C(154)-C(155)-H(15C)	119.9
Mn(2)-P(1)-Mn(1)	75.13(3)	C(156)-C(155)-H(15C)	119.9
C(131)-P(1)-Au(1)	104.57(11)	C(155)-C(156)-C(151)	120.0(4)
Mn(2)-P(1)-Au(1)	126.09(4)	C(155)-C(156)-H(15D)	120
Mn(1)-P(1)-Au(1)	115.71(4)	C(151)-C(156)-H(15D)	120
C(151)-P(2)-C(141)	104.89(15)	C(162)-C(161)-C(166)	119.1(3)
C(151)-P(2)-C(161)	105.88(14)	C(162)-C(161)-P(2)	122.1(3)
C(141)-P(2)-C(161)	106.28(15)	C(166)-C(161)-P(2)	118.8(3)
C(151)-P(2)-Au(1)	114.76(11)	C(161)-C(162)-C(163)	120.0(4)
C(141)-P(2)-Au(1)	110.39(10)	C(161)-C(162)-H(16A)	120
C(161)-P(2)-Au(1)	113.90(11)	C(163)-C(162)-H(16A)	120
O(111)-C(111)-Mn(1)	176.3(4)	C(164)-C(163)-C(162)	120.7(4)

C(164)-C(163)-H(16B)	119.7
C(162)-C(163)-H(16B)	119.7
C(165)-C(164)-C(163)	119.8(4)
C(165)-C(164)-H(16C)	120.1
C(163)-C(164)-H(16C)	120.1
C(164)-C(165)-C(166)	120.4(4)
C(164)-C(165)-H(16D)	119.8
C(166)-C(165)-H(16D)	119.8
C(165)-C(166)-C(161)	120.0(4)
C(165)-C(166)-H(16E)	120
C(161)-C(166)-H(16E)	120
C(145)-C(144)-C(143)	119.8(3)
C(145)-C(144)-H(14E)	120.1
C(143)-C(144)-H(14E)	120.1
C(132)-C(131)-C(136)	117.5(4)
C(132)-C(131)-P(1)	122.4(3)
C(136)-C(131)-P(1)	120.0(3)
C(131)-C(132)-C(133)	120.9(5)
C(131)-C(132)-H(13A)	119.6
C(133)-C(132)-H(13A)	119.6
C(153)-C(154)-C(155)	120.2(4)
C(153)-C(154)-H(15E)	119.9
C(155)-C(154)-H(15E)	119.9
C(131)-C(136)-C(135)	120.5(5)
C(131)-C(136)-H(13B)	119.8
C(135)-C(136)-H(13B)	119.8
C(134)-C(133)-C(132)	120.7(5)
C(134)-C(133)-H(13C)	119.7
C(132)-C(133)-H(13C)	119.7
C(135)-C(134)-C(133)	119.4(5)
C(135)-C(134)-H(13D)	120.3
C(133)-C(134)-H(13D)	120.3
C(134)-C(135)-C(136)	121.1(5)
C(134)-C(135)-H(13E)	119.5
C(136)-C(135)-H(13E)	119.5

Table A VII. 3 Anisotropic displacement parameters ($Å^2 \times 10^3$) for $FeMn(CO)_8[\mu\text{-}PPh(AuPPh_3)]$. The anisotropic displacement factor exponent takes the form: $-2\pi^2[(ha^*)^2U_{11} + ... + 2\ h\ k\ a^*b^*U_{12}]$

	U11	U22	U33	U23	U13	U12
Au(1)	19(1)	23(1)	30(1)	-2(1)	1(1)	-6(1)
Mn(1)	21(1)	26(1)	27(1)	-1(1)	1(1)	1(1)
Fe(1)	21(1)	26(1)	27(1)	-1(1)	1(1)	1(1)
Mn(2)	25(1)	20(1)	53(1)	-2(1)	1(1)	1(1)
Fe(2)	25(1)	20(1)	53(1)	-2(1)	1(1)	1(1)
P(1)	19(1)	24(1)	29(1)	-3(1)	1(1)	-6(1)
P(2)	20(1)	24(1)	26(1)	0(1)	1(1)	-6(1)
C(111)	43(2)	32(2)	38(2)	-6(2)	-5(2)	3(2)
C(112)	33(2)	46(2)	36(2)	6(2)	3(2)	-5(2)
C(113)	39(2)	40(2)	47(2)	-3(2)	-1(2)	10(2)
C(114)	44(2)	39(2)	36(2)	-1(2)	6(2)	-1(2)
C(121)	34(2)	34(2)	67(3)	3(2)	-2(2)	7(2)
C(122)	43(2)	39(2)	60(3)	-11(2)	8(2)	-16(2)
C(123)	43(2)	40(2)	99(4)	-21(2)	10(2)	2(2)
C(124)	34(2)	37(2)	69(3)	5(2)	3(2)	4(2)
C(141)	27(2)	25(2)	23(2)	1(1)	3(1)	-7(1)
C(142)	29(2)	44(2)	34(2)	-7(2)	-1(2)	-1(2)
C(152)	44(2)	34(2)	39(2)	3(2)	15(2)	6(2)
C(143)	36(2)	48(2)	47(2)	-8(2)	5(2)	6(2)
C(153)	62(3)	41(2)	55(2)	19(2)	23(2)	13(2)
C(145)	48(2)	34(2)	34(2)	-10(2)	-2(2)	-14(2)
C(146)	28(2)	35(2)	35(2)	-4(2)	-2(1)	-8(1)
C(151)	17(1)	31(2)	27(2)	4(1)	2(1)	0(1)
C(155)	51(2)	64(3)	28(2)	-1(2)	1(2)	5(2)
C(156)	35(2)	40(2)	32(2)	-2(2)	1(2)	-1(2)
C(161)	23(2)	26(2)	31(2)	1(1)	-3(1)	-1(1)
C(162)	26(2)	50(2)	62(3)	27(2)	-3(2)	-5(2)
C(163)	24(2)	75(3)	89(4)	37(3)	-4(2)	-2(2)
C(164)	31(2)	60(3)	82(3)	20(2)	-14(2)	9(2)
C(165)	46(2)	54(2)	60(3)	26(2)	-7(2)	7(2)
C(166)	36(2)	38(2)	44(2)	11(2)	1(2)	-6(2)
O(111)	66(2)	62(2)	68(2)	-20(2)	-35(2)	-5(2)
O(112)	43(2)	99(3)	61(2)	14(2)	-20(2)	-28(2)
O(113)	83(2)	40(2)	100(3)	-5(2)	-7(2)	27(2)
O(114)	81(2)	67(2)	50(2)	12(2)	27(2)	-8(2)
O(121)	36(2)	69(2)	105(3)	1(2)	-25(2)	-1(2)
O(123)	75(3)	83(3)	166(5)	-60(3)	33(3)	20(2)
O(124)	63(2)	61(2)	82(2)	29(2)	15(2)	7(2)
C(144)	52(2)	30(2)	36(2)	-7(2)	8(2)	0(2)

C(131)	28(2)	36(2)	30(2)	-1(2)	2(1)	-12(1)
O(122)	69(2)	95(3)	90(3)	-25(2)	-11(2)	-46(2)
C(132)	41(2)	66(3)	39(2)	20(2)	3(2)	3(2)
C(154)	49(2)	69(3)	34(2)	19(2)	13(2)	13(2)
C(136)	78(4)	73(3)	40(2)	-19(2)	-2(2)	10(3)
C(133)	56(3)	97(4)	58(3)	39(3)	-14(2)	-16(3)
C(134)	99(4)	88(4)	45(3)	23(3)	-29(3)	-57(4)
C(135)	133(6)	82(4)	38(3)	-22(3)	-3(3)	-22(4)

Table A VII. 4 Hydrogen coordinates (× 10^4) and isotropic displacement parameters (Å^2 × 10^3) for $FeMn(CO)_8[\mu\text{-}PPh(AuPPh_3)]$.

	x	y	z	U(eq)
H(14A)	579	5396	1130	42
H(15A)	-852	4028	1635	46
H(14B)	993	4112	618	53
H(15B)	-977	3121	2344	63
H(14C)	-1000	3714	104	47
H(14D)	-1438	4963	635	39
H(15C)	-1091	5858	3044	57
H(15D)	-922	6775	2345	43
H(16A)	-2250	5659	1646	55
H(16B)	-3392	6189	1416	75
H(16C)	-3537	7420	825	69
H(16D)	-2540	8157	468	64
H(16E)	-1391	7695	713	47
H(14E)	213	3288	98	47
H(13A)	2067	7830	1860	58
H(15E)	-1088	4037	3044	61
H(13B)	607	9905	2328	76
H(13C)	2537	7713	2614	84
H(13D)	2064	8706	3218	93
H(13E)	1093	9760	3079	101

Appendix VIII: Curriculum Vitae

Adam C. Colson

Rice University, MS-60
6100 Main Street
Houston, TX 77005-1892
(208) 406-6455
ac10@rice.edu

Education

December 2011 — **Ph.D. – Inorganic Chemistry**
Rice University
(Thesis Advisor – Kenton H. Whitmire) GPA 4.00

January 2010 — **Master of Arts - Chemistry**
Rice University GPA 4.00

May 2007 — **Bachelor of Science (w/ High Honors) - Chemistry**
Idaho State University GPA 3.97

Research Experience and Skills

- Trained in the synthesis and manipulation of air and moisture sensitive materials, especially low-valent transition metal complexes and pyrophoric main group compounds.
- Experienced in the synthesis and characterization of inorganic nanomaterials as well as rudimentary metalorganic chemical vapor deposition.
- Familiar with numerous molecular and materials analytical techniques, including GC-MS, NMR (^{1}H, ^{13}C, ^{31}P), FT-IR, X-ray photoelectron spectroscopy (XPS), transmission electron microscopy (TEM), inductively-coupled plasma optical emission spectroscopy (ICP-OES), scanning electron microscopy (SEM), atomic force microscopy (AFM), single-crystal and powder X-ray diffraction.
- Prepared research presentations for local, regional, and national scientific symposia and conferences.
- Authored technical papers for consideration in peer reviewed scholarly journals as well as internal technical correspondence.

Awards, Honors, and Scholarships

Rice University

- Stephen C. Hoffman Fellowship (Recognizes outstanding early achievement towards the Ph.D. Degree, 2009)
- Harry B. Weiser Teaching Award (In recognition of student teaching excellence, 2009)
- Harry B. Weiser Excellence in Leadership Award (For departmental service, particularly in the recruitment of talented prospective graduate students, 2011)

Idaho State University

- Member of the Honor Society of Phi Kappa Phi
- Member of the ISU Chapter of Mortar Board
- Member of the Golden Key International Honor Society

- Received Outstanding Senior Award from the local chapter of the American Chemical Society
- Graduated with High Honors in the top 5% of 2007 graduating class
- Two-year scholarship for tuition and fees from Department of Chemistry at Idaho State University (2005-2007)
- Teaching Assistantship from Department of Chemistry
- Received ACS Polymer Education Committee Award for Outstanding Performance in Organic Chemistry (2004) at Idaho State University

Professional Associations/Societies

- American Chemical Society
- Honor Society of Phi Kappa Phi
- Mortar Board Honor Society
- Golden Key International Honor Society

Publications

- **Colson, A.C.**; Chen, C.W.; Morosan, E.; Whitmire, K.H. "Synthesis of Phase-Pure Ferromagnetic Fe_3P Films from Single-Source Molecular Precursors" *Submitted for Review*
- **Colson, A.C.**; Whitmire, K.H. "Synthesis of Heterobimetallic Phosphide Films from Single-Source Molecular Precursors" *Submitted for Review*
- **Colson, A.C.**; Whitmire, K.H. "Synthesis of $Fe_{2-x}Mn_xP$ Nanoparticles from Single-Source Molecular Precursors" *Chemistry of Materials.* **2011**, *23*, 3731-3739.
- Stavila, V.; Bulimestru, I.; Gulea, A.; **Colson, A.C.**; Whitmire, K.H. "Hexaaquacobalt(II) and hexaaquanickel(II) bis(-pyridine-2,6-dicarboxylato)bis[(pyridine-2,6-dicarboxylato)bismuthate(III)] dihydrate" *Acta Cryst.* **2011**, *C67*, m65-m68.
- Mandal, T.; Piburn, G.; Stavila, V.; Rusakova, I.; Ould-Ely, T.; **Colson, A.C.**; Whitmire, K.H. "New Mixed Ligand Single-Source Precursors for PbS Nanoparticles and Their Solvothermal Decomposition to Anisotropic Nano- and Microstructures" *Chemistry of Materials.* **2011**, *23*, 4158-4169.
- **Colson, A.C.**; Whitmire, K.H. "Synthesis, Characterization, and Reactivity of the Heterometallic Dinuclear μ-PH_2 and μ-PPhH Complexes $FeMn(CO)_8(\mu\text{-}PH_2)$ and $FeMn(CO)_8(\mu\text{-}PPhH)$" *Organometallics.* **2010**, *29*, 4611-4618.

Presentations

- *Synthesis of heterometallic metal phosphides from single-source precursors*, 238th American Chemical Society National Meeting & Exposition, August 16-20, 2009, Washington DC. (Oral Presentation)
- *Progress toward the synthesis of nitrogen-substituted hexabenzocoronene derivatives* , 229th American Chemical Society National Meeting & Exposition, March 13-17, 2005, San Diego, CA. (Poster Sessions: Organic Division, Sci-Mix)
- *Synthesis and characterization of highly conjugated arenes as potential organic semiconductors,* 61st Northwest Regional Meeting of the American Chemical Society, June 25-28, 2006, Reno, NV. (Poster Session: Materials, Devices, and Nanoscience)
- *Dye-sensitized solar cell research at Idaho State University,* 2nd Annual AMI Semiconductor, Inc. Research Symposium, October 6, 2006, Pocatello, ID.

References

[1] R. Berger, *Acta Chem. Scand., Ser. A* **1981**, *A35*, 635-636.

[2] E. Parthé, E. Parthé, *Acta Crystallogr.* **1963**, *16*, 71.

[3] L. H. Brixner, *J. Inorg. Nucl. Chem.* **1960**, *15*, 199-201.

[4] T. Lundström, P. O. Snell, *Acta Chem. Scand.* **1967**, *21*, 1343-1352.

[5] T. Lundström, *Acta Chem. Scand.* **1963**, *17*, 1166-1167.

[6] R. Berger, L. E. Tergenius, *Acta Chem. Scand., Ser. A* **1976**, *A30*, 387-389.

[7] R. L. Ripley, *J. Less-Common Met.* **1962**, *4*, 496-503.

[8] F. Hulliger, *Nature (London, U. K.)* **1964**, *204*, 775.

[9] W. Jeitschko, U. Flörke, U. D. Scholz, *J. Solid State Chem.* **1984**, *52*, 320-326.

[10] P. V. M. Rao, H. D. Shashikala, K. S. Murthy, S. V. Suryanarayana, *J. Mater. Sci. Lett.* **1987**, *6*, 298-298.

[11] K. Selte, A. Kjekshus, A. F. Andresen, *Acta Chem. Scand.* **1972**, *26*, 4057-4062.

[12] R. J. Gambino, T. R. McGuire, Y. Nakamura, *J. Appl. Phys.* **1967**, *38*, 1253-1255.

[13] M. Artigas, M. Bacmann, D. Fruchart, R. Fruchart, *J. Solid State Chem.* **1996**, *123*, 306-312.

[14] S. Rundqvist, *Acta Chem. Scand.* **1962**, *16*, 287-292.

[15] W. Jeitschko, P. C. Donohue, *Acta Crystallogr., Sect. B: Struct. Sci* **1973**, *29*, 783-789.

[16] W. Jeitschko, P. C. Donohue, *Acta Crystallogr., Sect. B: Struct. Sci* **1972**, *28*, 1893-1898.

[17] M. Yuzuri, *J. Phys. Soc. Jpn.* **1960**, *15*, 2007-2012.

[18] H. Watanabe, N. Kazama, Y. Yamaguchi, M. Ohashi, *J. Appl. Phys.* **1969**, *40*, 1128-1129.

[19] S. Rundqvist, *Acta Chem. Scand.* **1962**, *16*, 992-998.

[20] R. Rühl, W. Jeitschko, *Acta Crystallogr., Sect. B: Struct. Sci* **1981**, *37*, 39-44.

[21] K. Cenzual, L. M. Gelato, M. Penzo, E. Parthé, *Acta Crystallogr., Sect. B: Struct. Sci* **1991**, *47*, 433-439.

[22] M. A. Nylund, M. M. A. Roger, J. P. Sénateur, R. Fruchart, *J. Solid State Chem.* **1972**, *4*, 115-122.

[23] G. E. Bacon, R. Street, *Nature (London, U. K.)* **1955**, *175*, 518.

[24] H. Fujii, Y. Uwatoko, K. Motoya, Y. Ito, T. Okamoto, *J. Phys. Soc. Jpn.* **1988**, *57*, 2143.

[25] E. Dahl, *Acta Chem. Scand.* **1969**, *23*, 2677-2684.

[26] W. Jeitschko, D. J. Braun, *Acta Crystallogr., Sect. B: Struct. Sci* **1978**, *34*, 3196-3201.

[27] A. Kjekshus, K. E. Skaug, *Acta Chem. Scand.* **1972**, *26*, 2554-2556.

[28] K. Selte, A. Kjekshus, *Acta Chem. Scand.* **1973**, *27*, 1448-1449.

[29] H. Holseth, A. Kjekshus, A. F. Andresen, *Acta Chem. Scand.* **1970**, *24*, 3309-3316.

[30] S. Rundqvist, *Acta Chem. Scand.* **1960**, *14*, 1961-1979.

[31] K. Selte, A. Kjekshus, *Acta Chem. Scand.* **1971**, *25*, 3277-3284.

[32] P. C. Donohue, T. A. Bither, H. S. Young, *Inorg. Chem.* **1968**, *7*, 998-1001.

[33] J. G. Thompson, A. D. Rae, R. L. Withers, T. R. Welberry, A. C. Willis, *J. Phys. C: Solid State Phys.* **1988**, *21*, 4007-4015.

[34] O. Olofsson, *Acta Chem. Scand.* **1972**, *26*, 2777-2787.

[35] R. O. Demchyna, S. I. Chykhrij, Y. B. Kuz,Äôma, *J. Alloys Compd.* **2002**, *345*, 170-174.

[36] R. D. Heyding, G. J. G. Despault, *Can. J. Chem.* **1960**, *38*, 2477-2481.

[37] J. Naud, P. Priest, *J. Solid State Chem.* **1974**, *9*, 48-53.

[57] E. Muthuswamy, P. R. Kharel, G. Lawes, S. L. Brock, *ACS Nano* **2009**, *3*, 2383-2393.

[58] A. T. Kelly, I. Rusakova, T. Ould-Ely, C. Hofmann, A. Lüttge, K. H. Whitmire, *Nano Lett.* **2007**, *7*, 2920-2925.

[59] J. Park, B. Koo, Y. Hwang, C. Bae, K. An, J.-G. Park, H. M. Park, T. Hyeon, *Angew. Chem. Int. Ed.* **2004**, *43*, 2282-2285.

[60] J.-H. Chen, M.-F. Tai, K.-M. Chi, *J. Mater. Chem.* **2004**, *14*, 296-298.

[61] J. Park, B. Koo, K. Y. Yoon, Y. Hwang, M. Kang, J.-G. Park, T. Hyeon, *J. Am. Chem. Soc.* **2005**, *127*, 8433-8440.

[62] C. Qian, F. Kim, L. Ma, F. Tsui, P. Yang, J. Liu, *J. Am. Chem. Soc.* **2004**, *126*, 1195-1198.

[63] S. C. Perera, P. S. Fodor, G. M. Tsoi, L. E. Wenger, S. L. Brock, *Chem. Mater.* **2003**, *15*, 4034-4038.

[64] K. A. Gregg, S. C. Perera, G. Lawes, S. Shinozaki, S. L. Brock, *Chem. Mater.* **2006**, *18*, 879-886.

[65] S. C. Perera, G. Tsoi, L. E. Wenger, S. L. Brock, *J. Am. Chem. Soc.* **2003**, *125*, 13960-13961.

[66] W. Maneeprakorn, M. A. Malik, P. O'Brien, *J. Mater. Chem.* **2010**, *20*, 2329-2335.

[67] D.-H. Ha, L. M. Moreau, C. R. Bealing, H. Zhang, R. G. Hennig, R. D. Robinson, *J. Mater. Chem.* **2011**, *21*, 11498-11510.

[68] K. Senevirathne, A. W. Burns, M. E. Bussell, S. L. Brock, *Adv. Funct. Mater.* **2007**, *17*, 3933-3939.

[69] K. Senevirathne, R. Tackett, P. R. Kharel, G. Lawes, K. Somaskandan, S. L. Brock, *ACS Nano* **2009**, *3*, 1129-1138.

[70] K. Y. Yoon, Y. Jang, J. Park, Y. Hwang, B. Koo, J.-G. Park, T. Hyeon, *J. Solid State Chem.* **2008**, *181*, 1609-1613.

[71] E. Ye, S.-Y. Zhang, S. H. Lim, M. Bosman, Z. Zhang, K. Y. Win, M.-Y. Han, *Chem. Eur. J.* **2011**, *17*, 5982-5988.

[72] R. G. Palgrave, I. P. Parkin, *New J. Chem.* **2006**, *30*, 505-514.

[90] L. Manojlovic-Muir, M. J. Mays, K. W. Muir, K. W. Woulfe, *J. Chem. Soc., Dalton Trans.* **1992**, 1531-1538.

[91] A. J. M. Caffyn, M. J. Mays, G. A. Solan, D. Braga, P. Sabatino, A. Tiripicchio, M. Tiripicchio-Camellini, *Organometallics* **1993**, *12*, 1876-1885.

[92] A. D. Harley, G. J. Guskey, G. L. Geoffroy, *Organometallics* **1983**, *2*, 53-59.

[93] A. D. Horton, M. J. Mays, P. R. Raithby, *J. Chem. Soc., Chem. Commun.* **1985**, 247-250.

[94] F. Allen, *Acta Crystallogr., Sect. B: Struct. Sci* **2002**, *58*, 380-388.

[95] I. J. Bruno, J. C. Cole, P. R. Edgington, M. Kessler, C. F. Macrae, P. McCabe, J. Pearson, R. Taylor, *Acta Crystallogr., Sect. B: Struct. Sci* **2002**, *58*, 389-397.

[96] J. Xiao, R. J. Puddephatt, *Coord. Chem. Rev.* **1995**, *143*, 457-500.

[97] M. M. Dell'Anna, S. J. Trepanier, R. McDonald, M. Cowie, *Organometallics* **2000**, *20*, 88-99.

[98] M. Hidai, A. Fukuoka, Y. Koyasu, Y. Uchida, *J. Mol. Catal.* **1986**, *35*, 29-37.

[99] T. Shima, H. Suzuki, *Organometallics* **2000**, *19*, 2420-2422.

[100] P. Kalck, *Polyhedron* **1988**, *7*, 2441-2450.

[101] R. D. Adams, T. S. Barnard, Z. Li, W. Wu, J. Yamamoto, *J. Am. Chem. Soc.* **1994**, *116*, 9103-9113.

[102] R. D. Adams, B. Captain, M. D. Smith, *Angew. Chem. Int. Ed.* **2006**, *45*, 1109-1112.

[103] R. D. Adams, T. S. Barnard, *Organometallics* **1998**, *17*, 2885-2890.

[104] D. D. Perrin, W. L. Armarego, *Purification of Laboratory Chemicals*, 5th ed., Pergamon Press, New York, **1993**.

[105] J. Holz, O. Zayas, H. Jiao, W. Baumann, A. Spannenberg, A. Monsees, T. H. Riermeier, J. Almena, R. Kadyrov, A. Börner, *Chemistry - A European Journal* **2006**, *12*, 5001-5013.

[106] K. J. Reimer, A. Shaver, *Inorg. Synth.* **1990**, *28*, 154-159.

[107] R. Bartsch, S. Hietkamp, S. Morton, O. Stelzer, *J. Organomet. Chem.* **1981**, *222*, 263-273.

[108] H. Schaefer, W. Leske, *Z. Anorg. Allg. Chem.* **1987**, *552*, 50-68.

[109] SAINTPlus, v. 7.23a ed., Bruker AXS Inc., Madison, WI, **2002**.

[110] G. M. Sheldrick, SADABS, v. 5.1 ed., University of Göttingen, Göttingen, **1997**.

[111] G. M. Sheldrick, SHELXTL, Univeristy of Göttingen, Göttingen, **2001**.

[112] G. Sheldrick, *Acta Crystallogr., Sect. A: Found. Crystallogr.* **2008**, *64*, 112-122.

[113] K. Brandenburg, v. 3.2e ed., Crystal Impact GbR, Bonn, Germany, **2010**.

[114] O. Kühl, *Phosphoros-31 NMR Spectroscopy*, Springer, Berlin, **2008**.

[115] J. E. Davies, M. J. Mays, E. J. Pook, P. R. Raithby, P. K. Tompkin, *J. Chem. Soc., Dalton Trans.* **1997**, 3283-3286.

[116] E. Lindner, T. Funk, *Chem. Ber.* **1991**, *124*, 1075-1082.

[117] J. Sugiura, T. Kakizawa, H. Hashimoto, H. Tobita, H. Ogino, *Organometallics* **2005**, *24*, 1099-1104.

[118] R. J. Doedens, W. T. Robinson, J. A. Ibers, *J. Am. Chem. Soc.* **1967**, *89*, 4323-4329.

[119] H. Vahrenkamp, *Z. Naturforsch., B: Anorg. Chem., Org. Chem.::::* **1975**, *30B*, 814-815.

[120] U. Flörke, H. J. Haupt, *Acta Crystallogr., Sect. C: Cryst. Struct. Commun.* **1995**, *51*, 573-575.

[121] K. Somaskandan, G. M. Tsoi, L. E. Wenger, S. L. Brock, *J. Mater. Chem.* **2010**, *20*, 375-380.

[122] O. Tegus, E. Brück, L. Zhang, Dagula, K. H. J. Buschow, F. R. de Boer, *Physica B* **2002**, *319*, 174-192.

[123] B. Chenevier, J. L. Soubeyroux, M. Bacmann, D. Fruchart, R. Fruchart, *Solid State Commun.* **1987**, *64*, 57-61.

[124] J. H. Thurston, K. H. Whitmire, *Inorganic Chemistry* **2003**, *42*, 2014-2023.

[125] A. Rousset, F. Chassagneux, J. Paris, *J. Mater. Sci.* **1986**, *21*, 3111-3115.

[126] J. Gopalakrishnan, *Chem. Mater.* **1995**, *7*, 1265-1275.

[127] T. Ould-Ely, J. H. Thurston, K. H. Whitmire, *Comptes Rendus Chimie* **2005**, *8*, 1906-1921.

[128] P. G. Hoertz, J. R. Niskala, P. Dai, H. T. Black, W. You, *J. Am. Chem. Soc.* **2008**, *130*, 9763-9772.

[129] A. P. Abbott, T. A. Claxton, J. Fawcett, J. C. Harper, *J. Chem. Soc., Faraday Trans.* **1996**, *92*, 1747-1749.

[130] J. Holz, O. Zayas, H. Jiao, W. Baumann, A. Spannenberg, A. Monsees, T. H. Riermeier, J. Almena, R. Kadyrov, A. Börner, *Chem. Eur. J.* **2006**, *12*, 5001-5013.

[131] A. C. Colson, K. H. Whitmire, *Organometallics* **2010**, *29*, 4611-4618.

[132] J. Park, K. An, Y. Hwang, J.-G. Park, H.-J. Noh, J.-Y. Kim, J.-H. Park, N.-M. Hwang, T. Hyeon, *Nat Mater* **2004**, *3*, 891-895.

[133] C. Hofmann, I. Rusakova, T. Ould-Ely, D. Prieto-Centurión, K. B. Hartman, A. T. Kelly, A. Lüttge, K. H. Whitmire, *Adv. Funct. Mater.* **2008**, *18*, 1661-1667.

[134] G. Bognolo, *Adv. Colloid Interface Sci.* **2003**, *106*, 169-181.

[135] S. P. Shields, V. N. Richards, W. E. Buhro, *Chem. Mater.* **2010**, *22*, 3212-3225.

[136] J. F. Bondi, K. D. Oyler, X. Ke, P. Schiffer, R. E. Schaak, *J. Am. Chem. Soc.* **2009**, *131*, 9144-9145.

[137] P. E. R. Blanchard, A. P. Grosvenor, R. G. Cavell, A. Mar, *Chem. Mater.* **2008**, *20*, 7081-7088.

[138] G. C. Allen, M. T. Curtis, A. J. Hooper, P. M. Tucker, *J. Chem. Soc., Dalton Trans.* **1974**, 1525-1530.

[139] J. C. Carver, G. K. Schweitzer, T. A. Carlson, *J. Chem. Phys.* **1972**, *57*, 973-982.

[140] H. J. Yang, H. J. Song, H. J. Shin, H. C. Choi, *Langmuir* **2005**, *21*, 9098-9102.

[141] B. J. Tan, K. J. Klabunde, T. Tanaka, H. Kanai, S. Yoshida, *J. Am. Chem. Soc.* **1988**, *110*, 5951-5958.

[142] D. Bellavance, M. Vlasse, B. Morris, A. Wold, *J. Solid State Chem.* **1969**, *1*, 82-87.

[143] J. Gopalakrishnan, S. Pandey, K. K. Rangan, *Chem. Mater.* **1997**, *9*, 2113-2116.

[144] G. Boda, B. Stenström, V. Sagredo, O. Beckman, B. Carlsson, S. Rundqvist, *Phys. Scr.* **1971**, *4*, 132.

[145] M. Sugitani, N. Kinomura, M. Koizumi, S. Kume, *J. Solid State Chem.* **1978**, *26*, 195-201.

[146] R. Gambino, *J. Appl. Phys.* **1967**, *38*, 1253.

[147] G. Huttner, J. Schneider, G. Mohr, J. Von Seyerl, *J. Organomet. Chem.* **1980**, *191*, 161-169.

[148] S. K. Zečević, J. B. Zotović, S. L. Gojković, V. Radmilović, *J. Electroanal. Chem.* **1998**, *448*, 245-252.

[149] K. Kamei, Y. Maehara, *J. Appl. Electrochem.* **1996**, *26*, 529-535.

[150] J. E. Mahan, A. Vantomme, *Phys. Rev. B: Condens. Matter* **2000**, *61*, 8516-8525.

[151] P. S. Ho, J. E. Lewis, H. S. Wildman, J. K. Howard, *Surf. Sci.* **1976**, *57*, 393-405.

[152] S. Hofmann, *Surf. Interface Anal.* **1980**, *2*, 148-160.

[153] S. Hofmann, *Rep. Prog. Phys.* **1998**, *61*, 827.

[154] J. Coburn, *J. Vac. Sci. Technol.* **1976**, *13*, 1037.

[155] H. W. Werner, N. Warmoltz, *Surf. Sci.* **1976**, *57*, 706-714.

[156] A. C. Colson, K. H. Whitmire, *Chem. Mater.* **2011**, *23*, 3731-3739.

[157] B. Chenevier, D. Fruchart, M. Bacmann, D. Boursier, R. Fruchart, *J. Phys. Condens. Matter* **1989**, *1*, 9599.